Experimental and Numerical Study of Composite Patch Repair on Open Hole Carbon Fiber Reinforced Polymer Panel under Tensile Loading

Mohammad Kashfuddoja

A Dissertation Submitted to
Indian Institute of Technology Hyderabad
In Partial Fulfillment of the Requirements for
The Degree of Doctor of Philosophy

भारतीय प्रौद्योगिकी संस्थान हैदराबाद
Indian Institute of Technology Hyderabad

Department of Mechanical and Aerospace Engineering

May 2014

Declaration

I declare that this written submission represents my ideas in my own words, and where ideas or words of others have been included, I have adequately cited and referenced the original sources. I also declare that I have adhered to all principles of academic honesty and integrity and have not misrepresented or fabricated or falsified any idea/data/fact/source in my submission. I understand that any violation of the above will be a cause for disciplinary action by the Institute and can also evoke penal action from the sources that have thus not been properly cited, or from whom proper permission has not been taken when needed.

_____

(Signature)

_____

(Mohammad Kashfuddoja)

_____

(ME10P003)

Approval Sheet

This Dissertation entitled Experimental and Numerical Study of Composite Patch Repair on Open Hole Carbon Fiber Reinforced Polymer Panel under Tensile Loading by Mohammad Kashfuddoja is approved for the degree of Doctor of Philosophy from IIT Hyderabad.

(Dr. M. Ramji) Adviser
Department of Mechanical and Aerospace Engineering
IIT Hyderabad

Acknowledgements

First of all, I would like to thank my PhD thesis advisor Dr. M. Ramji for his excellent guidance, patience, vital suggestions, continuous and instant support, consistent encouragement and motivation throughout my work. I wish to express a deep sense of gratitude towards him for encouraging and evaluating my reserach work.

I am very much grateful to Prof. V. Eswaran, Head, Department of Mechanical and Aerospace Engineering, for his continuous support throughout my research work, and for valuable suggestions and sufficient encouragement to pursue PhD degree on the first day of my joining.

I am highly obliged to Prof. K.V.L. Subramaniam (Head, Department of Civil Engineering, IIT Hyderabad), Dr. Pinaki P. Bhattacharjee (Head, Department of Material Science and Metallurgical Engineering, IIT Hyderabad), Dr. Abhay Sharma (Department of Mechanical and Aerospace Engineering) and Dr. Ashok Kumar Pandey (Department of Mechanical and Aerospace Engineering) for being on my Doctoral committee members and assessing my work constantly.

I am also thankful to Dr. Chandrika Prakash Vyasarayani (Department of Mechanical and Aerospace Engineering) for his valuable suggestions on optimization method.

I am very much grateful to Dr. R. Prasanth Kumar (Department of Mechanical and Aerospace Engineering) and Dr. B. Venkatesham (Department of Mechanical and Aerospace Engineering) for their informative and valuable lectures during my PhD course work.

I would also like to thank Dr. Viswanath Chinthapenta (Department of Mechanical and Aerospace Engineering) for his support, encouragement and for introducing me to Latex.

I am in debt to acknowledge all my teachers who have guided and supported me throughout my education.

The friendly nature, constant help and support of Mr. RGR Prasath, has been priceless on both academic and personal level for which I am extremely thankful.

I would like to express my sincere thanks to Mr. K. Sathyanarayana, Project Engineer, In charge, and all other staff members of Central Workshop, IIT Hyderabad, especially, Mr. A. Praveen Kumar, Mr. S. Jagadeesan, Mr. M. Praveen Kumar, Mr. R. Kiran Kumar, Mr. Velumurgan for their valuable help and support.

I am delighted to thank my fellow lab mates in Engineering Optics Lab, IIT Hyderabad, Mr. Bhanu Prakash. Mr. K. Amit, Mrs. R. Srilakshmi, Mr. Rahul Pai. Mr. Vikraant Veerkar, Mr. Jabir Ubaid, Mr. Viswajeet Bhise, Mr. Naresh Reddy, Mr. Prataprao Patil, Mr. Saranath, Mr. Sourabh Khedkar, Mr. Lokeshwara Rao, Mr. Yagnik, Mr. Milind, Mr. Yogesh, and Mr. Harilal, for providing a supportive and friendly environment.

I am delighted to thank my friends Mr. Hakimuddin, Mr. Zaid Ahmed, Mr. Murali K, Mr. Rajesh R, Mr. Harish, Mr. P. Kambli, Mr. S. Ali, Mr. Amir, Mr. Jagga, Mr. Pankaj, Mr. Karthik, Mr. Nageshwar Rao, Mr. Somashekhar, Mr. Raja, Mr. P. Srinivas, Mr. Shayantal Mandal, whose companionship has left with me a number of memories during my stay at IIT Hyderabad. I am very much thankful to all my friends in IIT Hyderabad for their help and support during the completion of my PhD degree.

My deepest gratitude goes to my father Prof. Mohammad Badruddoja, my mother and sisters for their understanding, untiring love that encouraged me to work hard and to continue pursuing PhD.

The financial support by Ministry of Human Resource Development (MHRD), Government of India and the facilities provided by IIT Hyderabad to carry out this research work are also greatly acknowledged.

Thanks to all.

– Mohammad Kashfuddoja –

Dedication

To

My Beloved Parents & Sisters

Abstract

Composite materials are widely used in aerospace applications due to their excellent properties like high specific strength, high specific stiffness, high damage tolerance, good corrosion and fatigue resistance, good formability etc. Despite having excellent properties the inherently brittle nature of composites makes them highly susceptible to low−velocity impact damage which may arise due to tool strike, ground handling, bird strike, lightning strike, environmental degradation etc., during their service life. In most of the cases, replacing the entire part is not economically feasible and therefore repair or reinforcement of damaged structure is necessary to improve its structural integrity and the service life. Adhesively bonded composite patch repair is one of the effective techniques for enhancing the integrity of the damaged structures. Hence, it is essential to understand the behaviour of patch repaired composite panels including its damage mechanism to ensure the higher efficiency of the repair.

The present research work focused on understanding the tensile behaviour of open hole carbon fiber reinforced polymer (CFRP) panel repaired with the adhesively bonded patch. Both pure uni−directional and quasi−isotropic panels are considered in this study. Whole field non−contact digital image correlation (DIC) technique is employed for experimental strain analysis. At first, DIC technique is used for the experimental characterization of CFRP laminates. Later, both 2D and 3D−DIC technique is employed for whole field strain analysis in unrepaired and repaired CFRP panels. Also, global and local strains are estimated over thin adhesive layer at patch/panel interface using magnified optics in combination with conventional DIC set−up to understand the behaviour of adhesive layer. Further, a progressive damage model (PDM) is developed using finite element analysis (FEA) to predict the complex damage mechanism and failure strength of unrepaired and repaired CFRP composite panels. The PDM helps in developing an efficient and damage tolerant design. The PDM predictions are compared with the experimental results for their accuracy. FEA based investigation is carried out to arrive at the effective patch shape. A genetic algorithm (GA) based optimization technique is employed in conjunction with FEA to arrive at an optimum patch size for a chosen shape of patch to result in higher repair performance. Finally, an experimental investigation of open hole patch repaired panel having the same optimum patch geometry is carried out for an overall comparison. Studies revealed that double sided patch repair is found to be the most efficient repair method. DIC is found to successfully capture the strain field over the thin adhesive layer in repaired panel. PDM model is found to accurately predict the damage mechanism in repaired panels.

Contents

Declaration ii
Approval Sheet iii
Acknowledgements iv
Abstract vii

Nomenclature **xiii**

1 Introduction and Literature Review **14**
1.1 Composite material and its application 14
1.1.1 An overview of composite material 14
1.1.2 Composites in aerospace application 15
1.2 Damage: An inevitable phenomena in fiber reinforced composites 17
1.2.1 Sources of damage 17
1.2.2 Impact damage as a most potential threat to the integrity of composite structures 17
1.2.3 Damage mechanism in composite material 18
1.2.4 Damage assessment in composites 21
1.3 Repair of composite structures in aerospace application 21
1.3.1 Need of repair 21
1.3.2 Repair methodology and practical application of patch repair 22
1.3.3 Methodology of externally bonded patch repair 24
1.4 Progressive failure analysis (PFA) of composite structures 27
1.4.1 Prominence of damage analysis 27
1.4.2 Steps involved in PFA 28
1.5 Optimization of fiber reinforced polymer composites using genetic algorithm (GA) . 30
1.5.1 Basic principle of GA 30
1.5.2 Basic operators of GA: reproduction,crossover,mutation 31
1.6 Digital image correlation(DIC) 33
1.6.1 Evolution of DIC technique 33
1.6.2 DIC measurement principle 33
1.6.3 Subset matching methodology 33
1.6.4 Random texture pattern (speckle pattern) 34
1.6.5 Correlation criterion 35
1.6.6 Whole field displacement estimation 37
1.6.7 Whole field strain estimation 37

1.6.8 Two-dimensional and three-dimensional DIC setup . . . 38
1.6.9 Advantages, disadvantages and accuracy of DIC . . . 39
1.7 Literature review . . . 40
1.7.1 Externally bonded patch repaired composite panel . . . 40
1.7.2 Progressive failure analysis . . . 43
1.7.3 Optimization of composite laminate using GA . . . 44
1.7.4 Motivation, Scope and Objectives . . . 45
1.8 Thesis layout . . . 48

2 Experimental Characterization of CFRP Composite Laminate using DIC 50
2.1 Introduction . . . 50
2.2 Materials detail and specimen fabrication . . . 51
2.2.1 Composite specimens . . . 52
2.2.2 Epoxy matrix specimens . . . 53
2.3 Experimental methodology for DIC measurement . . . 53
2.3.1 Random speckle pattern . . . 53
2.3.2 Experimental setup and test procedure . . . 54
2.4 Determination of CFRP composite properties . . . 56
2.4.1 Tensile properties . . . 56
2.4.2 Compression properties . . . 62
2.4.3 Shear properties . . . 64
2.4.4 Estimation of out−of−plane properties . . . 66
2.4.5 Summary of CFRP properties evaluated from DIC experiments . . . 67
2.4.6 Estimation of fiber volume fraction (V_f) in CFRP specimens . . . 67
2.5 Determination of epoxy matrix properties . . . 68
2.6 Comparison of CFRP properties estimated from experiment (DIC) and analytical approach . . . 70
2.6.1 Rule of Mixture . . . 70
2.6.2 Halpin−Tsai Model . . . 70
2.7 Sensitivity analysis of DIC parameters on matrix material properties . . . 72
2.7.1 Influence of speckle pattern . . . 72
2.7.2 Influence of subset size . . . 73
2.7.3 Influence of step size . . . 75
2.7.4 Influence of ROI size . . . 76
2.8 Sensitivity analysis of DIC parameters on CFRP properties . . . 77
2.8.1 Influence of subset size . . . 77
2.8.2 Influence of step size . . . 78
2.9 Optimum value/range of DIC parameters for material properties estimation . . . 79
2.10 Sensitivity analysis of DIC parameters on complex strain fields in an open cutout CFRP panel . . . 82
2.10.1 Specimen geometry and finite element analysis . . . 82
2.10.2 Influence of step size on longitudinal strain (ε_{xx}) . . . 84
2.10.3 Influence of step size on transverse strain (ε_{yy}) . . . 85
2.10.4 Influence of step size on shear strain (ε_{xy}) . . . 87

2.10.5 Influence of subset size on whole field strain maps . . . 88
2.11 Closure . . . 92

3 Whole Field Strain Analysis of Open Cutout and Repaired CFRP Panel using DIC and FEA 93
3.1 Introduction . . . 93
3.2 Specimen geometry and fabrication . . . 94
3.3 Experimental setup and test procedure . . . 97
3.4 Experimental results: pure UD panel $[0°]_4$ . . . 97
3.4.1 Panel with open circular cutout . . . 97
3.4.2 Single sided repaired panel . . . 99
3.4.3 Double sided repaired panel . . . 101
3.4.4 Failure mechanism . . . 103
3.4.5 Experimental performance of open cutout and repaired panels . . . 104
3.5 Finite element modeling and analysis results: pure UD panel $[0°]_4$ . . . 106
3.5.1 Panel with open cutout . . . 108
3.5.2 Single sided repaired panel . . . 109
3.5.3 Double sided repaired panel . . . 110
3.5.4 Strain variation in panel, patch and adhesive . . . 111
3.6 Experimental results: quasi−isotropic panel $[\pm 45/0/90]_s$ . . . 113
3.6.1 Panel with open cutout . . . 113
3.6.2 Single sided repair panel . . . 114
3.6.3 Double sided repair panel . . . 115
3.6.4 Failure mechanism of open cutout and repaired panel . . . 116
3.7 Finite element modeling and analysis results: quasi−isotropic panel $[\pm 45/0/90]_s$ . . . 116
3.7.1 Panel with open cutout . . . 117
3.7.2 Single sided repair panel . . . 118
3.7.3 Double sided repair panel . . . 119
3.7.4 Strength of open cutout and repaired panel . . . 120
3.8 Mechanics of externally bonded patch repair . . . 122
3.8.1 Damage prone locations in externally bonded patch repair . . . 122
3.8.2 Effect of patch stacking sequence . . . 123
3.8.3 Effect of patch thickness . . . 125
3.8.4 Effect of adhesive layer thickness . . . 127
3.8.5 Effect of patch diameter . . . 128
3.8.6 Comparison of open cutout and repaired panel . . . 130
3.9 Closure . . . 131

4 Progressive Failure Analysis of Open Cutout and Repaired CFRP Panel using Finite Element Method 133
4.1 Introduction . . . 133
4.1.1 Specimen configurations and experimental results . . . 134
4.1.2 Summary of experimental results: pure UD panel $[0°]_4$ . . . 134
4.1.3 Summary of experimental results: quasi−isotropic panel $[\pm 45/0/90]_s$ . . . 134

4.2 Progressive damage modeling (PDM) . . . 136
4.2.1 Stress analysis . . . 136
4.2.2 Damage prediction: failure criterions for panel, patch and adhesive . . . 137
4.2.3 Damage modeling . . . 139
4.2.4 Implementation of PDM . . . 140
4.3 Progressive failure analysis results: pure UD panel $[0°]_4$ . . . 141
4.3.1 Validation of PDM algorithm . . . 141
4.3.2 Panel with open cutout . . . 142
4.3.3 Single sided repaired panel . . . 144
4.3.4 Double sided repaired panel . . . 146
4.3.5 Load−displacement behaviour and strength of open cutout and repaired panel: PDM vs. Experiment . . . 148
4.3.6 Strength of repaired panel: Shear stress vs. Shear strain . . . 148
4.4 Progressive failure analysis results: quasi−isotropic panel $[\pm 45/0/90]_s$ . . . 150
4.4.1 Panel with open cutout . . . 150
4.4.2 Single sided repaired panel . . . 152
4.4.3 Double sided repaired panel . . . 154
4.4.4 Strength of open cutout and repaired panel: PDM vs. Experiment . . . 155
4.5 Mechanics of failure in single and double sided repaired panel . . . 156
4.6 Characteristic distance . . . 157
4.7 Closure . . . 158

5 Strain Measurement in Adhesive Layer and Critical Shear Transfer Length Determination using DIC and FEA 159
5.1 Introduction . . . 159
5.2 Determination of adhesive properties using 3D−DIC . . . 160
5.2.1 Adhesive materials detail . . . 160
5.2.2 Fabrication of adhesive specimens . . . 160
5.2.3 Experimental setup and test procedure . . . 160
5.2.4 Properties of adhesive material . . . 161
5.3 Specimen configurations and experimental methodology for adhesive strain measurement using DIC . . . 163
5.3.1 Fabrication of patch repaired specimens . . . 163
5.3.2 Adhesive thickness measurement . . . 165
5.3.3 Experimental setup and test procedure . . . 166
5.4 Global whole field strain analysis on Araldite 2011 adhesive layer: double sided patch repair configuration . . . 167
5.4.1 Longitudinal strain (ε_{xx}) distribution . . . 167
5.4.2 Peel strain (ε_{zz}) distribution . . . 170
5.4.3 Shear strain (ε_{xz}) distribution . . . 171
5.4.4 Failure mechanism and load displacement behaviour . . . 172
5.5 Localized whole field strain analysis in Araldite 2011 adhesive layer: double sided patch repair configuration . . . 175
5.5.1 Straight edge patch . . . 175

5.5.2 Tapered edge patch . . . 177
5.6 Localized behaviour of strain distribution in Araldite AV138/HV998 adhesive layer: double sided patch repair configuration . . . 179
5.7 Global whole field strain analysis on Araldite 2011 adhesive layer: single sided patch repair configuration . . . 180
5.7.1 In−plane displacement contours . . . 180
5.7.2 Longitudinal strain (ε_{xx}) distribution . . . 182
5.7.3 Peel (ε_{zz}) and shear strain (ε_{xz}) distribution . . . 184
5.7.4 Failure mechanism and load displacement behaviour . . . 185
5.8 Localized whole field strain analysis in Araldite 2011 adhesive layer: single sided patch repair configuration . . . 187
5.8.1 Straight edge patch . . . 187
5.8.2 Tapered edge patch . . . 189
5.9 Finite element modeling and analysis: double sided patch repair configuration . . . 192
5.9.1 Shear transfer length (L_s) from FEA . . . 194
5.10 Finite element modeling and analysis: single sided patch repair configuration . . . 195
5.10.1 Shear transfer length (L_s) from FEA . . . 196
5.11 Closure . . . 197

6 Optimization of Repair Parameters using GA and FEA 198
6.1 Introduction . . . 198
6.2 Specimen geometry and material properties . . . 199
6.3 Finite element modeling . . . 200
6.3.1 Modeling of the damaged panel . . . 200
6.3.2 Modeling of the patch and repaired panel . . . 200
6.3.3 Square patch . . . 201
6.3.4 Rectangular patch . . . 201
6.3.5 Circular patch . . . 201
6.3.6 Elliptical patch . . . 201
6.3.7 Octagonal patch . . . 202
6.3.8 Oval patch . . . 203
6.4 Comparison of analytical and FEA results for an open cutout panel . . . 203
6.5 Efficiency of adhesively bonded patch repair . . . 204
6.6 Influence of patch shapes on repair efficiency: pure UD panel . . . 205
6.6.1 Square patch . . . 205
6.6.2 Rectangular patch . . . 205
6.6.3 Circular patch . . . 206
6.6.4 Elliptical patch . . . 206
6.6.5 Octagonal patch . . . 207
6.6.6 Oval patch . . . 208
6.7 Comparative study of different patch shapes: pure UD panel . . . 209
6.7.1 Based on SCF . . . 209
6.7.2 Based on peel stress . . . 210
6.7.3 Based on strength predicted using failure criterions . . . 211

6.8 Influence of patch shapes on repair efficiency: quasi−isotropic panels 212
6.8.1 Based on SCF and peel stress 212
6.9 Parametric optimization using genetic algorithm approach 213
6.9.1 Optimization of repair parameters: pure UD panel 214
6.10 Optimization of repair parameters using multi−objective genetic algorithm with Tsia−Wu and maximum shear stress failure criteria 217
6.10.1 Multi−objective optimization problem statement 217
6.10.2 Optimized repair parameters: pure UD $[0^\circ]_4$ and quasi−isotropic repaired panel $[\pm 45/0/90]_s$ 219
6.10.3 Experimental study with optimized patch dimensions and adhesive thickness 222
6.10.4 Whole field strain analysis: pure UD configuration 222
6.10.5 Whole field strain analysis: quasi−isotropic panel configuration 223
6.10.6 Strength of panels repaired with optimized patch geometry: pure UD and quasi−isotropic panel configuration 225
6.11 Closure 227

7 Conclusions and Recommendations for Future Work 228
7.1 Conclusions 228
7.1.1 Concluding Remarks 232
7.2 Recommendations for future work 233

References 235

Nomenclature

1	Longitudinal or loading direction
2	Transverse direction
3	Thickness direction
E	Young's modulus
E_{11}	Modulus in x direction
E_{22}	Modulus in y direction
E_{33}	Modulus in z direction
G	Shear modulus
G_{12}	In−plane shear modulus
G_{13}	Out of plane shear modulus
G_{23}	Out of plane shear modulus
S_{12}	In−plane shear strength
S_{13}	Out of plane strength
S_{23}	Out of plane strength
V_f	Fiber volume fraction
x	Longitudinal or loading direction
X_C	Compressive strength in x direction
X_T	Tensile strength in x direction
y	Transverse direction
Y_C	Compressive strength in x direction
Y_T	Tensile strength in y direction
z	Thickness direction
Z_C	Compressive strength in z direction

Z_T Tensile strength in z direction

γ_{12} In−plane shear strain

ν Poisson's ratio

ν' Degraded Poisson's ratio

ν_{12} In−plane Poisson's ratio

ν_{13} Out of plane Poisson's ratio

ν_{23} Out of plane Poisson's ratio

ν_f Poisson's ratio of fiber

ν_m Poisson's ratio of matrix

σ_o Remote or applied stress in x direction

σ_{xx} Stress in x direction

σ_{yy} Stress in y direction

σ_{zz} Stress in z direction

τ_{12} In−plane shear stress

ε_{xx} Strain in x direction

ε_{xx} Strain in y direction

ε_{xy} Shear strain in xy plane

ε_{xz} Strain in xz plane

ε_{zz} Strain in z direction or Peel strain

ξ Geometry packing factor

A Cross sectional area

Ap Patch correctional area

C_{CC} Cross correlation coefficient

C_{SSD} Sum of squared difference coefficient

C_{ZNCC} Zero normalized cross correlation coefficient

C_{ZNSSD} Zero normalized sum of squared difference coefficient

$CFRP$ Carbon fiber reinforced panel

D Patch diameter

d Hole or cutout diameter

E'	Degraded Young's modulus
E_f	Modulus of fiber
E_m	Modulus of matrix
FI_τ	Shear failure index
FI_{TW}	Tsai−Wu failure index
G'	Degraded shear modulus
L	Panel length
Le	Load transfer length
Ls	Shear transfer length
P	load
PMC	Polymer matrix composites
r	Hole radius
t	Panel thickness
t_p	Patch thickness
ta	Adhesive thickness
u	Displacement in x direction
v	Displacement in y direction
W	Panel width
w	Displacement in z direction
Wp	Patch width

List of Figures

1.1 Phases of a composite material 14
1.2 Applications of composite materials [1] 15
1.3 Trend of material usage in Boeing aircrafts [2] 16
1.4 Breakdown of materials used in Boeing 787 Dreamliner [2] 16
1.5 Example of impact damage on Boeing 787 aircraft [3] (a) BVID (b) location of BVID (C) VID 18
1.6 Schematic representation of failure modes is fiber reinforced composites [4] (a) matrix cracking (b) fiber−matrix debonding (c) fiber fracture (d) fiber pull out (e) delamination 19
1.7 Fracture propagation in fiber−reinforced composite [5] 20
1.8 SEM micrographs of fracture surface of fiber reinforced plastics failed under different failure modes [4, 6] (a) matrix cracking (b)fiber fracture (c) fiber−matrix debonding (d) fiber pull out 20
1.9 Damage on composite fuselage of Boeing 787 Dreamliner aircraft whose repair process utilizing adhesively bonded patch is underway [7] 22
1.10 Application of bonded patch repair on an aircraft [8] 23
1.11 Schematic diagram of scarf and externally bonded patch repair 24
1.12 Methodology of externally bonded patch repair 25
1.13 Single and double sided externally bonded patch repair 26
1.14 Steps involved in progressive failure analysis 28
1.15 Classification of failure theories for fibrous composite materials 29
1.16 Flow chart depicting fundamental operators and principle of genetic algorithm for optimization problem 31
1.17 Single−point crossover in a GA 32
1.18 Mutation in a GA 32
1.19 Schematic illustration of a reference square subset before deformation and a deformed subset after deformation 34
1.20 Random speckle pattern 34
1.21 Schematic diagram of 2D−DIC setup 38
1.22 Schematic diagram of 3D−DIC setup 39
1.23 Brief summary of contributions made in this thesis 47

2.1 Different steps involved in CFRP specimen preparation 52
2.2 Typical speckle pattern 54
2.3 Experimental setup consisting of 3D DIC and MTS machine 55

2.4 Tensile test geometry for [0°] coupon as per ASTM−D3039 standard 56
2.5 Tensile test geometry for [90°] coupon as per ASTM−D3039 standard 57
2.6 Tensile specimen (a) extensometer, subset, ROI (b) speckle pattern (zoomed view) (c) v−displacement (mm) in ROI 58
2.7 Stress−strain curve for longitudinal modulus (E_{11}) obtained from tensile test of [0°] coupon (a) DIC (b) MTS 59
2.8 Comparison of stress−strain curve for (E_{11}): DIC vs. MTS 60
2.9 In−plane Poisson's ratio (ν_{12}) obtained using from tensile test of [0°] coupon 60
2.10 Stress−strain curve obtained from DIC for transverse modulus (E_{22}) 61
2.11 Compression test geometry for [0°] coupon as per ASTM−D3410 standard 62
2.12 Compression test geometry for [90°] coupon as per ASTM−D3410 standard 62
2.13 Shear test geometry as per ASTM−D3518 standard: [±45°] coupon 64
2.14 Stress−strain curve obtained from DIC for in−plane shear modulus (G_{12}) 65
2.15 Tensile test specimen geometry for epoxy matrix as per ASTM−D638 standard: matrix coupon 68
2.16 Stress−strain curve obtained from tensile test of matrix coupon using DIC (a) Young's modulus, E (b) Poisson's ratio, ν 69
2.17 Displacement field maps on front and back surface of matrix coupon obtained from DIC at 1.7 kN. (a) front face having speckle pattern A (b) horizontal displacement for pattern A (c) vertical displacement (loading direction) for pattern A (d) back face having speckle pattern B (e) horizontal displacement for pattern B (f) vertical displacement for pattern B 72
2.18 Stress−strain curve obtained from DIC for speckle pattern A & B 73
2.19 Influence of subset size on matrix material (a) Young's modulus (E) (b) Poisson's ratio (ν) 74
2.20 Influence of step size on matrix material (a) Young's modulus (E) (b) Poisson's ratio (ν) 75
2.21 Influence of ROI size on matrix material properties (a) Young's modulus (E) (b) Poisson's ratio (ν) 76
2.22 Influence of subset size on CFRP properties (a) longitudinal Young's modulus (E_{11}) (b) in−plane Poisson's ratio (ν_{12}) 77
2.23 Influence of step size on CFRP properties (a) longitudinal Young's modulus (E_{11}) (b) in−plane Poisson's ratio (ν_{12}) 78
2.24 Normalized variation of matrix properties as a function of DIC parameters (a) subset size (b) step size 79
2.25 Normalized variation of matrix properties as a function of ROI size 80
2.26 Normalized variation of CFRP properties as a function of DIC parameters (a) subset size (b) step size 81
2.27 Open cutout CFRP panel $[0°]_4$ 83
2.28 Longitudinal strain field (ε_{xx}) maps in an open cutout CFRP panel as a function of step size obtained from DIC 84
2.29 Variation of ε_{xx} along net section of an open cutout CFRP panel at different step size along distance from hole edge 85

2.30 Transverse strain field (ε_{yy}) maps in an open cutout CFRP panel as a function of step size obtained from DIC . . . 86
2.31 Variation of ε_{yy} along net section of an open cutout CFRP panel at different step size along distance from hole edge . . . 86
2.32 Shear strain field (ε_{xy}) maps in an open cutout CFRP panel as a function of step size obtained from DIC . . . 87
2.33 Variation of ε_{xy} along net section of an open cutout CFRP panel at different step size along distance from hole edge . . . 88
2.34 Longitudinal strain field (ε_{xx}) maps in an open cutout CFRP panel as a function of subset size obtained from DIC . . . 89
2.35 Transverse strain field (ε_{yy}) maps in an open cutout CFRP panel as a function of subset size obtained from DIC . . . 89
2.36 Shear strain field (ε_{xy}) maps in an open cutout CFRP panel as a function of subset size obtained from DIC . . . 90
2.37 Variation of ε_{xx} along net section of an open cutout CFRP panel at different subset size along distance from hole edge (9.78 kN) . . . 91
2.38 Variation of longitudinal strain (ε_{xx}) at net−section along distance from hole edge obtained from DIC test for on open cutout panel with and without clay . . . 91

3.1 Specimen geometry (a) open cutout panel (b) repaired panel (c) single sided repaired panel (d) double sided repaired panel (all dimensions are in mm) . . . 95
3.2 Fabricated CFRP UD specimens (a) open cutout panel (b) panel repaired with circular patch (c) double sided repaired panel (d) single sided repaired panel . . . 96
3.3 Adhesive thickness measured using optical microscope . . . 96
3.4 Damage development with the load for a panel with open circular cutout (ε_{xx} plot) . 98
3.5 Damage evolution with the load in case of single sided repaired panel (patch side− ε_{xx} plot) . . . 100
3.6 Damage evolution with the load in case of single sided repaired panel (unpatched side− ε_{xx} plot) . . . 101
3.7 Damage evolution with the load in double sided repaired panel (ε_{xx} plot) . . . 102
3.8 Failure mechanism (a) open cutout panel (b) single sided repaired panel (c) double sided repaired panel . . . 103
3.9 Variation of longitudinal strain (ε_{xx}) with respect to applied load . . . 104
3.10 Load−displacement curve for open cutout and repaired panels obtained from experiment: pure UD configuration . . . 105
3.11 Maximum longitudinal stress versus number of elements along the hole periphery: mesh sensitivity analysis . . . 106
3.12 Finite element model (a) damaged panel (b) repaired panel . . . 107
3.13 Comparison of whole field strain contour obtained from DIC and FEA for the open cutout panel (a) DIC (ε_{xx}) (b) FEA (ADS)− (ε_{xx}) (c) FEA (AS)− (ε_{xx}) (d) DIC (ε_{yy}) (e) FEA (ADS)− (ε_{yy}) (f) FEA (AS)− (ε_{yy}) (g) DIC (ε_{xy}) (h) FEA (ADS)− (ε_{xy}) (i) FEA (AS)− (ε_{xy}) (ADS − Adjusted scale to match with DIC scale, AS − Actual scale of FEA plot) . . . 108

3.14 Longitudinal stress variation (σ_{xx}) in a open cutout panel at an applied of 8.512 kN: FEA vs. DIC 109
3.15 Comparison of whole field strain contour obtained from DIC and FEA for single sided repair panel (a) DIC (ε_{xx}) (b) FEA (ADS)− (ε_{xx}) (c) DIC (ε_{yy}) (d) FEA (ADS)− (ε_{yy}) (e) DIC (ε_{xy}) (f) FEA (ADS)− (ε_{xy}) (ADS − Adjusted scale to match with DIC scale) 110
3.16 Comparison of whole field strain contour obtained from DIC and FEA for double sided repair panel (a) DIC (ε_{xx}) (b) FEA (ADS)− (ε_{xx}) (c) DIC (ε_{yy}) (d) FEA (ADS)− (ε_{yy}) (e) DIC (ε_{xy}) (f) FEA (ADS)− (ε_{xy}) (ADS − Adjusted scale to match with DIC scale) 111
3.17 Strain variation in the panel, patch and adhesive at a load of 8.512 kN 112
3.18 Whole field strain (ε_{xx}) distribution of a circular cutout panel under tensile load . . 113
3.19 Whole field strain (ε_{xx}) distribution of a single sided repair panel under tensile load 114
3.20 Whole field strain (ε_{xx}) distribution of a double sided repair panel under tensile load 115
3.21 Failure mechanism in $[\pm 45/0/90]_s$ panel under tensile load (a) open cutout panel (b) single sided repaired panel (c) double sided repaired panel 116
3.22 Comparison of whole field strain contour obtained from DIC and FEA for open cutout panel under tensile load of 10 kN (a) DIC (b) FEA (ADS) (c) FEA (AS) − ε_{xx} plot (d) DIC (e) FEA (ADS) (f) FEA (AS) − ε_{xy} plot (ADS − adjusted scale of FEA with DIC scale, AS − Actual scale of FEA plot) 117
3.23 Comparative line plot of ε_{xx} between DIC and FEA along the net−section of open cutout panel 118
3.24 Comparison of whole field strain contour obtained from DIC and FEA for single sided repair panel under tensile load of 10 kN (a) DIC (b) FEA (ADS) (c) FEA (AS) − ε_{xx} plot (d) DIC (e) FEA (ADS) (f) FEA (AS) − ε_{xy} plot (ADS − adjusted scale of FEA with DIC scale, AS − Actual scale of FEA plot) 119
3.25 Comparison of whole field strain contour obtained from DIC and FEA for double sided repair panel under tensile load of 10 kN (a) DIC (b) FEA (ADS) (c) FEA (AS) − ε_{xx} plot (d) DIC (e) FEA (ADS) (f) FEA (AS) − ε_{xy} plot (ADS − adjusted scale of FEA with DIC scale, AS − Actual scale of FEA plot) 120
3.26 Load−displacement curve for open cutout and repaired panels obtained from experiment: quasi−isotropic configuration 121
3.27 Whole field stress contour plots of various components in externally bonded double sided repair from 3D FEA (a) longitudinal stress (σ_{xx}) in repaired panel (b) peel stress (σ_{zz}) in adhesive (c) longitudinal stress (σ_{xx}) in patch 123
3.28 Effect of patch stacking sequence in single sided repair configuration on (a) SCF (b) normalized shear stress 124
3.29 Effect of patch stacking sequence in double sided repair configuration on (a) SCF (b) normalized shear stress 125
3.30 Variation of SCF in Zone A and B of panel with varying patch thickness 126
3.31 Variation of SCF and normalized shear stress with different patch thickness (adhesive thickness 0.15 mm) (patch diameter 40 mm) 126

3.32 Variation of SCF and normalized shear stress with adhesive thickness for double sided repair (patch diameter 40 mm) . . . 127
3.33 Variation of normalized shear stress along the longitudinal axis repaired with different adhesive thickness . . . 128
3.34 Variation of SCF and normalized shear stress with varying patch diameter . . . 129
3.35 Variation of normalized shear stress along the longitudinal axis for different patch diameter . . . 129

4.1 Whole field strain (ε_{xx}) distribution observed experimentally using DIC for $[0°]_4$ panel (a) open cutout panel (b) single sided repaired panel (c) double sided repiared panel 135
4.2 Whole field strain (ε_{xx}) distribution observed experimentally using DIC for $[\pm 45/0/90]_s$ panel (a) open cutout panel (b) single sided repaired panel (b) double sided repaired panel . . . 135
4.3 Finite element model (a) open cutout panel (b) repaired panel . . . 137
4.4 Flowchart depicting PDM algorithm . . . 140
4.5 Stress−strain curve for open cutout panel (pure UD) (a) predicted by PDM (b) obtained from experiment . . . 141
4.6 Stress strain curve for open cutout panel (pure UD): PDM vs. Experiment . . . 142
4.7 Damage initiation site near transverse edge of hole in an open cutout panel $[0°]_4$ at a load of 6.58 kN . . . 142
4.8 Damage progression in an open cutout panel $[0°]_4$ (a) 18.05 kN (b) 25.94 kN . . . 143
4.9 Damage mechanism in an open cutout panel $[0°]_4$ (a) predicted by PDM (b) experimentally observed . . . 143
4.10 Damage initiation site near transverse edge of hole in single sided repaired panel $[0°]_4$ at a load of 8.68 kN . . . 144
4.11 Damage progression in single sided repaired panel $[0°]_4$ (a−c) 15.88 kN (d−f) 24.19 kN (g−i) 27.18 kN . . . 145
4.12 Damage mechanism in single sided repaired panel $[0°]_4$ (a−c) damage predicted by PDM (d−f) experimentally observed . . . 146
4.13 Damage initiation site near overlap edge of the patch in double sided repaired panel $[0°]_4$ at a load of 16.77 kN . . . 146
4.14 Damage mechanism in double sided repaired panel $[0°]_4$ (a−c) 21.34 kN (d−f) 25.13 kN (g−i) 28.83 kN . . . 147
4.15 Damage mechanism in double sided repaired panel $[0°]_4$ (a−c) damage predicted by PDM (d−f) experimentally observed . . . 148
4.16 Load−displacement curve for open cutout and repaired panels: PDM vs. Experiment 149
4.17 Damage initiation site in the 90° layer near transverse edge of hole in an open cutout quasi−isotropic panel $[\pm 45/0/90]_s$ at a load of 2.94 kN . . . 150
4.18 Ply wise damage progression in an open cutout quasi−isotropic panel $[\pm 45/0/90]_s$. 151
4.19 Damage mechanism in open cutout quasi−isotropic panel $[\pm 45/0/90]_s$ (a) predicted by PDM (b) experimentally observed . . . 152
4.20 Damage progression in single sided repaired quasi−isotropic panel $[\pm 45/0/90]_s$ (a−c) 20.53 kN (d−f) 26.03 kN . . . 153

4.21 Damage mechanism in single sided repaired quasi−isotropic panel $[\pm 45/0/90]_s$ (a−c) damage predicted by PDM (d−f) experimentally observed . . . 153
4.22 Damage mechanism in double sided repaired quasi−isotropic panel $[\pm 45/0/90]_s$ (a−c) 21.99 kN (d−f) 28.71 kN . . . 154
4.23 Damage mechanism in double sided repaired quasi−isotropic panel $[\pm 45/0/90]_s$ (a−c) damage predicted by PDM (d−f) experimentally observed . . . 155
4.24 Damage prone locations in repaired panel . . . 156
4.25 Comparison of longitudinal stress through the thickness of an open cutout, single and double sided repaired panel $[0°]_4$ obtained from FEA . . . 157

5.1 Split aluminium mold used for casting of adhesive specimens . . . 161
5.2 Adhesive specimen casting (a) Araldite AV138 / HV998 specimen (b) Araldite 2011 specimen . . . 161
5.3 Comparative plot of stress−strain curve obtained from DIC and extensometer: Araldite AV138/HV998 adhesive . . . 162
5.4 Comparative plot of stress−strain curve obtained from DIC and extensometer: Araldite 2011 adhesive . . . 162
5.5 Specimen geometry of adhesively bonded patch repaired CFRP panel (a) front view (b) side view of single sided repair configuration (b) side view of double sided repair configuration . . . 164
5.6 Adhesive thickness measured using optical microscope at a magnification of 10x (a) Araldite 2011 (b) Araldite AV138/HV998 . . . 165
5.7 Experimental setup for localized adhesive strain measurement involving 2D DIC with tube lens . . . 166
5.8 Strain distribution in panel, patch and adhesive layer in symmetrical patch repair configuration at 54% of failure load in case of Araldite 2011 (a) ε_{xx} (b) ε_{zz} (c) ε_{xz} . . 168
5.9 Strain distribution in panel, patch and adhesive layer in symmetrical patch repair configuration at 70% of failure load in case of Araldite 2011(a) ε_{xx} (b) ε_{zz} (c) ε_{xz} . . 169
5.10 Longitudinal strain variation in CFRP panel under double sided patch at 54% and 70% of failure load (Araldite 2011) . . . 170
5.11 Peel strain variation in adhesive layer of double sided patch repaired panel at 54% and 70% of failure load (Araldite 2011) . . . 171
5.12 Shear strain variation in adhesive layer of double sided patch repaired panel at 54% and 70% of failure load (Araldite 2011) . . . 172
5.13 Damage progression with increasing load in double sided patch repaired panel repaired with Araldite 2011 adhesive . . . 173
5.14 Load−displacement curve for DSPR panel . . . 174
5.15 Localized whole field strain distribution in double sided patch repaired panel at a tensile load of 13.51 kN (Araldite 2011) (a) ε_{xx} (b) ε_{zz} (c) ε_{xz} (d) failure mechanism 175
5.16 Comparison between localized peel and shear strain variation along adhesive thickness at 13.51 kN (Araldite 2011) . . . 176
5.17 Localized peel strain variation along bondline in adhesive layer at 13.51 kN (Araldite 2011) . . . 177
5.18 Patch edge tapering details (a) line diagram (b) angle depicted on actual joint . . . 177

5.19 Whole field strain distribution in the adhesive layer for a panel repaired with tapered patches at a tensile load of 13.5 kN (Araldite 2011) (a) peel strain − ε_{zz} (b) shear strain− ε_{xz} 178
5.20 Comparative plot of shear strain (ε_{xz}) for the panel repaired with straight edge and tapered edge double sided patch using Araldite 2011 adhesive 178
5.21 Localized whole field shear strain distribution in double sided patch repaired panel at 13.51 kN (Araldite AV138/HV998) 179
5.22 Comparative plot of shear strain (ε_{xz}) in adhesive layer for the panel repaired with Araldite 2011 and AV138/HV998 adhesive systems 180
5.23 Displacement (mm) contours in single sided patch repaired panel (Araldite 2011) at 38.5 kN (a) longitudinal displacement, u (b) transverse displacement, w 181
5.24 Variation of transverse displacement (mm) of point P in center of single sided patch repaired panel with increasing load using DIC 182
5.25 Strain distribution in panel, patch and adhesive layer in unsymmetrical patch repair configuration at 56% of failure load in case of Araldite 2011(a) ε_{xx} (b) ε_{zz} (c) ε_{xz} . . 183
5.26 Longitudinal strain variation in CFRP panel under single sided patch at 56% and 68% of failure load (Araldite 2011) 184
5.27 Shear strain variation in adhesive layer of single sided patch repaired panel at 56% and 68% of failure load (Araldite 2011) 185
5.28 Damage progression with increasing load in panel repaired with Araldite 2011 adhesive186
5.29 Load displacement curve for single sided patch repaired panel 187
5.30 Localized whole field strain distribution in adhesive layer for a panel repaired with single sided straight edge patch at a tensile load of 23.9 kN (Araldite 2011) (a) ε_{xx} (b) ε_{zz} (c) ε_{xz} 188
5.31 Damage monitoring in adhesive layer of single sided repair with increasing load based on peel strain − ε_{zz} 189
5.32 Localized whole field strain distribution in adhesive layer for a panel repaired with single sided tapered edge patch at a tensile load of 23.9 kN (Araldite 2011) (a) ε_{xx} (b) ε_{zz} (c) ε_{xz} 190
5.33 Comparative plot of strain variation in adhesive layer for the panel repaired with tapered edge patch obtained from DIC at a tensile load of 23.9 kN (Araldite 2011) . 190
5.34 Comparative plot of peel strain variation in adhesive layer between panels repaired with straight and tapered edge patch obtained from DIC at a tensile load of 23.9 kN (Araldite 2011) 191
5.35 Finite element model of DSPR panel (zoomed up view) 192
5.36 Whole field strain distribution in adhesive layer from FEA at a tensile load of 13.5 kN (a) peel strain − ε_{zz} (b) shear strain − ε_{xz} (Araldite 2011) 193
5.37 Shear strain variation in double sided repair panel at 13.51 kN (Araldite 2011): DIC vs. FEA 193
5.38 Shear strain distribution along adhesive length at 13.51 kN (Araldite 2011): DIC vs. FEA 194
5.39 Shear transfer length from shear strain distribution along adhesive length at 50.5 kN (Araldite 2011): DIC vs. FEA 195

5.40 Strain distribution in Araldite 2011 adhesive layer at a tensile load of 23.9 kN obtained from FEA (a) peel strain − ε_{zz} (b) shear strain − ε_{xz} . . . 195
5.41 Shear strain variation in the adhesive layer of a panel repaired with single sided straight edge patch at 46.8 kN (Araldite 2011): DIC vs. FEA . . . 196

6.1 Specimen geometry of double sided repaired panel (a) front view (b) side view . . . 199
6.2 Geometry of different patch shapes (a) square (b) rectangle (c) circular (d) elliptical (e) octagonal (f) oval . . . 201
6.3 Finite element model of double sided patch repaired panel with different patch shapes (a) square (b) rectangle (c) circular (d) elliptical (e) octagonal (f) extended octagon (g) oval . . . 202
6.4 Longitudinal stress variation along the net−section in case of open cutout panel: analytical vs. FEA . . . 204
6.5 Comparative plot of longitudinal stress variation between open cutout and repaired panel along the net−section . . . 205
6.6 Variation of SCF with the side length S of square patch . . . 206
6.7 Variation of SCF with rectangular patch size B or H . . . 206
6.8 Variation of SCF with the diameter D of circular patch . . . 207
6.9 Variation of SCF with major axis b for elliptical patch . . . 207
6.10 Variation of SCF with the distance l for regular octagonal patches . . . 208
6.11 Variation of SCF with the distance l for extended octagonal patch . . . 208
6.12 Variation of SCF with the dimension h for oval patch . . . 209
6.13 Comparative plot showing SCF variation with respect to patch area for different patch shapes . . . 210
6.14 Comparative plot of peel stress for different patch shapes . . . 211
6.15 Optimization flowchart depicting the methodology implemented . . . 214
6.16 Convergence plot for GA algorithm . . . 216
6.17 Optimized patch geometry for extended octagonal patch shape (in mm) . . . 216
6.18 Pareto front obtained from multi−objective optimization study: pure UD double sided repaired panel . . . 220
6.19 Pareto front obtained from multi−objective optimization study: quasi−isotropic double sided repaired panel . . . 221
6.20 Optimized patch geometry for oval patch shape (in mm) . . . 222
6.21 Whole field strain longitudinal strain (ε_{xx}) distribution observed experimentally using DIC for $[0°]_4$ panel repaired with optimized extended octagonal patch at a load of 7.5 kN (a) single sided repair (b) double sided repair . . . 223
6.22 Whole field strain (ε_{xx}) distribution observed experimentally using DIC for $[\pm 45/0/90]_s$ panel repaired with oval patch at a load of 8.8 kN(a) single sided repair (b) double sided repair . . . 224
6.23 Shear strain variation in adhesive layer of single sided patch repaired panel at load of 18.08 kN(Araldite 2011)(a) Peel strain (ε_{xx}) strain (b) Shear strain (ε_{xz}) . . . 224
6.24 Shear strain variation in adhesive layer of double sided patch repaired panel at load of 18.01 kN(Araldite 2011)(a) Peel strain (ε_{xx}) strain (b) Shear strain (ε_{xz}) . . . 225

List of Tables

1.1 Source of damage. 17

2.1 Tensile test matrix for material characterization. 56
2.2 DIC results from [0°] tensile test. 61
2.3 Results from [90°] tensile test. 61
2.4 Compression test matrix for material characterization. 62
2.5 Results from [0°] compression test. 63
2.6 Results from [90°] compression test. 63
2.7 Shear test matrix for material characterization. 64
2.8 Results from [±45°] tensile test. 66
2.9 Material properties of CFRP laminate and Matrix obtained using DIC technique. . . 67
2.10 Test matrix for epoxy material characterization. 68
2.11 Results from epoxy matrix tensile test. 69
2.12 Comparison of CFRP properties obtained from experiment (DIC) and analytical approach. 71

3.1 Configurations selected for experimental study. 95
3.2 Ultimate tensile strength of virgin, open cutout and repaired panels: pure UD configuration. 105
3.3 Ultimate tensile strength of virgin, open cutout and repaired panels: quasi−isotropic configuration. 121
3.4 SCF and normalized shear stress values obtained for models of different patch stacking sequences. 124
3.5 SCF comparison between open cutout, single and double sided repair model. 130

4.1 Configurations selected for experiment and progressive failure analysis. 134
4.2 Material property degradation rules (fiber orientation is along $x-$direction): $(\times)$ property to be degraded, $(-)$ unaffected property. 139
4.3 Maximum strength and displacement for $[0°]_4$ panel. 149
4.4 Debonding load, maximum strength and maximum displacement predicted by two different failure criteria used for adhesive layer. 149
4.5 Maximum strength and displacement for $[\pm 45/0/90]_s$ panel. 155

5.1 Material properties of adhesives and CFRP laminate (230 gsm) estimated using DIC technique. 163

6.1 Influence of patch shape on patch debonding load and failure initiation strength (pure UD panel) . . . 212
6.2 Influence of patch shape on SCF for different quasi−isotropic panels . . . 213
6.3 Influence of patch shape on peel stress (σ_{zz}) in MPa for different quasi−isotropic panels. 213
6.4 Parameters used in optimization scheme: pure UD repaired panel. . . . 215
6.5 Optimized repair parameters. . . . 216
6.6 Optimized repair parameters: pure UD $[0°]_4$ panel. . . . 221
6.7 Lower and upper bound of design variables: quasi−isotropic repaired panel. . . . 221
6.8 Optimized repair parameters: quasi−isotropic panel. . . . 222
6.9 Ultimate Load of the panels repaired with optimized patch dimensions and adhesive thickness: pure UD and quasi−isotropic configuration. . . . 226
6.10 Percentage restoration in ultimate strength of the panels repaired with optimized patch dimensions and adhesive thickness (with respect to virgin panel strength): pure UD and quasi−isotropic configuration. . . . 226

Chapter 1

Introduction and Literature Review

1.1 Composite material and its application

1.1.1 An overview of composite material

Composite material is usually defined as a combination of two or more distinct constituents or phases separated by a distinct interface. As a result, they offer desirable combination of properties based on principle of combined action to meet a particular requirement which may not be possible if any one of the constituent used alone. Typically, a composite material will have at least two constituents as shown in Fig. 1.1. One of the constituent is called as reinforcement and the one in which it is embedded is known as matrix. Reinforcement phase provides low density, high stiffness and strength to the composites. The reinforcement is the primary load−bearing constituent in the composite and its shape, volume, and arrangement adversely affect the properties of the composite material. Reinforcements can be in the form of long fibers, short fibers, particles, or whiskers. The matrix is the component that encloses and binds the reinforcement together and provides an effective means of load transfer to the reinforcement and protects them from outside and hostile environment. Composite materials are classified in accordance with the type of matrix material into metal matrix, ceramic matrix or polymer matrix composites. Composites are further classified based on arrangement and geometry of reinforcement into particulate reinforced (random, preferred orientation) and fiber reinforced (continuous, discontinuous, aligned, random) composites.

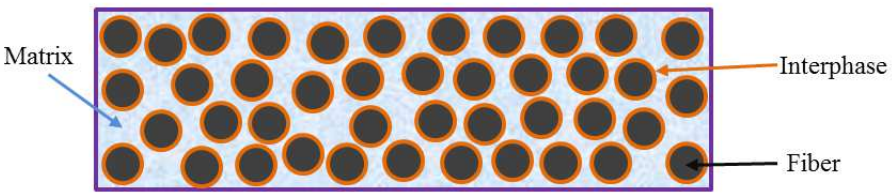

Figure 1.1: Phases of a composite material

1.1.2 Composites in aerospace application

Polymer matrix composites (PMC) have become the fastest growing and most widely used composite materials because of its inherent characteristics like high specific strength, high specific stiffness, high damage tolerance, good fatigue resistance, good corrosion resistance, low cost, good formability and simple fabrication methodology. These composites consist of a polymer matrix reinforced by smaller diameter fibres. Polymer matrix may be from thermoplastics (melt at high temperature) such as polystyrene, poly−ether−ether−ketone (PEEK) etc, or it could be thermosets (can not be melted by heating) such as epoxy, unsaturated polyester, phenolics, vinylesters etc,. In recent years, polymer−reinforced composites especially epoxy based carbon fiber reinforced composites are being exploited in many engineering applications like aerospace, automobile, civil, marine, commodity and sports, to name a few. The typical applications of composites are shown in Fig. 1.2.

Figure 1.2: Applications of composite materials [1]

Carbon fiber reinforced polymer (CFRP) composites have seen a remarkable increase and extensive usage in today's commercial aircrafts. This is due to the fact that in competitive environment of aircraft industries it becomes absolutely necessary to constantly improve the efficiency, performance and reduce the costs considerably, in order to capitalize the market. Efficiency and performance can be improved by decreasing the aircraft weight through considerable usage of composite materials in the aircraft structures. Advanced fiber reinforced composite materials have been originally developed for aerospace industry to use as primary structural materials. All the major aircraft manufacturers have been trying to develop the next generation of airliners using increased percentage of composite materials. This trend is expected to continue well into the future with significant improvement in fuel economy among other benefits. New generation of aircrafts tends to use thicker laminates carrying more loads. Commercial aircrafts such as the Boeing 757, 767 and 777 rely on composites in their control surfaces, ailerons, flaps, elevators, and rudders, and in their wing/body fairings and

engine nacelles. In the Airbus family, and the Boeing 777, the vertical and horizontal stabilizers are also made of carbon fiber construction. CFRP continue to replace traditional metallic materials in aerospace industry and the trend of increasing use of composites and decreasing use of aluminum alloys in Boeing aircrafts is shown in Fig. 1.3. The Boeing 787 Dreamliner makes greater usage of composite materials than any previous commercial airliner. Up to 50% of the Boeing 787 Dreamliner aircraft is built using CFRP and other composite materials including the primary structures namely fuselage and wing. A350 XWB has roughly 53% of composites utilized in the fuselage and wing. Utility of composite materials in Boeing 787 Dreamliner aircraft is illustrated Fig. 1.4. With time and service, composite material tend to degrade and damage, therefore understanding it's damage phenomena is of primary concern.

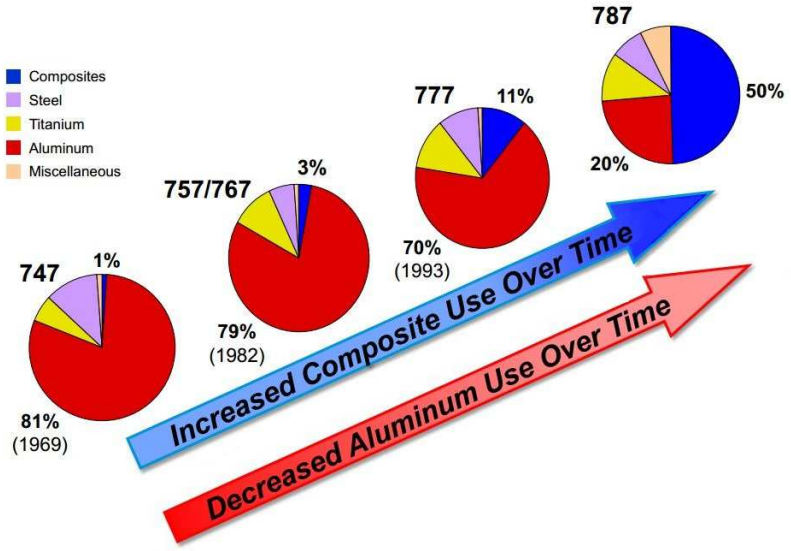

Figure 1.3: Trend of material usage in Boeing aircrafts [2]

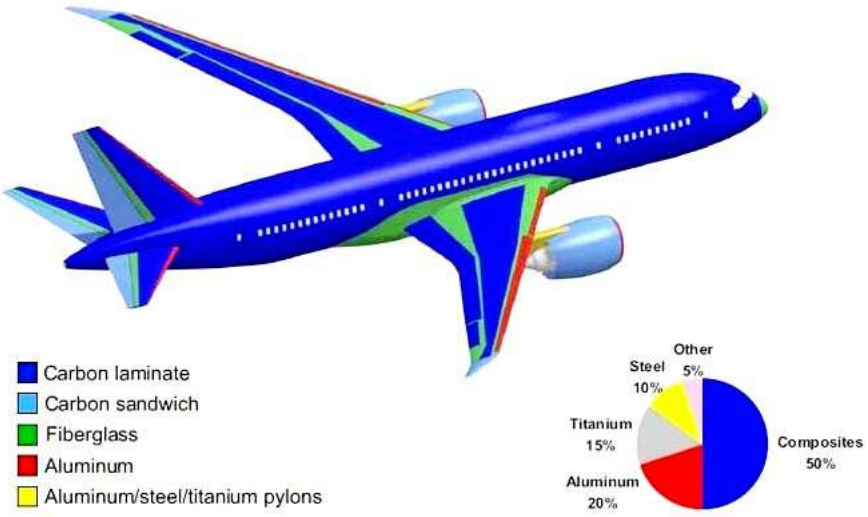

Figure 1.4: Breakdown of materials used in Boeing 787 Dreamliner [2]

1.2 Damage: An inevitable phenomena in fiber reinforced composites

1.2.1 Sources of damage

The term damage refers to a collection of all the irreversible changes brought about in a material by a set of energy dissipating either by physical or chemical processes, resulting from the application of thermo−mechanical loadings [9]. In FRPs, damage is manifested as a multitude of surfaces formed within a composite that permanently changes its response to external loads. Damage in composite is generally discussed in two frames of reference−by stage of occurrence and by physical anomaly. Stage of occurrence is separated into manufacturing and in−service categories [10]. The damage in composite aircraft part may originate during fabrication/manufacturing stage or may arise in−service. The different sources that could lead to damage in fiber−reinforced composites are summarized in Table 1.1 [10, 11].

Table 1.1: Source of damage.

Fabrication/Manufacturing	In−service Damage	Physical imperfection/defects
Improper cure or processing	Hailstones	Debonds
Improper machining	Runway debris	Delaminations
Mishandling	Ground vehicles	Inclusions
Improper drilling	Lightning strike	Voids, blisters
Tool drops	Tool drops	Fiber misalignment
Contamination	Bird strike	Cut or broken fibers
Improper sanding	Fire	Abrasions, scratches
Substandard material	Wear	Wrinkles
Inadequate tooling	Ballistic damage (Military)	Resin cracks, crazing
Mislocation of holes or details	Rain erosion	Density variations
Impact	Ultraviolet exposure	Improper cure
	Hygrothermal cycling	Machining problems
	Oxidative degradation	
	Repeated loads	
	Chemical exposure	
	Impact	

1.2.2 Impact damage as a most potential threat to the integrity of composite structures

Among several damage threat sources, impact is considered to be the most potentially dangerous and key source of damage in composites especially in fiber reinforced polymer composites [11]. In general, impact damage is not considered to be a threat in metallic structures because of their ductile nature and the large amount of energy that can be absorbed by them through plastic deformation [11]. However, low transverse and interlaminar shear strength of composite due to lack of through thickness reinforcement, lack of or no plastic deformation due to inherently brittle nature of composite, and laminar construction makes impact the most dangerous loading conditions for fiber reinforced polymer composites.

The damage caused by the impact is categorized according to the velocity of impact as low,

intermediate and high velocity impact damage. A low velocity impact event can be a result of dropped tools or in−service damage, intermediate impact can be due to runway debris at take−off and landing or caused by a bird strike and high velocity impact is mainly due to a ballistic impact.

Off primary concern in case of composite structure especially used in the aerospace industry is the low velocity impact damage. This is because the low velocity impact may cause the damage that may not be visible to the naked eye and potentially undetectable without non−destructive evaluations (NDE) techniques or it may produce a very small indentation on the impacted surface. This level of damage is often referred to as barely visible impact damage (BVID). While BVID is subjective by nature, it is often defined as damage visible within a range of 1.5 m, or damage causing a specific permanent indentation [3]. However, the low velocity impact could lead to significant amount of internal permanent damage in the form of subsurface delamination, matrix cracking and fiber breakage and result in a substantial loss in structure integrity, strength (50% reduction in tensile and 60% reduction in compressive), stiffness and may lead to catastrophic failure of the structure in extreme scenarios [10]. Thus, the low velocity impact damage particularly BVID has become an important and a challenging design problem in the aerospace industry. The example of an impact damage namely BVID and VID (visible impact damage) on wing skin of Boing 787 aeroplane is shown in the Fig. 1.5.

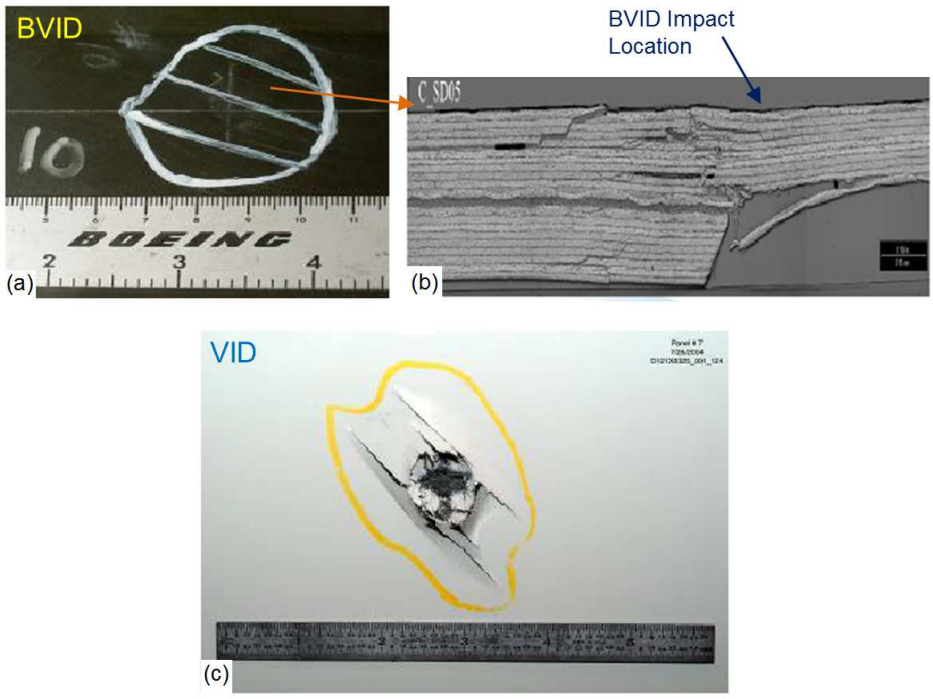

Figure 1.5: Example of impact damage on Boeing 787 aircraft [3] (a) BVID (b) location of BVID (C) VID

1.2.3 Damage mechanism in composite material

In laminated composites, damage is a complex mixture of three principal failure modes, namely, interlaminar damage (delamination), intralaminar damage between fibres (transverse matrix cracking

and fiber−matrix interface debonding) and intralaminar damage across fibres (fiber fracture and fiber pullout) [12, 13]. These are all also the possible damage mechanisms faced by composite laminates usually used in aircraft applications in the event of a low−velocity impact [11]. The different failure modes are shown individually in Fig. 1.6, and the process of damage evolution in laminated composite plate subjected to in−plane tensile load is depicted in Fig. 1.7.

Matrix cracking is usually the first failure mode that occurs in fiber−reinforced matrix composite due to an overload of tension and it originates from the resin rich area or defects like voids. The matrix crack and its density increases with increasing load and as the advancing matrix crack approaches to the neighboring fiber, the fiber due to its high stiffness inhibits the matrix crack opening and disrupts the crack growth. Also, the stress field ahead of the matrix crack tip is not sufficient enough to break the fiber because of its too high strength. As the load increases, the matrix and fiber at the crack tip deform differentially and induces shear stress at the fiber/matrix interface. The development of significant shear stress leads to localized *debonding* of the fiber from matrix at the interface. With further increase in load, debond grows along the fiber due to high interfacial shear stress development and the debond extension aids in further opening of matrix crack beyond the fiber and the process is repeated at the next fiber. The increase in debond length increases the load on fiber and as the debond reaches its critical length the fiber gets heavily loaded leading to *fiber fracture*. The load is then transferred to the adjacent fiber through matrix and the failure process continues. When the fiber failure occurs away from the crack plane, many of the broken fibers will remain *bridging* the crack, preventing it from growing and therefore for further crack opening to occur the embedded end of the fibers must be *pulled out* of the matrix.

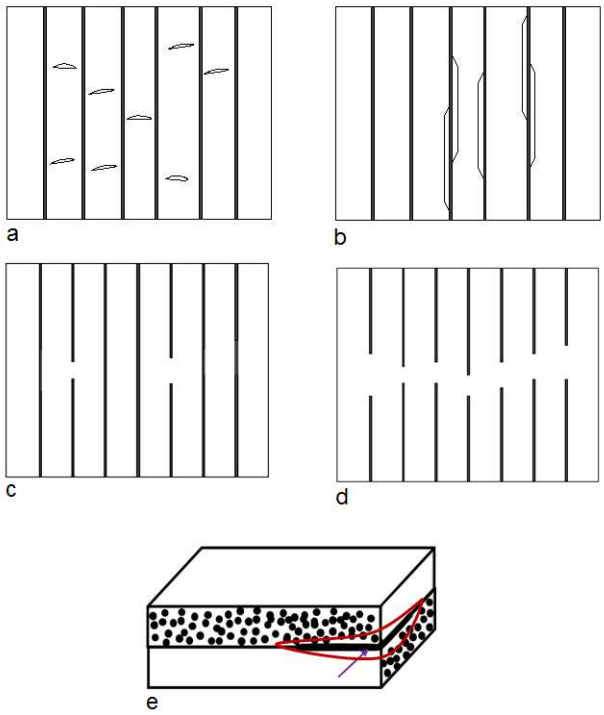

Figure 1.6: Schematic representation of failure modes is fiber reinforced composites [4] (a) matrix cracking (b) fiber−matrix debonding (c) fiber fracture (d) fiber pull out (e) delamination

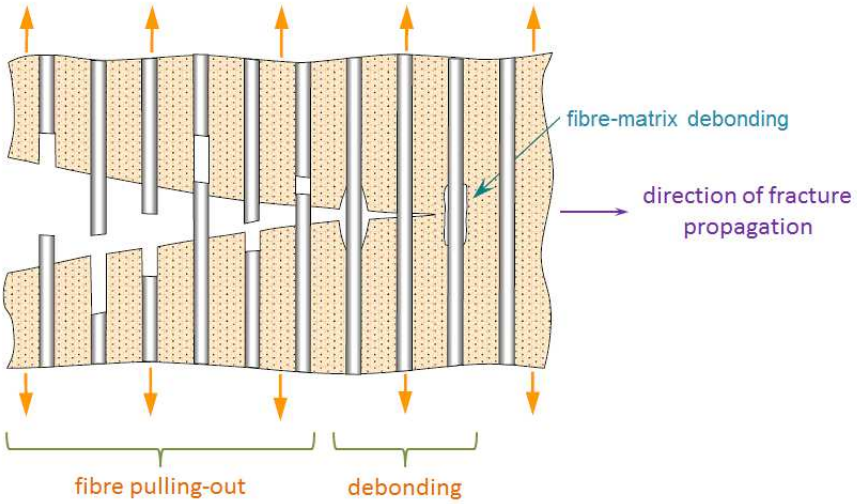

Figure 1.7: Fracture propagation in fiber−reinforced composite [5]

As the load reaches the critical/ultimate load the fibers are pulled apart from matrix separating the sample in two parts resulting in final failure. *Delamination* is another failure mode commonly observed in fiber reinforced laminated composites having plies of different orientation (off−axis plies) especially in cross plies . The high interlaminar shear stress due to the differential deformation of adjacent plies having varying fiber orientation leads to the separation of adjacent plies from one another and this kind of damage is known as delamination and it is more severe near the free edge. Figure 1.8 shows the SEM micrographs of the fracture surface of fiber reinforced plastics failed under different failure modes.

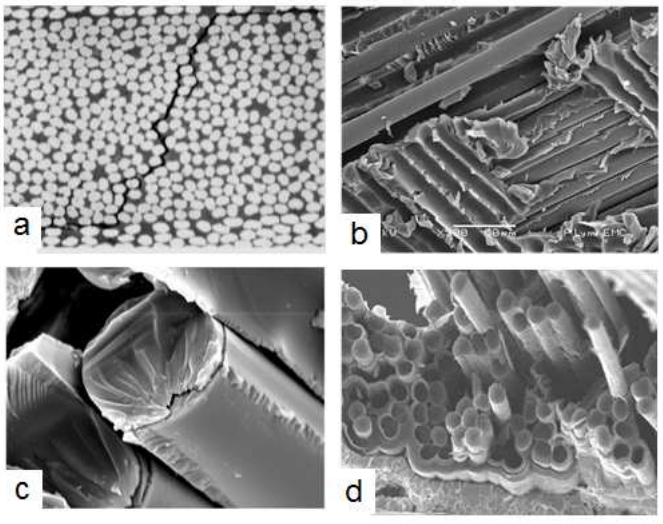

Figure 1.8: SEM micrographs of fracture surface of fiber reinforced plastics failed under different failure modes [4, 6] (a) matrix cracking (b)fiber fracture (c) fiber−matrix debonding (d) fiber pull out

1.2.4 Damage assessment in composites

The defects in composite materials are inevitable either at fabrication stage or during the service life and they may act as the damage initiation site and could facilitate the damage propagation under the advancing load. Therefore, the assessment of defects in composite materials at both the stages are essential as they provides information about the integrity of structure. A number of NDE methods has been evolved for assessing manufacturing and service defects in conventional metallic materials [13, 14]. Some of these techniques such as visual inspection, eddy current technique, ultrasonic inspection and acoustic emission are being utilized in aircraft industry for fiber−reinforced composite materials with appropriate modification. More details on these techniques can be obtained from Ref. [15–17].

Other conventional or emerging NDT methods that are being employed in recent years includes: X−ray radiography, thermography and digital image correlation (DIC). Radiography utilizes gamma rays or X−rays and measures the degree of absorption from the inspected structure, which in turn indicates the presence of defect or damage. Thermography detects potential damage by collecting thermal images using infrared camera after heating the sample material. Then, the material emits thermal energy based on its thermal conductivity, its temperature and its emissivity of defects. Each time the generated energy meets a defect, it is reflected back and absorbed by a infrared camera. DIC technique usually detects the damage or damage prone locations based on surface strain anomalies in thin samples. DIC technique has been employed in the recent work and it is elaborately discussed in later section of this chapter.

1.3 Repair of composite structures in aerospace application

1.3.1 Need of repair

The presence of damage significantly reduces the structural integrity, stiffness and strength of the composite structure and hence their service life. They may also lead to catastrophic failure of the structure in extreme scenarios. Therefore, once the damage is identified in composite structure using anyone of the NDE technique the damaged part needs to be either replaced or repaired accordingly considering the constraints of operational conditions.

Since, the low velocity impact damages especially in aerospace industry are quite common and they are generally localized in the structure therefore in most of the practical situation repair of the damage portion is preferred over the replacement of the entire part due to economic constraints. A situation wherein the operational limitations usually time, environment and facilities are severe the repair is only the preferred, feasible and safe option. To be more specific, one of the recent scenario wherein the repair of damaged portion is preferred over the replacement of entire structure is shown in the Fig. 1.9. The shown example represents the damage on upper portion of composite fuselage of a Boeing 787 Dreamliner aircraft which took place due to fire. Since, Boeing 787 is the first largest commercial jet made from CFRP, there is no precedent of such substantial damage. The Boeing engineers have preferred bonded composite patch repair of damage portion over the replacement of entire aft fuselage section which Boeing fabricates as a single−piece barrel. This is because, even though the patch repair process in such scenario will be complex and difficult, they realized that it would have been even more trouble to take the other approach disconnecting all the wiring, air and

Figure 1.9: Damage on composite fuselage of Boeing 787 Dreamliner aircraft whose repair process utilizing adhesively bonded patch is underway [7]

fuel systems and then inserting a full fuselage section that would mesh exactly with the section in front of it and the tail behind it [7].

1.3.2 Repair methodology and practical application of patch repair

The repair of damaged portion can possibly be achieved either by using mechanical fasteners or adhesively bonded patches. In case of mechanical fastener high stresses arise at the fastener holes resulting in significant stress concentration factor (SCF) thereby making it more damage prone compared to the bonded patch repair. In contrast, adhesively bonded repair offer smooth load transfer from panel to patch as large load transfer area is available making it much stiffer than mechanical joint.

Adhesively bonded repairs are relatively lightweight, highly cost effective and proven method for enhancing the structural integrity by reducing the stress concentration in the damaged area. They also provide very high level of bond durability under various operating conditions. Repair of aircraft aluminum structures using composite patch has been initiated by Baker et al. [18] in the early 1970s mainly in order to enhance fatigue life of cracked components. Some of the practical applications of adhesively bonded repair performed on an aircraft are shown in the Fig. 1.10.

Figure 1.10: Application of bonded patch repair on an aircraft [8]

Scarf and externally bonded patch repair

From application point of view, two kinds of adhesively bonded patch repair are employed: *scarf bonded* and *externally patch bonded* as shown in Fig. 1.11 [19].

Scarf patch repair is usually adopted for the repair of thick panels in presence of severe damage. This repair technique is a prime choice in a situation wherein the surface smoothness is essential to maintain the aerodynamic properties even after installation of the patches. The design of scarf patch repair typically requires removal of material around the damaged area with appropriate machining of surface in the parent laminate and then replacement or repair plies are inserted in its place. The scarf repair application procedure also requires taper around the repair area to obtain the correct scarf angle and requires same ply orientation in patch and panel. The repair can be accomplished either by soft patch wherein the repair plies are laid down in the scarf cavity and allowed for subsequent curing in its place or by hard patch wherein the pre−cured patch is placed in the cavity and it is

bonded to the panel using an adhesive. This repair technique offers high peel and shears strength and therefore provides the highest joint efficiency among all the repair techniques [20]. However there are certain disadvantages that has to be considered before the implementation of a scarf repair such as the design procedure. First of all the manufacturing of a scarf repair requires a higher level of expertise than the external patch and it results to the removal in excessive amount of undamaged material for the achievement of a scarf angle which may results in stiffness and strength degradation.

*External patch repair*approach is usually considered as a temporary repair solution in order to keep an airplane in serviceable condition or it can serve as a permanent repair in lightly loaded and relatively thin structures. The external patches transfer the load over and around the damage and reduce the localized stress concentration at the damage area. With this technique, the damaged material is removed by cutting a hole, cleaned and applied with filler and adhesive material before the patches are attached. This repair methodology has been used on aircraft, ship, and wind turbine blades. The application procedure of external patches is relatively simpler than the scarf approach and can be accomplished faster. The present thesis is focused on externally bonded repair using hard patches.

Figure 1.11: Schematic diagram of scarf and externally bonded patch repair

1.3.3 Methodology of externally bonded patch repair

Once the damage is identified in the composite structure, the recommended methodology is to remove the damaged portion. The damaged portion is usually removed in the form of cutouts most preferably in circular shape as shown in the Fig. 1.12. The cutout introduces discontinuity in the structure and disrupts the load transfer across it thereby reducing the strength of the structure. Also, the cutout acts as a stress raiser and causes the premature failure with the damage emanating from it. To alleviate the stress concentration, a patch is bonded on to the panel over the damaged area using an adhesive which acts as a load transfer medium between patch and panel. The patch redistributes the load across the damaged area thereby improving the strength of the damaged structure.

From geometrical point of view, two different configurations are adopted to repair the damaged panel: single and double sided patch repair as shown in Fig. 1.13. If only one face of the damage area is accessible (like in fuselage, wing) then the patch is bonded onto one side over the damaged

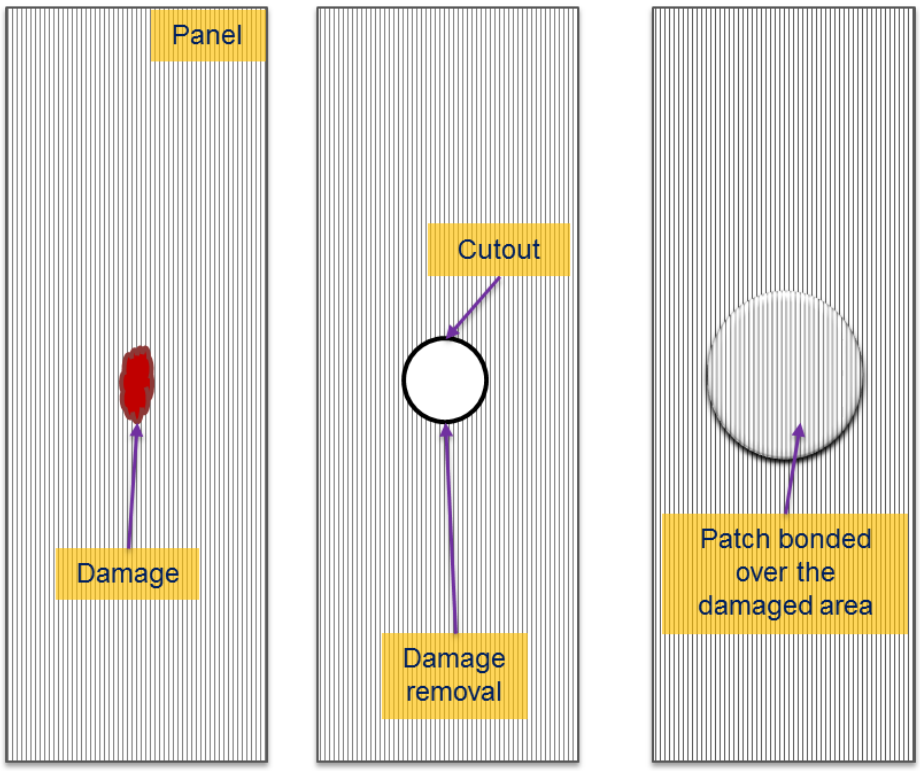

Figure 1.12: Methodology of externally bonded patch repair

portion and it is known as single sided patch repair. It is also termed as unsymmetrical patch repair since there is a slight shift in neutral axis of the repaired system due to a patch placed on only one side. The shift in neutral axis introduces bending stress in addition to in−plane applied stress and this bending increases the stress levels at the unpatched surface. If it is possible to access both the surface of damage portion, patch is bonded onto both side of the panel over the damaged area and therefore it is known as double sided patch repair. Double sided patch repair is also termed as symmetrical patch repair since the patch is placed on both side of the panel and the neutral axis after the repair remains unaltered which ensures that there is only in−plane applied loading.

From technological aspects composite repair is also categorized as active and passive repair. Over past two decades, repair of the damaged structures is carried out using a passive patch work methodology. In the recent years, attention has been paid by the researchers to explore active patch repair technique by inserting smart materials [21]. In active patch repair, the smart patches made of piezoelectric actuators are used which can enable the active restoration of strength and stiffness of repaired structure by introducing a local moment/force in opposite sense thereby reducing the stress level around the damage [22].

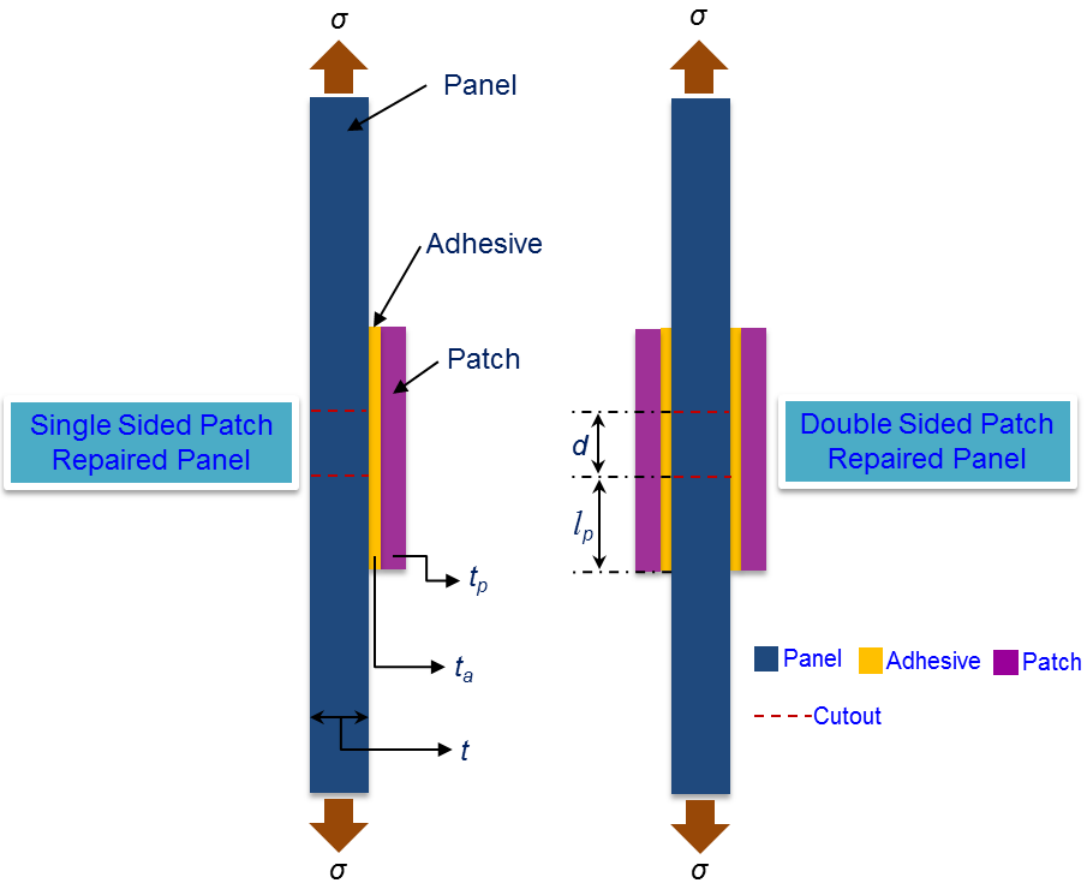

Figure 1.13: Single and double sided externally bonded patch repair

1.4 Progressive failure analysis (PFA) of composite structures

1.4.1 Prominence of damage analysis

The damage in fiber laminated composite material is quite complex than the conventional metallic materials and it develops locally through a number of mechanism or modes like matrix failure, fiber breakage, fiber−matrix debonding, delamination etc. All of these modes may have strong interactions with one another and they grow under the advancing load thereby affecting the structural integrity of the structure and eventually causing the ultimate or final failure of them. However, before the ultimate failure, composite structure with local damages can tolerate or sustain the operating load much better than the metallic counterparts. In general, the residual load bearing capability of composite structure from onset or initiation of damage to ultimate failure can be quite significant. Therefore, to exploit the full potential of composite structures it is of paramount importance to study the initiation and propagation of damage, damage mechanism as well as the load bearing capacity of them.

The problem of damage evolution, accurate strength and failure mechanism prediction in composite structure is also essential for developing a more reliable and safer design. Accurate prediction of the damage behaviour of composite laminated structures will lead us to the design of efficient structures which will in turn reduce the cost of manufacturing significantly. Further, the accurate determination of failure modes and their progression helps either to devise structural features for damage containment or to define fail safe criteria (damage tolerant design). However, the strength and failure mechanism prediction in composite structures are more involved and challenging because of several onset interacting failure modes as well as their inherently brittle, inhomogeneous and anisotropic nature. Hence, a reliable methodology is needed for predicting failure initiation and propagation in CFRP laminates. Employing experimental techniques would be very expensive, time consuming and complicated for studying the failure mechanism and strength determination for all the possible complex stress state because of the higher number of tests involved. Analytically, it would be very complicated or may not be possible due to complexity involved in the problem. Numerical technique based on finite element method is gaining more importance and wider acceptance in recent years due to the rapid development in computational resources and algorithm for reliable prediction of such phenomenon with a greater degree of accuracy. However, there is still a lot of work to be done in this area to exactly capture the mechanism of failure with improved accuracy. Nevertheless, the use of numerical simulation tools allow us to replace structural component testing with virtual testing to predict the damage behaviour and the mode of failure of CFRP laminated structures, thus paving way for lower development time.

Numerically, the strength based failure criteria have been commonly used to predict the damage phenomenon in composite structures. The use of failure criterion can only predict the onset of the different damage mechanisms in most of the cases and provide no information on post failure response and residual load bearing capacity or ultimate strength of the composite structure. However, the knowledge of damage modes, damage initiation and propagation, residual strength of the structures made of composite is essentially important and very crucial especially in aerospace application to prevent premature failure thereby designing a damage tolerant one. Therefore, it is

necessary to perform progressive failure analysis which facilitates the simulation of degraded structural response from initiation to propagation of damage, revealing various damage modes and their residual strength.

1.4.2 Steps involved in PFA

A typical progressive failure analysis comprises three important steps: stress or strain analysis, damage prediction and damage modeling as depicted in Fig. 1.14.

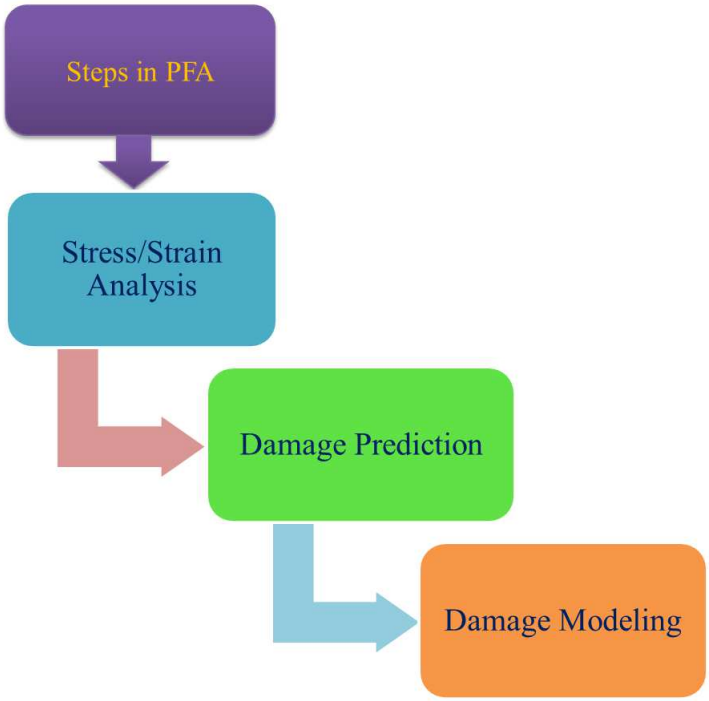

Figure 1.14: Steps involved in progressive failure analysis

Stress/strain analysis

Initially, the finite element model (FEM) of composite structure is developed. Then the stress analysis is carried out using finite element analysis under given loading and boundary conditions in order to obtain the stresses or strains in principal material directions of the laminate.

Damage prediction

In second step, the stress or strain values obtained from FE analysis together with experimentally evaluated material strength parameters are substituted into a failure criterion to predict the failure of composite structure. For this purpose, several failure theories have been proposed in the literature to predict the failure state of composite structures and the detailed review on failure theories for fibrous composites can be found in Ref. [23–28]. Most of these theories are developed by extending the well−established failure theories for isotropic materials to account for the anisotropy in stiffness

and strength of the composites. Broadly, the failure theories for fibrous composite materials can be categorized into two groups as shown in Fig. 1.14: non−interactive and interactive failure theories.

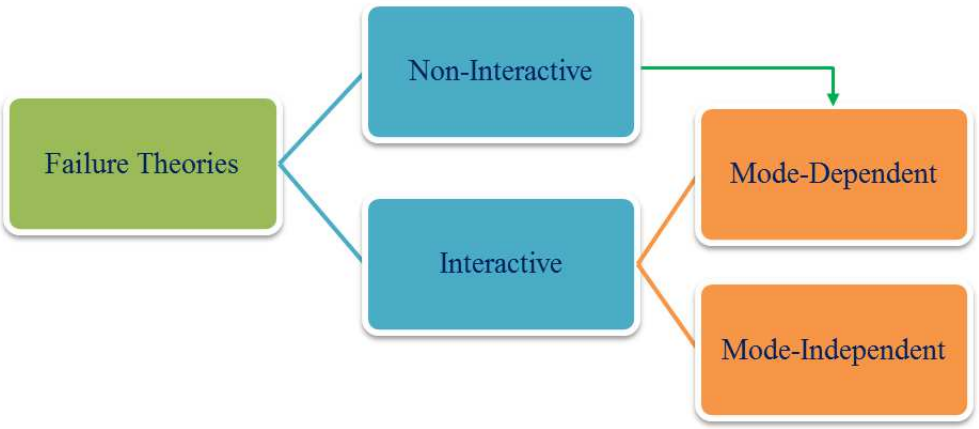

Figure 1.15: Classification of failure theories for fibrous composite materials

Non−interactive failure theories are those in which the interaction between stress/strain components is not taken into account for predicting the failure. The failure is predicted by comparing the individual stresses/strains with corresponding allowable strengths or strains therefore distinguishing the nature of failure mode from fiber to matrix. Maximum stress [29] and maximum strain [30] failure theories are most common example in this category. These failure theories are also known as independent failure criterion because they assume that the failure has occurred whenever any one of the stress or strain components attains its critical value, independent of the values of all other stress or strain components.

Interactive failure theories are those in which all or some of the stress or strain components are included in the criterion representing the failure. These failure theories provide a better correlation with the experimental data because of taking into account the stress or strain interaction effect. Interactive failure theories are categorized as mode−independent failure criterion and mode−dependent failure criterion. Mode−independent failure criterions are those that predict the failure without distinguishing the nature of failure modes. Examples of such theory includes: Tsai−Wu [31], Tsai−Hill, Azzi−Tsai [32], Hoffman [33], Chamis etc. [34]. Mode−dependent failure theories are those that predict the failure together with failure modes (such matrix failure or fiber failure) which essentially stimulates the failure in composites and reveals the way the composite material would fail. Hashin−Rotem [35], Hashin [36], Puck's [37] failure criterions are some of the examples in this category of failure theories.

Damage modeling

In third step, once the damage is detected by a failure theory, a damage modeling technique is essential to take into account the effect of damage on load bearing capacity of the laminate and further post−damage analysis is performed. Material property degradation method (MPDM) [38–41] is one of the most popular and widely used approach to account for progressive damage in composites once the damage is identified by a failure criterion. MPDM assumes that the damaged material can

be replaced by an equivalent material with degraded material properties or stiffness properties. Therefore, once damage is identified in composite materials by a failure criterion, the MPDM is applied either at ply level or at elemental level to reflect the loss on load−bearing capabilities of these materials by degrading their properties. At ply level, once the damaged ply is identified by a failure criterion, the material properties of the failed ply are degraded completely [42] based on the assumption that the damaged ply cannot sustain any more load and therefore the loss in load bearing capacity is taken into account. This method is known as *ply−discount method* and it is repeated till the final failure is reached. The ply−discount method is simple to understand and implement however it is highly conservative and could lead to underestimation of strength and stiffness of the composite laminate. To overcome the limitation of ply−discount method, MPDM is applied at *elemental level* and the properties of failed element are degraded rather than that of whole ply to reflect the damage [38]. Mathematically, the MPDM approach can be expressed as

$$E' = D\,E, \quad \nu' = D\,\nu, \quad G' = D\,G \tag{1.1}$$

where E', ν' and G' corresponds to Young's modulus, Poisson's ratio and shear modulus of damaged ply/element respectively whereas E, ν and G describe the corresponding properties for undamaged ply/element. Operator D represents the factor by which the material properties needs to be degraded.

1.5 Optimization of fiber reinforced polymer composites using genetic algorithm (GA)

1.5.1 Basic principle of GA

Optimization can be defined as a process to obtain a set of design variables that minimize or maximize the objective function while satisfying the prevailing constraints. Optimization methods can be broadly classified as *gradient−based methods* and *stochastic methods*. Typically gradient based methods can be used to solve diverse optimization problems [43] but they pose difficulty in presence of local minima and optimization with discrete or integer design variables [44]. However, the design of composite structures often involves the optimization of discrete variables such as number of plies, ply orientation, stacking sequence etc., and therefore it is essential to use a more sophisticated optimization technique which takes into account the design space with discrete and integer variables. Recently, evolutionary optimization algorithms such as genetic algorithms has been employed for the optimization of composite laminates for higher strength or lower weight for a chosen application. It is well suited for searching a discrete design space and provides global minima rather than a local one.

GA is an evolutionary based optimization technique which was developed by John Holland [45]. It is an efficient global search optimization method which operates on a population of potential solutions applying the principle of survival of the fittest (*Darwin's theory*) to produce successively better approximations to a solution [46]. At each generation of a GA, a new set of approximations is created by the process of selecting individuals according to their level of fitness in the problem domain. Over successive generations, the population *evolves* towards an optimal solution. Genetic

algorithm maintains a population pool of candidate solutions called *strings or chromosomes*. Each chromosome is associated with a fitness value which is determined by a user defined function, called the *fitness function*. The function returns a suitable and optimal magnitude which is proportional to the candidate solutions.

1.5.2 Basic operators of GA: reproduction,crossover,mutation

The basic operators of genetic algorithms are *reproduction (selection)*, *crossover (recombination)* and *mutation* [46]. The structure of a GA based optimization scheme is shown in Fig 1.16.

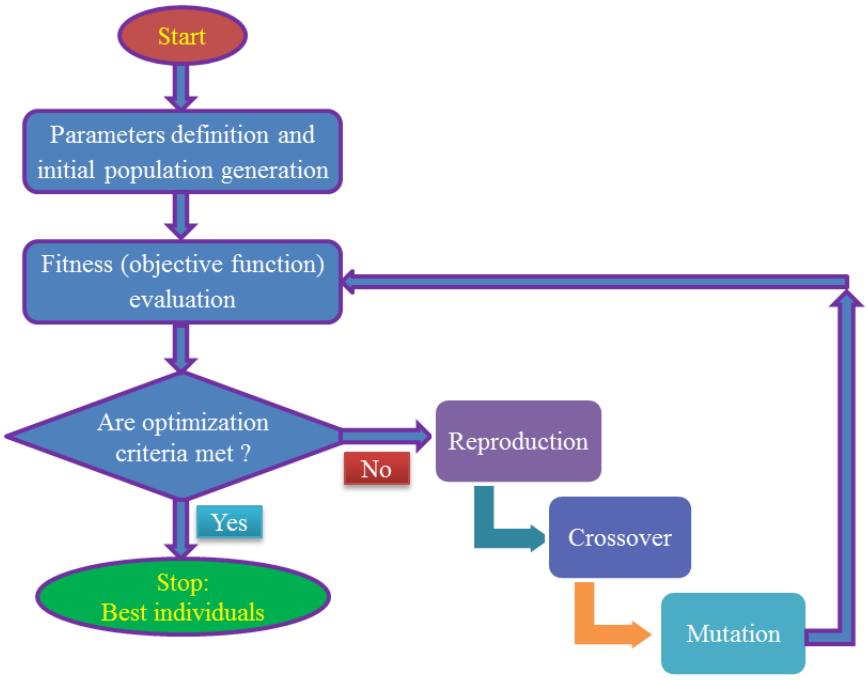

Figure 1.16: Flow chart depicting fundamental operators and principle of genetic algorithm for optimization problem

The process of a genetic algorithm begins with the generation of *initial population*. The initial population is most commonly generated by seeding (initial input or guess) the population with random values. The *population* is the collection of all the chromosomes or design variables which are usually represented by binary coding or floating points in GA. A *generation* is the population after a specific number of iterations of the genetic loop.

A *fitness value* is then assigned to each chromosome based on fitness function (objective function) which provides a way for the GA to analyze the performance of each chromosome in the population.

In *reproduction*, chromosomes based on their fitness value are selected from the current generation to be the parents for next generation. In addition, the first best or few best chromosomes of current generation are copied to the population of new generation to carry forward the best qualities and this process is called as *elitism*. The selection based on fitness value and elitism essentially drives the GA to improve the population fitness over the successive generations. Population enriched with only better individuals or chromosomes are called as *mating pool*. The most commonly used methods of

selection includes: Roulette wheel, rank, Boltzmann, steady state and tournament selection.

The *crossover* is the primary operator in GA by which new designs are created. The crossover operator is applied to the mating pool to combine (mates) two chromosomes (parents) to produce a new one called as *offspring* (child) that may be better than both of the parents retaining only the best characteristics from each of them. The crossover operator may be of types: One−point, Two−point, Uniform, Arithmetic and Heuristic cross over. One point crossover is shown in Fig. 1.17.

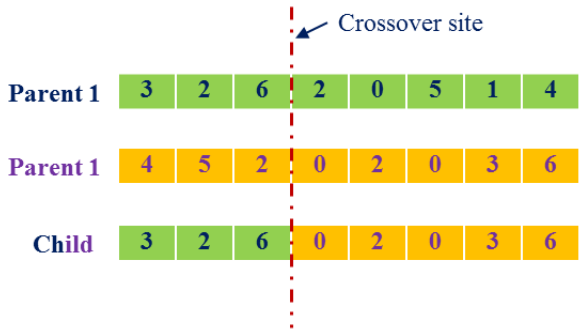

Figure 1.17: Single−point crossover in a GA

Mutation operator helps in maintaining the genetic diversity from one generation to the next. It randomly alters one or more gene values of a chromosome in mating pool to produce entirely a new gene in anticipation of arriving at a better solution. Mutation prevents the algorithm to be trapped in local minima by introducing new features into the population of chromosomes and preventing them from becoming too similar to each other. The mutation operator may be of types: Flip bit, Boundary, Uniform, Non−uniform and Gaussian. An example of mutation is shown in Fig. 1.18.

Figure 1.18: Mutation in a GA

GA has become one of the most widely accepted and primary choice for the optimization in composite domain because it involves simple operations that are easy to program [47]. It uses objective function information rather than its derivatives therefore it can be applied to the problems where the gradient is hard to obtain or no gradient exist. It works well with mixed discrete/continuous problems and therefore offers flexibility of being applied to a large variety of problems with different types of variables and objective functions particularly for the problems with multimodal functions. It is more robust in a sense that it is not being at the risk of getting stuck at a local minima or maxima. It does search from a population of points rather than a single point and provides a set of optimal solutions instead of a single one, thus giving the designer a set of options. It can be easily parallelized and can be linked well with other technique to perform hybrid optimization. Despite several advantages, the most important disadvantage of GA technique is that they are computationally expensive.

1.6 Digital image correlation(DIC)

Digital image correlation is a non−contact optical−numerical full field measurement technique that facilitates the determination of deformation and strain fields over the specimen surface. The underlying concept of DIC is based on pattern matching wherein the displacement field is identified by correlating or comparing an image of specimen taken in undeformed state with a second image of the same specimen (or series of images) taken in deformed state. The image grabbed in undeformed state or under no load condition is termed as master or reference image whereas the image taken during the deformation or under a load is known as slave image. The DIC technique is also known as digital speckle correlation method (DSCM), texture correlation (TC), computer−aided speckle interferometry (CASI) and electronic speckle photography (ESP) [48]. Over the last decades, DIC has been widely accepted and commonly used as a powerful and flexible tool for full field deformation measurement in the field of experimental solid mechanics due to the simplicity of the measurement setup. A 2D−DIC involves a single camera (monocular) and provides only in−plane displacement/strain fields whereas a 3D−DIC utilizes two cameras (stereo vision) and facilitates out of plane displacement measurement.

1.6.1 Evolution of DIC technique

The photogrammetry technique developed in the early 1850's to obtain geometric data from a photograph is the root of all image−based measurement technique and the progress in image processing methods over the years has led to the evolution of digital image correlation (DIC). The method of DIC was first proposed by Peter and Ranson [49] in the field of experimental mechanics in the early 1980's. Sutton and co−workers at the University of South Carolina developed the initial implementation of DIC technique [50–57]. Since then it has been evaluated and improved significantly [53, 54, 58–60]. However, the fundamental principles of the method remain unchanged and are well explained in Ref. [49, 51, 52].

1.6.2 DIC measurement principle

The basic principle of DIC is to track or match the surface points in the images recorded before and after deformation to obtain their displacement. The displacement of a surface point on a specimen under test is estimated by comparing the gray level pixel value between two digital images taken before (reference image) and after (deformed image) deformation as shown schematically in Fig. 1.19 [48]. Consider that the location of surface point P in undeformed/reference image is represented by pixel (x_0, y_0) and after the deformation the point P has moved to a new location P' whose pixel coordinate is (x_0', y_0') in deformed image. The displacement of surface point P is then determined by calculating the difference in the coordinates of P' (x_0', y_0') and $P(x_0, y_0)$. Therefore, the displacement of surface point P is $(x_0' - x_0)$ pixels in the x-direction and $(y_0' - y_0)$ pixels in the y-direction [48].

1.6.3 Subset matching methodology

The position of the pixel (x_0', y_0') in deformed image corresponding to the surface point P is generally not possible to determine by comparing single pixel, as many pixels in the deformed image may have

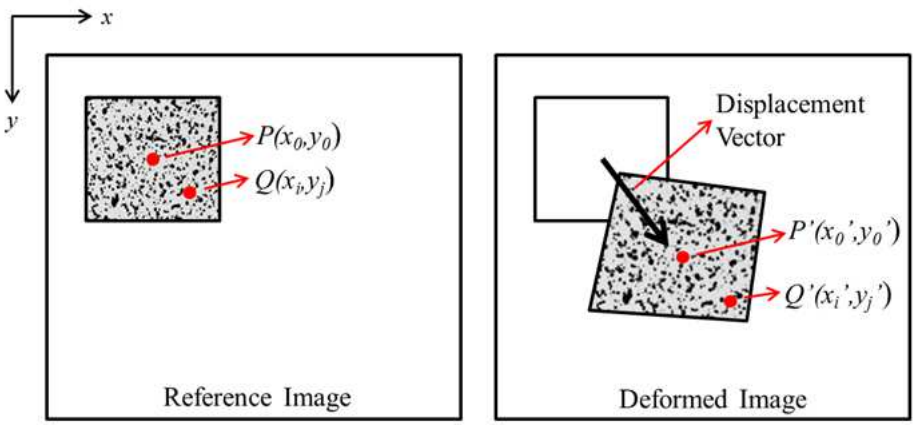

Figure 1.19: Schematic illustration of a reference square subset before deformation and a deformed subset after deformation

the same gray level pixel value. Therefore, a square area with multiple pixels [(2M+1)×(2M+1) pixels] centered at point P in reference image (called as undeformed subset) is compared with the regions of the same size in deformed image (called as deformed subset). The subset matching methodology provides a better correspondence because a square subset, rather than an individual pixel, will have the distinguish pattern of gray level pixel which will differentiate it from other subsets and therefore it can be more uniquely identified in the deformed image. The DIC algorithm looks for the deformed subset that best matches the undeformed subset in the reference image. Once the location of the best matching deformed subset is identified, the difference in the coordinates of center of the deformed subset and undeformed subset gives the displacement vector of the surface point P that corresponds to the pixel (x_0, y_0) [48].

1.6.4 Random texture pattern (speckle pattern)

To achieve a unique correspondence (only one valid matching position) of the subset during matching process, a random texture is required rather than a regular texture such that the *correspondence* and *aperture problem* can be avoided [60]. Most of the material may not exhibit natural random textures and therefore the random textures are applied artificially over the specimen surface before the test is performed. The applied random textures over the specimen surface as shown in Fig. 1.20 is commonly known as the *speckle pattern*.

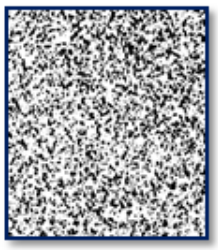

Figure 1.20: Random speckle pattern

1.6.5 Correlation criterion

In order to evaluate quantitatively the degree of similarity between the subset in reference image and deformed image to identify the position P' in the whole deformed image that best matches with P in reference image, different correlation criterions has been used. These criterions can be broadly categorized into two groups; *cross−correlation criterion (CC)* and *sum of squared differences criterion (SSD)*. In CC approach P' can be identified as a position that maximizes the cross correlation function between the subset in reference and deformed image whereas in SSD approach it is the position that minimizes the bidimensional error function [61–63].

If f and g is the reference and deformed image and $f($x, y$)$ and $g(x', y')$ represent the gray levels of reference and deformed images with (x, y) and (x', y') being the co−ordinates of a point in the subset before and after deformation, respectively. Then the two criterions can be defined as [48]:

Cross−correlation (CC)

$$C_{cc} = \sum_{i=-M}^{M} \sum_{j=-M}^{M} \left[f(x_i, y_j)\, g(x_i^{'}, y_j^{'}) \right] \tag{1.2}$$

Sum of squared differences (SSD)

$$C_{SSD} = \sum_{i=-M}^{M} \sum_{j=-M}^{M} \left[f(x_i, y_j) - g(x_i^{'}, y_j^{'}) \right]^2 \tag{1.3}$$

These criteria are proven to be sensitive to the issues that may easily arise during a standard test such as offset and linear scale in illumination [60], and consequently their normalized version namely *zero normalized cross correlation(ZNCC)* and *zero normalized sum of squared differences (ZNSSD)* are generally preferred [48]:

Zero−normalized cross−correlation (ZNCC)

$$C_{ZNCC} = \sum_{i=-M}^{M} \sum_{j=-M}^{M} \left\{ \frac{[f(x_i, y_j) - f_m] \times [g(x_i', y_j') - g_m]}{\Delta f \Delta g} \right\} \tag{1.4}$$

Zero−normalized sum of squared differences (ZNSSD)

$$C_{ZNSSD} = \sum_{i=-M}^{M} \sum_{j=-M}^{M} \left[\frac{f(x_i, y_j) - f_m}{\Delta f} - \frac{g(x_i', y_j') - g_m}{\Delta g} \right]^2 \tag{1.5}$$

where,

$$f_m = \frac{1}{(2M+1)^2} \sum_{i=-M}^{M} \sum_{j=-M}^{M} f(x_i, y_j) \tag{1.6}$$

$$g_m = \frac{1}{(2M+1)^2} \sum_{i=-M}^{M} \sum_{j=-M}^{M} g(x'_i, y'_j) \tag{1.7}$$

$$\Delta f = \sqrt{\sum_{i=-M}^{M} \sum_{j=-M}^{M} [f(x_i, y_j) - f_m]^2} \tag{1.8}$$

$$\Delta g = \sqrt{\sum_{i=-M}^{M} \sum_{j=-M}^{M} \left[g(x'_i, y'_j) - g_m\right]^2} \tag{1.9}$$

$$x' = x + u_0 + \frac{\partial u}{\partial x} dx + \frac{\partial u}{\partial y} dy \tag{1.10}$$

$$y' = y + v_0 + \frac{\partial v}{\partial x} dx + \frac{\partial v}{\partial y} dy \tag{1.11}$$

The normalized version are proven to successfully overcome lighting related issues. Here, u_0 and v_0 are the translations of center of sub−image in x and y direction respectively.

The matching procedure is completed through searching the peak position of the distribution of correlation coefficient. Once the correlation coefficient extremum is detected, the position of the deformed subset is determined. The differences in the positions of the reference subset center and the deformed subset center yields the in−plane displacement vector at point P, as illustrated in Fig 1.19.

The discrete nature of the digital image enables computation of the integer displacements with unit pixel accuracy. However, the coordinates of point in the deformed subset may located at non−integer pixel positions (i.e., sub−pixel location) therefore certain sub−pixel registration algorithms are required to further improve displacement measurement accuracy. Generally, to achieve sub−pixel accuracy, the implementation of 2D DIC comprises of two consecutive steps, namely initial deformation estimation and sub−pixel displacement measurement. 2D DIC method normally requires an accurate initial guess of the deformation before achieving sub−pixel accuracy. For e.g., the most commonly used iterative spatial cross−correlation algorithm (e.g. the Newton Raphson method) only converges when an accurate initial guess is provided. The techniques to achieve reliable initial guess of deformation are discussed in Ref. [48]. Also, the various sub−pixel registration algorithms such as coarse−fine search algorithm, peak−finding algorithm, iterative spatial domain cross−correlation algorithm, spatial−gradient−based algorithm, genetic algorithms, finite element method and B−spline algorithm etc., proposed in the literature to improve the accuracy of DIC measurement are introduced and discussed in the same Ref. [48]. However, the iterative spatial domain cross−correlation algorithm and the peak−finding algorithms are the most widely used algorithms due to their simplicity and accuracy.

1.6.6 Whole field displacement estimation

Once the single subset tracking is achieved, its extension to full filed displacement or motion estimation is quite trivial [48]. The estimation of full field displacement begins with the manual selection of an area over the specimen surface in reference image, called as area of interest (AOI) or region of interest (ROI) or zone of interest (ZOI). The ROI is divided into number of subsets and the correlation is performed by tracing the center point of each and every subset during the deformation. The center points are equally spaced in both horizontal and vertical direction and spacing between the two consecutive center points is known as step which essentially defines the analysis spatial resolution [48]. Conventional correlation calculation generally starts with the upper−left point of the ROI. The calculation analysis is then carried out point by point along each row or column. The subset tracking procedure as discussed earlier can be applied on every subset to determine the displacement of every point but it makes the correlation more time consuming. To save the computational time the computed displacements of the current point are used as the initial guess of the next point. This makes the conventional DIC as path dependent and it may produce erroneous results in presence of discontinuity like crack, holes et., as transfer of initial guess will be lost. Therefore, more recently a universally applicable reliability−guided DIC (RG −DIC) method has been proposed by Pan [64] for reliable image deformation measurement. In this method, the ZNCC coefficient is used to identify the reliability of the point computed. The correlation calculation begins with a seed point and is then guided by the ZNCC coefficient. That means the neighbors of the point with the highest ZNCC coefficient in the queue for the computed points will be processed first. Thus, the calculation path is always along the most reliable direction and possible error propagation of the conventional DIC method can be entirely avoided. The RG−DIC method is very robust and effective. It is universally applicable to the deformation measurement of images with area and/or deformation discontinuities.

1.6.7 Whole field strain estimation

Whole field strain distributions are more important and desirable in the area of experimental solid mechanics such as mechanical testing of material and structural stress analysis. Less work has been devoted on the reliable estimation of strain fields from the displacement field given by DIC [48]. This is because the displacement gradient (i.e. strain) can be directly estimated using the Newton−Raphson, quasi−Newton−Raphson, Levenberg−Marquart or genetic algorithm. Also, the strains can be computed as a numerical differentiation process of the estimated displacement [48]. It should be noted that the error of estimated displacement gradients using the Newton−Raphson or genetic method normally limits its use only to local strains greater than approximately 0.010. Although the relationship between the strain and displacement can be described as a numerical differentiation process in mathematical theory, unfortunately, the numerical differentiation is considered as an unstable and risky operation, because it can amplify the noise contained in the computed displacement. Therefore, the resultant strains are unreliable if they are deduced by directly differentiating the estimated noisy displacements [48].

The accuracy of strain estimation can be improved by smoothing the computed displacement fields first and subsequently differentiating them to calculate strains. Based on these considerations, Sutton et al. [56] proposed a technique that involves smoothing the computed displacement fields with the penalty finite element method first and subsequently differentiating them to calculate

strains. Meng et al. [65] further improved the FEM smoothing technique. In addition, thin plate spline smoothing technique and generalized cross validation technique were introduced by Wang et al. [66] to remove the noises contained in displacement fields. However, smoothing noisy discrete data using the penalty finite element method or thin plates spline is quite cumbersome. More recently, Xiang et al. [67] used the moving least−squares (MLS) method to smooth the displacement field followed by a numerical differentiation of the smoothed displacement field to get the strain fields. The more practical and recent technique for strain estimation being used in DIC measurement is the point wise local least−squares fitting technique used and advocated by Pan et al. [68]. In this method, the estimated displacement fields are locally fitted by polynomial functions and the strains are estimated starting from the computed regression coefficients. Further details on the implementation of local least−squares fitting technique for strain estimation can be found in Ref. [48, 68].

1.6.8 Two-dimensional and three-dimensional DIC setup

A schematic of 2D DIC configuration is given in Fig. 1.21. The 2D DIC technique involves a single camera with its optical axis must be aligned perpendicular to the specimen surface. The 2D DIC measurement is applicable only for planar objects (specimen with only flat surface) and can be used in a situation where the expected displacement field is predominantly in−plane because relatively small out−of−plane motion will change the magnification and introduce errors in the measured in-plane displacement [69]. Therefore, non-planar geometry is difficult to analyze with 2D DIC approach and also the out−of−plane displacement may not always be possible to be avoid in actual practice. To overcome these fundamental limitations, three−dimensional (3D) DIC method is developed which uses a stereo vision system employing at least two or more cameras to accurately measure the full three−dimensional shape and deformation of a curved or planar object, even when the object undergoes large out−of−plane rotation and displacement [48, 60, 69].

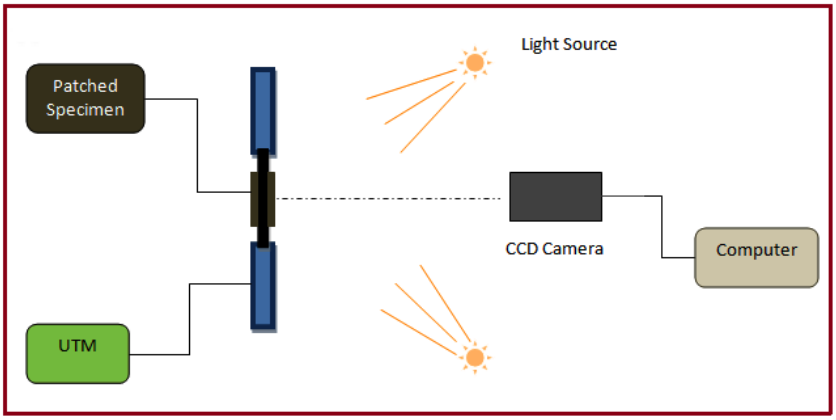

Figure 1.21: Schematic diagram of 2D−DIC setup

A schematic of a typical 3D DIC configuration is given in Fig. 1.22. The cameras can be arranged in any orientation with respect to each other, and to the specimen surface as long as the area of interest lies within the area of view of both the cameras. To make a 3D measurement possible, the stereo camera pair model must first be calibrated to find the relative position and orientation between the cameras [70, 71]. Once calibrated, the 3D geometry of the object in image pair is reconstructed

using triangulation techniques [72]. Similar to 2D DIC, image pairs of the specimen's reference and deformed configuration are acquired using the stereo−vision setup. The material surface is then three−dimensionally reconstructed for every deformed image pair. The three−dimensional reconstruction in the reference and the deformed image is compared to find the displacement field for the object surface. This process is called temporal matching [71]. Local strains are computed in small windows of the displacement field.

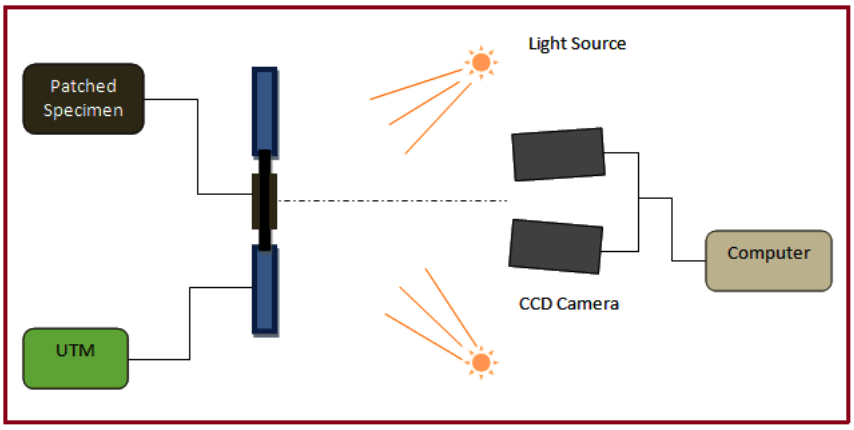

Figure 1.22: Schematic diagram of 3D−DIC setup

The core of the algorithm or matching process described in the earlier sub−sections is shared by both 2D and 3D DIC approaches. The basic idea for out−of−plane displacement measurement using 3D DIC method is outlined as follows. When an object undergoes an out−of−plane displacement, the magnification of the imaging system changes and the image captured after the displacement is different from the original image. The resulting expansion or contraction of the images can be detected by use of the method of DIC. The unknown out−of−plane displacement is subsequently determined quantitatively after a calibration.

1.6.9 Advantages, disadvantages and accuracy of DIC

The method of DIC has many advantages over other optical methods. Firstly, any class of material could be studied and the specimen surface preparation is simpler. Secondly, optics involved is quite simpler. Thirdly, the displacement information is retrieved by direct comparison of the speckle patterns before and after deformation, therefore no fringe analysis and phase−unwrapping is needed in this method. Fourthly, there is no fringe density limitation in DIC, so the measurement range is much larger than other techniques. Finally, the resolution for DIC method is adjustable by using optical systems with various magnifications. Additionally, it is truly a non−contact by nature and provides full field data

Nevertheless, digital image correlation still suffers some disadvantages or limitations. It requires specimen with random speckle pattern and needs optical access to the specimen. It is sensitive to light fluctuations and rigid body motion. It requires moderately large amount of computation time and poses difficulty of correlation at the edge. It does not provide full−field strain resolution better than 0.1%.

The DIC technique provides displacement resolution of sub−pixel accuracy typically 1/50th of a pixel and the maximum strain accuracy is of the order of 0.02 %. The least strain that can be measured using DIC is 50 microstrain. However, there are several parameters like subset size, step size and strain window size which can influence the accuracy of measurements [73].

In the case of macro−object measurement, DIC method would give an accuracy of up to 0.01 pixels for rigid−body displacement. However, for in−plane deformation measurement, the accuracy drops to 0.1 pixels. In the case of micro−object measurement using images from a scanning tunneling microscopy, an accuracy of 0.5 pixels have been reported.

1.7 Literature review

1.7.1 Externally bonded patch repaired composite panel

Soutis and Hu [20] have carried out bonded repair study on damaged CFRP panel subjected to compressive load. The panel was repaired with circular and square patch shape and only the double sided patch repair configuration were analyzed. The influence of different repair parameters such as patch overlap length, patch thickness and adhesive thickness on repair performance is studied. They predicted the optimum patch overlap length to be approximately 12−15 mm and the optimum patch thickness is about half of the panel thickness provided if the membrane stiffness (i.e. the product of elastic modulus and thickness) of patch and panel is same. With optimized parameters, the bonded repair can recover 80 percent of undamaged laminate strength. They concluded that the use of over−stiff patches is harmful as they introduce high peel and shear stress concentration which in turn can cause premature failure of the adhesive layer thereby reducing the strength of the repair. Tapering the patch edges and increasing the local adhesive thickness improves the repair performance. They too have studied the failure mechanism and have shown possible modes of failure such as adherend delamination, fiber buckling and patch debonding.

Soutis et al. [74] in another study based on FEM has reported the influence of several repair or geometric parameters on compressive strength of double sided patch repaired panel. Only circular patch were used to repair the panel and the effect of using plug filling in the drilled hole is also evaluated. To predict the damage initiation and strength, maximum normal stress criterion is chosen for identifying the failure in composite whereas the damage in adhesive layer leading to patch debonding is monitored using average shear stress criterion. It is concluded that the method of plugging the open hole in the specimen before patching is shown to reduce the stress concentration at the hole edge and further improve the repair strength. It was also reported that fibre micro−buckling is always the governing failure mechanism for the ultimate failure for the cases of intermediate and high patch thicknesses, whereas patch debonding was the final failure mechanism for thin patch system. The damage mechanism were observed by X−ray radiographs and SEM (and scanning electron micrographs) which reveals the presence of matrix cracking at notch edges, delamination, patch debonding at patch edges and fibre micro−buckling in 0° layers.

Hu and Soutis [75] carried out another numerical study based on finite element method (FEM) to predict the compressive strength of CFRP panel repaired with double sided patch of circular shape. A fracture−mechanics−based criterion (cohesive zone model) with damage initiation and growth governed by a stress−based criterion has been used to predict the compressive strength repaired

panel. The contribution of panel, patch and adhesive on the stress distribution and stress intensity factor (SIF) were assessed through linear−superposition approach. It is concluded that the failure load and the corresponding critical buckling length could be obtained from the intersection of stress and SIF distribution curves. The strength predicted by numerical approach is found to be lower than the experimental results with a maximum error of 15%.

Liu and Wang [76] presented a progressive failure analysis of bonded composite repairs and verified its prediction with experimental results. The panel was repaired with circular patch bonded on both sided and the influence of different repair parameters like patch size, patch thickness, patch stacking sequence and adhesive thickness on failure initiation and ultimate strength of repaired panel has been investigated. Stress based Tsai−Wu criterion has been implemented to identify the matrix cracking and fiber breakage in addition with Ye criterion for detecting delamination in composite panel whereas maximum shear stress criterion has been used to account for failure in adhesive layer. Material properties degradation method has been used to for damage modeling. The predicted failure strength reported was always lower than the experimental results with a maximum error of approximately 20%. The optimum repair parameters were investigated through parametric study and it has been concluded that the with overlap length of 15 mm, patch thickness to panel thickness ratio of 0.6 for fixed patch to parent panel stiffness ratio of 0.3 and adhesive thickness between 0.2−0.3 mm, one can achieve a better repair performance.

Gong [77] have reported a study on effect of local stress on static tensile strength and fatigue life of a CFRP panel repaired with double sided externally bonded patch having different shapes like circular, rectangle, elliptical. The panel was repaired by soft patches (patches cured directly on panel without using adhesive) and hard patches (pre−cured patch bonded to panel using adhesive). It is showed that the square patches make the system more rigid and do the best repair due to biggest adhesive joint surface whereas the performance of circular patch increases with increasing diameter. For the same bonded surface, the longitudinal ellipse patch appears the most efficient. The application of Z−pins can also improve the repair performance. A numerical study based on FEM is carried out to identify the critical zones in repaired configuration and then the effect of local stress concentration on fatigue life was discussed as a function of patch configurations. It was found that in patched composite repairs the high stress concentration in critical zones leads to early patch debonding and results in low fatigue life.

Campilho et al. [78] have carried out both experimental and numerical study to investigate the tensile behaviour of damaged CFRP laminates repaired with circular patches. It is reported that the smaller patch overlap length (5 mm) reduces the strength of single and double sided patch repaired panel due to a premature patch debonding. At higher patch overlap length, only double sided patch repaired panel shows improvement in failure strength. The patch thickness shows smaller influence on repaired strength and the double sided repair has more strength in comparison to single sided one.

Campilho et al. [79] in another publication has reported the compressive behaviour of damaged CFRP laminates repaired with circular patches as discussed above. The influence of patch overlap length and patch thickness for the case of single and double sided patch repair was evaluated through a parametric study based on FEM. Cohesive element together with mixed−mode criteria is taken into account in finite element analysis (FEA) to simulate a cohesive fracture of adhesive layer. It was reported based on experimental observation that the tensile strength increases with increasing

overlap length and patch thickness. From both tensile and compressive behaviour study it was concluded that double−sided repair is better than the single−sided one and the optimum repair could be achieved with double−sided repair with 15 mm patch overlap length and patch thickness being half the panel thickness considering the weight penalty and aerodynamics disturbance.

Cheng et al. [80] have presented a work on optimization of parameters involved in the repair of a CFRP panel with double sided circular patch under tensile loading. Hoffman's criterion has been used to predict the damage initiation in composite material whereas failure in adhesive layer is predicted based on critical plastic strain. Based on strength ratio it is reported that the patches with different stacking sequences having same membrane stiffness does not influence the repaired tensile strength which is further validated experimentally. Lower adhesive stiffness and lower patch thickness yields improved repair strength. A design parameter K was introduced to take into account the interaction between the different parameters of a patched repair and it was concluded that the repair is said to be optimum if the value of K reaches unity.

Cheng et al. [81] in another publication have further investigated the similar repair configuration as discussed above in preceding paragraph and then reported the failure process of repaired panel under the same tensile loading. Fracture surface were examined by low magnification photography to describe the failure mechanism. Acoustic emission technique was used to detect the damage initiation and propagation during testing and it is concluded that this technique is very efficient to locate damage initiation and follow damage propagation. Cheng et al. [82] extended the earlier work as discussed above and performed an non destructive technique (NDT) investigation using infra−red thermography to detect the damage in the same repaired configuration. FEA based study also carried out to analyze the influence of plug material on repair tensile strength and it is reported that the repair strength ratio increases slightly as the modulus of plug material (adhesive) varied from 0 to 80 GPa.

Park and Kong [83] have experimentally studied the compressive behaviour of a CFRP panel wherein the damage was first introduce by a low velocity impact and then the damaged portion was repaired with external patches bonded using adhesive. Both UD laminate and sandwich structure is considered for repair study. The compressive strength of the UD laminates and sandwich specimen after repair is recovered to 90% and 89% of the compressive strength before damage, respectively. Finite element analysis study is also carried out and the obtained results are compared with the experimental data.

Shiuh and Chao [84] have performed stress analysis on damaged composite panel repaired with double sided adhesively bonded square patch to study. They studied the influence of repair parameters on repair efficiency. The repair efficiency is evaluated by comparing the stress concentration factor in the damaged hole before and after repair. It is reported that the stiffer and thicker patch reduces the load across the damaged area yielding less stress concentration in the damaged hole thereby increasing the repair efficiency. Thin adhesive layer together with high shear modulus results in less load transfer to the patch leading to high stress concentration in the damaged hole. Based on numerical results, they concluded that the patch parameter has got more influence on repair performance than the adhesive system.

1.7.2 Progressive failure analysis

Chang et al. [38–41] have presented a two dimensional progressive damage model (PDM) for notched laminated composites. Their model can assess damage in laminates with different ply orientations and predict ultimate strength of notched laminates. A modified Yamada−Sun failure criterion [85] is used for damage identification and damage modeling is done with the help of material MPDM. Numerical results are validated with experimental data on laminates containing open circular hole. But this study is carried out for panel with single cut out.

Tan [86] have proposed a two dimensional progressive damage model for laminates containing central holes subjected to in−plane loading. Instead of reducing the elastic constants to zero, three internal state variables are used to simulate the stiffness degradation of failed elements. The predicted ultimate strength, stress−strain behavior and the damage progression are found agreeing reasonably well with the experimental result.

Yang and Chow [87] have carried out progressive damage analysis of unidirectional graphite/epoxy composites containing a circular cut−out. Experimental and finite element results are presented to describe the anisotropic state of stress, strain and the damage of composite panel containing circular hole subjected to tensile load. Their study revealed that redistribution of stresses and strains due to damage accumulation determine the subsequent path of damage development and also the load carrying capacity of composite structure. They used Moiré interferometry technique to study the deformation in the composite laminates.

Progressive failure analysis of laminated composite plates under transverse loading has been carried out in linear and elastic range by Pal and Ray [42]. Stiffness degradation is implemented for the damage modeling. The results in terms of first ply failure load obtained in the study are compared with the results already available in the published literature.

Hallet and Wisnom [88] have performed an experimental investigation of progressive damage on notched specimen under tensile load. It is observed that failure mechanism varied with both layup and specimen size.

Lapczyk and Hurtado [89] have presented a study on the progressive damage of fiber reinforced materials. Four different failure modes are considered and modeled separately. Damage initiation is predicted using Hashin's failure criteria and damage evolution is carried out using a separate law. The damage evolution law is based on fracture energy dissipation happening during damage process.

A comparative study of open hole laminates made of glass and carbon fiber reinforced composite materials has been performed by O'Higgins et al. [90]. Experimental study has been carried out and non−destructive tests are conducted to map the damage progression. The damage progression and failure mechanism for these two materials is found to be very similar.

Tay et al. [91] have carried out a study on the progressive failure analysis of composite laminates. Their study is based on a novel method called EFM for damage modeling. Results for notched as well as pin loaded laminates are shown and compared with the experimental behavior.

Zhang and Zhao [92] have developed a PDM for fiber reinforced composite laminates containing a hole. They have employed micromechanical model to evaluate the failure criteria at the micro level.

In externally bonded patch repair domain, Liu and Wang [76] have performed progressive failure analysis on only double sided patch repaired composite panel subjected to tensile load, as discussed above. They concluded that the parameters of patches not only influence the patch performance

but also the failure mechanism of repaired structures.

Tay et al. [93] have also studied the performance of notched and double-sided repaired composite panel using progressive failure analysis. They have used cohesive element to model the adhesive layers between patch and panel. EFM and MPDM in conjunction with multicontinuum theory (MCT) based on micromechanics are implemented in their analysis. They concluded that the FEM together with MPDM and MMF (Micromechanics failure criteria) criterion can provide better predictions of initial and ultimate failure of composite structures. Combined with cohesive elements, these methods can be very useful to analyze damaged and repaired composite structures.

1.7.3 Optimization of composite laminate using GA

GA has been the most popular and widely used method for the optimization of diverse problems involved in composite domain [47]. Callahan and Weeks [94], Nagendra et al. [95], Riche and Haftka [96], Ball et al. [97] are among the first who adopted and employed GA for the optimization of stacking sequence in laminated composite materials. Followed by then, the GA technique has been used extensively in laminated composite structures and explored to a great extent for the optimization of several objective functions such as strength [96, 98], buckling loads [96], dimensional stability [99], strain energy absorption [100], weight (either as a constraint or as an objective to be minimized) [101], stiffness [100], fundamental frequencies [101]. GA has also been applied to the design of a variety of composite structures ranging from simple rectangular plates to complex geometries such as sandwich plates [98], stiffened plates [102], bolted composite lap joints [103]. Pawar and Ganguli [104] used GA for the design of composite rotor blades for structural health monitoring applications. Ramon et. al. [105] implemented micro−genetic algorithms to carry out the multi−objective optimization of the drilling process of a laminate composite material. Two mutually conflicting objectives were optimized namely material removal rate and delamination factor. Swann and Chattopadhyay [106] studied the optimization of piezoelectric sensor location for delamination detection in composite laminates with the help of GA. GA is being used by many researchers for multi−objective optimization problems. Jacob and Senthil [107] used a multi−objective GA for optimization of composites for strength, stiffness and minimal mass. Almedia [108] have presented a technique for design optimization of composite laminate structure using GA for multi objective optimization of weight and deflection in composite structures. GA can be often combined with finite element packages that analyze the stress and strain response of the composite structure. Walker [109] presented a methodology for using genetic algorithm with finite element method to minimize a weighted sum of mass and deflection of fiber reinforced structure through multi−objective optimization. Lopez [47] analyzed different failure criteria used in optimization of composite structures. These works clearly shows the power and versatility of genetic algorithms in composite design optimization.

In externally bonded patch repair domain, Mathias et al. [110] presented a GA based approach for the optimization of bonding orientation and stacking sequence of composite patch bonded on aluminium panel containing a circular hole to reduce the stress level in repaired configuration.

Brighenti et al. [111] investigated the optimum design scheme using genetic algorithm for composite patch repair on cracked plates having a center crack such, to minimize the SIF and thereby improving the life of repaired panel.

1.7.4 Motivation, Scope and Objectives

Today, composite materials can be found in every aspects of daily life ranging from sporting goods to aircrafts. The consistent revolution in the usage of CFRP in place of aluminium structures in aerospace industry has led to the existence of today's new generation commercial aircrafts (Boeing 787 and Airbus 380) which contains almost 50 % CFRP. The focused goal of aerospace industry to develop new era of stiffer, stronger and lighter aircrafts with improve usage of CFRP composites for gaining higher fuel efficiency, has put forth a question of repair and maintenance of structures made of composites. The repair−ability and maintenance is a primary concern to the end−users as well as manufacturers which has been learned from the issues associated with aluminium structures in aging aircrafts built in past decades. Now, the modern day aircraft structures are made of composites, the probability of damage occurrence and issues associated with its repair is expected to arise as well, quickly or in the near future. Since, more and more composites are now being used in today's aircrafts, more repairs on composite structures have to be administered in near future. Therefore, the problem of repair on structures made from composites and understanding of associated challenges and issues is more demanding. Therefore, it is essential to understand the behaviour and mechanics of patch repaired composite panels including its damage mechanism which would essentially help in pushing up the envelop of performance of repaired structure by restoring the structural integrity of damaged part closer to the original one and thereby providing prolonged service life.

Traditionally, researchers have used reflection polariscope, strain gauges, grid method and electronic speckle pattern interferometry (ESPI) for strain measurements in repair study. Reflection photoelasticity involves bonding of a reflective coating layer on to the specimen. It is not a straightforward process and one has to be adept in bonding the coating layer on to the specimen. Moreover, one does not get individual strain components. In case of strain gauges, measurement is highly localized and one cannot get the whole field distribution of strain. ESPI is very sensitive to vibration and involves phase shifting technique for data deduction. In recent years, digital image correlation technique has become the most popular in the field of experimental mechanics [60]. DIC is non−interferometric technique wherein the surface deformation is determined by comparing the images of the object surface before and after deformation. DIC is easy to use since no heavy surface preparation is required. Moreover, the optics involved is simple and easy to implement. The technique is reliable and it can be applied for any class of material. Moreover, it is truly a whole field technique. Off late DIC is employed for strain analysis in repair study [112]. However, no significant experimental work related to the study of mechanics of adhesively bonded patch repair especially using DIC technique exist in the literature, which would be of great interest. Therefore, in this study, at first, DIC technique is employed for material characterization of CFRP laminate. As the composites are of heterogeneous nature and offers non−uniform strain distribution, therefore the material properties estimated based on whole field strain measurement technique would be more accurate rather than a localized single point wise measurement offered by conventional technique. Further, the sensitivity of DIC parameters on material properties is investigated and their optimum range/value is identified. DIC technique is then successfully used for whole field surface displacement and strain measurement in open cutout, single and double sided bonded patch repaired composite panel for understanding their mechanics.

The efficiency of the repaired structures not only relies on patch and adhesive parameters but also to great extent depends on the failure mechanism of repaired structures [76]. So, to realize

the full potential of composite structures and also to improve the performance of bonded repair structure, it is of paramount importance to study the damage mechanism as well as its propagation for an efficient, reliable and safer design. However, the strength and failure mechanism prediction in composite structures are more involved and challenging because of several interacting failure modes (matrix cracking, fiber breakage, fiber−matrix debonding etc.) coupled with their brittle nature with added inhomogeneity and anisotropic nature. The strength and failure mechanism prediction by experiment is more involved, expensive and time consuming whereas finite element based progressive failure analysis is gaining more importance and wider acceptance in recent years. PFA facilitates the simulation of degrading structural response and helps in developing the damage tolerant design which is a prime concern in aerospace industry. Couple of work exist on progressive failure analysis of repaired composite panel and they are limited to double sided patch repair configuration and no work has been reported yet on PFA of single sided patch repair which is of practical importance (in case of repair on wings, fuselage etc.,). Therefore, in the present work, a finite element based 3D progressive damage model is developed for predicting the load−displacement behaviour, damage initiation and propagation as well as the damage mechanism in open cutout, single and double sided repaired panel. The accuracy of developed progressive damaged model is assessed by comparing its prediction with experimentally obtained results.

Since, the adhesive layer in repaired structure plays a critical role in transferring the loads; adhesive layer constitute the weakest link and acts as a common source of failure. An extensive amount of analytical, numerical and experimental research has been carried out to understand the behavior of adhesively bonded joints [113, 114]. Most of the works exist on adhesive lap joint study between metal (like steel, aluminium) and composites. However, no significant whole field experimental work has been reported yet on analyzing the behaviour of adhesive layer in patch repaired composite panel. To improve the performance of bonded repair of composite structures, it is essential to understand the strength, stress/strain distribution and failure mechanism of adhesively bonded joints between composite adherends. Assessment of joint behaviour between composite adherend is very critical from design stand point. Therefore, in this study, the behaviour of adhesively layer in single and double sided patch repaired panel configurations are being investigated experimentally involving DIC. The global cum local whole field strain analysis in the adhesive layer is thoroughly studied using 2D−DIC technique. Effective load/shear transfer length which is an essential parameter in patch design in repair domain is predicted based on global strain analysis. The results obtained from FEA are compared with the DIC results for their accuracy.

Most of the research group have studied the influence of repair parameters such as patch thickness, patch overlap length, patch stacking sequence, adhesive thickness, adhesive strength etc., on repair efficiency; however none of them have studied the influence of patch shape on repair performance. Till date, parametric study exists on understanding the influence of various parameters individually on repair efficiency. However, it is difficult to arrive at the optimum value of different repair parameters independently through parametric study. Therefore, one needs to use regular optimization method for obtaining the optimized repair parameters, however, no significant work has been reported in literature. It will be of interest to see the influence of patch shape on repair performance as well as the influence of optimized parameters on repair strength. Therefore, at first the influence of different form of patch shapes on repair efficiency is studied. The best performing patch shape is identified and then the dimensional optimization of patch and adhesive layer is performed using

multi−objective genetic algorithm by developing an interface between GA and FEA for gaining higher repair performance. Tsai−Wu failure criteria for composite panel and maximum shear stress failure criteria for adhesive layer is implemented in optimization scheme. Experimental study is then carried out with the arrived optimum patch dimensions and adhesive thickness, and the obtained results are discussed.

The brief summery of of contributions made in this thesis is depicted by a flowchart as shown in Fig 1.23, and they are discussed briefly in the subsequent sections.

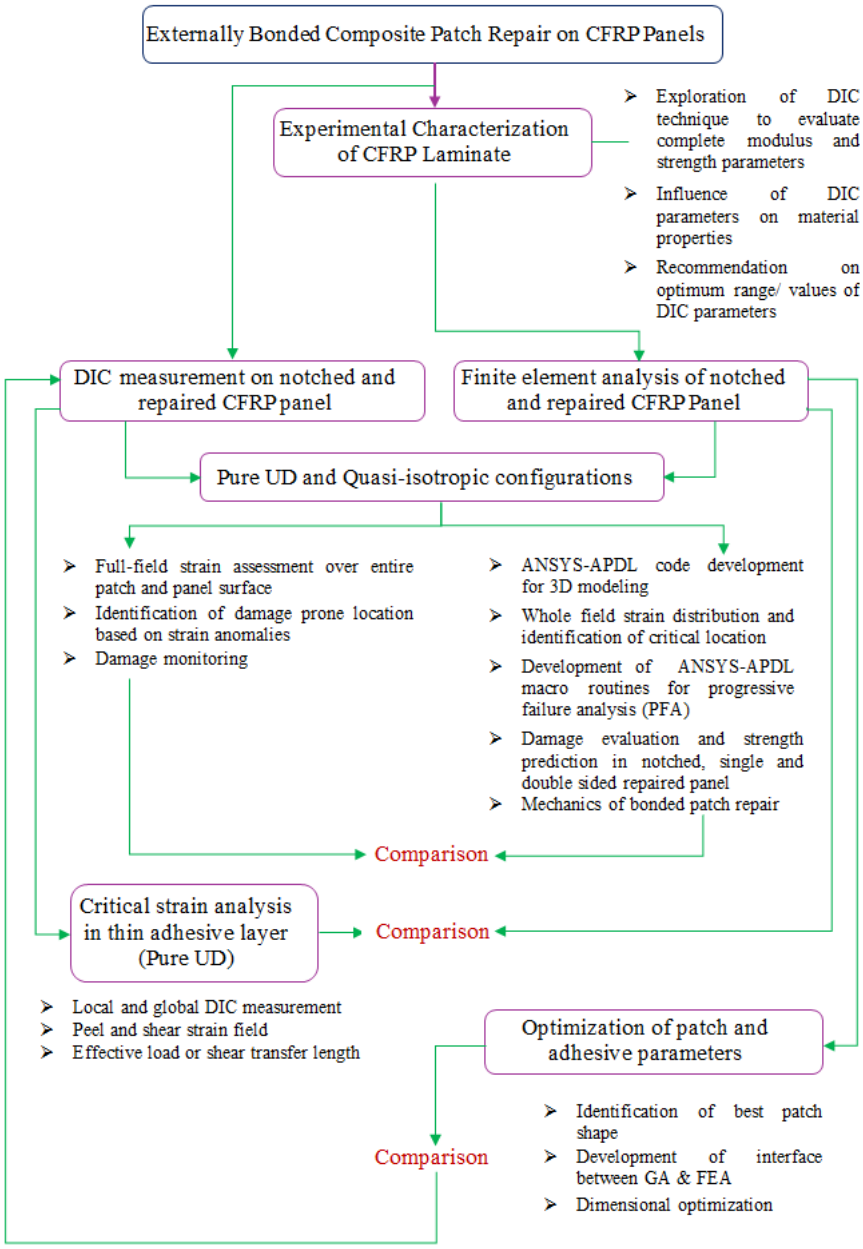

Figure 1.23: Brief summary of contributions made in this thesis

1.8 Thesis layout

Chapter 1 explains briefly about composite materials, its application in aerospace sector, failure mechanism in composite materials followed by repair study on damaged CFRP laminates. A brief literature review on damage and repair study on composite panel as well as progressive failure analysis of composite laminates is presented. Also, a brief discussion on various experimental techniques being used to study the mechanical behavior of composites is discussed. Further, a brief introduction of DIC technique employed in the present experimental work is presented. Motivation, scope and objectives including layout for the work carried out is included at the end.

In chapter 2, the fabrication process of CFRP composite laminate coupons using hand lay−up technique and their experimental characterization based on full field data obtained from DIC technique are presented. It also includes the comparison of evaluated properties with analytical models. Further, sensitivity of DIC parameters (speckle pattern, subset size, step size etc.) on material properties is presented and their optimum value is identified. Also, an open cutout panel made of same composite laminate is taken into consideration and the sensitivity of DIC parameters on predicting complex strain field surrounding the hole is demonstrated and appropriate value is recommended.

Chapter 3 presents the the behaviour of adhesively bonded patch repair of carbon−epoxy unidirectional composite laminates under tensile loading. Both pure UD and quasi−isotropic panels are considered. Damage initiation and propagation in open cutout and repaired panel as well as patch debonding are studied using 3D DIC. The influence of various repair parameters on repair performance in case of quasi−isotropic panel is analyzed and prioritized using FEA. Whole field strain patterns obtained from FEA are compared with the DIC results both qualitatively as well as quantitatively.

Chapter 4 deals with the development of a progressive damage model that can be applied to open cutout and repaired composite panels. A 3D finite element based progressive damage model is developed for predicting the failure and post failure behaviour of open cutout and repaired panel under tensile load. The CFRP panels of pure UD and quasi−isotropic configurations are considered. Failure initiation load, ultimate strength and failure mechanisms are investigated through the developed PDM. The accuracy of developed PDM is assessed by comparing its prediction with the experimental results based on DIC technique as shown in chapter 3.

In chapter 5, the critical strain field measurement in thin adhesively layer of single and double sided patch repaired CFRP composite panel under tensile load using DIC is studied. Longitudinal, peel and shear strain distribution in adhesive layer is analyzed thoroughly in repaired panel by performing global cum local strain field analysis involving DIC. The influence of adhesive nature is also investigated. Effective load/shear transfer length in repair configuration is estimated based on global strain analysis and further it is compared with the one predicted from FEA. Localized strain analysis using magnified optics approach is also presented for analyzing the complex strain field in small but critical zones closer to the patch edge responsible for failure. The influence of patch edge tapering on strain filed is also analyzed.

Chapter 6 presents a 3D finite element based study to investigate the influence of various patch shapes on repair efficiency in case of double sided patch repaired panel. The SCF reduction and peel stress are compared for various patch shapes maintaining constant patch volume. Stress based 3D−Hashins failure criterion is employed for predicting the strength at damage initiation along with failure modes in notched and repaired panel. Optimal patch shape is then brought-out based

on higher repair efficiency. Finally, a genetic algorithm based approach in−conjunction with finite element analysis is used for the optimization of patch geometry and adhesive thickness in order to obtain higher repair performance. Experimental study based on optimal dimension is also executed to make the study complete.

Chapter 7 presents the conclusion and recommendation for the future work.

Chapter 2

Experimental Characterization of CFRP Composite Laminate using DIC

2.1 Introduction

The properties of composite material mainly depends on the type of reinforcing fiber, matrix material as well as processing technique. The fact that these materials can be custom tailored to enhance their properties to make them suitable for a specific application, they necessitate a special consideration for determining their mechanical properties accurately [115]. Also, the accuracy of finite element analysis prediction strongly depends on the properties of materials determined experimentally. The experimental evaluation of material properties essentially rely on accurate measurement of displacement or strain [116]. The accurate measurement of these parameters has always been an important topic of research in experimental mechanics which has led to the evolution of several contact and non−contact measurement techniques. Optical full−field measurement techniques such as reflection photoelasticity, moiré interferometry, holographic and speckle interferometry, grid method and digital image correlation are found very promising for the experimental stress/strain analysis of materials and structures [117–121]. Among them, DIC technique is being used in several applications because it offers several advantages over the other experimental technique as mentioned in Chapter 1.

Even though DIC technique has found profound application in various domains but accuracy is a primary issue [122]. The error in DIC measurement could arise due to many sources such as illumination variations, quality of acquisition system, camera lens distortion, image noise etc., or it could be due to the error associated with the implementation of correlation algorithm like subset size, step size, strain window size, sub−pixel optimization algorithm, sub−pixel intensity interpolation scheme etc. [122–124]. The effect of some of these parameters has been investigated thoroughly by many researchers. They have addressed the issue of unmatched subset shape function [125], intensity interpolation [58], sub−pixel registration algorithm [126], intensity pattern noise [127], subset size [123, 124, 128–131], step size [123, 129, 131], strain window size [123, 131], speckle pattern [130],

in−plane rotation, in−plane rigid body translation, out of plane rigid body rotation [131] and errors that arise in the derivation of strain fields based on displacement fields [132]. Most of the above mentioned study is for metallic samples.

Now, the researchers have started using DIC technique for experimental characterization of composites [121, 133–140] which are of heterogeneous nature and offers non−uniform strain distribution. Therefore, the material properties estimated based on whole field strain measurement technique would be more accurate rather than a localized single point wise measurement offered by conventional technique [133–136]. Even though the researchers have started exploring the mechanical characterization of composite material using DIC, a thorough investigation needs to be done to study the influence of various DIC parameters on material property estimation.

Therefore, at first, a detailed methodology is presented in this chapter for evaluating all the elastic constants towards characterizing CFRP laminate. Full field non−contact 3D−DIC technique has been employed for this purpose as it offers several advantages over 2D−DIC [121]. The properties of unidirectional carbon/epoxy composite laminate are estimated by performing a series of tests as per ASTM standards. The properties of epoxy matrix is also determined using the same technique as they are required for estimating the composite properties using micro−mechanics based analytical models namely *rule of mixture* and *Halpin− Tsai model*. Fiber volume fraction is determined by matrix burn−off test method recommended by ASTM (American Society for Testing and Materials) standard and it is used in analytical models. The experimental values are then compared with the theoretical ones qualitatively. Further, an elaborate study is carried out to investigate the influence of DIC parameters such as speckle pattern, subset size, step size and region of interest size on properties of epoxy matrix and CFRP laminate. The optimum value/range of considered DIC parameters are predicted and recommended for accurate characterization.

Recently, DIC technique is also being used as a non−destructive technique [141, 142] to predict damage evolution in composite panels based on strain anomalies observed on the panel surface. Using DIC, the damage initiation site is generally predicted based on highly strained zone whereas the damage propagation is monitored based on appearance of uncorrelated/discontinuity area over the specimen surface. For accurate prediction, the sensitivity of DIC parameters on complex strain field such as in the case of open cutout composite panel needs to be investigated for instilling confidence in DIC's utility. Considering above discussion, a sensitivity analysis of DIC parameters on complex strain field around the hole of an open cutout composite panel is presented in the last section of this chapter. Also, the DIC results are compared with FEA prediction to ascertain the suitable value of DIC parameters towards archiving better accuracy.

2.2 Materials detail and specimen fabrication

The composite material used in this work is made from unidirectional (UD) carbon fiber mat of 200 g/m^2 (gsm). The UD carbon film is of Golbond® make. The matrix material is made from a mixture of epoxy resin LY−556 with hardener HY−951. The resin and hardener are manufactured by Huntsman [143].

2.2.1 Composite specimens

Figure 2.1 illustrates the various steps involved in specimen preparation. Composite laminates are fabricated by hand layup technique with UD carbon fiber mat of 200 g/m^2 (gsm). Epoxy resin LY−556 and hardener HY−951 are taken in the ratio of 10:1 by weight. A high precision weighing machine is used to weigh the resin and hardener. The resin and hardener is then mixed thoroughly with due care taken to avoid bubbles formation. Formation of bubbles could cause formation of air voids in the finished casting. A flat perspex sheet is used as mold for the fabrication. The perspex sheet is cleaned with isopropyl alcohol and a mylar sheet is placed over the mold surface to achieve the better surface finish . Appropriate quantity of resin−hardener mixture is poured over the mylar sheet and mixture is spread over the mold area using brush. First layer of carbon fiber is then placed over the mold in appropriate direction and Teflon roller is rolled over the carbon fiber mat in the direction of fiber in order to squeeze out the excess resin.

Figure 2.1: Different steps involved in CFRP specimen preparation

Successive layers of carbon fiber in required direction are placed and resin hardener mixture is poured over each layer and the same process is repeated. Another layer of mylar film is finally placed on top of the laminates and squeezed firmly with roller so as to remove the entrapped air and excessive resin. The composite laminate is then allowed to cure at room temperature for twenty four hours. Specimens are cut from molded laminates to over dimension (about 3−5 mm on each side) using abrasive cut−off wheel mounted on hand−held saw. Specimens are then accurately machined to the required dimension by a milling machine with diamond coated end mills (supplied by SECO TOOLS) at a speed of 80 rpm. Backing plates are used while machining to avoid edge delamination. Also care is taken while machining the specimen having 0° fibers so that it can be machined parallel to the fibers. CFRP tabs of ±45° sequences or aluminium tabs of required dimension are bonded to the test specimen using AV138/HV998 adhesives system. Before bonding the tabs, bonding surface of the tabs and specimens are roughened using 200−grit sandpaper and then cleaned with isopropyl alcohol. Tabs are provided at the end of the specimen for obtaining a better grip and to avoid damage while specimen is loaded in the fatigue testing machine.

2.2.2 Epoxy matrix specimens

Matrix specimens are prepared from epoxy sheet casted in house by using commercially available LY−556 epoxy resin and HY−951 hardener. The resin and hardener are taken in the ratio of 10:1 by weight and mixed thoroughly and gently for about 30 minutes at room temperature. Due care is taken to avoid bubble formation. The resin−hardener mixture is then poured into a mold and allowed to cure at room temperature for 24 hours. The specimens of required dimensions are then milled from casted epoxy sheet with due precaution taken during the machining to avoid high cutting forces and excessive amount of heat generation.

2.3 Experimental methodology for DIC measurement

2.3.1 Random speckle pattern

To perform the DIC experiment, random speckle patterns are created over the specimen surface by spraying acrylic paints of black and white color (from Golden® Artist Colors Inc.). The specimen surface is first cleaned using isopropyl alcohol. Golden® acrylic paint of titanium white color (8380−Series NA) is then applied over the specimen surface using an air brush (from Iwata−Medea, Inc.). Only one layer of white paint is applied to avoid changing the shape of the surface and increasing shear effect due to the higher thickness of paint coating. Once the specimen is dried, acrylic paint of carbon black color (8040−Series NA) is applied over the specimen surface (white color painted) in a random fashion using an air brush to get a random speckle pattern. The air brush used is having a nozzle of diameter 0.5 mm. Based on observation of pattern made at different air pressures, an air pressure of 0.15 MPa is chosen at which adequate size and density of the black dots are obtained. An example of typical random speckle pattern obtained using this procedure is shown in the Fig. 2.2

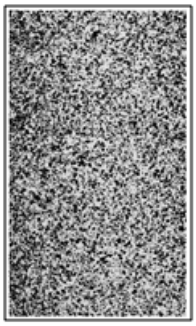

Figure 2.2: Typical speckle pattern

2.3.2 Experimental setup and test procedure

A typical experimental setup used for material characterization is shown in Fig. 2.3. It consists of a 3D−DIC system (from Correlated Solutions, Inc.) and computer−controlled MTS Landmark® servo−hydraulic cyclic test machine of 100 kN capacity. The 3D−DIC setup consists of two Grasshopper® CCD Camera (POINTGREY−GRAS−50S5M−C) having a spatial resolution of 2448 x 2048 pixels^2, coupled with Schneider Xenopla lenses of 35 mm focal length.

Both cameras are mounted on a tripod having inbuilt spirit level to ensure horizontal level. Specimen having random speckle pattern is fixed in hydraulic wedge grips and much care is taken with regard to specimen alignment. An axial extensometer of 25 mm gauge length is attached at center of the specimen. The cameras are aligned properly with respect to the specimen. Uniform illumination of the specimen surface is ensured by keeping two standard halogen light sources on either side of the camera. Area of interest is zeroed on by adjusting the focal length of both the lenses. Aperture of the lenses are adjusted to achieve good field of view and also to avoid saturation of the pixels over the field of view. Camera is then calibrated for its position and orientation using an appropriate calibration grid plate.

Cameras are connected to image grabbing workstation laptop and a reference image is first grabbed at zero load after calibration. Number of images are then recorded during the test at a predefined rate. For material characterization, ten images per second are grabbed during the tests so that more number of data points can be retrieved to obtain a smooth experimental plot. Vic−Snap 2009 software supplied by Correlated Solutions, Inc. [144] is used for image grabbing. A data acquisition card (DAC) supplied by National Instruments is used to provide an interface between MTS controller and image grabbing system for storing the load and displacement data for every image being grabbed during the test. All the tests are performed in displacement controlled mode at room temperature and the testing rate for material characterization is specified in accordance to ASTM standards. Post−processing of the grabbed images are carried out in Vic−3D software supplied by Correlated Solutions, Inc. [144].

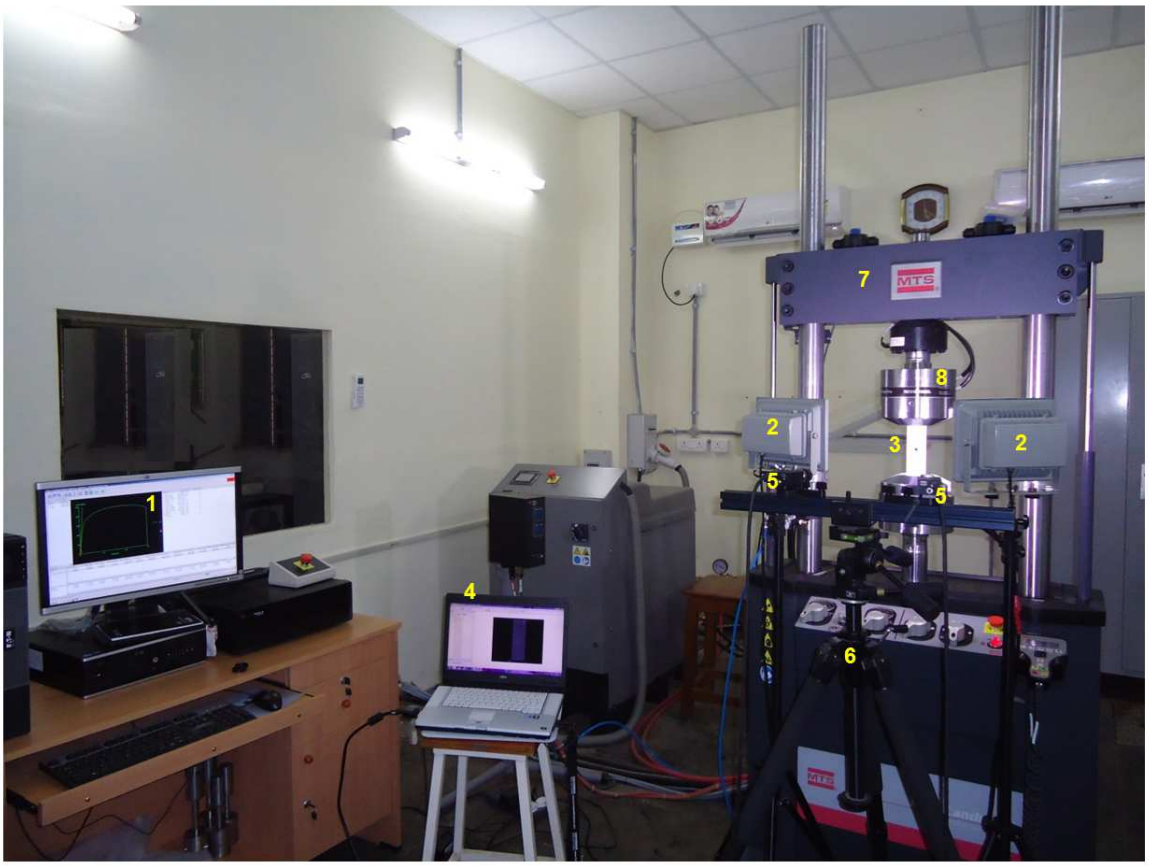

1. User interface for MTS 2. Light source 3. Specimen 4. Image grabbing system 5. Camera 6. Tripod
7. MTS fatigue machine 8. Hydraulic wedge grip

Figure 2.3: Experimental setup consisting of 3D DIC and MTS machine

2.4 Determination of CFRP composite properties

The composite coupons for material characterization are prepared as per the recommendation of ASTM standards and they are briefly discussed in next sub−sections.

2.4.1 Tensile properties

Tensile tests on CFRP coupons are performed to obtain the elastic and strength parameters in longitudinal and transverse direction. Test is carried out according to the test matrix shown in Table 2.1, recommended by ASTM D−3039 standard [145]. The dimensions and geometry for [0°] and [90°] tests coupons are shown in Fig. 2.4 and 2.5 respectively.

Table 2.1: Tensile test matrix for material characterization.

Test Type	ASTM Standard	Lay−up	Geometry	Test Speed (mm/min)	Properties
Tensile	D−3039	$[0°]_3$	Fig. 2.4	2	E_{11}, ν_{12}, X_T
Tensile	D−3039	$[90°]_6$	Fig. 2.5	1	E_{22}, ν_{12}, Y_T

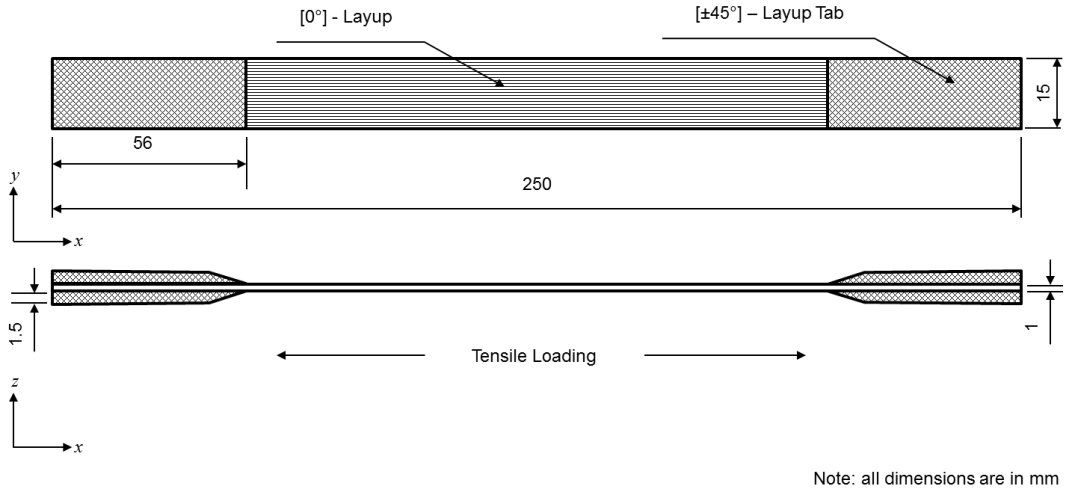

Figure 2.4: Tensile test geometry for [0°] coupon as per ASTM−D3039 standard

CFRP coupons with staking sequence of $[0°]_3$ are tested at a speed of 2 mm/min to obtain the longitudinal elastic and strength parameter whereas coupons with staking sequence of $[90°]_6$ are tested at a speed of 1 mm/min to obtain the elastic and strength parameter in transverse direction. The zero−degree fibre orientation is along x−axis which corresponds to the loading direction, 90−degree fiber orientation is along y−axis representing in−ply transverse direction and the laminate thickness direction is along z−axis. The axes x , y , and z is also denoted by *1*, *2* and *3* respectively.

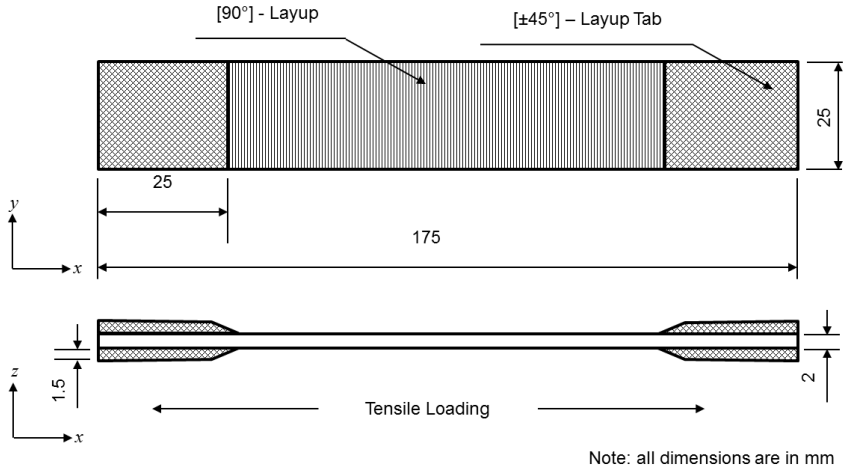

Figure 2.5: Tensile test geometry for [90°] coupon as per ASTM−D3039 standard

Images are grabbed during the test and then they are post−processed in Vic−3D software. An example of CFRP tensile specimen and its post−processing in Vic−3D software is shown in Fig. 2.6. The specimen region within the gauge length (25 mm) of extensometer is selected as ROI for correlation. The resolution of ROI is 119 x 224 pixels^2 which correspond to 10.5 mm x 19.5 mm on physical scale. The spatial resolution is 11.35 pixel/mm. The average speckle size is 2.8 pixels.

A subset size of 37 x 37 pixels^2 along with a step size of 7 pixels is chosen for performing the DIC post−processing. Once the strain computation is completed, average value of each strain component from every strain map corresponding to each image grabbed during the test is extracted to generate the complete stress−strain curve.

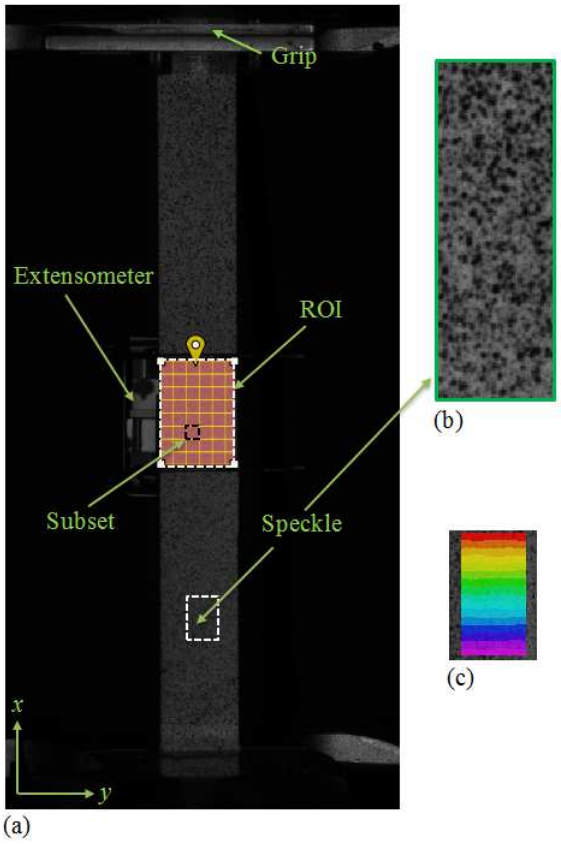

Figure 2.6: Tensile specimen (a) extensometer, subset, ROI (b) speckle pattern (zoomed view) (c) $v-$displacement (mm) in ROI

The stress−strain curve obtained from DIC for [0°] tensile test is shown in Fig. 2.7. In−plane Young's modulus in longitudinal direction (E_{11}) is obtained from initial slope of stress−strain curve. The stress−strain curve for E_{11} estimation obtained from both DIC and MTS (using extensometer) is shown in Fig. 2.7 (a) & (b) respectively. The comparison between them is shown in Fig. 2.8.

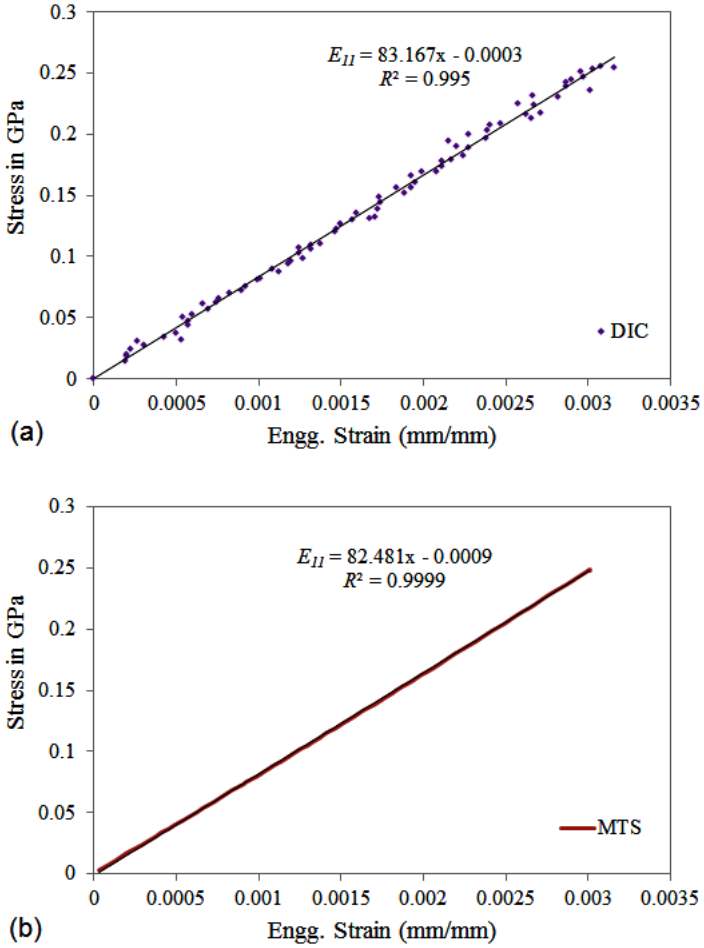

Figure 2.7: Stress−strain curve for longitudinal modulus (E_{11}) obtained from tensile test of [0°] coupon (a) DIC (b) MTS

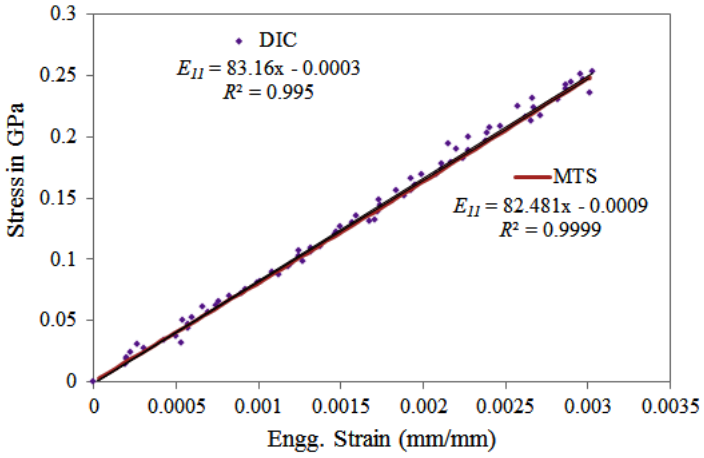

Figure 2.8: Comparison of stress−strain curve for (E_{11}): DIC vs. MTS

The comparative plot clearly shows that the DIC data is mostly scattered as compared to the one obtained from MTS. However, one can clearly see that the slope of stress−strain curve obtained from both MTS and DIC is in close agreement with an error of 0.8 % for E_{11}.

In−plane major Poisson's ratio (ν_{12}) is obtained from the ratio of lateral strain (ε_{yy}) to longitudinal strain (ε_{xx}) plot obtained from DIC for [0°] test coupon, as shown in Fig. 2.9.

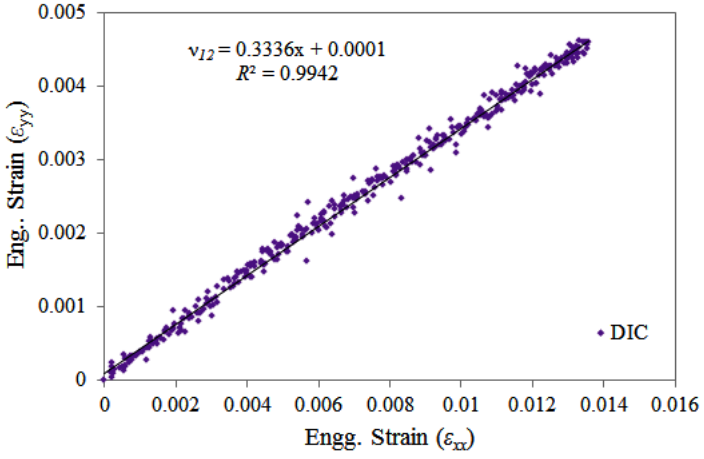

Figure 2.9: In−plane Poisson's ratio (ν_{12}) obtained using from tensile test of [0°] coupon

The stress−strain curve for E_{22} obtained from DIC measurement on [90°] tensile test coupon is shown in Fig. 2.10.

The longitudinal (X_T) and transverse tensile strength (Y_T) is estimated by dividing the maximum load (P_{max}) before fracture with the cross−sectional area (A) of respective specimen. The longitudinal modulus and strength parameter obtained from five independent measurements using DIC technique together with mean, standard deviation (Std. Dev.) and coefficient of variation (CV) is summarized in Table 2.2. The longitudinal modulus (E_{11}) measured from DIC varies between 79.88 and 84.76 GPa with an average of 81.9 GPa, and the coefficient of variation is 2.4% .

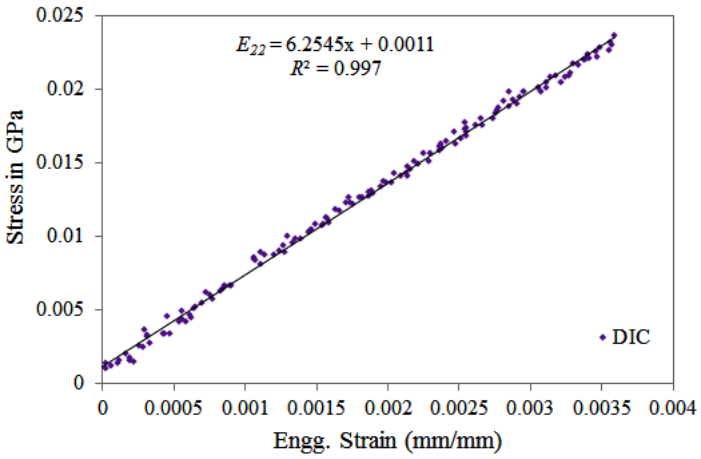

Figure 2.10: Stress−strain curve obtained from DIC for transverse modulus (E_{22})

Table 2.2: DIC results from [0°] tensile test.

Specimen #	X_T (MPa)	E_{11} (GPa)	ν_{12}
1	1245.05	79.88	0.35
2	1368.14	84.76	0.33
3	1334.00	82.99	0.325
4	1235.81	81.23	0.37
5	1317.12	80.65	0.35
Mean	1300.02	81.90	0.345
Std. Dev.	57.51	1.96	0.018
CV (%)	4.42	2.40	5.22

The transverse modulus and strength parameter of CFRP laminate obtained from five independent measurements using DIC technique is summarized in Table 2.3. The CV for E_{22} is 5.2%.

Table 2.3: Results from [90°] tensile test.

Specimen #	Y_T (MPa)	E_{22} (GPa)
1	23.47	6.64
2	15.64	5.73
3	27.41	6.07
4	25.37	6.17
5	22.95	6.16
Mean	22.97	6.15
Std. Dev.	4.45	0.32
CV (%)	19.38	5.28

2.4.2 Compression properties

The objective of compression test is to estimate the strength of CFRP laminate under compressive load essentially required for predicting the failure using failure criteria. Compression test is performed according to the test matrix given in Table 2.4, recommended by ASTM D−3410 standard [146]. The geometric details of compression tests coupons are shown in Fig. 2.11 and 2.12.

Table 2.4: Compression test matrix for material characterization.

Test Type	ASTM Standard	Lay−up	Geometry	Test Speed (mm/min)	Properties
Compression	D−3410	$[0°]_6$	Fig. 2.11	1.125	X_C
Compression	D−3410	$[90°]_6$	Fig. 2.12	1.125	Y_C

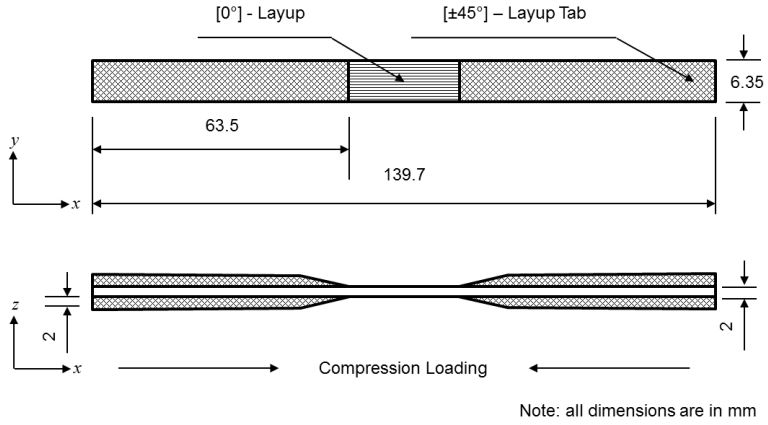

Figure 2.11: Compression test geometry for [0°] coupon as per ASTM−D3410 standard

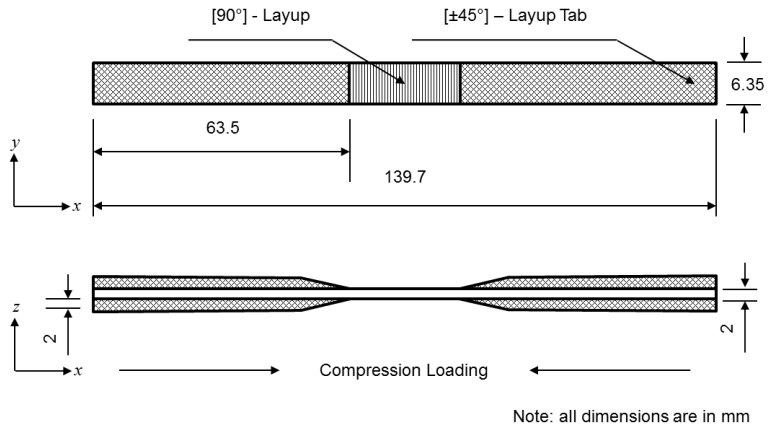

Figure 2.12: Compression test geometry for [90°] coupon as per ASTM−D3410 standard

CFRP coupons with staking sequence of $[0°]_6$ and $[90°]_6$ are tested to obtain the longitudinal and transverse compressive strength parameters respectively. The testing speed for both the cases are same.

The longitudinal compressive strength (X_C) is estimated from the ratio of maximum load (P_{max}) taken by [0°] sample to its cross−sectional area. Strength X_C obtained from five independent measurements together with mean, standard deviation and coefficient of variation is given in Table 2.5.

Table 2.5: Results from [0°] compression test.

Specimen #	X_C (MPa)
1	648.91
2	641.74
3	636.21
4	642.03
5	631.21
Mean	640.02
Std. Dev.	6.67
CV(%)	1.04

Similarly, the transverse compressive strength (Y_C) obtained from five independent measurements on [90°] samples is given in Table 2.6.

Table 2.6: Results from [90°] compression test.

Specimen #	Y_C (MPa)
1	97.32
2	93.31
3	91.43
4	90.11
5	94.10
Mean	93.25
Std. Dev.	2.75
CV(%)	2.95

2.4.3 Shear properties

Shear test coupons of CFRP laminate are prepared according to ASTM D−3518 standard [147]. This test methodology provides an indirect means of evaluating the shear properties of the composite laminate because the test on specimen is carried out in tensile mode rather than shear, as recommended by standard. CFRP coupons with staking sequence of $[45°]_6$ are tested to obtain the shear modulus and shear strength. The test matrix representing the lay−up configuration, testing speed etc., is given in Table 2.7. The dimensions and geometry of tests coupons are shown in Fig. 2.13.

Table 2.7: Shear test matrix for material characterization.

Test Type	ASTM Standard	Lay−up	Geometry	Test Speed (mm/min)	Properties
Shear	D−3518	$[\pm 45°]_6$	Fig. 2.13	1	G_{12}, S_{12}

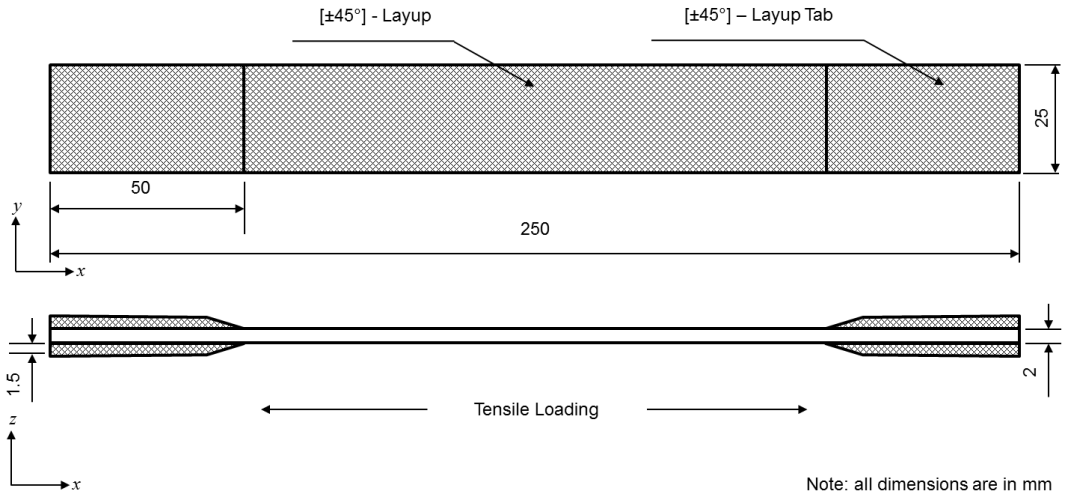

Figure 2.13: Shear test geometry as per ASTM−D3518 standard: $[\pm 45°]$ coupon

The tensile test on $[45°]$ specimen presents a nonlinear behaviour because of its stacking sequence. Only linear region of stress−strain curve is considered for estimating the shear modulus. The in−plane shear modulus (G_{12}) is obtained by initial slope of shear stress−shear strain curve. Procedure for finding shear stress, shear strain and shear strength is followed from ASTM standard and it is briefly explained below.

In−pane shear modulus

For finding the shear modulus, shear stress at each data point is evaluated by Eq. 2.1.

$$\tau_{12i} = \left(\frac{P_i}{2A}\right) \tag{2.1}$$

The symbols τ_{12i} and P_i corresponds to shear stress and load respectively at i^{th} data point. The symbol A represents the cross−sectional area of the specimen.

The longitudinal and lateral normal strains are first obtained from the DIC measurement and the shear strain is then estimated by Eq. 2.2.

$$\gamma_{12i} = \varepsilon_{xi} - \varepsilon_{yi} \tag{2.2}$$

The symbols γ_{12i} correspond to shear strain respectively at i^{th} data point, ε_{xi} and ε_{yi} represents the longitudinal and lateral normal strains respectively at i^{th} data point.

In−plane shear modulus is then evaluated from the initial slope of shear stress−shear strain curve as shown in Fig. 2.14.

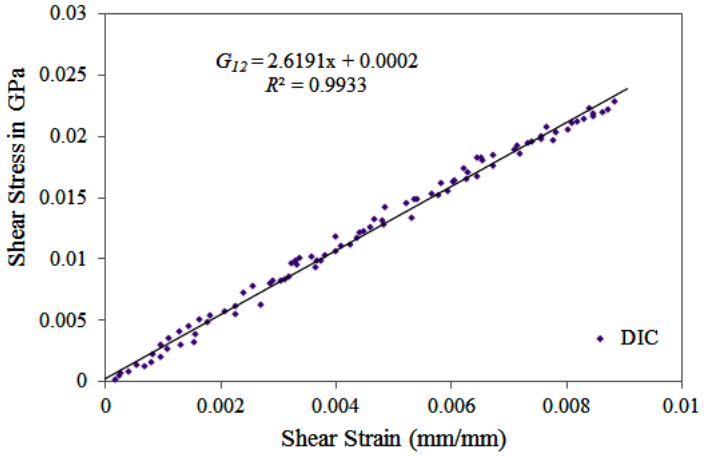

Figure 2.14: Stress−strain curve obtained from DIC for in−plane shear modulus (G_{12})

In−pane shear strength

The in−plane shear strength for the [±45°] laminate is estimated using Eq. 2.3.

$$\tau_{12}^{m} = \left(\frac{P^m}{2A}\right) \tag{2.3}$$

where τ_{12^m} is the maximum shear stress or shear strength,and P^m is the maximum load at or below 5% shear strain.

The shear modulus and shear strength obtained from five independent measurements on [±45°] samples in tensile mode using DIC technique together with mean, standadrd deviation and coefficient of variation is given in Table 2.8. The value of shear modulus varies from 2.61 to 2.91 GPa with an average of 2.77 GPa, and the coefficient of variation is 4.62%.

Table 2.8: Results from [±45°] tensile test.

Specimen #	S_{12} (MPa)	G_{12} (GPa)
1	41.91	2.61
2	44.84	2.91
3	47.47	2.68
4	45.26	2.88
5	46.08	2.79
Mean	45.11	2.77
Std. Dev.	2.05	0.12
CV (%)	4.54	4.62

2.4.4 Estimation of out−of−plane properties

The orthotropic material is characterized by nine elastic constants namely in−plane properties E_{11}, E_{22}, ν_{12} and G_{12} and out−of−plane properties E_{33}, G_{13}, G_{23}, ν_{13} and ν_{23}. In−plane properties have been evaluated experimentally using DIC technique as presented earlier, whereas out−of−plane properties need to be estimated. For estimating out−of−plane properties, procedure is adopted from Ref. [148] and it is briefly outlined here.

Since, a UD fiber composite laminate is a special class of orthotropic material and it appears isotropic in planes perpendicular to the fiber direction. Here, CFRP laminate contains fibers parallel to the $1-axis$, and therefore it presents isotropic nature in 2−3 plane. This would results in $E_{22} = E_{33}$, $G_{12} = G_{13}$ and $\nu_{12} = \nu_{13}$. Further, the shear modulus G_{23} can be expressed in terms of E_{22} and ν_{23} by Eq. 2.4. Hence, five independent elastic constants are required to characterize the UD fiber composites and it can be treated as transversely isotropic material [148]. Also, the Poisson's ratio ν_{21} can be expressed in terms of ν_{12} by Eq. 2.5. Christensen [149] has shown that ν_{23} can be related to ν_{12} and ν_{21} by Eq. 2.6 in case of UD fiber reinforced composites. Thus, UD fiber reinforced composites can be characterized by four independent elastic constants.

$$G_{23} = \frac{E_{22}}{2\left(1 + \nu_{23}\right)} \tag{2.4}$$

$$\nu_{21} = \nu_{12}\left(\frac{E_{22}}{E_{11}}\right) \tag{2.5}$$

Using Eq. 2.5, ν_{23} can be estimated as [149],

$$\nu_{23} = \nu_{12}\left(\frac{1 - \nu_{21}}{1 - \nu_{12}}\right) \tag{2.6}$$

where E, G and ν are the Young's modulus, shear modulus and Poisson's ratio respectively.

2.4.5 Summary of CFRP properties evaluated from DIC experiments

The summery of in −plane and out−of−plane properties obtained from DIC measurement together with the strength parameters of CFRP composite are given in Table 2.9.

Table 2.9: Material properties of CFRP laminate and Matrix obtained using DIC technique.

CFRP Composite Laminate Properties	Values	
	Avg.	Std. Dev.
Longitudinal modulus , E_{11} (GPa)	81.9	1.96
Transverse modulus, E_{22} (GPa)	6.15	0.32
In−plane Shear modulus, G_{12}(GPa)	2.77	0.12
Out−plane Shear modulus, G_{23} (GPa)	2.05	-
In−plane Poisson's ratio (ν_{12})	0.34	0.018
Out−plane Poisson's ratio (ν_{23})	0.5	-
Longitudinal tensile strength, X_T (MPa)	1300	57.51
Transverse tensile strength, Y_T (MPa)	22.97	4.45
Longitudinal compressive strength, X_C (MPa)	640	6.67
Transverse compressive strength, Y_C (MPa)	93.2	3.23
In−plane Shear strength, S_{12} (MPa)	45.1	2.05

To validate the experimental results, one needs to compare them with theoretical formulations if feasible.

To compare the in−plane CFRP properties obtained from DIC experiment with the analytical results, fiber volume fraction (V_f) and the mechanical properties of matrix material are required. The estimation of V_f and matrix material properties are describes in subsequent sub−sections.

2.4.6 Estimation of fiber volume fraction (V_f) in CFRP specimens

The fiber volume fraction is estimated by considering the matrix burn−off test method recommended by ASTM D−3171 [150]. The samples are cut from tensile coupons and the weights of the samples are recorded. A crucible is preheated to a temperature of 900°C for about 10 minutes and then cooled to room temperature. The weight of crucible with and without sample is recorded. The crucible containing the sample is then placed in the furnace and heated gradually to a temperature of 585°C for a certain time (about 30 minutes) so that matrix completely disappears leaving only the reinforcement. The crucible containing the remains is cooled to room temperature and finally post burn−off weights are recorded. The fiber volume fraction is then evaluated using the procedure given in Ref. [150]. The average value of fiber volume fraction obtained using three different samples is 35%.

2.5 Determination of epoxy matrix properties

The matrix coupons are prepared from epoxy sheet casted in house by mixing resin LY−556 and hardener HY−951 (Huntsman grade). The resin and hardener are taken in the ratio of 10:1 by weight and mixed thoroughly and gently for about 30 minutes at room temperature. Due care is taken to avoid bubble formation. The resin-hardener mixture is then poured into a mold and allowed to cure at room temperature for 24 hours. Tensile test coupons as per ASTM D−638 [151] are then prepared from the casted sheet. The testing detail is given in Table 2.10 and the specimen dimension is shown in Fig. 2.15.

Table 2.10: Test matrix for epoxy material characterization.

Test Type	ASTM Standard	Geometry	Test Speed (mm/min)	Properties
Tensile	D−638	Fig. 2.15	3.75	E, ν

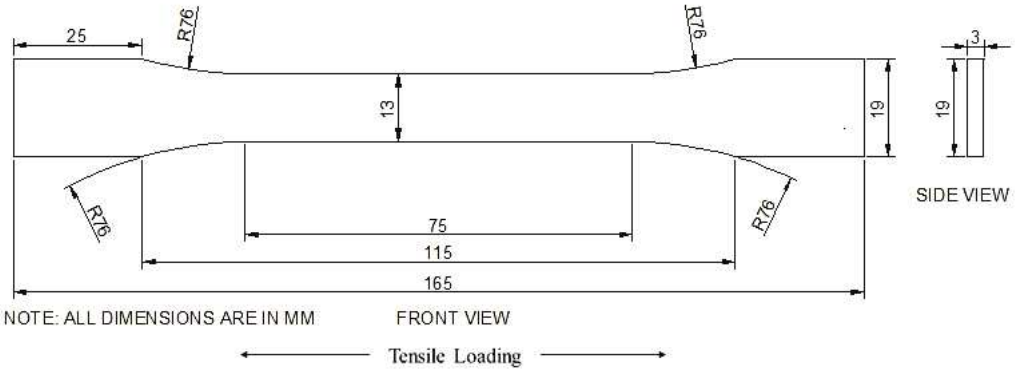

Figure 2.15: Tensile test specimen geometry for epoxy matrix as per ASTM−D638 standard: matrix coupon

The tensile test on matrix coupons/epoxy specimen is performed in a similar way using 3D−DIC technique as explained earlier to obtain the elastic modulus (E) and Poisson's ratio (ν). The stress−strain curve for matrix specimen obtained from DIC is shown in the Fig. 2.16. The modulus value is evaluated from initial slope of stress−strain curve. Poisson's ratio is estimated from the ratio of lateral strain (ε_{yy}) to longitudinal strain (ε_{xx}). These strain components are obtained from the full−field data of DIC measurement epoxy sample. The properties of matrix material obtained from five different samples are summarized in Table 2.11. The value of E varies from 3.73 to 4.25 GPa with an average of 3.96 GPa. The ν ranges from 0.33 to 0.35 with an average of 0.34. The coefficient of variation for E and ν are 3.4% and 1.7% respectively.

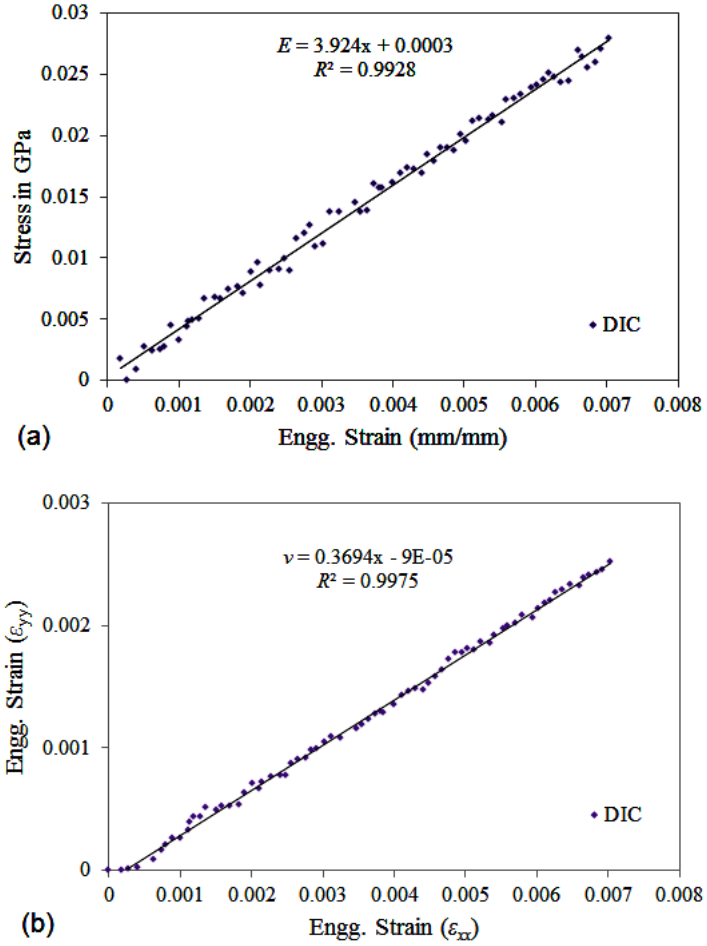

Figure 2.16: Stress−strain curve obtained from tensile test of matrix coupon using DIC (a) Young's modulus, E (b) Poisson's ratio, ν

Table 2.11: Results from epoxy matrix tensile test.

Specimen #	E (GPa)	ν
1	4.25	0.33
2	3.73	0.35
3	3.88	0.35
4	4.05	0.34
5	3.92	0.34
Mean	3.96	0.34
Std. Dev.	0.19	0.008
CV (%)	4.93	2.47

2.6 Comparison of CFRP properties estimated from experiment (DIC) and analytical approach

Two different analytical approaches namely *rule−of−mixture* and *Halpin− Tsai model* are used to evaluate in−plane properties of CFRP composite laminate. These two analytical models are well established and elaborately explained in Ref. [152, 153]. The mathematical formulation for the evaluation of in−plane composite properties are given in the following sub−section.

2.6.1 Rule of Mixture

Rule of mixture is a micro−mechanics based approach used for approximate estimation of composite laminate properties based on an assumption that a laminate property is the volume weighted average of its constituent properties i.e, fiber and matrix [148, 152].

The longitudinal elastic modulus is given by

$$E_{11} = E_f\, V_f + E_m\, V_m \tag{2.7}$$

Equation 2.7 gives the longitudinal Young's modulus as a weighted mean of the fiber and matrix modulus. The transverse elastic modulus is given by

$$E_{22} = \frac{E_f\, E_m}{E_f\, V_m + E_m\, V_f} \tag{2.8}$$

The in−plane Poisson's ratio is given by

$$\nu_{12} = \nu_f\, V_f + \nu_m\, V_m \tag{2.9}$$

The in−plane shear modulus is given by

$$G_{12} = \frac{G_f\, G_m}{G_f\, V_m + G_m\, V_f} \tag{2.10}$$

2.6.2 Halpin−Tsai Model

Halpin and Tsai developed a micro−mechanics based generalized semi−empirical model to predict the composite laminate properties. The Halpin−Tsai equation for both E_{11} and ν_{12} is same as that of rule of mixture approach given by Eq. 2.7 and 2.9 [148, 152], but it differs in the formulation of E_{22} and G_{12}. The value of E_{22} and G_{12} can be approximated from the following equations

$$M = M_m \frac{(1 + \xi\, \eta\, V_f)}{(1 - \eta\, V_f)} \tag{2.11}$$

$$\eta = \frac{\left(\frac{M_f}{M_m} - 1\right)}{\left(\frac{M_f}{M_m} + \xi\right)} \tag{2.12}$$

where M represents the composite modulus E_{22} or G_{12}. M_f corresponds to fiber modulus E_f, G_f or ν_f and M_m corresponds to the matrix modulus E_m, G_m or ν_m. The modulus (E_f) and Poisson's ratio (ν_f) of carbon fiber is 230 GPa and 0.3 respectively. The modulus (E_m) and Poisson's ratio

(ν_m) of matrix is obtained from DIC and it is given in Table 2.11. The term ξ is a measure of reinforcement called reinforcing factor and depends on the fiber geometry, packing geometry and loading condition. The value of ξ for circular fiber in square array is 2 for E_{22} and 1 for G_{12} estimation which is taken from Ref. [148, 152].

The in−plane CFRP properties obtained from analytical models are compared with the DIC results and they are presented in Table 2.12. It can be observed from the table that the theoretical results are closer to the experimental one for the case of E_{11} and ν_{12} showing a percentage error of 1.3 and 2.9 respectively. However, the experimental and analytical results for E_{22} and G_{12} do not compare very well. The rule of mixture underestimates the value of E_{22} and G_{12}. However, Halpin−Tsai model overestimate the value of E_{22} but gives a reasonable result of G_{12}. The value of E_{22} using Halpin−Tsai model is comparatively more than that by rule of mixture approach and this difference could be attributed to the fact of difficulty involved in suitable determination of value ξ [147, 152, 153]. The observations made here are very much consistent with the results presented in Ref. [152, 153].

Table 2.12: Comparison of CFRP properties obtained from experiment (DIC) and analytical approach.

Parameters	Values		
	Experiment	Analytical Model	
	(DIC)	Rule of Mixture	Halpin-Tsai
Longitudinal modulus , E_{11} (GPa)	81.9	82.97	82.97
Transverse modulus, E_{22} (GPa)	6.15	5.80	9.4
In−plane Shear modulus, G_{12} (GPa)	2.77	2.14	2.85
In−plane Poisson's ratio (ν_{12})	0.34	0.33	0.33

2.7 Sensitivity analysis of DIC parameters on matrix material properties

2.7.1 Influence of speckle pattern

To study the influence of speckle patterns on displacement and strain measurement, different random speckle patterns are achieved on front and back surface of a matrix coupon as shown in Fig. 2.17. Both face of the specimen is focused with a CCD camera (kept at distance of 1.7 m from specimen surface) on each side fitted with a TAMRON lens (Model: SP AF 180 mm f/3.5 Di) and images are grabbed simultaneously. An area of 12 mm x 24 mm is chosen on both face for correlation along with subset size of 29 x 29 pixels^2 and step size of 5 pixels. The spatial resolution in both cases is 32.5 pixels /mm and the average speckle size for speckle pattern A and B is 3.2 pixel and 6.5 pixels respectively.

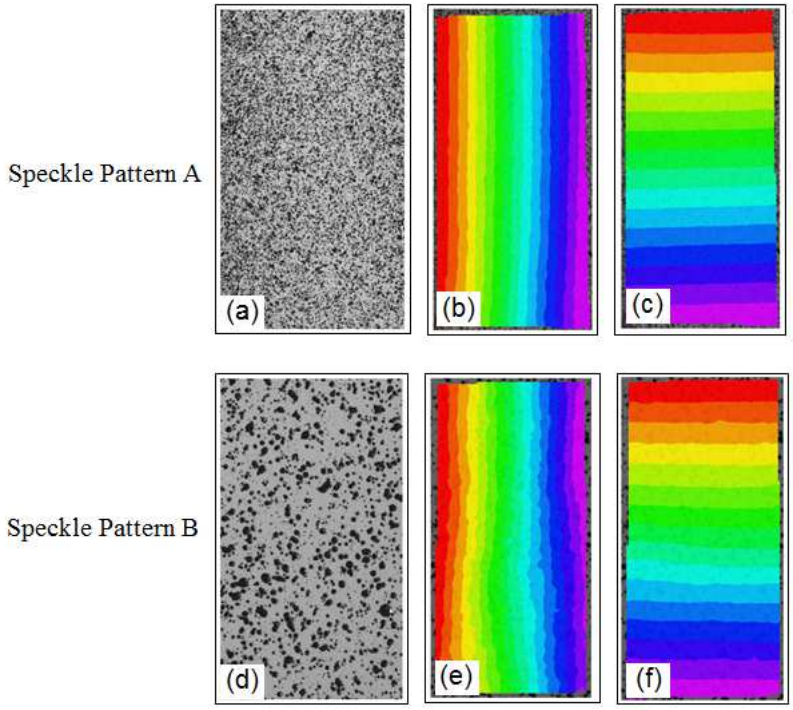

Figure 2.17: Displacement field maps on front and back surface of matrix coupon obtained from DIC at 1.7 kN. (a) front face having speckle pattern A (b) horizontal displacement for pattern A (c) vertical displacement (loading direction) for pattern A (d) back face having speckle pattern B (e) horizontal displacement for pattern B (f) vertical displacement for pattern B

Figure 2.17 shows the horizontal and vertical displacement for the both speckle pattern obtained at a load of 1.7 kN. It can be observed from the figure that the speckle pattern A presents smooth displacement field leading to less erroneous and noisy data as compared to speckle pattern B. Also the displacement field shows expected symmetric straight bands demonstrating the absence of rotation or translation which could occur due to improper experimental setup like misalignment of specimen [131].

Stress strain curve obtained from DIC for speckle pattern A and B is shown in Fig. 2.18. The Young's modulus using DIC is evaluated using the same procedure as discussed earlier, and it is found that the difference in magnitude of Young's modulus between two speckle patterns 1.8%. This can be attributed to the fact that the speckles are relatively small and closely spaced (denser) in speckle pattern A as compared to speckle pattern B. When speckle size is smaller, the gray level gradients in each subset of a given size i.e., the essential information used for pattern matching, increases allowing therefore an improved displacement resolution [130]. Thus, speckle pattern with smaller speckle size captures the minute of strain gradient which ultimately has led to the slight shift in strain values. However, the speckle pattern (B) with larger speckle size could not captures the minute of strain gradient and therefore causes the averaging effect of strain, resulting in a low strain level in comparison to speckle pattern with smaller speckle size. The results presented in subsequent sections are obtained based on speckle pattern of type A.

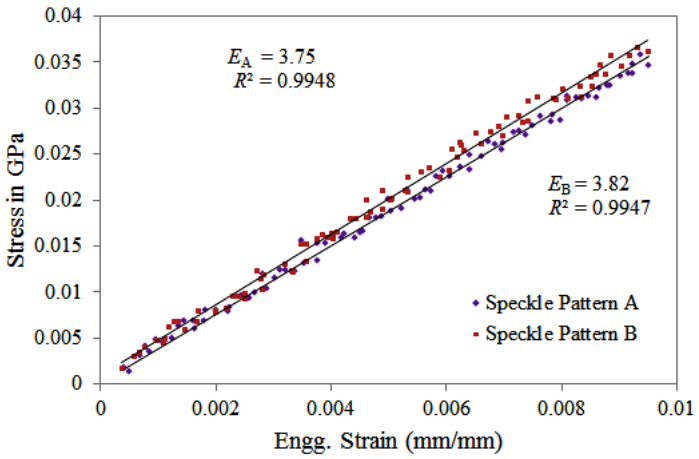

Figure 2.18: Stress−strain curve obtained from DIC for speckle pattern A & B

2.7.2 Influence of subset size

The influence of subset size on Young's modulus (E) and Poisson's ratio (ν) of matrix material is shown in Fig. 2.19. The resolution of ROI is 91 x 400 pixels^2 which correspond to 9.4 mm x 40.8 mm on physical scale. The spatial resolution is 9.75 pixel/mm. The value of E and ν are estimated based on average value of strain components extracted from DIC as explained earlier.

The variation of E and ν with different subset size 9 x 9, 15 x 15, 21 x 21, 29 x 29, 35 x 35, 41 x 41, 61 x 61 and 71 x 71 pixels^2 for a step size of 7 pixel is shown in Fig. 2.19 (a) & (b). It can be observed that the value of E is constant with initial increase of subset size; later it increases slightly up to a subset size of 61 x 61 pixel^2 and then decreases with further increase in subset size. However, the value of ν increases with initial increase in subset size, constant over a subset range of 21 x 21 pixel^2 to 41 x 41 pixel^2 and then steadily decreases with further increase in subset size. The percentage of variation in E and ν based on their minimum and maximum value obtained using subset size variation is 8 and 1.45 respectively. Several uncorrelated portion in ROI are observed at lower subset size which indicate that the subset size is lower than speckle size in those zones.

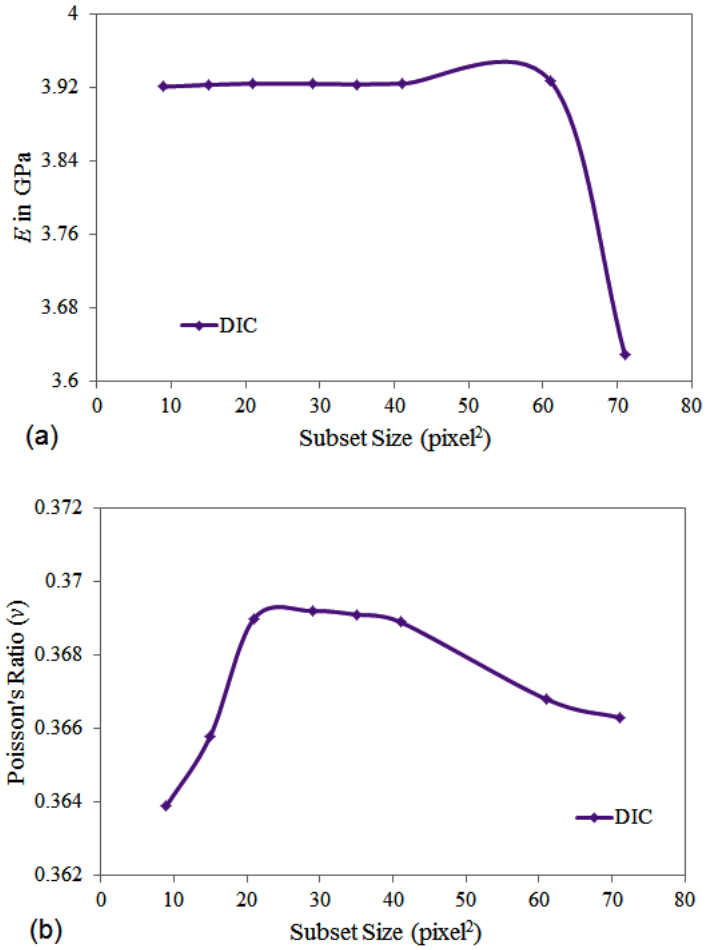

Figure 2.19: Influence of subset size on matrix material (a) Young's modulus (E) (b) Poisson's ratio (ν)

The subset size therefore should be large enough to contain sufficient information for a good correlation and also it must be greater than the largest speckle size to avoid the data loss. It is found that at lower subset size the strain field contains noisy data and it starts filtering with increase in subset size since it allows averaging of strain over a large zone at the expense of computational time. However, a too large subset size presents smoothening and averaging of strain over a larger portion of ROI and results in a significant reduction in strain magnitude and hence resulting in a large variation in E and ν (see Fig. 2.19(a) & (b)). However, one can clearly notice that the variation in both E and obtained ν remains constant for a subset range of 21 x 21 to 41 x 41 pixels^2.

2.7.3 Influence of step size

Further, a subset size of 29 x 29 pixels^2 is chosen to investigate the influence of step size on E and ν by keeping the same ROI size. Six different step sizes are used: 3, 7, 9, 15, 21 and 27 pixels. It is observed that the lower step size increases the number of data points for computation and thereby increases the computational time and vice versa. It is found from the Fig. 2.20 (a) & (b) that the maximum variation in E and ν due to step size variation is 0.11% and 0.45% respectively. So, one can conclude from the variation that the step size has negligible influence on E and ν value as compared to the subset size. This is because the step size is associated with the density of data points to be computed and may affect the sensitivity of local strain rather than the subset size which is essentially involved in matching process [123].

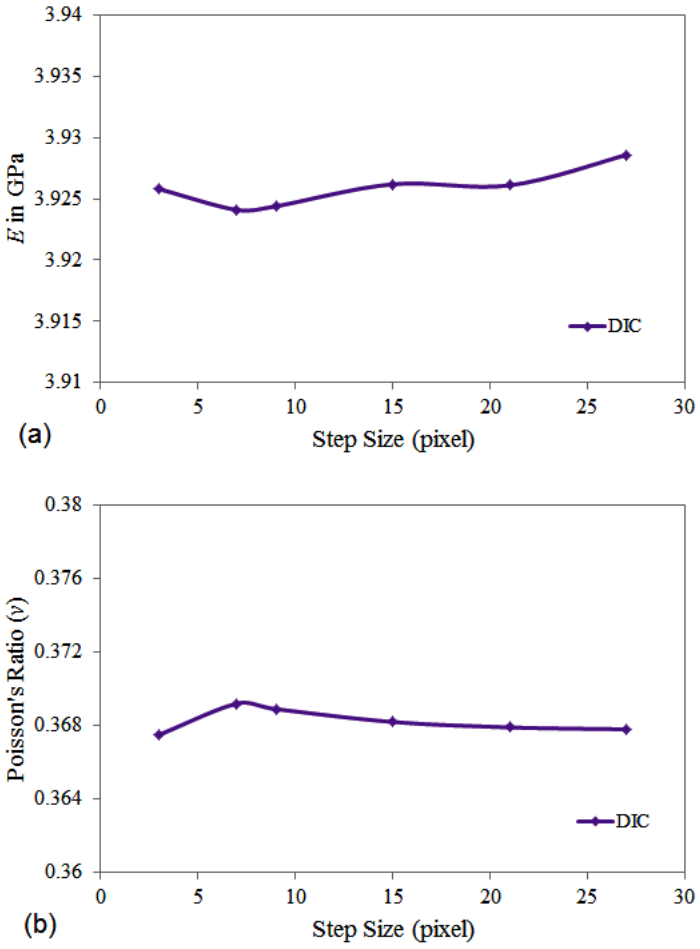

Figure 2.20: Influence of step size on matrix material (a) Young's modulus (E) (b) Poisson's ratio (ν)

2.7.4 Influence of ROI size

Also, the impact of ROI size is analyzed by keeping the same step size of 7 pixels and subset size of 29 x 29 pixels^2. The ROI of different sizes 91 x 84, 91 x 210, 91 x 448 and 91 x 680 pixels^2 are considered, and its influence on E and ν is shown in Fig. 2.21 (a) & (b) respectively. The ROI could not be increased along y direction because of specimen width constraint. One can observe that the variation of ROI size has no significant effect on E and ν value and their variation shows a similar trend as observed in the case of step size variation.

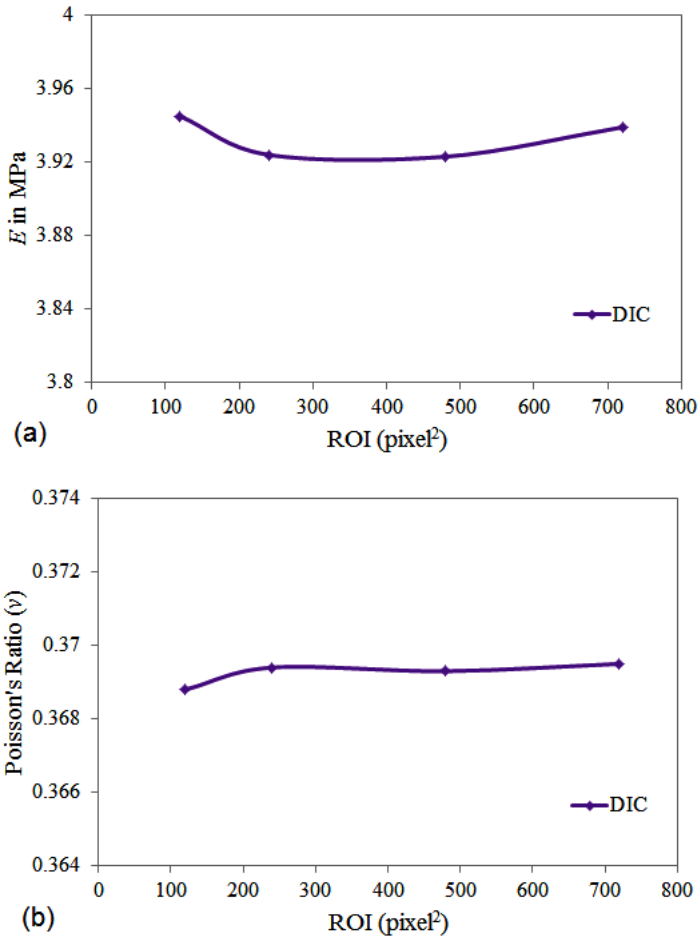

Figure 2.21: Influence of ROI size on matrix material properties (a) Young's modulus (E) (b) Poisson's ratio (ν)

2.8 Sensitivity analysis of DIC parameters on CFRP properties

2.8.1 Influence of subset size

The influence of subset size on longitudinal Young's modulus (E_{11}) and in−plane Poisson's ratio (ν_{12}) of CFRP laminate is shown in Fig. 2.22 (a) & (b) respectively. The different subset size 21 x 21, 29 x 29, 41 x 41, 61 x 61 and 71 x 71 pixels^2 are considered with a step size of 7 pixels with ROI of size 119 x 224 pixels^2. As subset size increases, E_{11} gradually decreases as expected which is explained earlier whereas ν_{12} initially increases for certain subset size and then remains constant. The variation in E_{11} and ν_{12} is 0.94% and 7.38% respectively.

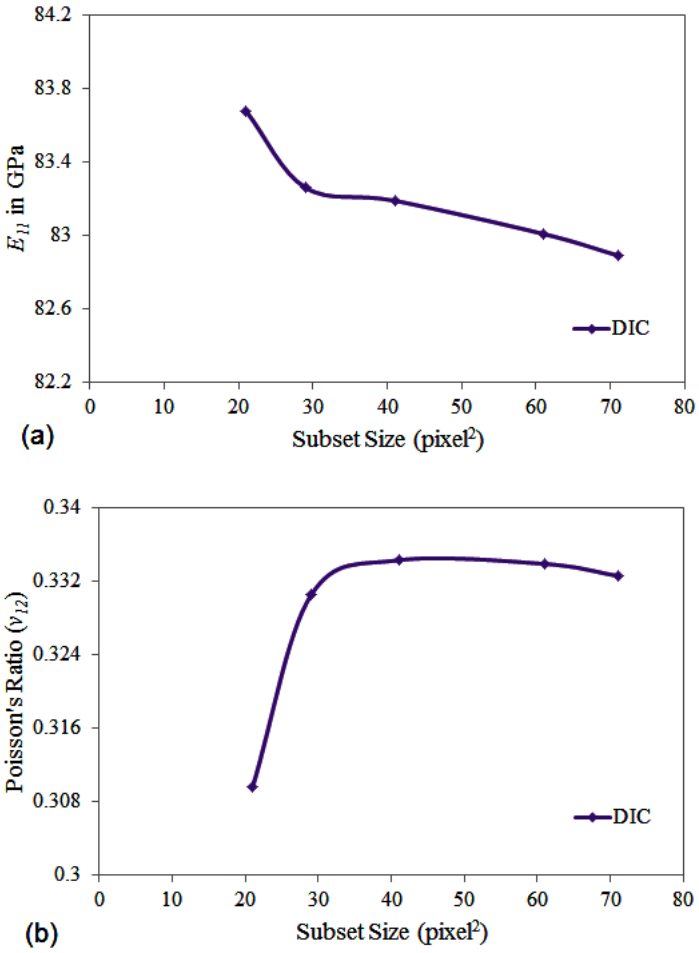

Figure 2.22: Influence of subset size on CFRP properties (a) longitudinal Young's modulus (E_{11}) (b) in−plane Poisson's ratio (ν_{12})

2.8.2 Influence of step size

The variation in E_{11} and ν_{12} as a function of step size, while retaining the same ROI size, is shown in Fig. 2.23 (a) & (b) respectively. The step size of 3, 7, 15, 21 and 27 pixels along with the subset size of 41 x 41 pixels^2 and ROI of 119 x 224 pixels^2 are chosen in this study. It can be observed from figure that with increasing step size, the variation of E_{11} and ν_{12} is of a zigzag nature unlike the one obtained for matrix coupon. Such variation could be due to local sensitivity of strain data which is expected in case of heterogeneous deformation. It is found that the percentage change in the value of E_{11} and ν_{12} due to step size variation is 0.45 and 6.95 respectively. Therefore, one can conclude that the influence of subset and step size on E_{11} is comparatively lower in contrast to ν_{12}.

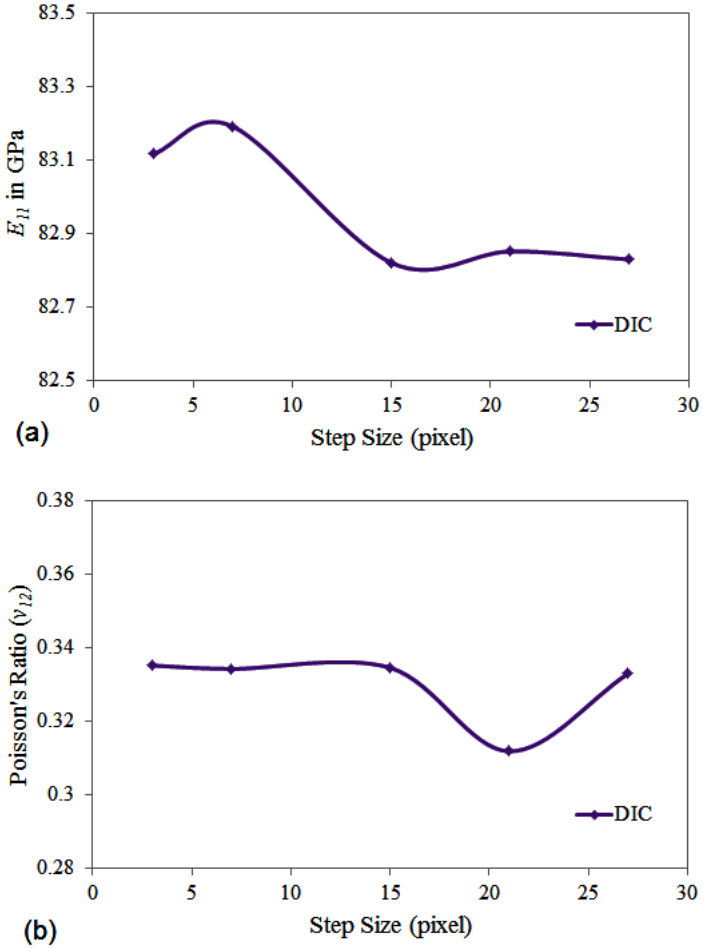

Figure 2.23: Influence of step size on CFRP properties (a) longitudinal Young's modulus (E_{11}) (b) in−plane Poisson's ratio (ν_{12})

2.9 Optimum value/range of DIC parameters for material properties estimation

Further, to arrive at an optimum range or suitable value of considered DIC parameters, the variation of modulus and Poisson's ratio as a function of DIC parameters are presented in normalized form, as shown in Fig. 2.24, 2.25 and 2.26 . The normalized value of modulus and Poisson's ratio are obtained by dividing them with their maximum value for the respective case. The point at which the line of variation for E and ν intersect each other is considered as the optimum value for corresponding DIC parameter, as obtained in Fig. 2.25. However, more than one intersection point is regarded here as an optimum range representing lower (LB) and upper bound (UB) for the respective DIC parameter, as obtained in Fig. 2.24. On close observation of Fig. 2.24 (a) & (b), one can conclude that the optimum range of subset and step size in case of epoxy matrix properties measurement is 21 x 21−41 x 41 pixels^2 and 6−9 pixels respectively.

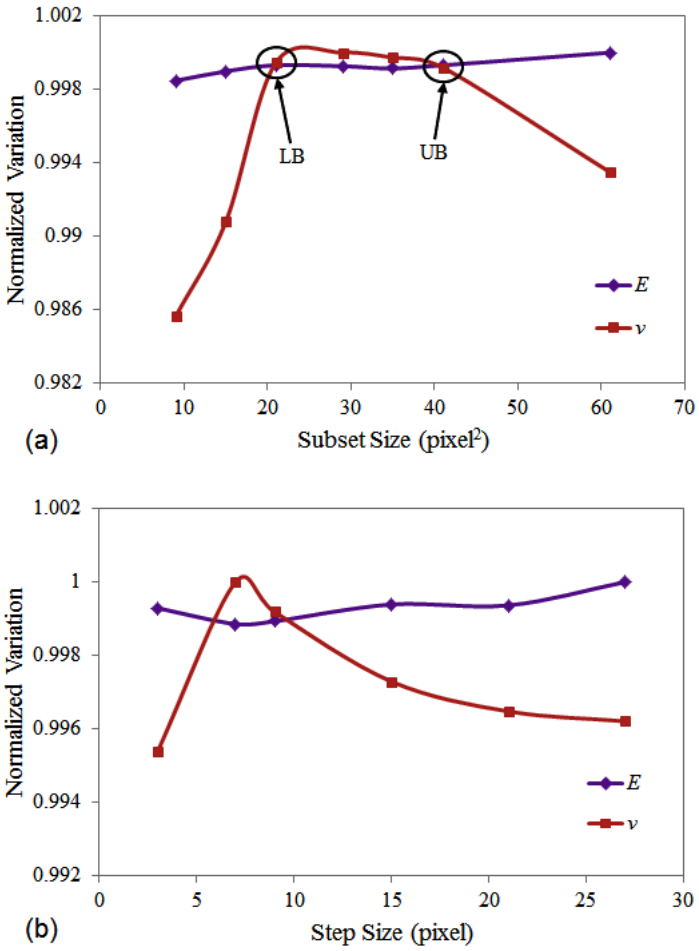

Figure 2.24: Normalized variation of matrix properties as a function of DIC parameters (a) subset size (b) step size

The predicted optimum range of subset size here is also justified by the fact that the subset size within this range shows a negligible variation in E and ν values as mentioned earlier.

The normalize variation of matrix properties as function ROI size is shown in Fig. 2.25. The optimum size for ROI is found to be 91 x 112 pixels^2 which correspond to 9.4 mm (specimen width) x 11.5 mm (specimen height) respectively on a physical scale. The aspect ratio of predicted ROI is 1.23 which is very much close to the aspect ratio of camera resolution 1.2 being used here. It is important to note here that the aspect ratio of specimen area chosen for correlation should be same as that of camera resolution aspect ratio and this observation is very much consistent with Ref. [154], which further strengthens our recommendation.

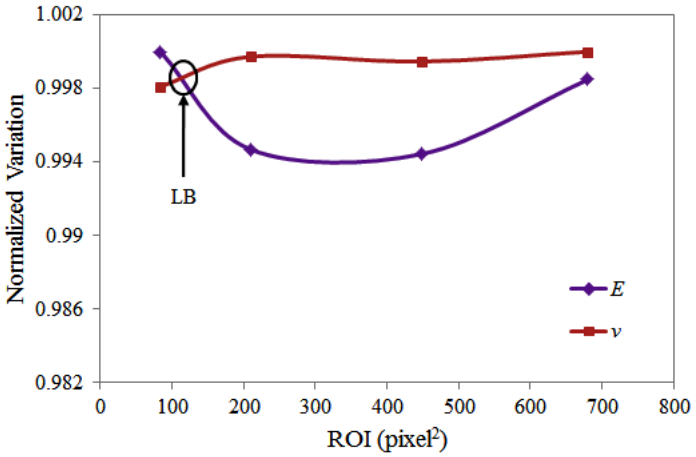

Figure 2.25: Normalized variation of matrix properties as a function of ROI size

The normalize variation of CFRP properties as function of subset and step size is shown in Fig. 2.26 (a) & (b) respectively. For the case of CFRP properties, it is found that the line variation of E_{11} and ν_{12} intersect at one point and then remains constant till a very higher subset size. Therefore, the optimum value of subset size is found to be 31 x 31 pixels^2 whereas the lower and upper bound for the step size from Fig. 2.26 (b) is found to be 4 and 9 pixels respectively. One can notice here that the predicted optimum range or values of DIC parameters for matrix and CFRP properties estimation are very much consistent with each other.

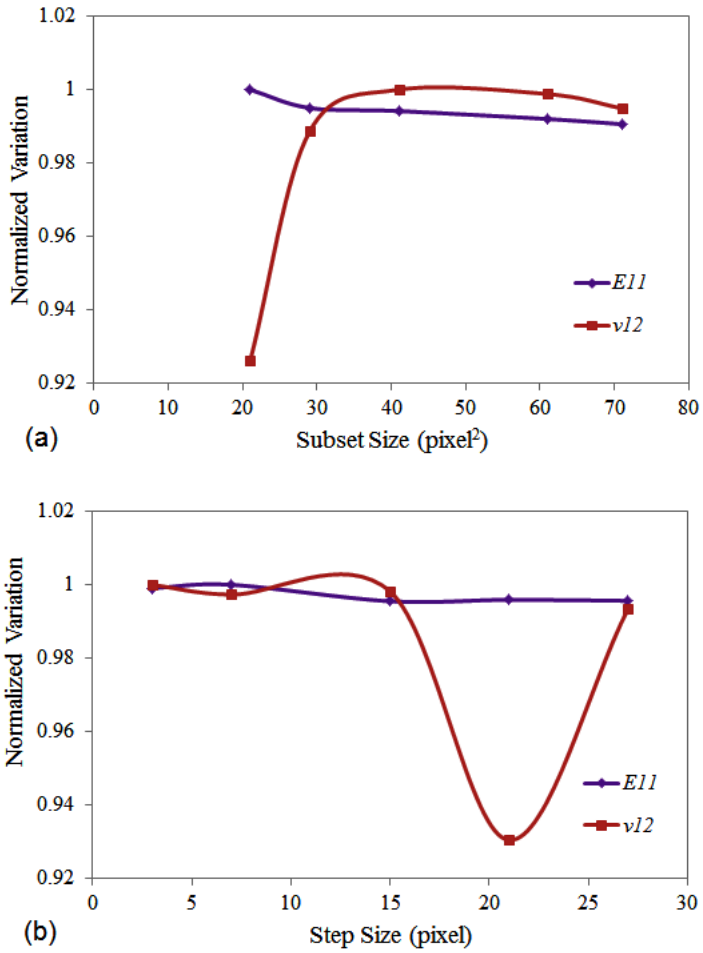

Figure 2.26: Normalized variation of CFRP properties as a function of DIC parameters (a) subset size (b) step size

2.10 Sensitivity analysis of DIC parameters on complex strain fields in an open cutout CFRP panel

DIC technique is recently being used by many researchers [141, 142] as a non−destructive technique to predict damage evolution in composite panels based on strain anomalies observed on the panel surface. Using DIC, the damage initiation site is generally predicted based on highly strained zone whereas the damage propagation is monitored based on appearance of uncorrelated/discontinuity area over the specimen surface [141, 142]. In an open cutout panel, the presence of hole complicates the strain field and a highly localized strained zone develops around it. The maximum strain is normally observed around transverse edge of the hole perpendicular to loading direction whereas minimum strain is across the longitudinal edge of the hole parallel to loading direction. Here, the influence of subset size and step size on whole field strain maps in an open cutout panel subjected to tensile load is investigated and they are compared with FEA results. All the results presented in this section correspond to a tensile load of 9.78 kN (149.88 MPa).

2.10.1 Specimen geometry and finite element analysis

The specimen geometry of open cutout panel is shown in Fig. 2.27. The CFRP laminate is 1.45 mm thick with a staking sequence of $[0°]_4$. The width (W) and length (L) of panel are 45 and 250 mm respectively. A circular hole of 10 mm diameter (d) is drilled at the center of panel. The drilling operation in specimen is performed using a diamond coated drill bit of 10 mm diameter. Wooden backing plate is used at the bottom of specimen to avoid hole−exit delamination induced due to drilling operation. Beveled aluminum tabs of dimension 50 mm x 45 mm x 2 mm are bonded to each end of the specimen after necessary bonding surface preparation as explained earlier.

A linear static 3D finite element analysis of an open cutout is carried out using ANSYS−13 software [155]. The geometry and dimensions of the panel is kept same as that of experimental model. The mesh pattern around the hole is kept very fine in order to capture the high stress concentration around it. The mesh morphology surrounding the hole is chosen based on mesh convergence study and it is discussed next chapter. Every layer in panel is meshed with one element in thickness direction. The panel is meshed with four elements in thickness direction corresponding to four layers in the laminate. The model is built with 3D 20−noded solid 186 brick element. Fibers in the panel are aligned parallel to the loading direction. The panel is fixed at bottom face and an in−plane tensile load of 9.78 kN is applied at the top face along x−direction so as to simulate the experimental boundary conditions. The results obtained from FEA are compared with the DIC data for the same load (9.78 kN).

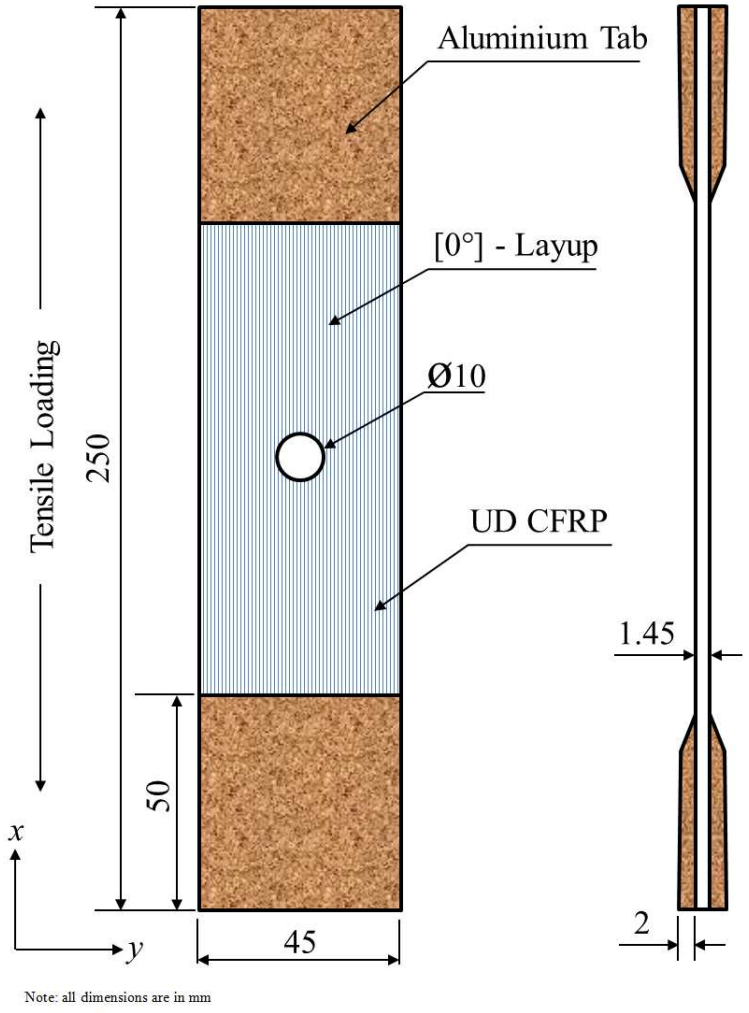

Figure 2.27: Open cutout CFRP panel $[0°]_4$

2.10.2 Influence of step size on longitudinal strain (ε_{xx})

A strain window size or ROI of 520 x 610 pixels^2 (41.4 mm x 48.8 mm) is chosen along with a subset size of 29 x 29 pixels^2 to analyze the influence of step size variation. The step size chosen are 1, 3, 5, 7, 9, 11, 13, 15, 17, 21 and 25 pixels.

Figure 2.28 shows the longitudinal whole field strain maps in an open cutout panel as a function of step size obtained from DIC. FEA plot with same scale as that of DIC plot is shown in the figure for a qualitative comparison. The gray areas on FEA plot represent the over saturation of scale, appeared because of maintaining the same scale. One can clearly observe the disparity in strain maps of ε_{xx}, as the step size increases. The longitudinal strain plots shows a scattered random location of peak strain over specimen surface at step size-1 pixels, localization of maximum strain zone around transverse edge of the hole at step size-3 pixels, symmetrical nature of strain distribution at step size-7 pixels and then asymmetry sets up in strain field at higher step size. Also, one can see that the size of maximum strain zone of (ε_{xx}) increases with increase in step size and swiftly propagates from transverse edge of the hole towards the panel edge, as the step size keeps increasing.

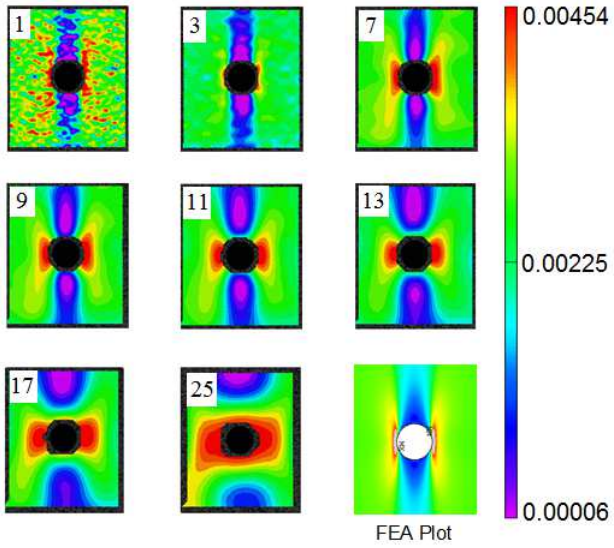

Figure 2.28: Longitudinal strain field (ε_{xx}) maps in an open cutout CFRP panel as a function of step size obtained from DIC

Furthermore, the maximum strain zone also appears at longitudinal edge of the hole at a higher step size which is unexpected in case of an open cutout panel subjected to tensile load. Since the step size is essentially associated with pixel/data density so one can infer from these observation that at lower step size (say 1 pixel), the strain field is highly pixilated, showing sensitivity of local strain at the expense of computational time and involves scattered noisy pattern. At higher step size (say 9 pixels), the strain field is less pixilated and mitigates the noisy pattern at the expense of losing the sensitivity of local strain variation.

The variation of ε_{xx} along net section of the panel as a function of horizontal distance from the hole edge is shown in Fig. 2.29. The line considered for the plot is also shown in figure. It can be observed from the figure that the variation of ε_{xx} shows random peaks and valleys at lower step size (1, 3), representing a realistic nature of strain variation i.e., peak at hole edge and reduces as one

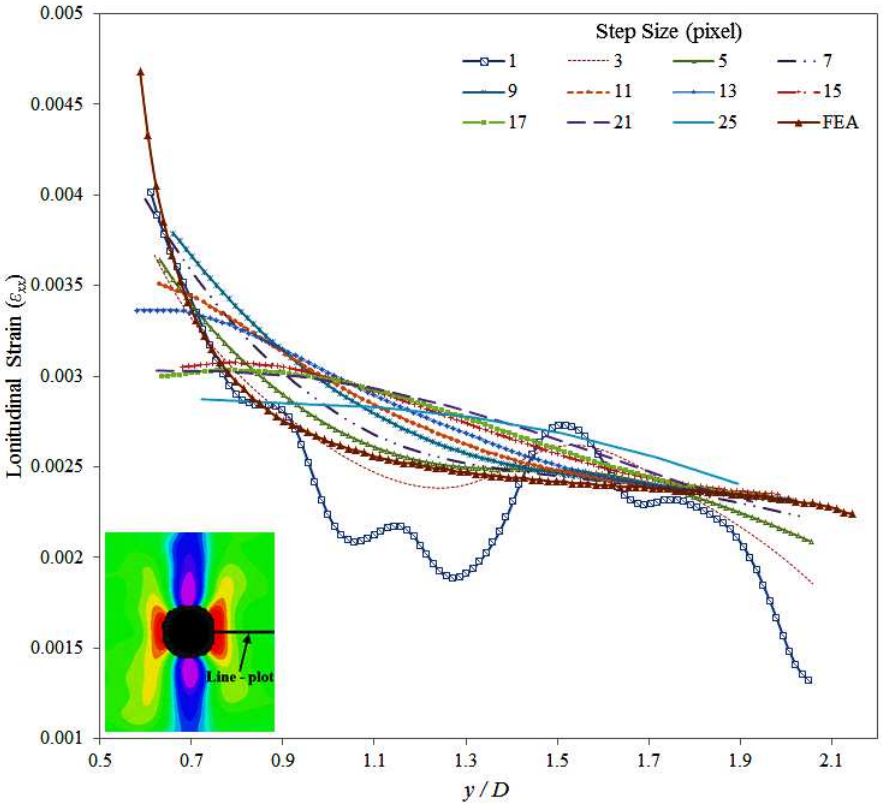

Figure 2.29: Variation of ε_{xx} along net section of an open cutout CFRP panel at different step size along distance from hole edge

move away from hole edge towards panel edge at higher step size (5, 7, 9) and then presents too much softening with further increase in step size. One can also observe from the figure that the variation of ε_{xx} at step size 5 and 7 are in close match with FEA result pertaining to the trend and magnitude.

2.10.3 Influence of step size on transverse strain (ε_{yy})

The whole field transverse strain maps in an open cutout panel as a function of step size obtained from DIC is shown in Fig. 2.30. The transverse strain, ε_{yy} plot shows a similar behaviour as observed in case of ε_{xx}. However, one can see that with increasing step size, the zone of maximum (ε_{yy}) strain starts shifting from transverse edge of the hole towards the panel edge.

The variation of ε_{yy} along net section of the panel as a function of horizontal distance from the hole edge is shown in Fig. 2.31. The line considered for the plot is also shown in figure. The variation of ε_{yy} shows a reversal nature with increasing step size. At lower step sizes (3, 5, 7, 9), ε_{yy} is maximum near the hole edge (at a distance of 8.2 mm away from hole edge), steadily decreases with distance and becomes minimum near the panel edge. However, further increase in step size leads to minimum value of ε_{yy} near hole edge, increase with distance and then becomes maximum at panel edge which is inappropriate. In comparison with FEA plot, the ε_{yy} variation at step size 7 shows a similar trend besides the difference in magnitude.

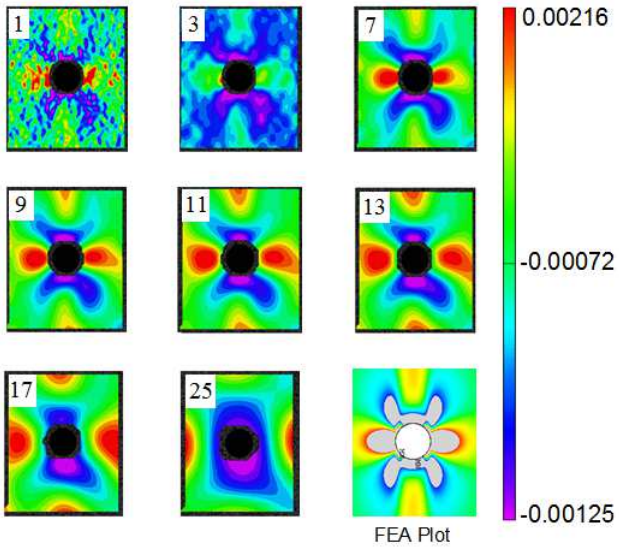

Figure 2.30: Transverse strain field (ε_{yy}) maps in an open cutout CFRP panel as a function of step size obtained from DIC

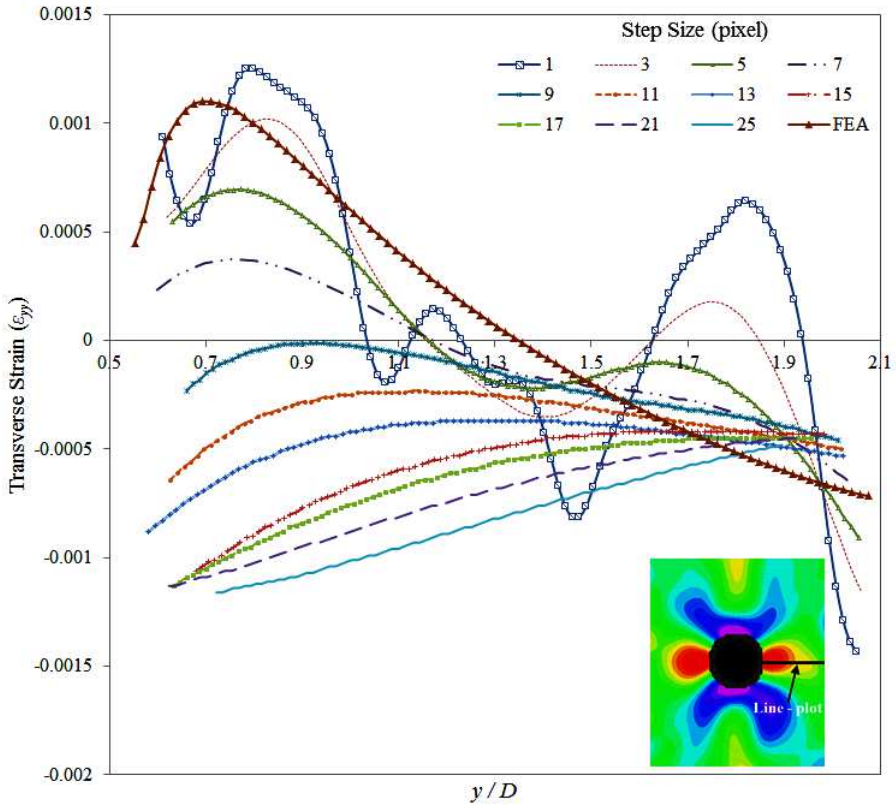

Figure 2.31: Variation of ε_{yy} along net section of an open cutout CFRP panel at different step size along distance from hole edge

2.10.4 Influence of step size on shear strain (ε_{xy})

The whole field transverse strain maps in an open cutout panel as a function of step size obtained from DIC is shown in Fig. 2.32. The shear strain ε_{xy} plot also presents a similar trend as that of strain ε_{xx}.

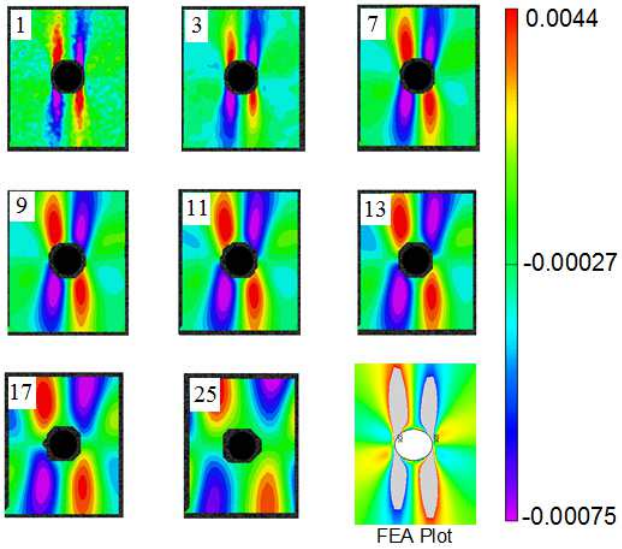

Figure 2.32: Shear strain field (ε_{xy}) maps in an open cutout CFRP panel as a function of step size obtained from DIC

Also, the variation of ε_{xy} obtained from FEA and DIC (for different step size) as a function of panel width at distance of 4.1 mm above the hole edge is shown in Fig. 2.33. It can be observed from the figure that the ε_{xy} plot for different step size shows a similar trend as FEA except at lower step size (1, 3) which results in unexpected local peaks and valleys. However, the expected peak value of ε_{xy} is significantly influenced by step size variation as it smoothens with increasing size and step size 5 or 7 could be chosen on compromise between magnitude and natural trend.

The strain variation plots obtained from DIC measurement in all the cases shows a similar trend as that of FEA plots, with slight deviation in magnitudes. The significant loss in displacement/strain data near the hole due to edge (boundary) un−correlation, presence of noise in computed displacement field, low displacement resolution and presence of high strain gradient could affect the experimental results and may contribute to the deviation between DIC and FEA results.

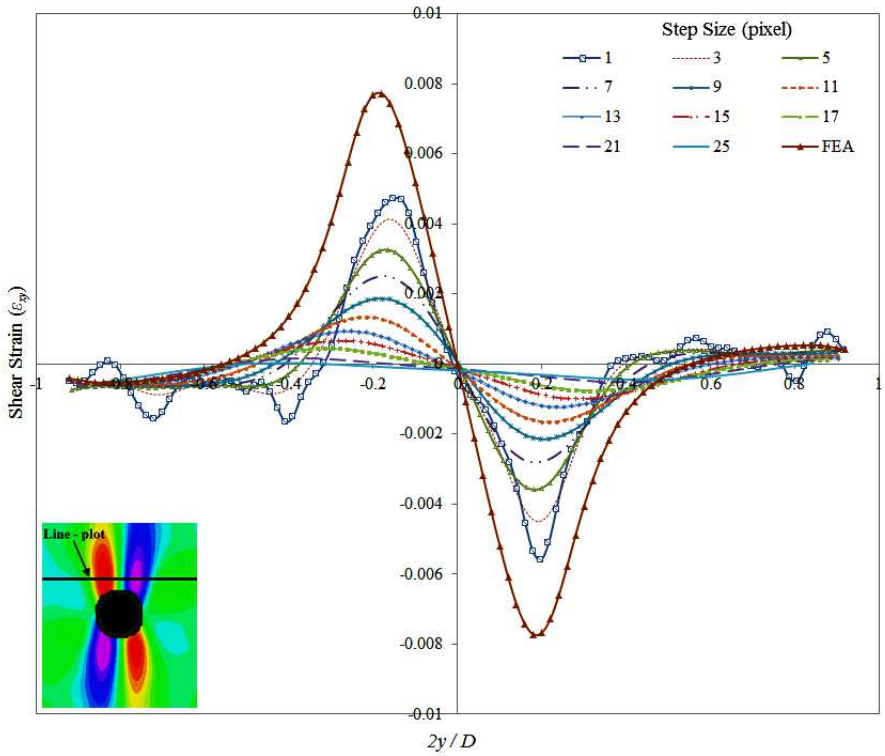

Figure 2.33: Variation of ε_{xy} along net section of an open cutout CFRP panel at different step size along distance from hole edge

2.10.5 Influence of subset size on whole field strain maps

A strain window size (ROI) of 520 x 610 pixels^2 (41.4 mm x 48.8 mm) is chosen along with a step size of 7 pixels to analyze the influence of subset size variation. The subset size considered here are: 11 x 11, 15 x 15, 21 x 21, 29 x 29, 37 x 37, 43 x 43, 51 x 51, 63 x 63 and 81 x 81 pixels^2.

The whole field longitudinal (ε_{xx}), transverse (ε_{yy}) and shear (ε_{xy}) strain maps at different subset size are shown in Fig. 2.34, 2.35 and 2.36 respectively. FEA plot for different strain components are also shown in the figure for a qualitative comparison.

It can be observed from ε_{xx}, ε_{yy} and ε_{xy} plots that, at lower subset size, there are several uncorrelated zone within ROI which indicates that the subset size in these zones are lower than speckle size. So, the subset size should be large enough to contain sufficient information for a good correlation and also it must be greater than the largest speckle size to avoid the data loss. One can realize from these strain contour plots that the major impact of subset size is the smoothening effect on strain field as discussed earlier. One can also observe from the strain plots that the uncorrelated area at the hole edge increases with increasing subset size resulting in more data loss nearer to hole boundary.

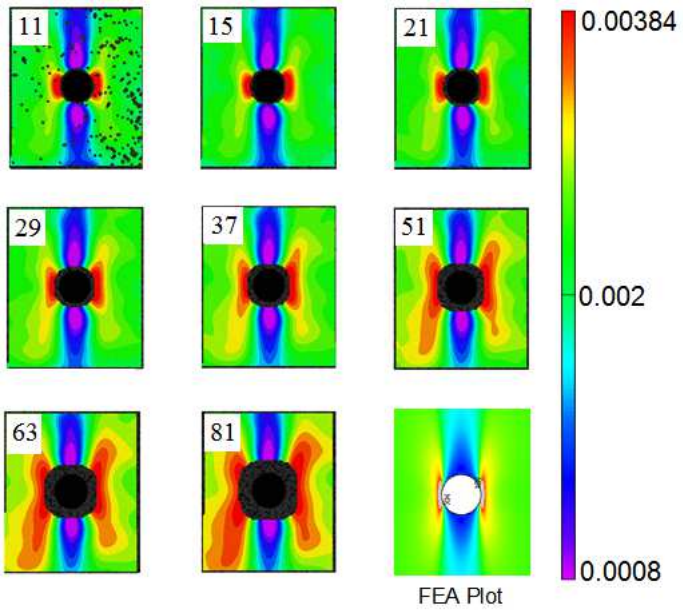

Figure 2.34: Longitudinal strain field (ε_{xx}) maps in an open cutout CFRP panel as a function of subset size obtained from DIC

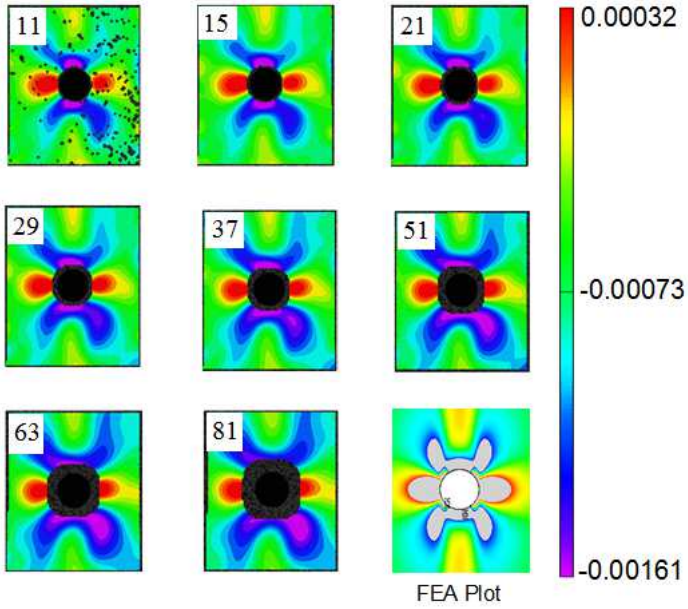

Figure 2.35: Transverse strain field (ε_{yy}) maps in an open cutout CFRP panel as a function of subset size obtained from DIC

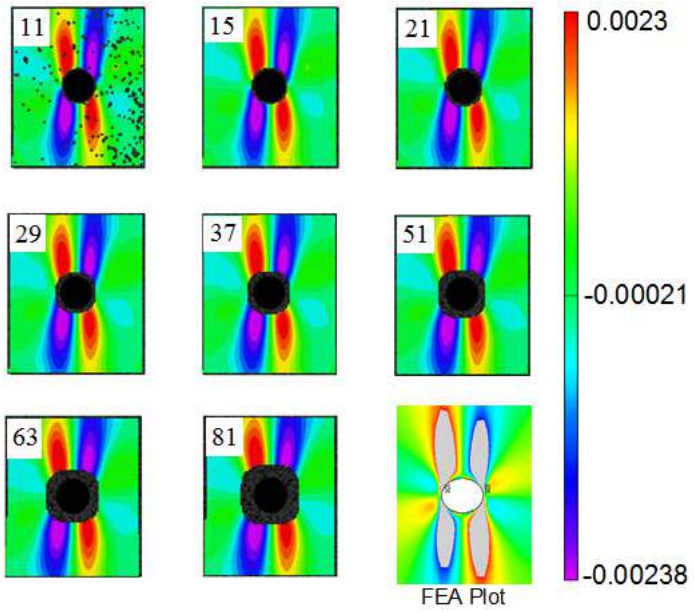

Figure 2.36: Shear strain field (ε_{xy}) maps in an open cutout CFRP panel as a function of subset size obtained from DIC

The variation of longitudinal strain (ε_{xx}) obtained from DIC for different subset sizes along with FEA prediction at net section from the hole edge is shown in the Fig. 2.37. The line considered for the plot is shown in respective figures.

It can be observed from the figures that the variation of ε_{xx} for all subset size shows a similar trend as that of FEA. However, a significant difference in magnitude is notice between DIC and FEA results especially at the hole due to edge correlation. The variation in subset size seems to have an impact on sensitivity of local strain surrounding the hole near transverse edge whereas zone away from hole is unaffected. The peak magnitude of ε_{xx} near transverse edge of the hole changes from 0.00384 to 0.00299 as the subset size increases from 11 x 11 to 81 x 81 pixels^2.

It is also found that the subset size variation has negligible influence on magnitude of strains ε_{yy} and ε_{xy} and they present a similar variation as that of FEA. Therefore, one needs to choose an appropriate step size together with subset size to achieve accurate results.

It can also be noticed here that the discontinuity in panel due to presence of hole poses difficulty in achieving correlation at hole edge leading to significant loss in strain data at this location. To quantify the loss due to edge un−correlation, a DIC test is carried out for an open cutout panel having same configuration and under the same experimental condition. However, prior to the test the hole was filled with clay so that a continuous correlation could be achieved at hole edge. The longitudinal strain (ε_{xx}) along the net-section is compared with the one obtained from DIC test on an open cutout panel without clay and it is shown on the Fig. 2.38. It is found that the use of clay facilitates in improved correlation at hole edge without affecting the panel behaviour and the magnitude increases to 0.008744 for the panel with clay whereas it is 0.00396794 (at a distance of 1.03 mm from hole edge due to un−correlation) without clay, clearly presenting a significant improvement in peak value.

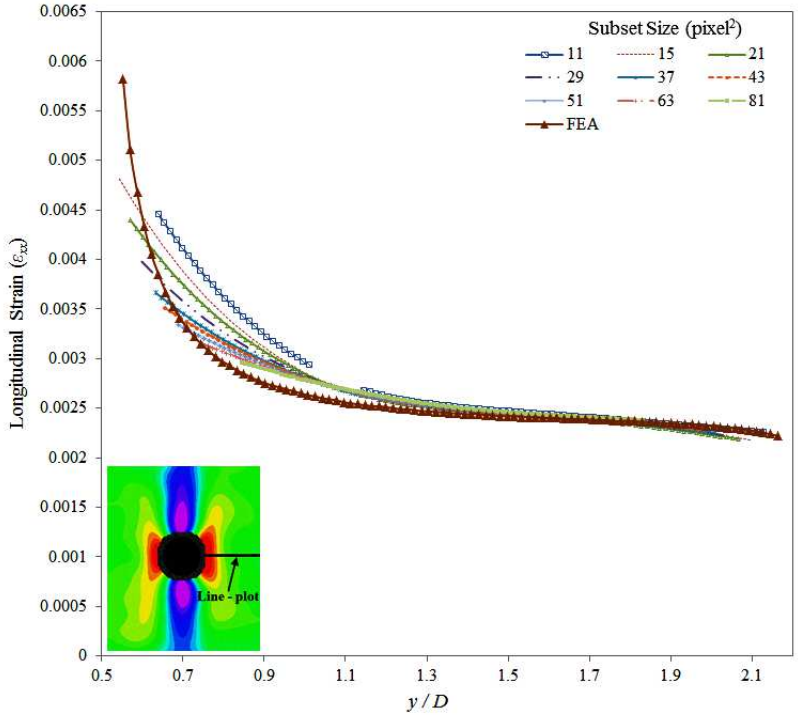

Figure 2.37: Variation of ε_{xx} along net section of an open cutout CFRP panel at different subset size along distance from hole edge (9.78 kN)

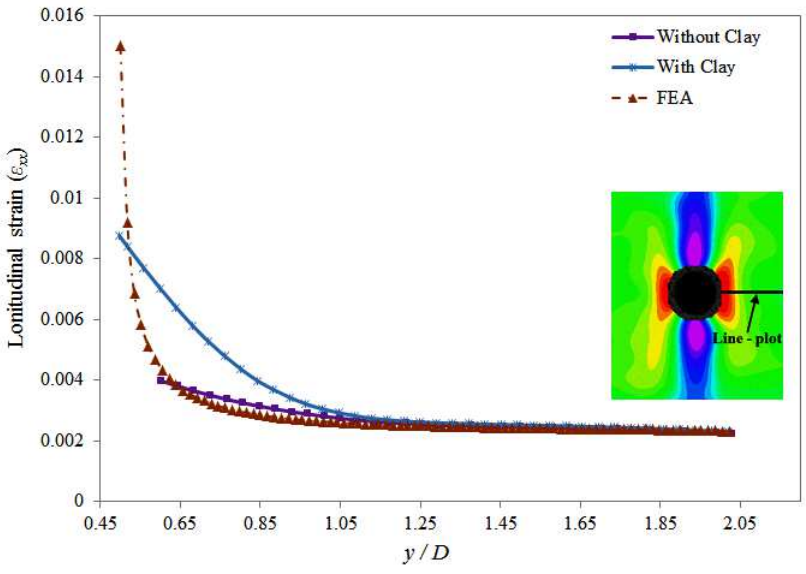

Figure 2.38: Variation of longitudinal strain (ε_{xx}) at net−section along distance from hole edge obtained from DIC test for on open cutout panel with and without clay

2.11 Closure

In this chapter, full field non−contact three−dimensional DIC technique has been employed to evaluate the mechanical properties of epoxy matrix and UD CFRP laminate by performing a series of tests as per ASTM standards. The DIC results are compared with the conventional standard test values and also with the theoretical one involving both *rule of mixture* and *Halpin− Tsai model*. The value of longitudinal modulus obtained from DIC measurement and extensometer is in close agreement with an error of 0.8%. The error between DIC measurement and theoretically estimated value for the case of longitudinal modulus and in−plane Poissons ratio is found to be 1.3% and 2.9% respectively, thereby confirming the accuracy of DIC technique.

Further, an elaborate study is also carried out to investigate the influence of DIC parameters such as speckle size, subset size, step size and region of interest on material properties of matrix and composite laminate. It is found that the speckles with relatively small and closely spaced (denser) pattern provides improved displacement resolution and helps in capturing minute strain gradient. The subset size has shown to have more influence on material properties as compared to step size. Optimum value of subset size and step size predicted for characterization of both matrix and composite material are found to be consistent with each other. The lower and upper bound for subset size is found to be 21 × 21 and 41 × 41 pixels^2 whereas for step size it is of 6 and 9 pixels respectively. The aspect ratio of predicted optimum ROI is found to be 1.23 which is very much close to the aspect ratio of camera resolution 1.2 being used here. Therefore, it is suggested that the aspect ratio of ROI chosen for correlation should be the same as that of camera's aspect ratio for better correlation.

Furthermore, an open cutout CFRP panel is also studied to demonstrate the influence of DIC parameters on complex strain field applications. It is observed that the strain field surrounding the hole is more sensitive to step size rather than subset size. Lower step size results in highly pixilated strain field, showing sensitivity of local strain at the expense of computational time along with random scattered noisy pattern whereas higher step size mitigates the noisy pattern at the expense of losing the detail present in the actual data. It even changes the natural trend of strain field resulting in erroneous maximum strain location. Based on comparison between DIC and FEA results, it is found that a step size of 5 or 7 pixels can be chosen as it provides a close match with FEA result pertaining to the trend and magnitude. The subset size variation mainly presents a smoothing effect, eliminating noise from the strain field while maintaining the details in the data and their natural trend. The subset size variation has shown negligible influence on magnitude of strains. However, increase in subset size significantly reduces the strain value at hole edge due to discontinuity in correlation. Also, the subset size in general should be larger than the step size to achieve a better correlation.

The present study has shown that the DIC technique is most comprehensive and accurate method for composite characterization utilizing whole field strain data. In the next chapter DIC technique is used for whole field surface displacement and strain measurement in damaged, single and double sided patch repaired CFRP panel for understanding their mechanics under tensile loading.

Chapter 3

Whole Field Strain Analysis of Open Cutout and Repaired CFRP Panel using DIC and FEA

3.1 Introduction

Repair of aircraft structures using composite patch has been initiated by Baker et al. [18] in the early 1970's mainly in order to enhance fatigue life of cracked aluminium structures. Till date, most of the repair study has been carried out on cracked aluminium components [156–160]. Among these, only few are experimental work [157–160]. Presently, aircraft structural components are mostly made of composites, which are more prone to damage due to low velocity impacts during its service life. Since more and more composites are now being used in today's applications, more repair of composite structures have to be administered in the near future. Therefore, it is essential to understand the behaviour of patch repaired composite panels including its damage mechanism to ensure the higher efficiency of repair resulting in increased integrity closer to the original structure. However, only few experimental investigations are available on repair studies of composite panels having open cutout [20, 76, 82, 83, 112, 141, 161].

In this chapter, an experimental study is presented to analyze the behaviour of adhesively bonded patch repair of CFRP laminates under tensile loading. An elaborate study involving DIC is carried out to investigate the effects of patch reinforcement on the ultimate strength of the damaged composite panel under tensile load. The study is conducted on both pure UD $[0^{\circ}]_4$ and quasi−isotropic $[\pm 45/0/90]_s$ CFRP panels. To simulate the effect of damage, holes are drilled at the center of the panel, and it is repaired with adhesively bonded circular patch. The performance and behaviour of both single and double sided patch repaired panel are presented. The strain distribution on the patch and region closer to the overlap area are studied for better understanding of the load transfer across the damaged area using 3D DIC technique. Damage development and failure mechanism in panel with open cutout and also the repaired one are experimentally studied. A 3D linear finite element based numerical study is then carried out for the same model and obtained whole field strain distributions in open cutout and repaired panels are compared against the experimental results. In

the last section of this chapter, a mechanics based design approach using FEA is presented through parametric study that allows us to analyze the influence of different patch stacking sequence, patch thickness, overlap length and adhesive thickness on SCF in panel, shear and peel stress level in adhesive layer which further helps in improving the repair performance.

3.2 Specimen geometry and fabrication

The typical geometry and dimensions of damaged and repaired panel is shown in Fig. 3.1. Both patch and panel are prepared from composite laminates fabricated in−house using hand layup technique. The composite laminates are made from same UD carbon fiber mat of 200 gsm together with epoxy resin LY−556 mixed with hardener HY−951, as discussed in chapter−2. The average thickness of each layer of laminate after casting is found to be 0.35 mm.

The length (L) and width (W) of the panel are 250 and 50 mm respectively. A circular hole of 10 mm diameter (d) is drilled at center of the panel so as to simulate the effect of damage removal. The ratio of panel width to hole diameter is 5. This type of removal happens in the case of low velocity impact. The drilling operation in specimen is performed using special purpose diamond coated drill bit supplied by SECO TOOLS. Wooden backing plate is used at the bottom of specimen to avoid hole−exit delamination induced due to drilling operation. The circular patches are also fabricated from parent panel material which are first cut into octagonal shape slightly over dimension and then finally polished into circular shape of 40 mm diameter. This procedure is mainly adopted to prevent the edge delamination during machining. Bonding surface of both patch and panel is abraded with 200−grit sandpaper and cleaned with isopropyl alcohol. The surface preparation is done to provide good bonding and avoid premature adhesive failures. The damaged panel is repaired by bonding the circular patch over the damaged area using Araldite 2011 adhesive. The Araldite 2011 is an intermediate strength adhesive having higher toughness [162]. It is a two part adhesive system and is applied by an applicator gun to ensure through mixing and uniform thickness. Care is taken while bonding the patch so that it is kept concentric to hole in panel as well as fibers in the patch are parallel to fibers in panel. The panel is repaired by both single and double sided patch configurations. It is cured at room temperature for 24 hours. Beveled tabs of dimension 50 mm x 50 mm x 2.5 mm are bonded to each end of the specimen using AV138/HV998 adhesive system, after necessary bonding surface preparation. The fabricated specimens (zoomed view) are shown in Fig. 3.2. The configurations of the panel and patch considered in the present study are given in Table 4.1.

Adhesive thickness measurement

Figure 3.3 shows an image taken from optical microscope to evaluate adhesive thickness in repaired panel. The optical microscope is Leica DM6000 M with a resolution of 1 m. A small sample is cut from the net section (through the hole) of the repaired specimen so that the sample contains a portion of patch, panel and adhesive. The sample is then visualized in an optical microscope using HCX PL FLUOTAR 5X/0.15 BD lenses at 5X magnification. The measurement is taken at three different locations across the adhesive cross−section. The final value of adhesive thickness in each configuration is taken as an average of three independent measurements and they are reported in Table 4.1.

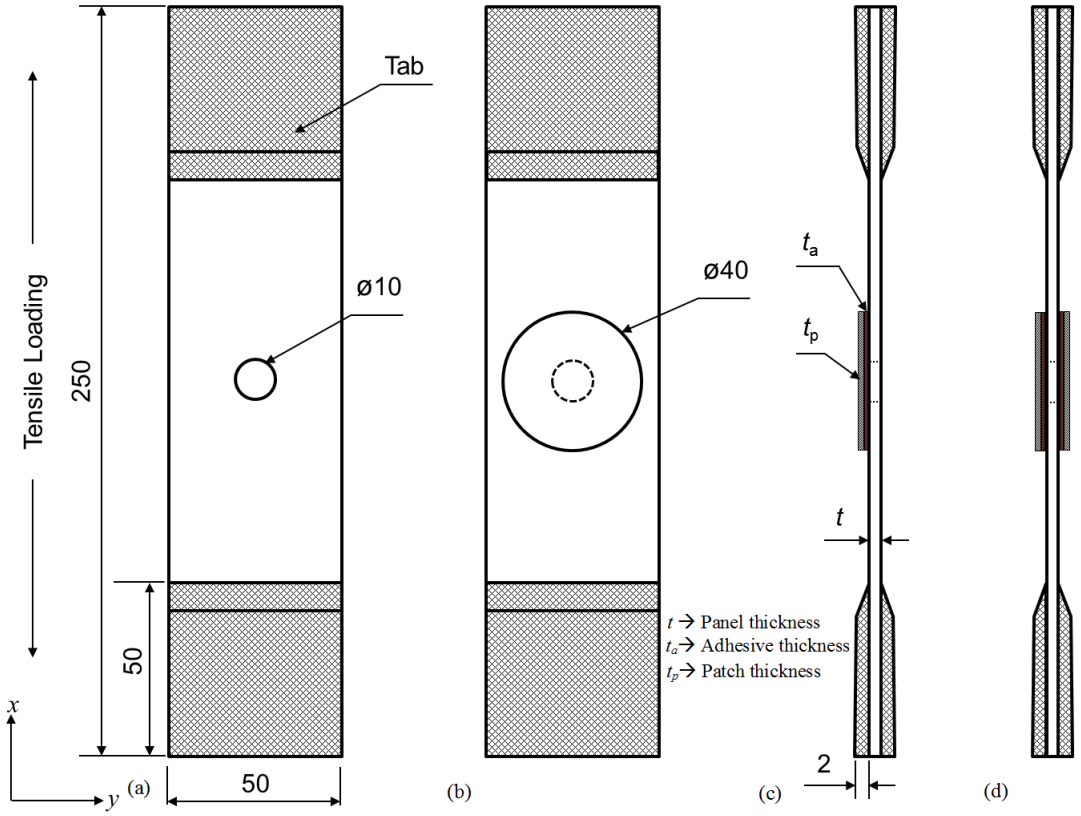

Figure 3.1: Specimen geometry (a) open cutout panel (b) repaired panel (c) single sided repaired panel (d) double sided repaired panel (all dimensions are in mm)

Table 3.1: Configurations selected for experimental study.

Label	Panel stacking sequence	Patch stacking sequence	Adhesive thickness (mm)
Pure UD laminate	$[0°]_4$	$[0°]_3$	0.185
Quasi−isotropic laminate	$[\pm 45/0/90]_s$	$[\pm 45]_s$	0.15

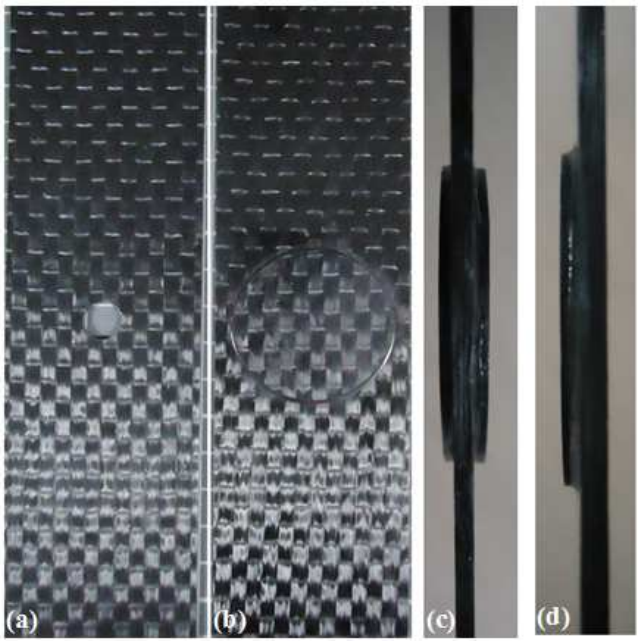

Figure 3.2: Fabricated CFRP UD specimens (a) open cutout panel (b) panel repaired with circular patch (c) double sided repaired panel (d) single sided repaired panel

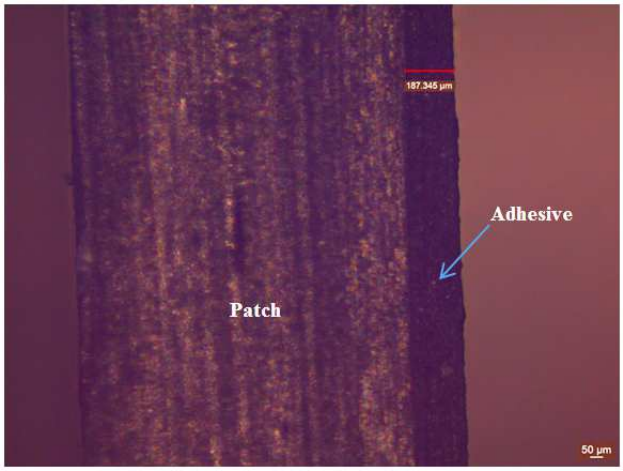

Figure 3.3: Adhesive thickness measured using optical microscope

3.3 Experimental setup and test procedure

The experimental setup used for damage and repair study is similar to Fig. 2.3, given in chapter−2. Prior to the testing, random speckle patterns on specimen surface are obtained using the procedure discussed in chapter−2. The specimen is then fixed in hydraulic wedge grips and a gripping pressure is maintained at 4 MPa to avoid slipping of specimen and also to prevent crushing of end tabs. All specimens are loaded in tension at room temperature and five images per second are grabbed at a displacement control rate of 1 mm/min, in addition with an initial image taken at no/zero load, termed as reference image . The grabbed images are post−processed in Vic−3D software by selecting required region of interest on reference image and assigning appropriate subset and step size prior to analysis.

3.4 Experimental results: pure UD panel $[0^\circ]_4$

Experimental results obtained from quasi−static tensile test of open cutout, single sided and double sided repair model obtained using DIC are presented in the subsequent sub−sections.

3.4.1 Panel with open circular cutout

The behaviour of damaged panel (panel with open circular cutout/hole) subjected to tensile load is studied using 3D−DIC technique. The ROI for correlation is chosen as 46.5 mm × 125 mm (535 × 1440 pixel^2) so as to observe the damage evolution till final failure. A subset size of 32 x 32 pixel^2 is chosen along with a step size of 7 pixels for performing the DIC calculations. The spatial resolution is 11.5 pixels/mm.

Figure 3.4 shows the strain field in the panel with open circular cutout at different loads. The presence of hole in panel complicates the strain field and a highly localized strained zone develops around it. Mostly damage initiation happens at the periphery of hole. The maximum strain is observed around transverse edge of the hole perpendicular to loading direction. The minimum strain is across the longitudinal edge of the hole parallel to loading direction. It can also be observed from the figure that the longitudinal strain (ε_{xx}) distribution as well as damage development is not perfectly symmetrical about x−axis. The magnitude of ε_{xx} is slightly higher on right hand side of the hole as compared to the left hand side. The reason to this can be attributed to several factors like asymmetrical damage evolution around the hole, non−circular hole, manufacturing defects (localized variation in specimen thickness) and misalignment of the specimen. The first visible damage is observed at 24.6 kN near the left edge of hole. With further increase in load at 25.8 kN, the damage accumulates in the same area in the form of matrix cracking and then propagates with longitudinal splitting along the fibers, tangential to the hole. This behaviour is in−line with Ref. [163]. As the load increases, next damage initiation is observed near the right edge of hole diagonally opposite to the first observed damage.

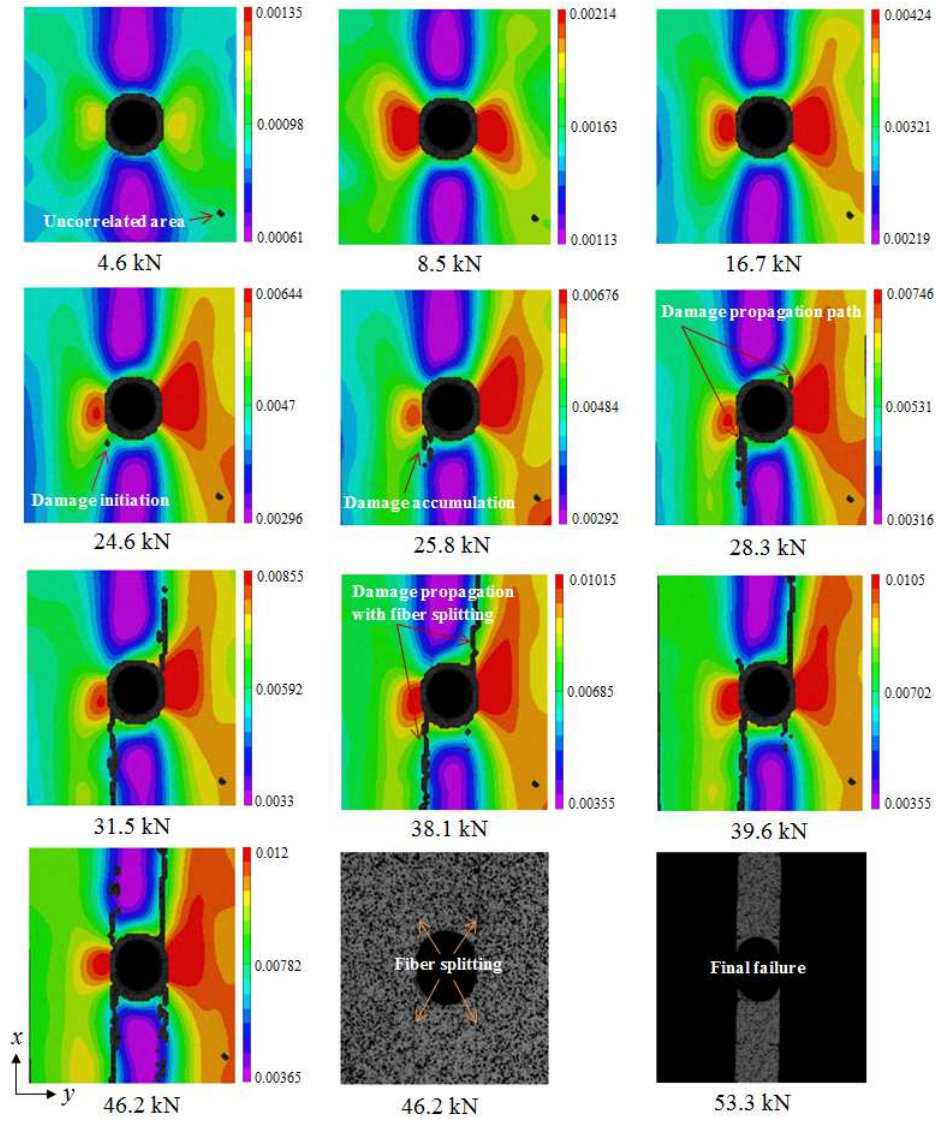

Figure 3.4: Damage development with the load for a panel with open circular cutout (ε_{xx} plot)

As test progresses, the damage accumulates around the hole and then propagates with longitudinal splitting of 0° fibers from both side of hole edge along the loading direction i.e. along $x-$axis towards the tab or loaded end. Damage zone development of panel with cutout having only 0° fibers is found to be similar to that described in Ref. [163]. Final failure of the panel involves several fracture mechanism such as matrix cracking, fiber splitting, fiber fracture and pull−out and it will be explained in sub−section 3.4.4.

3.4.2 Single sided repaired panel

The ROI for correlation is chosen as 46.2 mm × 109 mm which corresponds to 525 × 1260 pixels^2. The spatial resolution is 11.4 pixels/mm. Uncorrelated area is observed around the patch edge due to shading or sudden step. The damage progression observed in case of single sided repaired panel on patched side is shown in Fig. 3.5.

The maximum value of ε_{xx} is observed at upper and lower edge of the patch along $x-$direction (loading direction). Similar observations are made in the experimental study as described in Ref. [112, 141]. The minimum value of ε_{xx} is found at center of the patch over the hole. This indicates that the most of the load is reintroduced into the panel at the patch edge. Highly localized strain is also present at the patch edge inducing peeling effect around it and further aids in debonding of patch from the panel. As load increases to 14.6 kN, localized strain zone shifts to the upper patch edge. The localized internal damage (matrix cracking), high peeling and shear strain due to non−uniform thickness of adhesive could be the reasons for strain zone shifting. The first visible damage is observed at a load of 22.3 kN near upper edge of the patch. It can be seen from the figure that the localized debonding of patch from the panel is initiated around the highly strained zone at the upper patch edge. This indicates that the adhesive layer is subjected to high shear strain around the upper overlap region and it causes the debonding of the patch. With further increase in the load, debonding area of patch increases around the upper edge of the patch. As test proceeds, longitudinal splitting of 0° fibers is also observed parallel to loading direction ($x-$axis) towards tab, similar to the open cutout panel. The longitudinal splitting of the fibers increases with increasing load on either side of patch and patch debonds from the panel at a load of 63.43 kN.

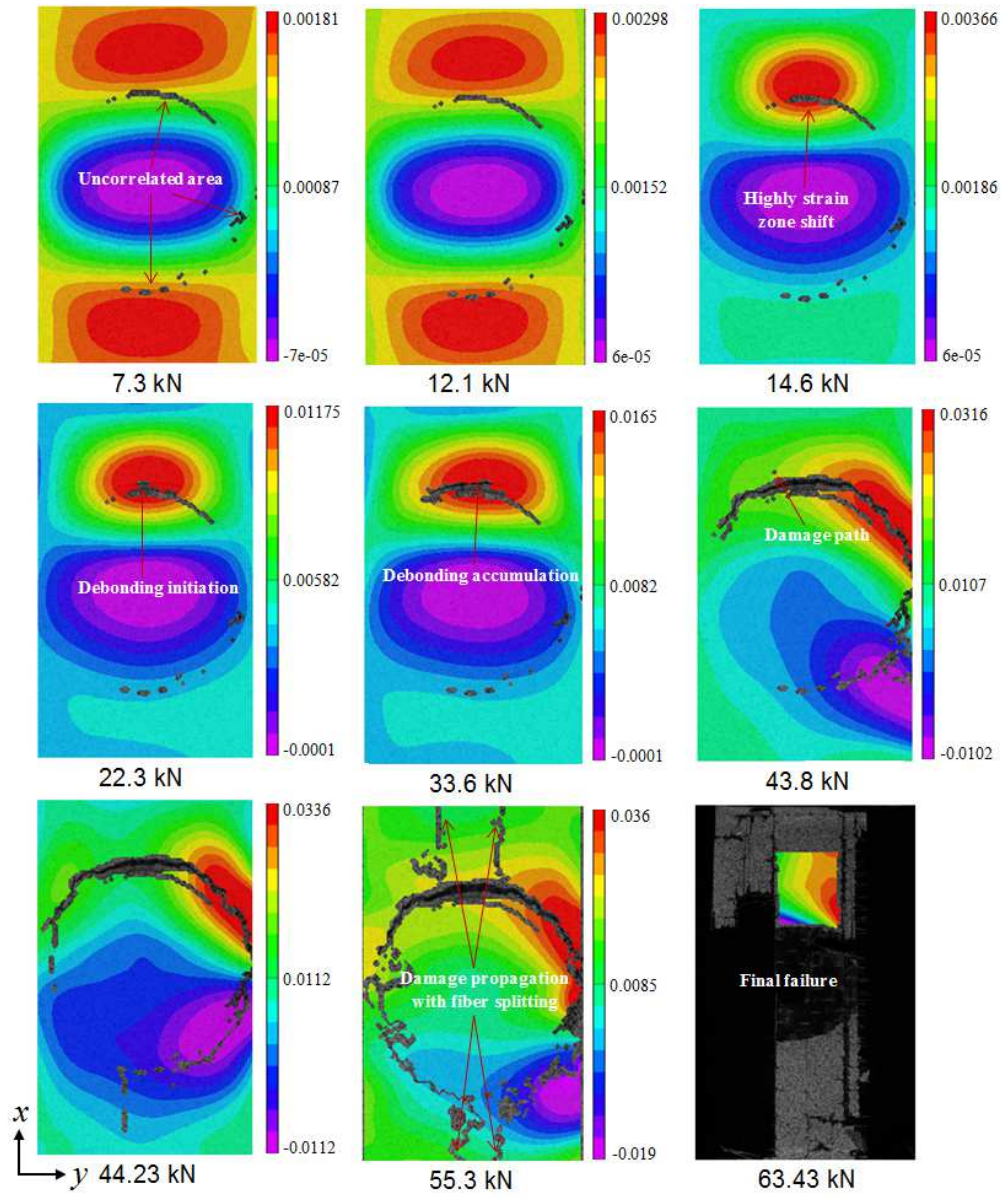

Figure 3.5: Damage evolution with the load in case of single sided repaired panel (patch side− ε_{xx} plot)

Figure 3.6 shows the progress of damage in single sided repair on unpatched side for different loads. It can be observed that the longitudinal strain (ε_{xx}) distribution on unpatched side is similar to that observed in open cutout panel.

The unpatched side of single sided repair reveals that the damage development is first initiated with partial patch debonding and then propagated with longitudinal splitting of the fibers at 30.47 kN. After patch debonding, final failure of the panel involves several fracture mechanism such as matrix cracking, debonding, fiber splitting, fiber fracture and pull−out and will be explained in further sub−section 3.4.4.

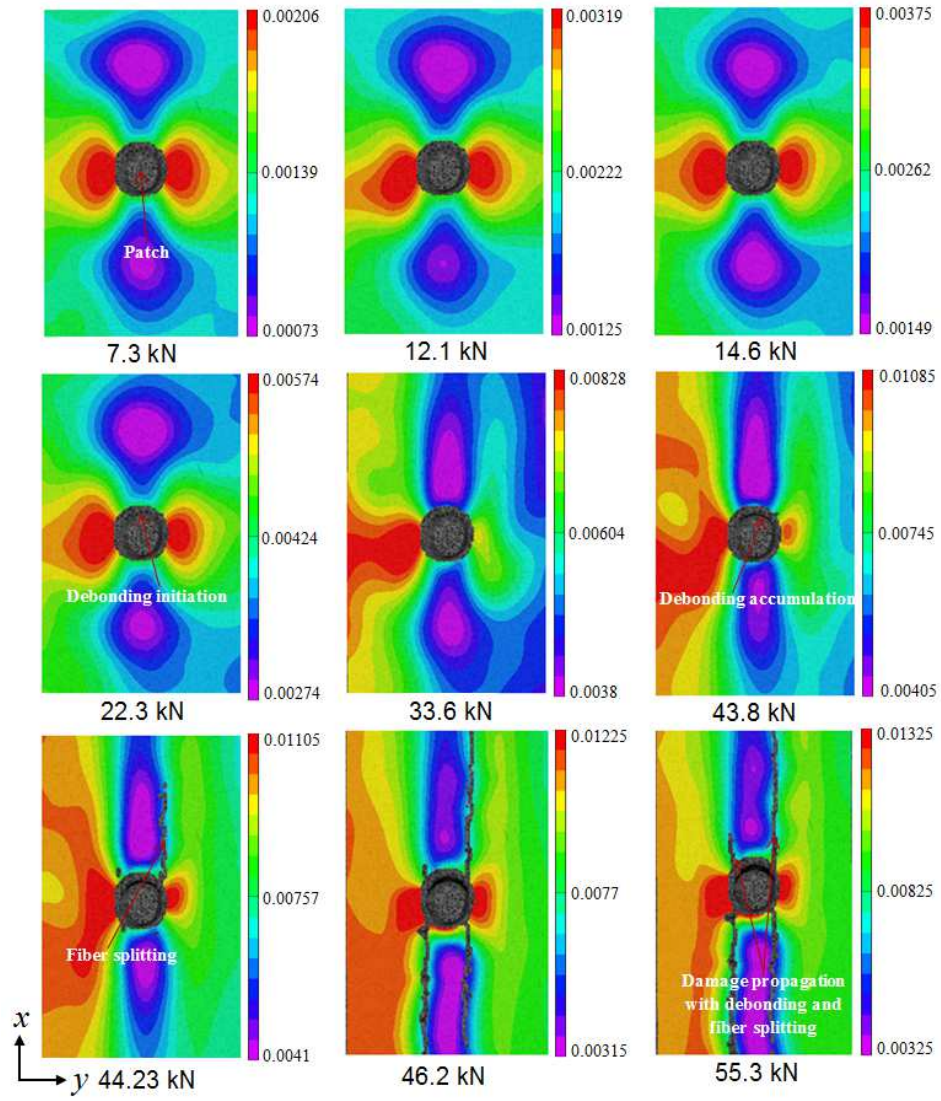

Figure 3.6: Damage evolution with the load in case of single sided repaired panel (unpatched side− ε_{xx} plot)

3.4.3 Double sided repaired panel

The ROI for correlation is chosen as 46.2 mm × 122.5 mm which corresponds to 530 × 1410 pixels^2. The spatial resolution is 11.4 pixels/mm. The damage progression observed in case of double sided repaired panel is shown in Fig. 3.7.

It is very much visible from different figures that the ε_{xx} distribution as well as damage development is not perfectly symmetrical about the $y-$axis. The reason to this can be attributed to the factors as explained earlier in sub−section 3.4.1. It can be observed from the figure that the high strained zone is present at the upper and lower edge of the patch similar to that of single sided repair. As the load increases the high strained zone gets shifted to the lower edge of the patch at 16.2 kN. The first visible damage is observed at the lower edge of the patch and it accumulates around there with increasing load.

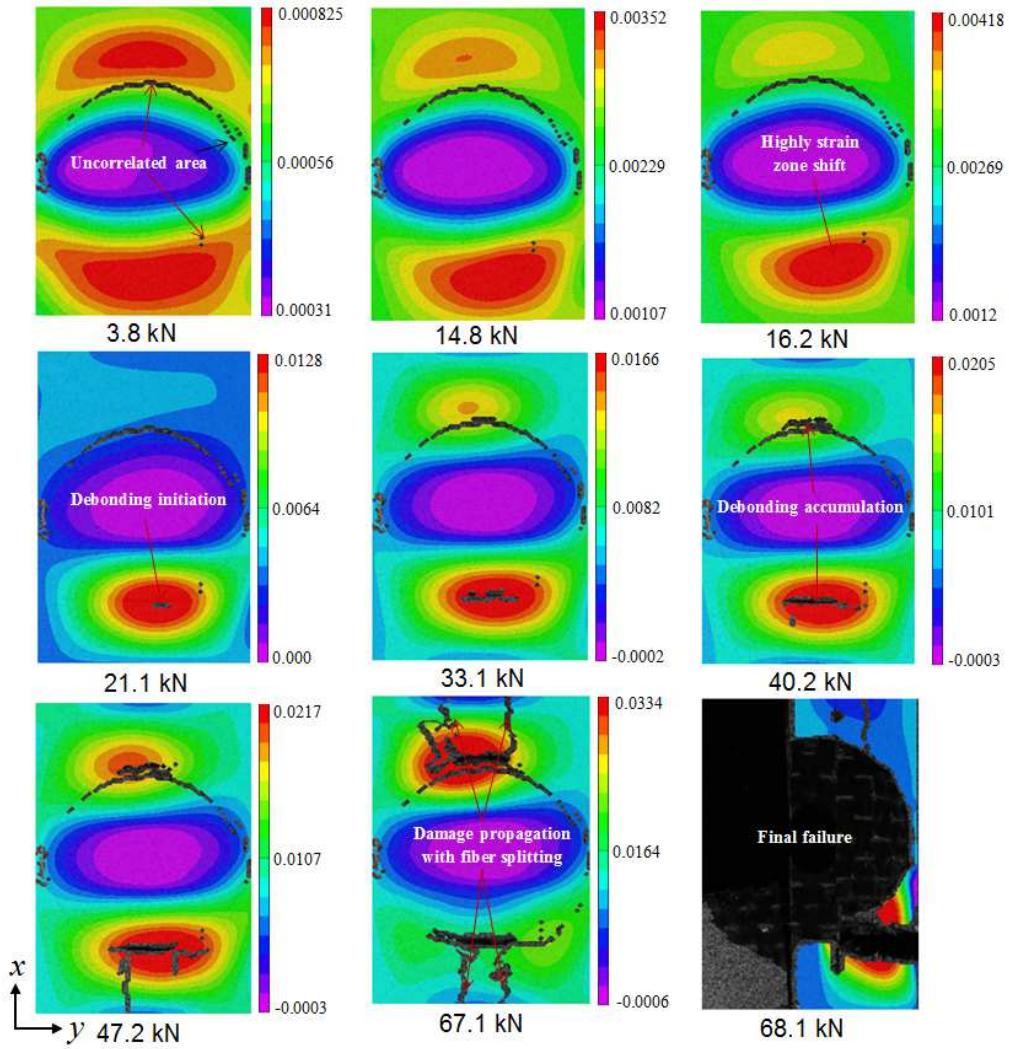

Figure 3.7: Damage evolution with the load in double sided repaired panel (ε_{xx} plot)

It can be seen from the figure that patch debonding initiates at lower patch edge and then shifts to upper edge with increasing load. With further increase of load, the debonding area increases on either side of the patch (in longitudinal direction) unlike single sided repair. As the load increases, longitudinal splitting of 0° fibers is observed around the patch edge propagating longitudinally towards the tab. Complete debonding of the patch takes place at a load of 68.1 kN and final failure mechanism in panel is found to be similar to that of single sided repaired panel as will be explained in next sub−section.

3.4.4 Failure mechanism

The failure modes observed in open cutout panel as well as single and double sided patch repaired panel are shown in Fig. 3.8. It can be observed from figure that the various failure modes dominant in open cutout and repaired panel is characterized by matrix cracking, fiber splitting and fiber fracture. Longitudinal splitting initiates from highly strained zone around the transverse edge of the hole. The final failure of open cutout panel involves a large extent of fiber fracture at various locations in the panel. This is due to the fact that the fibers held by the matrix could not sustain the load being applied on them and transferred through the matrix. Because of weak interfacial bonds between fiber/matrix they fail by rupture due to highly localized stress. It is clear from the figure that the failure mechanisms in single and double sided repair are similar to open cutout specimen. In the repaired panel, debonding of the patch is initiated from the overlap region at the patch edge due to the failure of the adhesive layer in this zone. When the patch is partially debonded from the panel fiber splitting is observed in repaired panel similar to that of open cutout one. The final failure of the repaired panel takes place with complete debonding of the patch followed by the localized fiber fracture failure mode. It can be observed that the patches remain intact with adhesive layer attached to them. The reason to this kind of failure mode can be attributed to the use of strong patch or poor bonding quality [141].

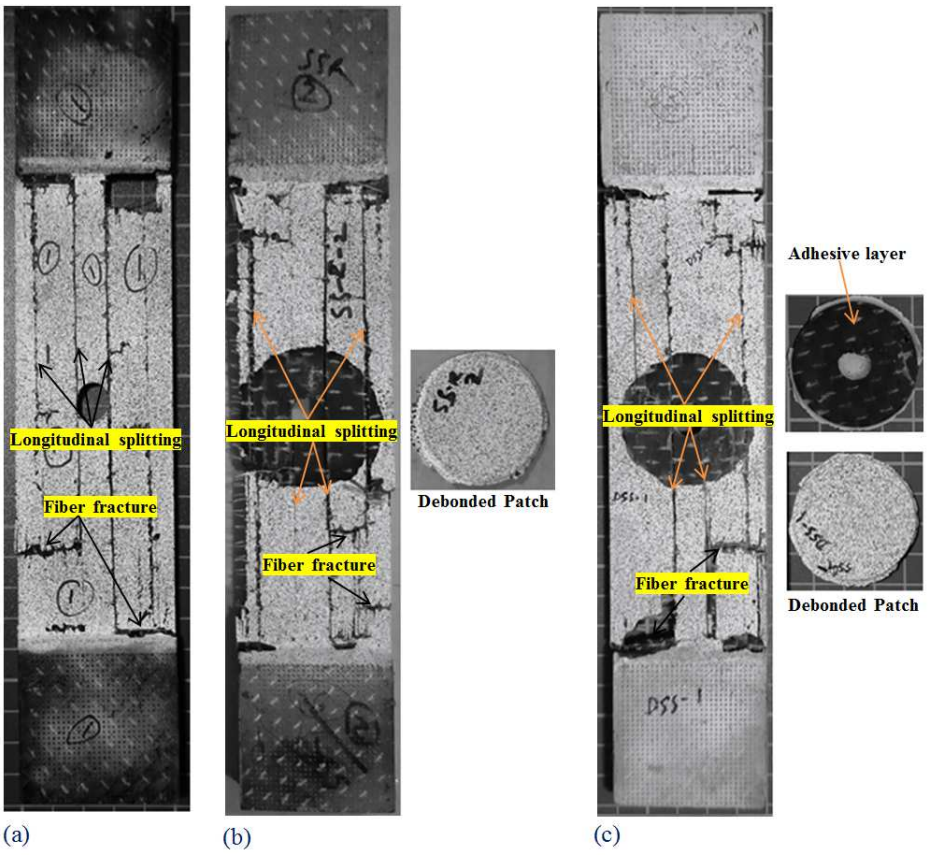

Figure 3.8: Failure mechanism (a) open cutout panel (b) single sided repaired panel (c) double sided repaired panel

3.4.5 Experimental performance of open cutout and repaired panels

The performance of open cutout and repaired panels are analyzed based on longitudinal strain variation and tensile strength and they are discussed in the following sub−sections.

Variation of longitudinal strain (ε_{xx})

The performance of the repaired structure and contribution made by the patches ares also investigated using the strain field data obtained from DIC technique. The variation of longitudinal strain (ε_{xx}) for open cutout and repaired panels are plotted with respect to applied load as shown in Fig. 3.9. It can be observed that the reduction in strain due to single sided repair at initial load is relatively good but at higher loads not much reduction is there and is very much comparable to strain values of the open cutout specimen. However, it is clear from the figure that the reduction in strain due to double sided repair is very significant as compared to single sided repair. The average reduction in strain magnitude for the case of single and double sided repair is 8% and 17% respectively. Therefore, double sided repair specimen performs better than single sided repair.

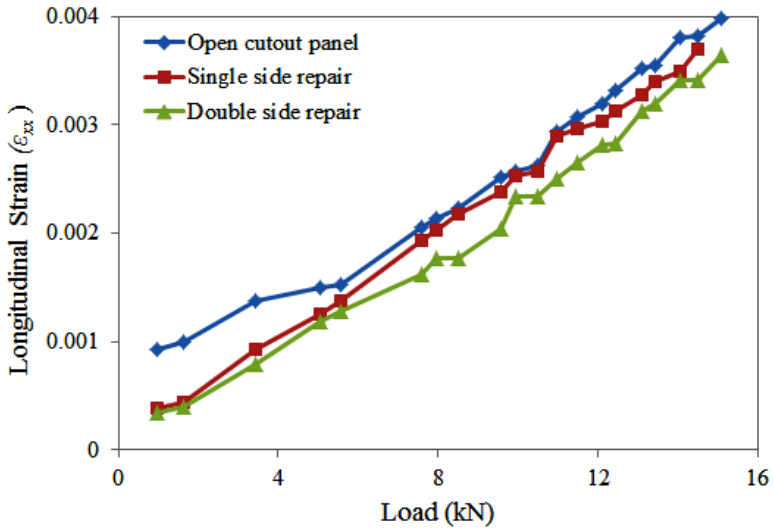

Figure 3.9: Variation of longitudinal strain (ε_{xx}) with respect to applied load

Strength of open cutout and repaired panel

To compare the strength of the damaged and repaired structure experimentally obtained load displacement curve for all the three cases are plotted in Fig. 3.10. It can be observed that the behavior of damaged and repaired panel is almost same till final failure. But there is a slight variation in the slope for the three specimens and it is due to differing stiffness. The sudden drop in load or kink in load displacement curve just before the ultimate load point in case of repaired panels represents the excessive patch debonding at the patch overlap edge.

The ultimate load taken by the virgin (without damage) panel, open cutout and repaired panels obtained from three independent measurements together with mean, standard deviation (Std. Dev.) and coefficient of variation (CV) is summarized in Table 3.2.

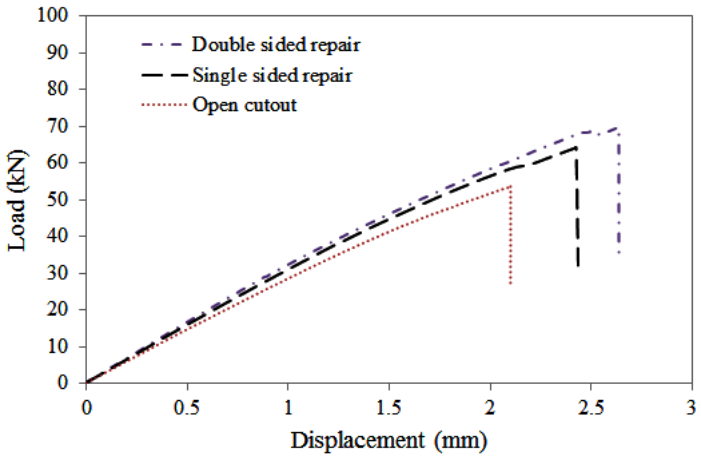

Figure 3.10: Load−displacement curve for open cutout and repaired panels obtained from experiment: pure UD configuration

The ultimate load in case of virgin panel varies between 78.65 and 82.84 kN with an average of 80.35 kN, and the coefficient of variation (CV) is 2.74%. Similarly, the CV for open cutout, single and double sided repaired panel is 3.03%, 3.12% and 2.08% respectively, which ensures the repeatability of the experimental data. It is also evident from the table that, once the damage is introduced in the virgin panel, the ultimate load value of virgin panel is reduced by 35%. The tensile strength of the specimen is estimated as failure load upon gross cross−sectional area of the specimens. On that ground, for damaged panel it is 594.12 MPa whereas for single and double sided repaired panel it is 704.65 MPa and 755.94 MPa respectively. Single sided repair restores 78.08% of virgin panel strength whereas double sided repair restores 85.43%. Therefore, double sided repair specimen has got 7.35% higher strength as compared to single sided repaired panel.

Table 3.2: Ultimate tensile strength of virgin, open cutout and repaired panels: pure UD configuration.

	Load (kN)			
Specimen #	Virgin panel	Open cutout	Single sided	Double sided
1	78.65	53.47	63.41	68.03
2	82.84	51.23	64.26	67.54
3	79.56	54.35	60.52	70.23
Mean	80.35	53.01	62.73	68.6
Std. Dev.	2.20	1.60	1.96	1.43
CV (%)	2.74	3.03	3.12	2.08
Restoration(%)	–	–	78.08	85.43

3.5 Finite element modeling and analysis results: pure UD panel $[0^\circ]_4$

A linear static 3−D finite element analysis of open cutout and repaired panel is carried out using ANSYS−13 software. The geometry and dimensions of the panel and patch are kept as same as that of experimental model as shown in Fig. 3.1. The FE model of open cutout and repaired panel is done using the same procedure as discussed in section 2.10.1. The mesh size in the present work is chosen based on the mesh dependence study. The maximum longitudinal stress (σ_{xx}) and number of elements along circumference of the hole is considered for mesh convergence study as zone around the hole periphery is subjected to high stress concentration. Fig. 3.11 shows the variation of maximum longitudinal stress with respect to number of elements along the circumference of hole. The number of elements around the hole ranges from 16 to 192. It can be observed from the figure that the magnitude of longitudinal stress steadily decreases with increasing number of elements along hole periphery. After 96 elements there is no significant change in the magnitude of σ_{xx} which implies the convergence of σ_{xx}. Hence, 96 elements around the hole periphery is considered for in the present analysis.

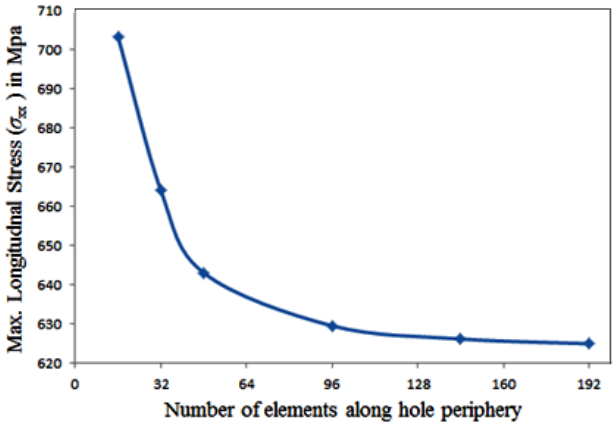

Figure 3.11: Maximum longitudinal stress versus number of elements along the hole periphery: mesh sensitivity analysis

The patch is bonded to the panel above the hole using Araldite 2011 adhesive material. The thickness of the adhesive is taken as 0.185 mm. Multi point constraint (MPC) algorithm is employed for ensuring a perfect bonding between patch/panel and panel/adhesive. In MPC algorithm, all the three degrees of freedom (dof) are constrained. The MPC algorithm involves contact and target surfaces which come into contact with one another. MPC internally adds constraint equations to tie the dof's of the corresponding nodes between contacting surfaces such that no relative displacement exists between nodes and surfaces. It is a direct, efficient way of bonding surfaces at interfaces [155].

The elastic modulus and Poisson's ratio of adhesive are 1.148 GPa and 0.4 respectively, taken from the manufacturer's data sheet [164]. The elastic properties of CFRP laminate used here are evaluated using DIC measurement and they are given in Table 2.9. Fibers in the panel and patch are aligned parallel to the loading direction. The panel is fixed at bottom face and an in−plane tensile load of 8.512 kN (94.57 MPa)is applied at the top face along $x-$direction so as to simulate the experimental boundary conditions. The results obtained from FEA are compared with the experimental data for the same load (8.512 kN). A lower load level is chosen as the damage would not have initiated. Both qualitative and quantitative comparison of strain is done between experiment and FEA model. Contour plots and line plots of elastic strains are used for the comparison between experimental and finite element data. The scales of FEA model contour plots are kept same as that of DIC plots for the direct comparison. The gray areas on the plot indicates the over saturation of scales. Finite element model (zoomed up view) of the damaged and repaired panel is shown in the Fig. 3.12.

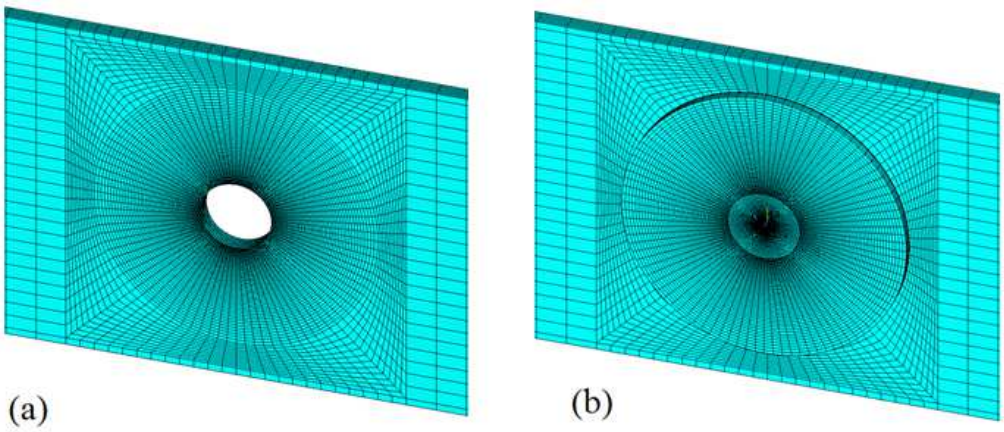

Figure 3.12: Finite element model (a) damaged panel (b) repaired panel

3.5.1 Panel with open cutout

The contour plots of strains ε_{xx}, ε_{yy} and ε_{xy} obtained from FEA and DIC are shown in Fig. 3.13 for qualitative comparison. The FEA plots are shown with adjusted scale (ADS) as well as actual scale (AS).Considering the variation of longitudinal strain ε_{xx} as shown in Fig. 3.13 (a), (b) and (c), it is clear from the qualitative comparison of both DIC and FEA contour plots that both the plots possess highly strained zone around the transverse edge of the hole and low strained zone around the longitudinal edge of the hole parallel to loading direction ($x-$axis). It can also be observed from the full scale FEA plot of elastic strain (ε_{xx}) that the magnitude of strain is very high near the transverse edge of the hole as compared to that obtained from DIC. The reason to this can be attributed to the fact that the correlation cannot be achieved exactly at the peak edge of the hole.

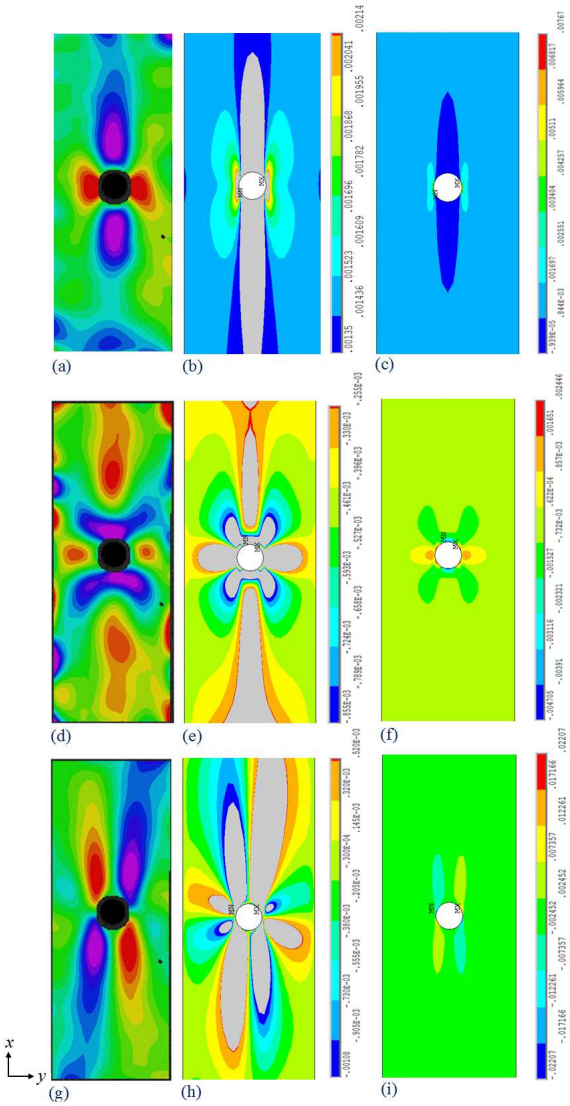

Figure 3.13: Comparison of whole field strain contour obtained from DIC and FEA for the open cutout panel (a) DIC (ε_{xx}) (b) FEA (ADS)$-$ (ε_{xx}) (c) FEA (AS)$-$ (ε_{xx}) (d) DIC (ε_{yy}) (e) FEA (ADS)$-$ (ε_{yy}) (f) FEA (AS)$-$ (ε_{yy}) (g) DIC (ε_{xy}) (h) FEA (ADS)$-$ (ε_{xy}) (i) FEA (AS)$-$ (ε_{xy}) (ADS $-$ Adjusted scale to match with DIC scale, AS $-$ Actual scale of FEA plot)

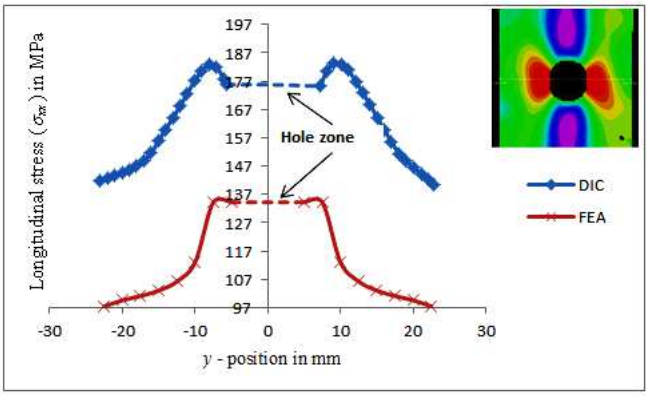

Figure 3.14: Longitudinal stress variation (σ_{xx}) in a open cutout panel at an applied of 8.512 kN: FEA vs. DIC

Figure. 3.14 shows the variation of longitudinal stress (σ_{xx}) along the net/center section of the notched specimen obtained from FEA and measured strain field from DIC. The longitudinal stress (σ_{xx}) around the hole can be calculated from the strain field (ε_{xx}) and (ε_{yy}) obtained from DIC using following Eq. (3.1) [73]. The range of data points collected from FEA model is kept same as that of DIC plot. It can be observed from figure that besides the difference in magnitude, the variation of σ_{xx} obtained from FEA and DIC technique has a similar trend and shows relatively a good agreement.

$$\sigma_{xx} = \frac{E_{11}\,\varepsilon_{xx}}{\left[1-\nu_{12}^2\left(\frac{E_{22}}{E_{11}}\right)\right]} + \frac{\nu_{12}\,E_{22}\,\varepsilon_{yy}}{\left[1-\nu_{12}^2\left(\frac{E_{22}}{E_{11}}\right)\right]} \tag{3.1}$$

The contour plot of strain ε_{yy} obtained from FEA and DIC is compared in Fig. 3.13 (d),(e) and (f). Although the strain magnitude predicted by the FEA model is higher than the experimental one, similarities exist between the contour plots of experimental and numerical model. The contour plot of shear strain ε_{xy} obtained from FEA and DIC is compared in Fig. 3.13 (g), (h) and (i). It can be observed from experimental plot that there is negative shear zone present diagonally at the upper right edge of the hole just adjacent to the high positive shear zone. However, contour plot from FEA is similar to that from DIC, but reverse in nature. The negative shear strain in DIC has become positive shear strain and vice−versa. These observations are found to be similar to that described in Ref. [112].

3.5.2 Single sided repaired panel

Comparison of contour plots of ε_{xx}, ε_{yy} and ε_{xy} for the single sided repaired panel obtained from FEA and DIC are shown in Fig. 3.15.

The FEA plots are shown only with the adjusted scale (AS). The experimental plot of strain ε_{xx} as shown in Fig. 3.15 (a), possess highly strained zone around the upper patch edge. However, contour plot from FEA shows highly strained zone around the hole edge. The magnitude of strain at patch edge predicted by FEA is just 24% lower than the experimental value. The experimental and numerical contour plot of ε_{yy} as shown in Fig. 3.15 (c) and (d) have a good agreement. Generally,

center of the patch is lowly strained. However it is difficult to determine the exact magnitude due to the over−saturation of FEA plot but it shows a moderately high strained zone at patch edge. The contour plot of ε_{xy} obtained from FEA and DIC is shown in Fig. 3.15 (e) and (f). A similar trend exists between DIC and FEA plots, but they are reverse in nature as explained earlier.

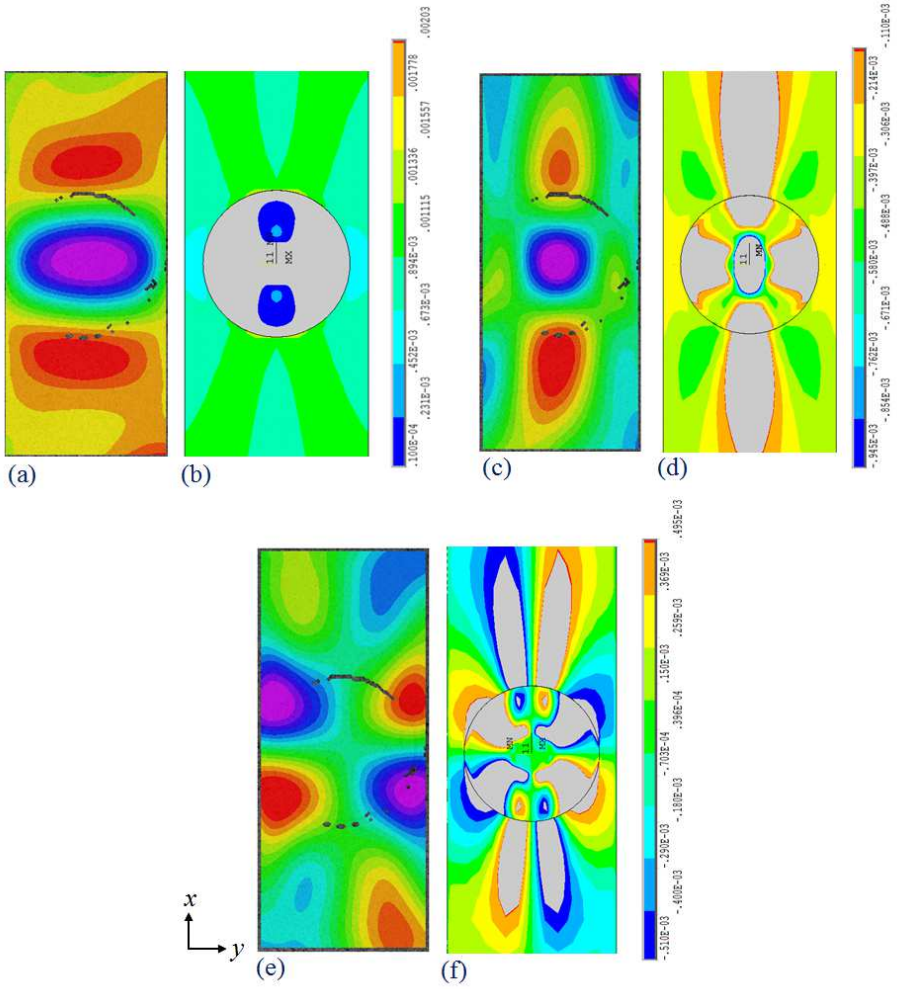

Figure 3.15: Comparison of whole field strain contour obtained from DIC and FEA for single sided repair panel (a) DIC (ε_{xx}) (b) FEA (ADS)− (ε_{xx}) (c) DIC (ε_{yy}) (d) FEA (ADS)− (ε_{yy}) (e) DIC (ε_{xy}) (f) FEA (ADS)− (ε_{xy}) (ADS − Adjusted scale to match with DIC scale)

3.5.3 Double sided repaired panel

Contour plots of ε_{xx}, ε_{yy} and ε_{xy} for double sided repaired panel obtained from FEA and DIC are shown in Fig. 3.16. The contour plot of ε_{xx} (see Fig. 3.16 (a)) is similar to that of single sided repaired panel. Highly strain zone in experimental plot appears at the patch edge, but in FEA plot they appear around the hole edge. The strain magnitude predicted at the patch edge by FEA is 15% lower than the experimental value. On close observation of Fig. 3.16 (c) shows highly strained zone is at the center of patch. The ε_{xy} contour plot too shows same trend as observed in previous section.

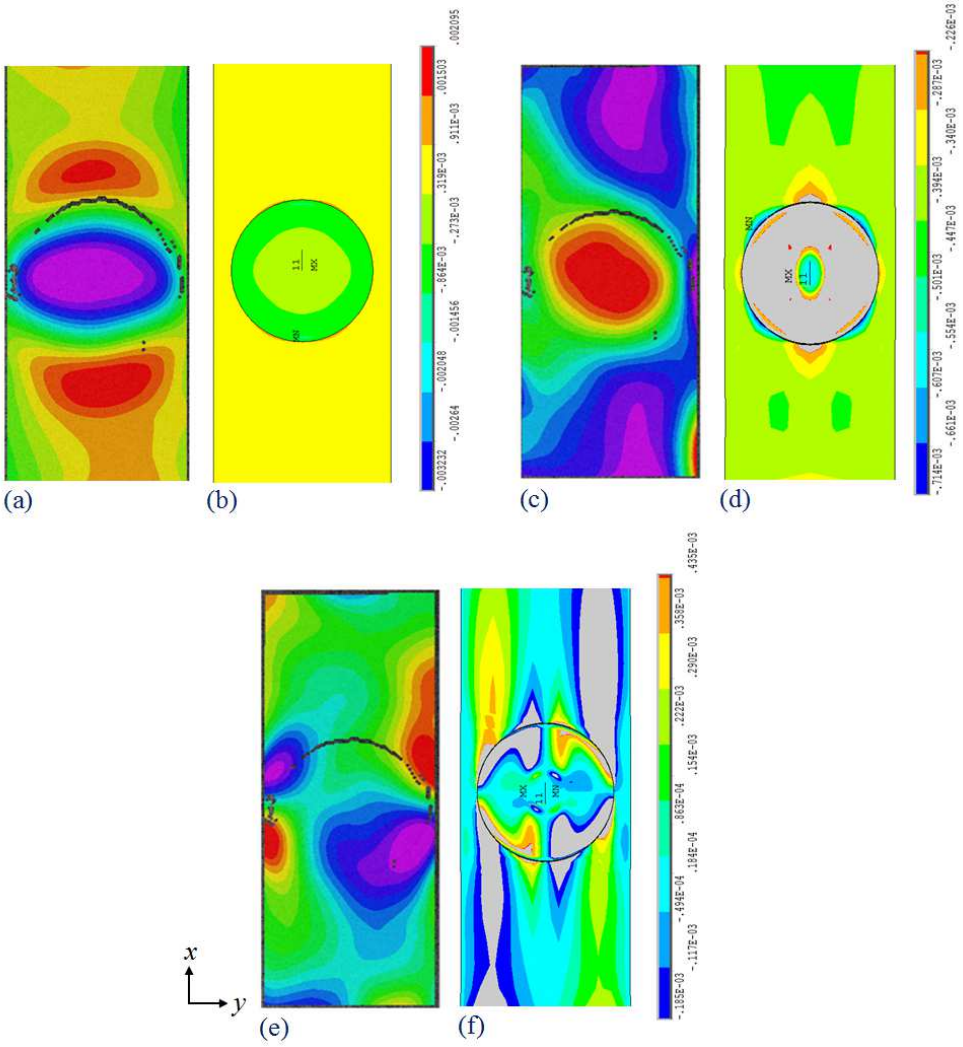

Figure 3.16: Comparison of whole field strain contour obtained from DIC and FEA for double sided repair panel (a) DIC (ε_{xx}) (b) FEA (ADS)− (ε_{xx}) (c) DIC (ε_{yy}) (d) FEA (ADS)− (ε_{yy}) (e) DIC (ε_{xy}) (f) FEA (ADS)− (ε_{xy}) (ADS − Adjusted scale to match with DIC scale)

3.5.4 Strain variation in panel, patch and adhesive

In case of repair specimen, two zone of stress concentration are present. One at the periphery of hole and other at the panel surface at patch over edge. The stress variation in panel, patch and adhesive layer in repaired configuration obtained from FEA at a applied load of 8.512 kN (94.57 MPa) are shown in the Fig. 3.17, so as to identify critical strain/ stress locations.

It can be clearly observed from figure that a high strain/stress location in the panel appears right at the transvers edge of the hole as well as at the longitudinal overlap region. It shows a good agreement with the experimental observation. The longitudinal strain (ε_{xx}) in the patch is higher at the hole edge (upper zone) whereas the peel strain (ε_{zz}) in the patch is found to be higher at the longitudinal patch edge along the loading direction ($x-$axis).

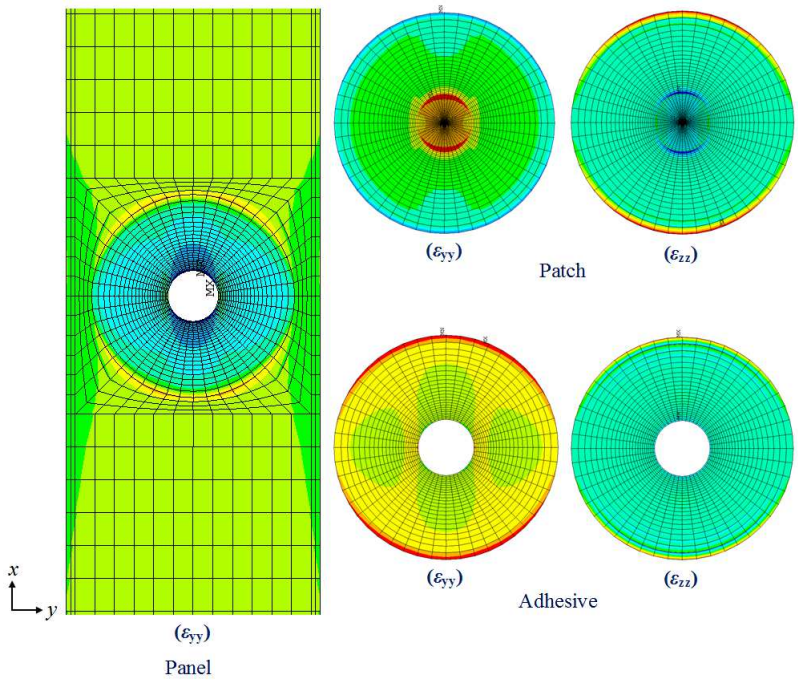

Figure 3.17: Strain variation in the panel, patch and adhesive at a load of 8.512 kN

However, in the adhesive layer both longitudinal strain (ε_{xx}) and peel strain (ε_{zz}) appears to be higher at the longitudinal edge of the adhesive around the upper overlap region.The presence of high peel strain at the overlap edge generally causes debonding of the patch from the panel [141].

3.6 Experimental results: quasi−isotropic panel $[\pm 45/0/90]_s$

Experimental results from tensile test of open cutout, single and double sided repaired quasi−isotropic panel obtained using DIC is presented in this section.

3.6.1 Panel with open cutout

To study the whole field strain distribution using DIC, an area of size 46.8 mm x 134 mm around the hole is selected as region of interest. A subset size 27 x 27 pixels^2 is chosen along with a grid step size of 7 pixels for post−image DIC analysis. Fig. 3.18 shows the whole field strain distribution over damaged panel at different load levels. It can be observed from figure that the ε_{xx} distribution is not perfectly symmetrical about central axis. The asymmetry in the strain distribution is mainly due to asymmetrical damage accumulation around the hole because of 45° surface ply. The damage development in circular cutout panel starts with 90° matrix cracking from the highly strained zone at the hole boundary as well as matrix crack in 45° surface ply across the width of specimen. The final failure in circular cutout panel involves 0° fiber splitting along with local delamination and fiber pullout. The final failure is at load of 32.57 kN and it is very sudden and it corresponds to a strength of 271.42 MPa. The corresponding tensile strength of the virgin panel measured at an equivalent displacement rate is 437.5 MPa (52.5 kN). The reduction in tensile strength due to circular cutout in panel is 38.74%.

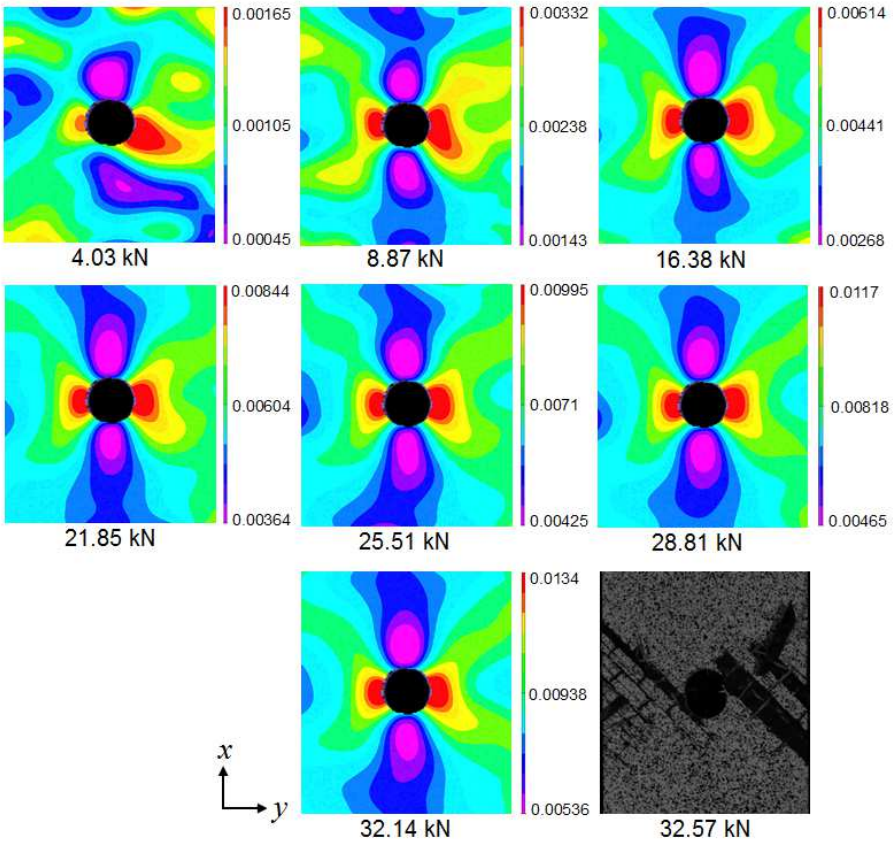

Figure 3.18: Whole field strain (ε_{xx}) distribution of a circular cutout panel under tensile load

3.6.2 Single sided repair panel

The circular cutout panel of stacking sequence $[\pm 45/0/90]_s$ repaired with single sided patch having layup $[\pm 45°]_s$ subjected to uni−axial tensile load is analyzed here. Uncorrelated region is observed around the patch edge due to shading and sudden change in depth between patches and panel planes. Fig. 3.19 shows the whole field strain distribution (ε_{xx}) over single sided repair panel at different load levels. From the figure, one can observe that the maximum strain value is at upper and lower edge of the patch along loading direction. The strain field predicted by DIC for the single sided repair panel under tensile loading is similar to that described by Caminero et al. [141]. Highly localized strain at the patch edge induces the skin damage to the panel as well as initiates the patch debonding due to peeling effect. As load increases, localized strain zone shifts towards the upper patch edge and patch debonding initiates from this zone. The patch debonding occurs at a load of 35.50 kN corresponding to 295.83 MPa. After patch debonding, final failure of the panel involves complex fracture mechanism involving matrix cracking, delamination and fiber fracture.

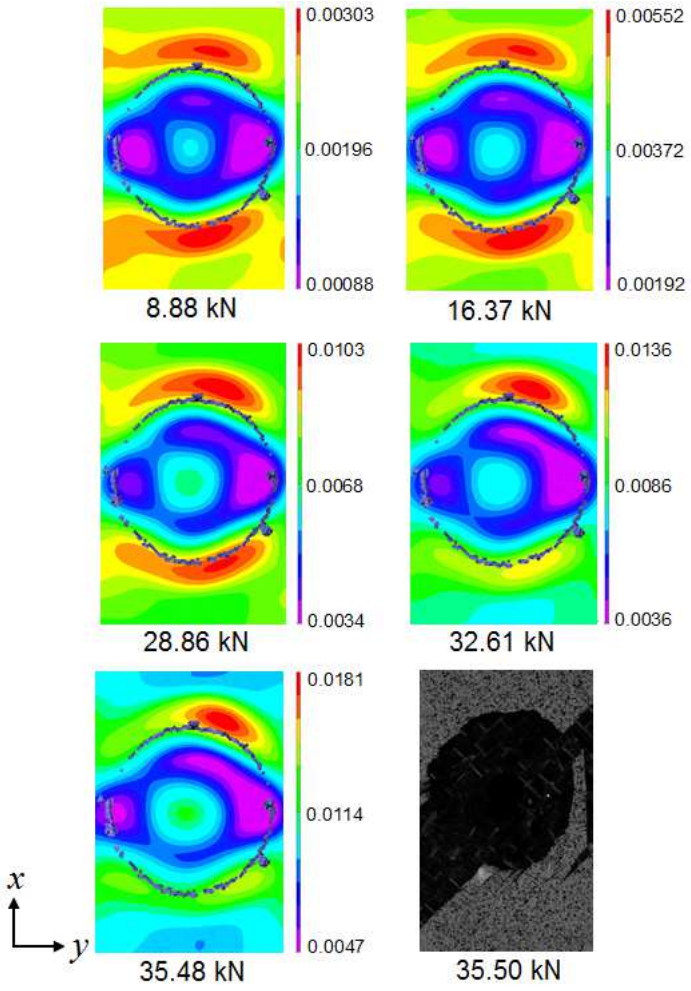

Figure 3.19: Whole field strain (ε_{xx}) distribution of a single sided repair panel under tensile load

3.6.3 Double sided repair panel

The circular cutout panel of stacking sequence $[\pm 45/0/90]_s$ repaired with double sided patch having layup $[\pm 45°]_s$ subjected to uni−axial tensile load is analyzed using DIC to assess the damage till final failure. Fig. 3.20 shows the whole field strain distribution (ε_{xx}) over double sided repair panel at different load levels. From the figure, one can observe that maximum strain value (ε_{xx}) is at upper and lower edge of the patch along $x-$direction and at center of the patch over the hole at a load value of 8.9 kN. As the load increases high strain zone gets shifted to the upper edge of the patch. It can be seen from the figure that damage initiates from the highly strained zone at the upper edge of the patch. Complete failure of double sided repair panel happens at a load of 42.23 kN corresponding to 351.92 MPa. Patches are completely separated from the panel at final failure. The damage mechanism for the double sided repair panel is very similar to that described by Pencheng et al. [82]. Final failure of the panel predominantly involves matrix cracking and delamination from both transverse sides of the hole.

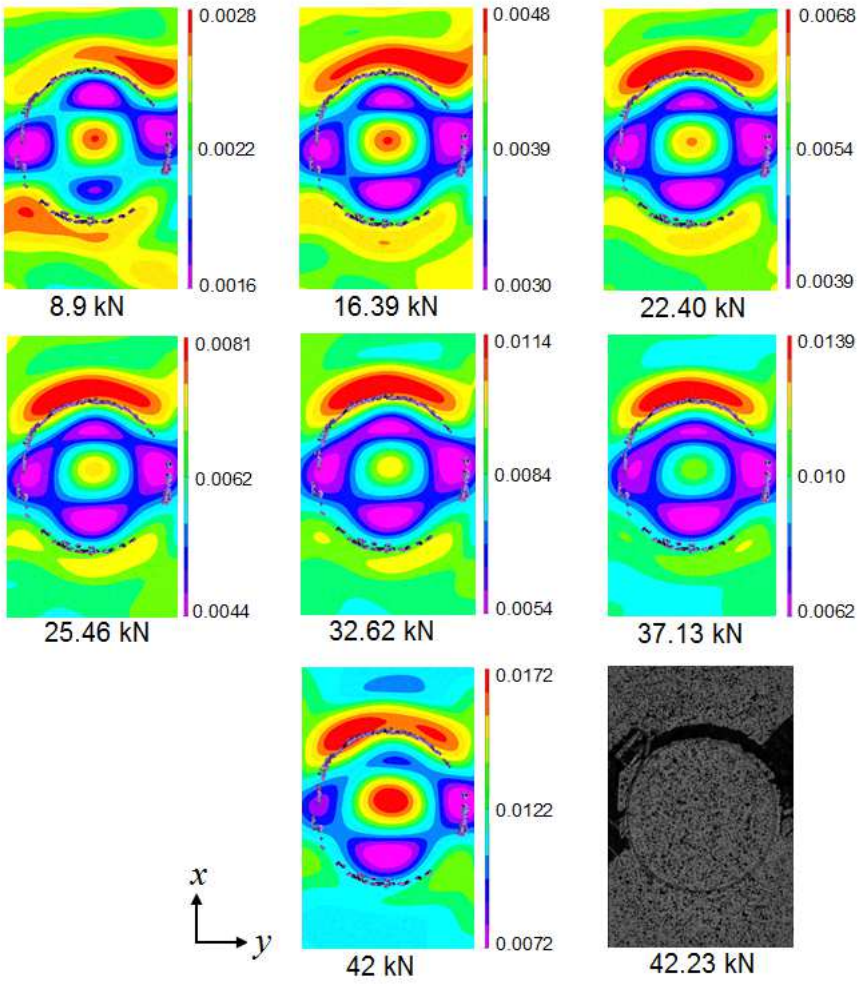

Figure 3.20: Whole field strain (ε_{xx}) distribution of a double sided repair panel under tensile load

3.6.4 Failure mechanism of open cutout and repaired panel

The final failure mechanism observed in open cutout and repaired panel (single and double sided repair) is shown in Fig. 3.21. It can be confirmed that various failure modes are present in open cutout and repaired panel such as matrix cracking, fiber splitting and fiber fracture etc. Both 90° and 45° matrix cracking initiate from highly strained zone around the transverse edge of the hole. It is evident from the figure that the failure mechanism in single and double sided repair is similar to open cutout panel. In single sided repair panel, debonding of the patch initiates from the overlap edge of patch due to adhesive layer breakdown at this zone due to high peel stress development. This is because of additional bending stress coming in the case of single sided repair. The final failure of single sided repair panel takes place with complete debonding of patch from parent panel followed by panel failure identical to that of open cutout panel. In double sided repair panel, failure gets initiated from transverse edges of the hole in the parent panel and partially detaching of patches from the top overlap edge. It happens as the damage accumulates at the transverse edge of the hole and then propagates across the panel. The final failure of double sided panel takes place with complete patch debonding.

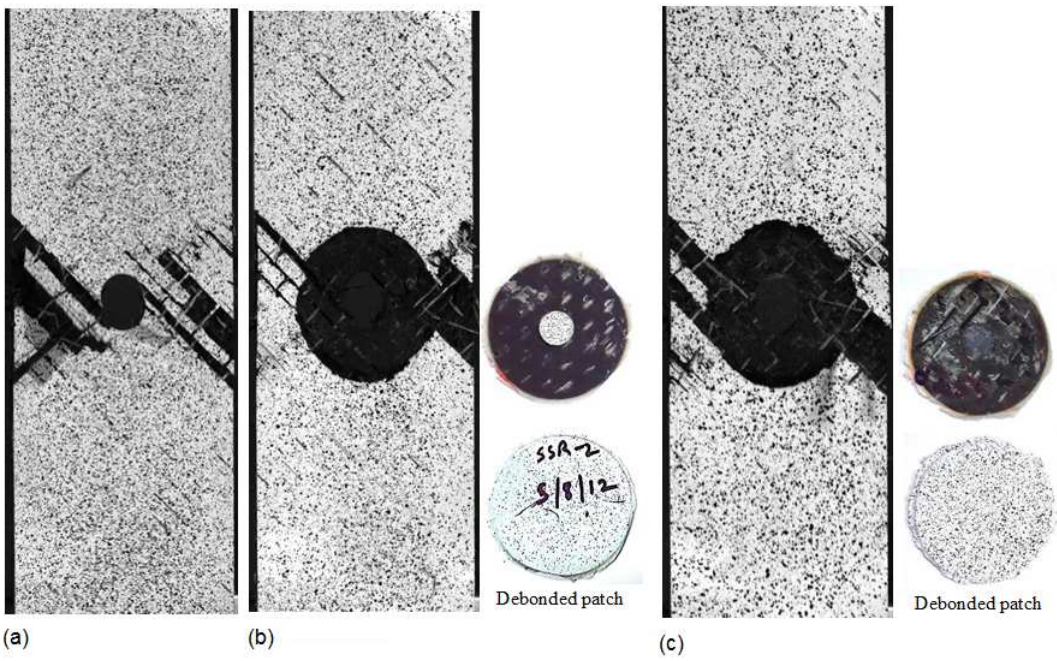

Figure 3.21: Failure mechanism in $[\pm 45/0/90]_s$ panel under tensile load (a) open cutout panel (b) single sided repaired panel (c) double sided repaired panel

3.7 Finite element modeling and analysis results: quasi−isotropic panel $[\pm 45/0/90]_s$

The finite element modeling of quasi−isotropic panel is similar to pure UD panel as discussed earlier. The whole field strain distribution obtained from 3D finite element analysis of quasi−isotropic open

cutout and repaired panel is compared with the results obtained from the DIC. Both qualitative and quantitative strain comparison is done between DIC and FEA result.

3.7.1 Panel with open cutout

The full−field strains on the specimen surface (+45° ply) corresponding to a load of 10 kN (83.33 MPa) predicted from DIC and FEA are compared in Fig. 3.22. For the illustrative purpose, the FEA plots are shown with adjusted scale similar to DIC. Looking at the strain plot, it is clear that the normal strain field (ε_{xx}) obtained from FEA is consistent with those from DIC experiment. Also the magnitude of strain is very high near the transverse edge of the hole (zone A) similar to that of DIC result. The contour plot of shear strain ε_{xy} obtained from both DIC and FEA is compared in Fig. 3.22 (d)−(f). There exists a good correlation between DIC and FEA results.

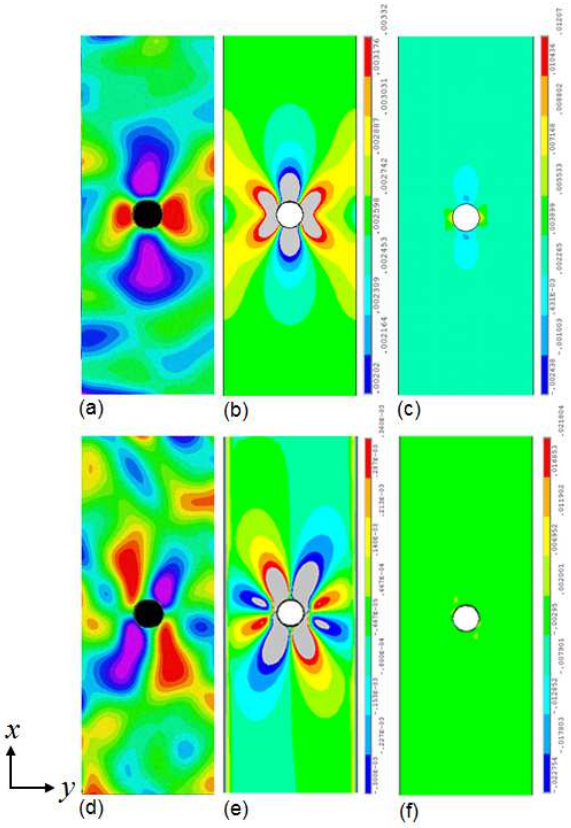

Figure 3.22: Comparison of whole field strain contour obtained from DIC and FEA for open cutout panel under tensile load of 10 kN (a) DIC (b) FEA (ADS) (c) FEA (AS) − ε_{xx} plot (d) DIC (e) FEA (ADS) (f) FEA (AS) − ε_{xy} plot (ADS − adjusted scale of FEA with DIC scale, AS − Actual scale of FEA plot)

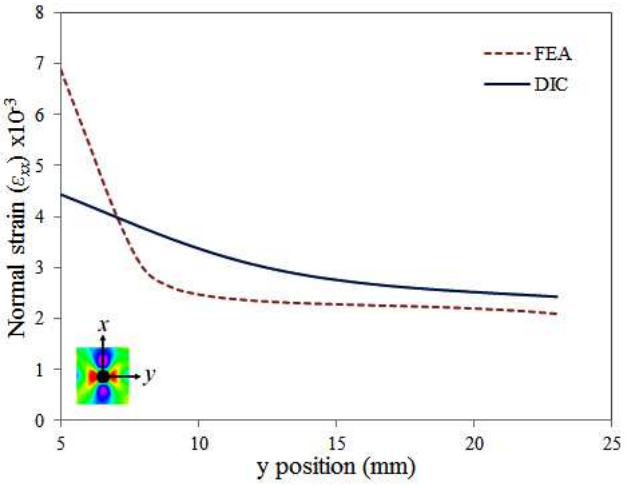

Figure 3.23: Comparative line plot of ε_{xx} between DIC and FEA along the net−section of open cutout panel

Figure 3.23 shows the variation of ε_{xx} value on the surface (+45° ply) obtained from both DIC and FEA along the net−section of the panel for a load of 10 kN. It is maximum at hole edge and subdues as one goes away from hole towards panel edge. Besides small difference in magnitude, ε_{xx} distribution from both DIC and FEA has a similar trend and relatively shows a good agreement.

3.7.2 Single sided repair panel

Comparison of contour plots of ε_{xx} and ε_{xy} for the single sided repaired panel corresponding to a load of 10 kN obtained from FEA and DIC are shown in Fig. 3.24. The DIC plot of ε_{xx} strain field as shown in Fig. 3.24 (a) possess highly strained zone around the upper and lower patch edge. But, contour plot from FEA shows highly strained zone along the unpatched edge of the hole. This is because unpatched side is at back side in case of DIC experiment and hence cannot be estimated. The magnitude of strain at patch edge predicted by FEA is lower than the experimental value. The contour plot of ε_{xy} obtained from DIC and FEA is shown in Fig. 3.24 (d)−(f). It is found that a similar trend exists between DIC and FEA plots.

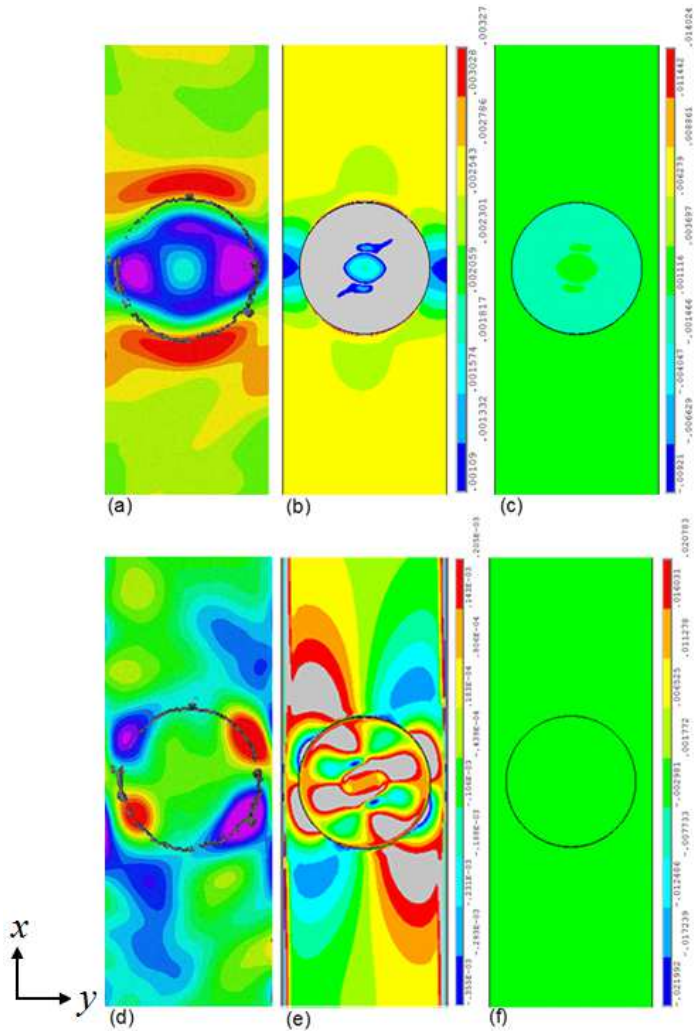

Figure 3.24: Comparison of whole field strain contour obtained from DIC and FEA for single sided repair panel under tensile load of 10 kN (a) DIC (b) FEA (ADS) (c) FEA (AS) − ε_{xx} plot (d) DIC (e) FEA (ADS) (f) FEA (AS) − ε_{xy} plot (ADS − adjusted scale of FEA with DIC scale, AS − Actual scale of FEA plot)

3.7.3 Double sided repair panel

Comparison of contour plots of ε_{xx} and ε_{xy} for the double sided repaired panel corresponding to load 10 kN obtained from DIC and FEA are shown in Fig. 3.25. Strain ε_{xx} as shown in Fig. 3.25 (a) possess highly strained zone around the upper patch edge. However, contour plot from FEA shows highly strained zone around the hole edge which is shown in Fig. 3.25 (b). This deviation exists as DIC measures only surface the strain and it can't access anything below the patch. The contour plot of ε_{xx} obtained from DIC and FEA is shown in Fig. 3.25 (d)−(f) and they are found to be in good agreement.

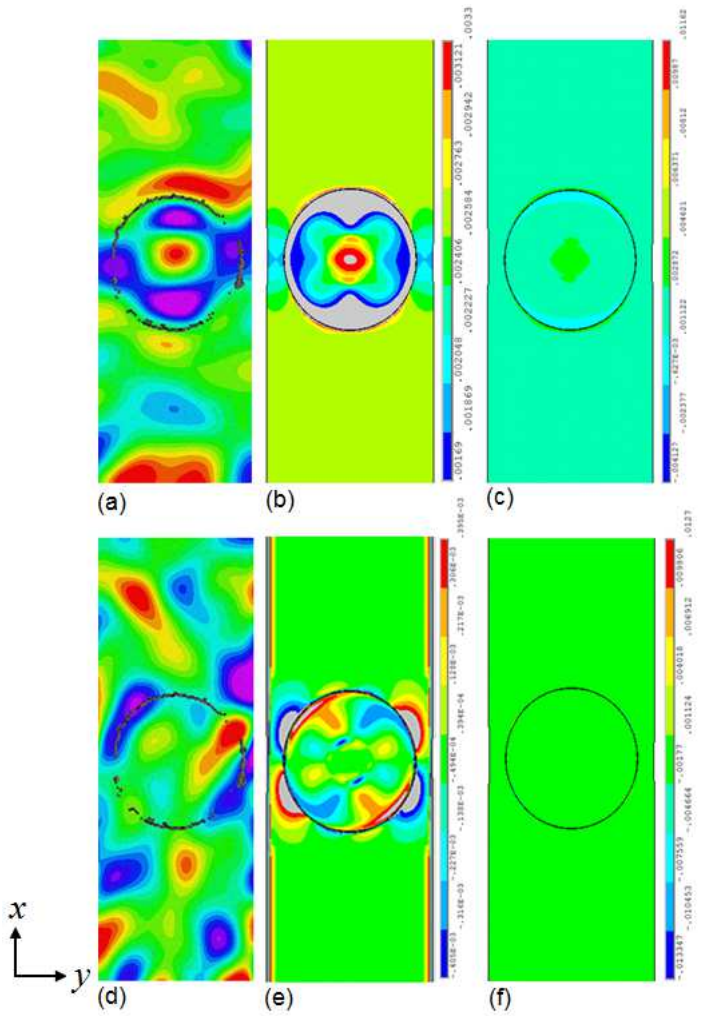

Figure 3.25: Comparison of whole field strain contour obtained from DIC and FEA for double sided repair panel under tensile load of 10 kN (a) DIC (b) FEA (ADS) (c) FEA (AS) − ε_{xx} plot (d) DIC (e) FEA (ADS) (f) FEA (AS) − ε_{xy} plot (ADS − adjusted scale of FEA with DIC scale, AS − Actual scale of FEA plot)

3.7.4 Strength of open cutout and repaired panel

To compare the strength of the the virgin, open cutout and repaired panel experimentally obtained load−displacement curve for all the three cases are plotted in Fig. 3.26. The ultimate load taken by the virgin (without damage) panel, open cutout and repaired panels obtained from three independent measurements together with mean, standard deviation (Std. Dev.) and coefficient of variation (CV) is summarized in Table 3.3. The load−displacement curve shows a similar behaviour as explained in pure UD case. The tensile strength for virgin panel is 437.5 MPa whereas for circular cutout panel it is 271.42 MPa. In case of single and double sided repair panel it is 295.83 MPa and 351.92 MPa respectively. Th CV for virgin, open cutout, single and double sided repair is 1.26%, 2.08%, 2.46% and 1.2% respectively.

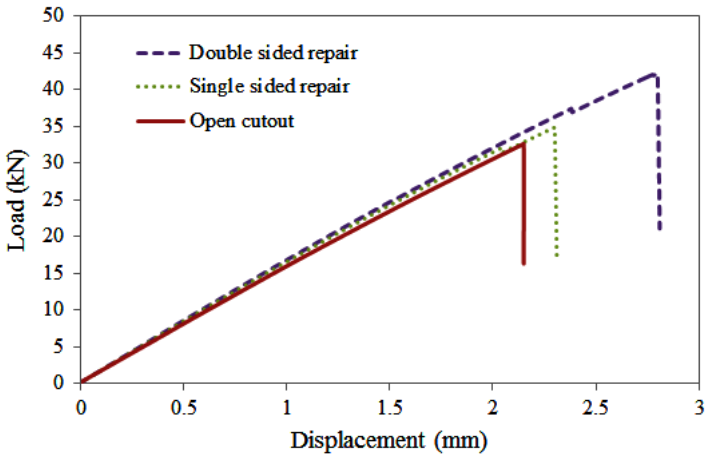

Figure 3.26: Load−displacement curve for open cutout and repaired panels obtained from experiment: quasi−isotropic configuration

The gain in ultimate strength in case of single and double sided repaired panel with respect to virgin panel is 67.59% and 80.43% respectively. Therefore, double sided repaired panel has got 12.84% higher strength as compared to single sided one and therefore it is recommended for repair applications.

Table 3.3: Ultimate tensile strength of virgin, open cutout and repaired panels: quasi−isotropic configuration.

	Load (kN)			
Specimen #	Virgin panel	Open cutout	Single sided	Double sided
1	53.12	31.89	36.33	42.65
2	52.5	32.57	35.5	42.319
3	51.79	33.25	34.58	41.65
Mean	52.47	32.57	35.47	42.20
Std. Dev.	0.66	0.68	0.87	0.51
CV (%)	1.26	2.08	2.46	1.20
Restoration (%)	–	–	67.59	80.43

3.8 Mechanics of externally bonded patch repair

An enormous growth has been taken place in the field of finite element analysis applied to optimization study and especially in the area of composite patch repair. To study the mechanics of composite patch repair finite element analysis is ideally preferred for its versatility and accuracy. In externally bonded repairs, some of the load is transferred from panel to the patch through the adhesive layer thereby increasing the static strength of damaged panel. The relative stiffness of the reinforcement as compared to the damaged panel determines not only the portion of load transferred but also the level of peak stresses in the adhesive layer and the stress concentrations in the repaired panel. The mechanics based design approach through parametric study allows us to analyze the influence of different patch stacking sequence, patch thickness, overlap length and adhesive thickness on SCF in panel, shear and peel stress level in adhesive layer which further helps in improving the repair performance. Different parameters like patch stacking sequence, patch thickness, overlap length and adhesive thickness that influence the repair performance are considered. The repair performance is analyzed based on SCF reduction in panel as well as peel and shear stress reduction in adhesive layer. A quasi−isotropic panel of configuration $[\pm 45/0/90]_s$ having a central hole of 10 mm diameter subjected to tensile load is considered here for the analysis. The geometry and dimensions of the quasi−isotropic panel studied here is kept as same as that of experimental model as shown in Fig. 3.1. Six different patch stacking sequences are chosen in this study. The analysis is done for different patch thickness ranging from 0.3 mm to 2.4 mm. The patch diameters are varied from 12 mm to 46 mm which correspond to the overlap length 1 mm to 18 mm and adhesive thickness from 0.05 mm to 0.25 mm. These parameters are studied in sequential manner and explained elaborately in subsequent sections.

3.8.1 Damage prone locations in externally bonded patch repair

The stress distribution in open cutout and repaired panel reveals that stress along the loading direction (σ_{xx}) is the primary stress component inducing damage. Fig. 3.27 shows the stress variation in panel, patch and adhesive layer for the repaired configuration at a load of 10 kN (83.33 MPa). From Fig. 3.27 (a), it can be observed that at two critical locations (A, B) high stress levels are present in the panel. Zone A is the transverse edge of the hole and zone B is the longitudinal edge of the patch. By closely observing Fig. 3.27 (b), it is found that zone C (overlap edge) is one of the most critical location on the adhesive layer from which damage could initiate in the form of patch debonding. Fig. 3.27 (c) reveals that σ_{xx} stress component in the patch is higher at the hole edge (Zone D). These locations are always referred in the subsequent sections for a quantitative study.

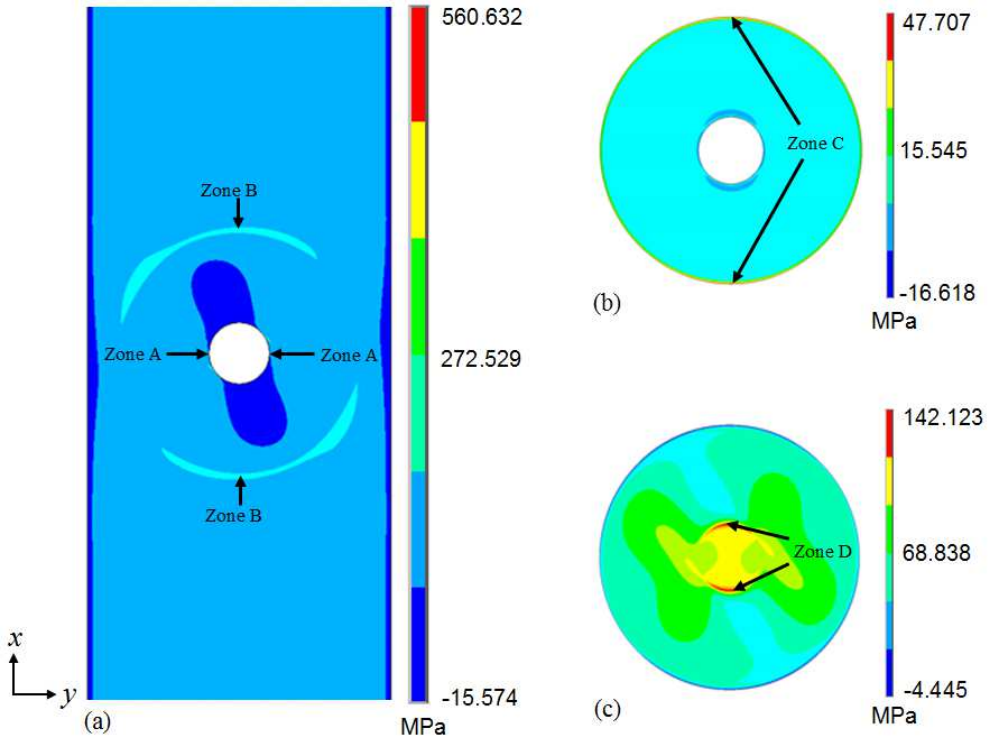

Figure 3.27: Whole field stress contour plots of various components in externally bonded double sided repair from 3D FEA (a) longitudinal stress (σ_{xx}) in repaired panel (b) peel stress (σ_{zz}) in adhesive (c) longitudinal stress (σ_{xx}) in patch

3.8.2 Effect of patch stacking sequence

Different stacking sequence considered here are given in Table 3.4. The effect of patch stacking sequence on variation of SCF at Zone A and normalized shear stress (τ_{xz}) in adhesive layer in case of single and double sided patch repair configuration is shown in Figure 3.28 and 3.29 respectively. The effect of stacking sequence is analyzed for a fixed value of adhesive thickness, patch thickness and patch diameter and they are 0.1, 1.2 and 40 mm respectively. In case of single sided repair, from Fig. 3.28 (a) and 3.28 (b), it is clear that the SCF is minimum but shear stress is higher for the patch configuration $[90°]_4$ but in contrast to this SCF is intermediate and shear stress is minimum for a patch stacking sequence of $[0°]_4$. Therefore, patch with $[90°]_4$ stacking sequence can be considered for single sided repair configuration. In case of double sided repair, from Fig. 3.29 (a) and Fig. 3.29 (b), it is clear that the SCF is lower while normalized shear stress is maximum for the patch stacking sequence of $[0°]_4$. In case of $[\pm 45°]_s$ layup, SCF is intermediate but shear stress is comparatively minimum and for $[\pm 45/0/90]$ configuration SCF is minimum but shear stress is intermediate. Therefore, patch layup of $[\pm 45°]_s$ and $[\pm 45/0/90]$ can be considered for double sided repair configuration. Similar observation is made in the experimental study given in Ref. [82]. In this study, patch of $[\pm 45°]_s$ configuration is considered for further study in case of double sided repair.

Table 3.4: SCF and normalized shear stress values obtained for models of different patch stacking sequences.

Name	Stacking sequence	SCF		Normalized shear stress	
		Single sided	Double sided	Single sided	Double sided
A	$[0°]_4$	5.7207	2.6143	0.2391	0.3530
B	$[90/0/\mp 45]$	5.8870	2.6143	0.2505	0.2530
C	$[0/90/\pm 45]$	5.7340	2.6143	0.26	0.2859
D	$[\pm 45/0/90]$	5.9622	2.6143	0.2693	0.2594
E	$[\pm 45°]_s$	6.1749	3.7934	0.2575	0.2000
F	$[90°]_4$	5.5515	4.2345	0.2614	0.2074

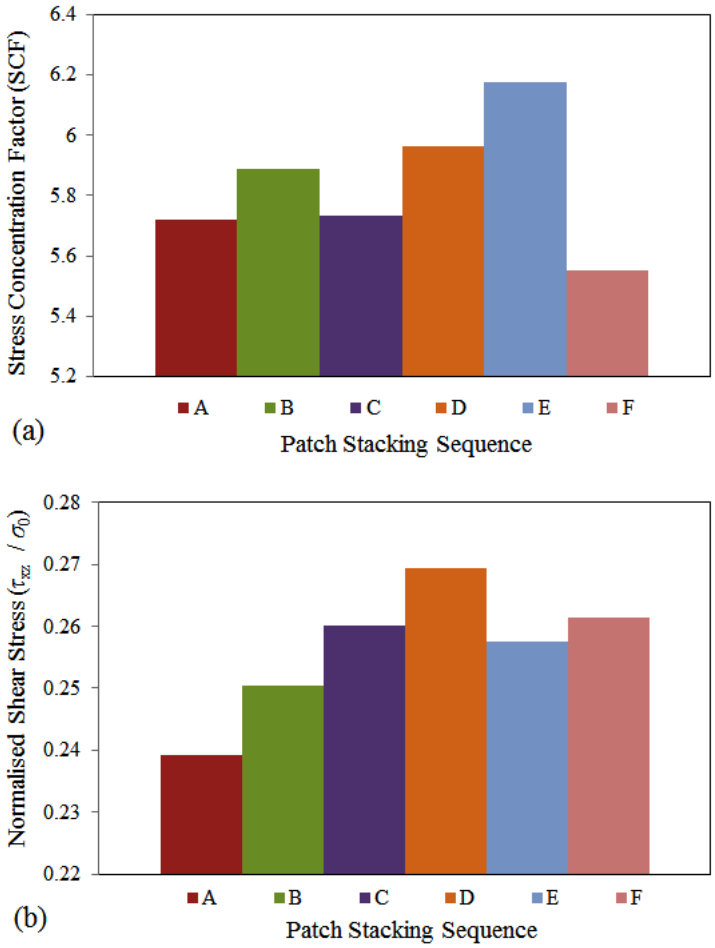

Figure 3.28: Effect of patch stacking sequence in single sided repair configuration on (a) SCF (b) normalized shear stress

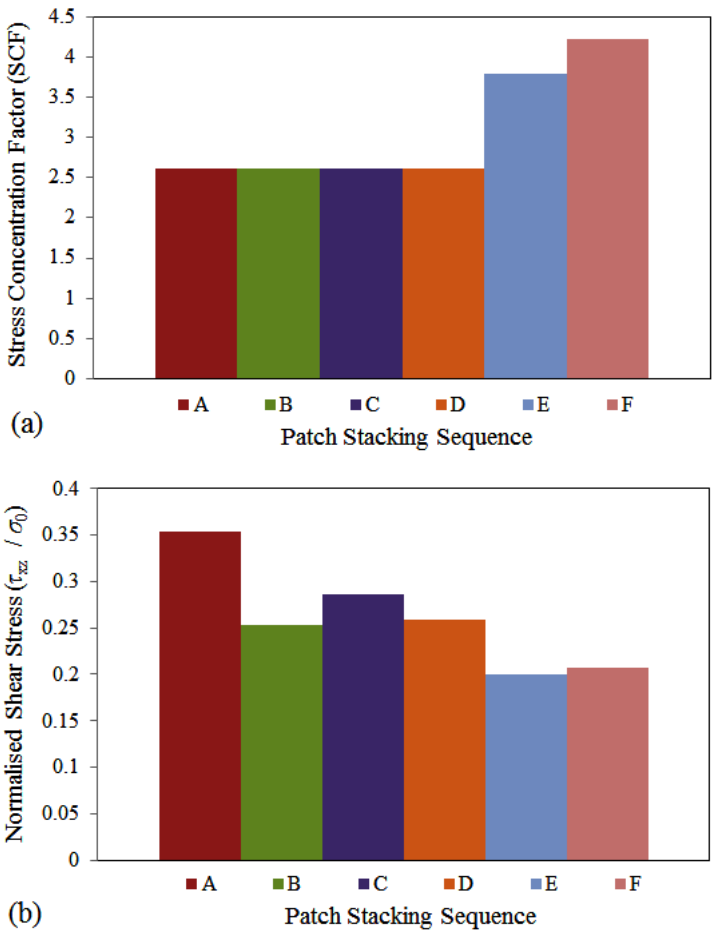

Figure 3.29: Effect of patch stacking sequence in double sided repair configuration on (a) SCF (b) normalized shear stress

3.8.3 Effect of patch thickness

Figure 3.30 shows the variation of SCF at zone A and B on the first layer ($+45°$ to loading direction) in the panel for different patch thickness in the case of double sided repair. The patch stacking sequence used here is $[\pm 45°]_s$. Initially most severe location is zone A but on increasing patch thickness it shifts towards zone B which may lead to skin damage on the panel. For a minimum SCF at both the locations, corresponding patch thickness is obtained as shown in Fig. 3.30. The thickness of the patch is found to be 1.3 mm. Also, the effect of different patch thickness on variation of SCF (at zone A in $0°$ layer) and normalized shear stress (in the adhesive layer) for a double sided repair model is shown in Fig. 3.31 (a) and (b) respectively. Looking at the plot, one could see that SCF decreases with patch thickness but shear stress in adhesive layer increases. On close observation of the plots, patch thickness of 1.3 mm leads to a lower SCF and an intermediate level of shear stress in the adhesive layer.

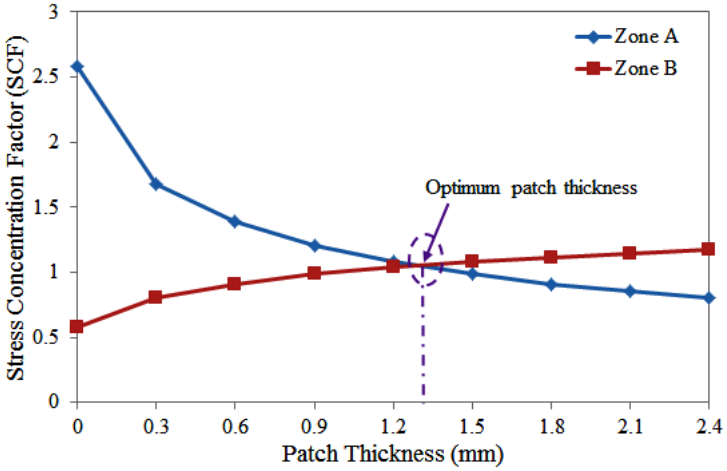

Figure 3.30: Variation of SCF in Zone A and B of panel with varying patch thickness

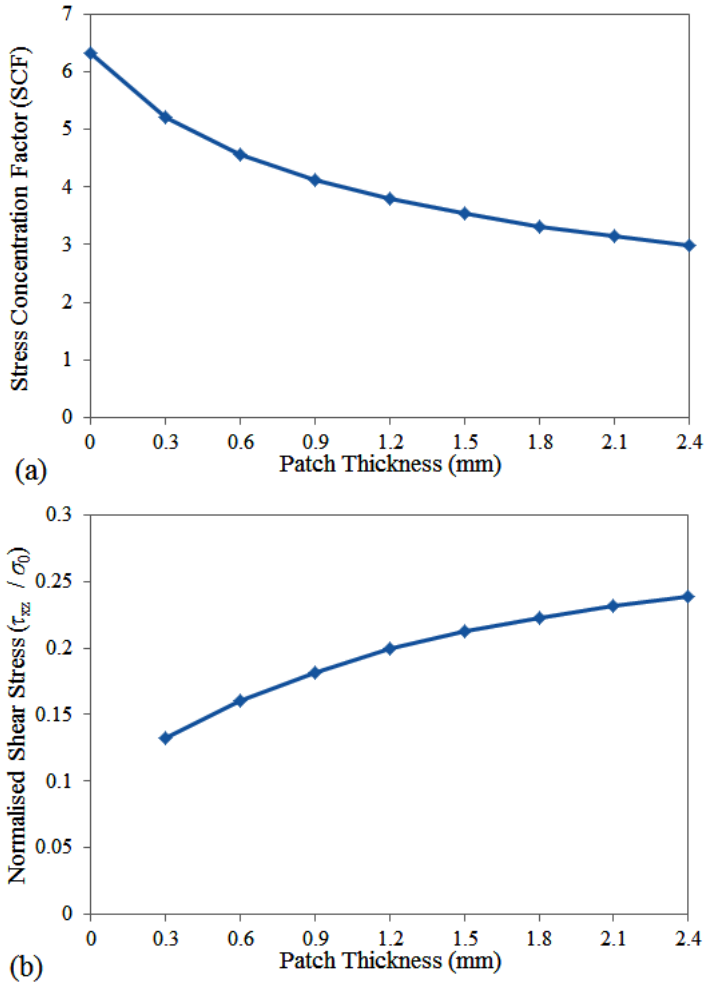

Figure 3.31: Variation of SCF and normalized shear stress with different patch thickness (adhesive thickness 0.15 mm) (patch diameter 40 mm)

3.8.4 Effect of adhesive layer thickness

Adhesive layer plays an important role in the structural integrity of a repaired panel. The peel (σ_{zz}) and shear (τ_{xz}) stress in the adhesive layer are the primary stress components responsible for patch debonding from the panel. The effect of adhesive thickness on shear stress and SCF variation is studied here because the behaviour of adhesive is influenced by its thickness. Higher adhesive thickness makes the adhesive porous and therefore may cause the weakening of interfaces whereas lower thickness makes the adhesive more stiff and brittle [20]. The variation of SCF at zone A and normalized shear stress in adhesive layer with adhesive thickness for a panel repaired with double sided patch of $[\pm 45^{\circ}]_s$ configuration is shown in the Fig. 3.32 (a) and (b) respectively. From the plot it can be observed that with increase in adhesive thickness, shear stress in adhesive layer decreases but SCF at zone A increases. Higher adhesive thickness strengthens adhesion but it weakens the load transfer towards the patch thereby decreasing the beneficial effect of the patch resulting in increase of SCF. On the other hand, lower adhesive thickness supports the load transfer towards the patch but increases the risk of adhesive layer failure [165].

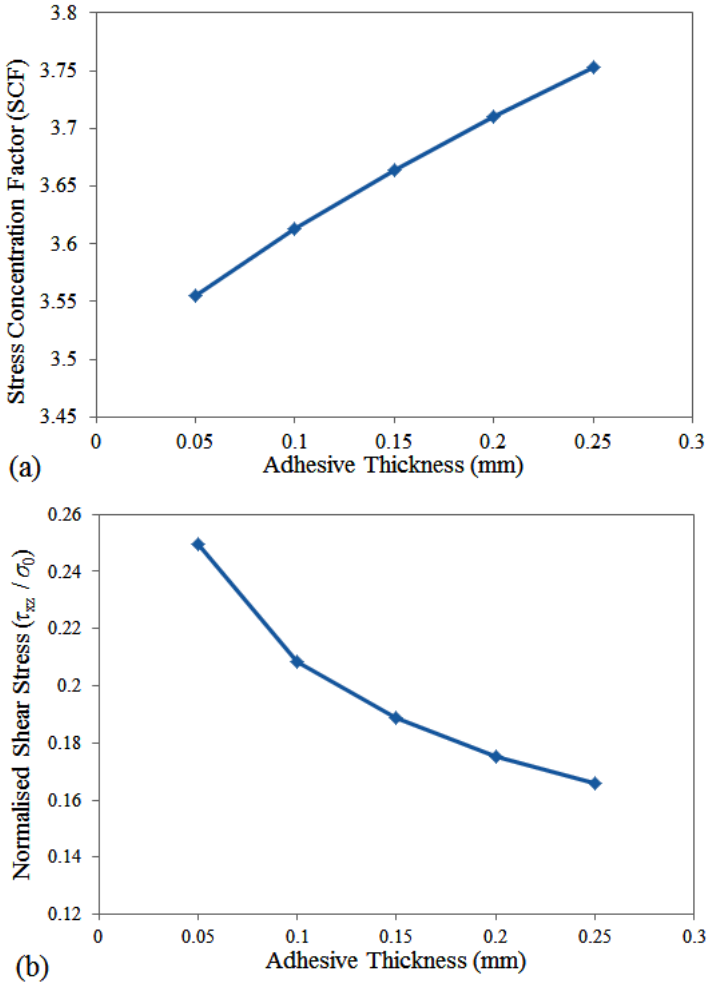

Figure 3.32: Variation of SCF and normalized shear stress with adhesive thickness for double sided repair (patch diameter 40 mm)

Figure 3.33 shows the variation of adhesive shear stress with overlap length for different adhesive thickness of 0.05, 0.1, 0.15, 0.2, 0.25 (all are in mm). From the graph it can be observed that shear stress distribution in thin and thick adhesive is almost same but there is a drastic reduction of shear stress at the overlap edge (zone C) with increasing adhesive thickness. At this zone load transfer occurs from the panel to patch and therefore it gets highly stressed while rest of the layer is of low stress. By looking at the plots, one can conclude that the an adhesive thickness of 0.15 mm gives an intermediate SCF as well as shear stress level.

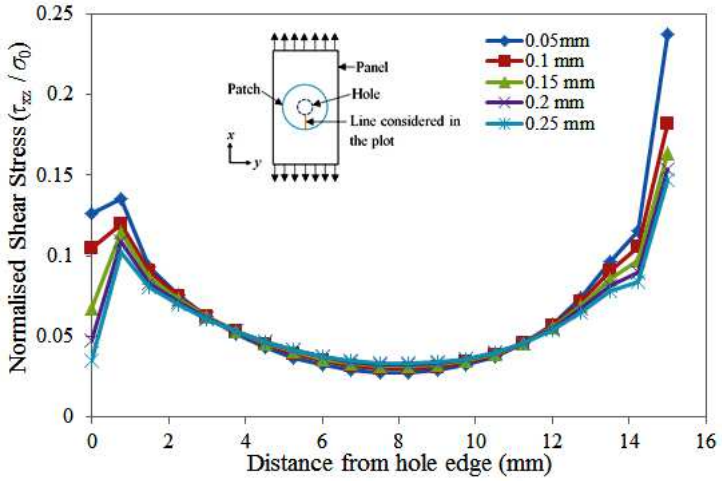

Figure 3.33: Variation of normalized shear stress along the longitudinal axis repaired with different adhesive thickness

3.8.5 Effect of patch diameter

Figure 3.34 (a) shows the SCF variation at the transverse edge of the hole with patch diameter and Fig. 3.34 (b) shows variation of normalized shear stress in the adhesive layer with patch diameter. Patch stacking sequence considered here is $[\pm 45°]_s$. It is evident that SCF and shear stress levels are inversely proportional to patch diameter. As the patch diameter increases, the SCF and shear stress reduces. Load transfer area from panel to patch increases with increase in patch area and therefore higher load is transferred by the patch leading to significant reduction in SCF. This trend is observed up to the patch diameter of 40 mm and it remains same beyond it. A similar trend is also seen in case of shear stress in the adhesive layer. Fig. 3.35 shows the distribution of normalized shear stress in adhesive layer with respect to the overlap length for different patch diameters. On careful observation, the patch with larger diameter shows greater reduction of shear stress along the overlap length but after 40 mm diameter there is not much reduction in shear stress at patch overlap edge. Therefore, one can conclude from Fig. 3.34 and 3.35 that over stiff patches are dangerous as they will induce high peel and shear stresses in the adhesive layer. Therefore, a patch diameter of 40 mm is chosen to reduce both SCF and shear stress in the adhesive layer towards an integral repair system.

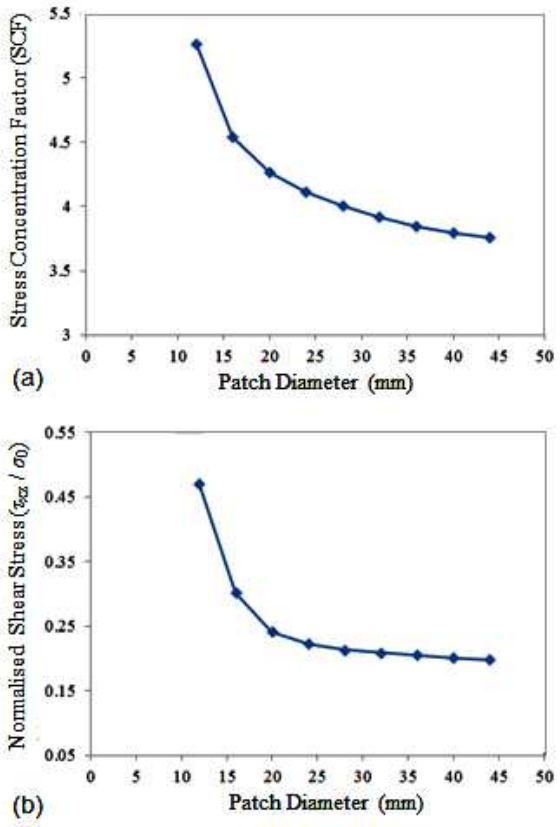

Figure 3.34: Variation of SCF and normalized shear stress with varying patch diameter

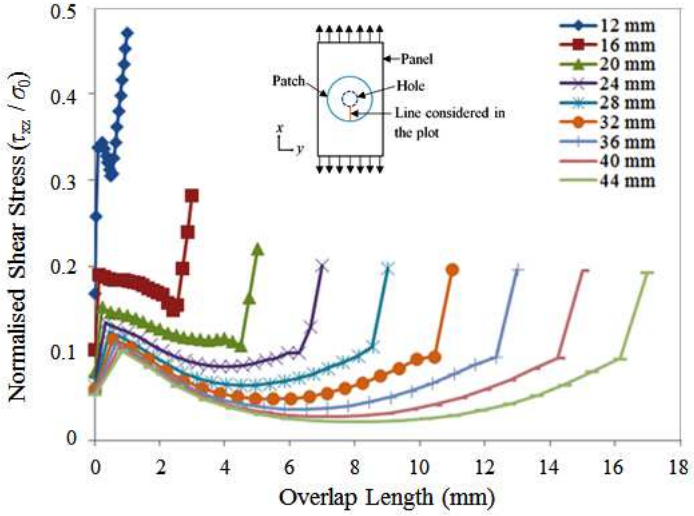

Figure 3.35: Variation of normalized shear stress along the longitudinal axis for different patch diameter

3.8.6 Comparison of open cutout and repaired panel

Comparison of SCF values between open cutout and repaired (single and double sided) panel is shown in Table 3.5. The mesh morphology for open cutout, single sided and double sided repaired panel is retained same for quantitative comparison. The patch stacking sequence is $[\pm 45^{\circ}]_s$. From the table one can observe that, in case of double sided repair there is a drastic reduction in SCF as compared to single sided repair. This is because there is a slight shift in neutral axis towards the patch in case of single sided repair, leading to bending effect in addition to in−plane loading. For quantitative comparison same patch dimensions are considered for both single and double sided repair panels. The SCF is reduced from 6.33 to 3.70 in case of double sided repair whereas for single sided repair it is 5.94. Based on SCF reduction one can emphasize that double sided repair is more efficient as compared to single sided repair.

Table 3.5: SCF comparison between open cutout, single and double sided repair model.

Parameter	Open cutout panel	Single sided repair	Double sided repair
SCF	6.33	5.94	3.71

3.9 Closure

In this chapter, results from both experiment and numerical study are presented to analyze the performance of externally bonded patch repair on pure UD $[0°]_4$ and quasi−isotropic $[\pm 45/0/90]_s$ CFRP panels under tensile loading. Full field strain variation over the surface of the panel as well as the patch is analyzed using 3D DIC technique. Damage initiation and its propagation in open cutout and repaired panel is successfully monitored using DIC. The strain field obtained from DIC shows up the critical locations (prone to damage) and further helps us in predicting the damage initiation since asymmetry in strain pattern appears with damage initiation. It is found that the highly localized strains always develop around the transverse edge of the hole as well as at patch overlap edge in both pure UD and quasi−isotropic panels. The damage in the panels always initiates with matrix cracking around the hole for both the cases. In case of pure UD panel, for both open cutout and repaired panel, the damage propagation is always perpendicular to the hole edge with extensive fiber splitting along the loading direction and it propagates towards the tab ends. It is also observed that the localized patch debonding occurs at the patch overlap edge normal to the loading direction and it is mainly because of development of high peel and shear stress in the adhesive layer. In case of quas−isotropic panel, damage propagates with extensive matrix cracking in all the plies and fiber failures running along the fiber direction in 45° and 0° plies across the panel width. The damage propagation in open cutout and repaired quasi−isotropic panels is very much confined around the net−section of the panels.

The final failure of repaired panels in both pure UD and quasi−isotropic cases happens with complete debonding of the patch. In case of pure UD configuration, single sided repair restores 76% of undamaged or virgin panel strength whereas double sided repair restores 85% of virgin panel strength. For the case of quasi−isotropic panels, single and double sided repair restores 71% and 82% of virgin panel strength respectively. Therefore, in both cases single sided repair is found to be less efficient in comparison to double sided repair and hence the later one is recommended for repair application. Finally, full field strain variations obtained from FEA are compared with the experiment results and they are found to be in good coherence.

Further,a finite element based study is carried out to understand the mechanics of composite patch repair on damaged CFRP panel of configuration $[\pm 45/0/90]_s$ under tensile load. The panel is repaired with circular patch. The influence of various parameters such as patch stacking sequence, patch thickness, overlap length and adhesive thickness is investigated. Based on SCF and shear stress level in adhesive layer, it is concluded that the patch stacking sequence $[90°]_4$ can be chosen for single side repair whereas $[\pm 45°]_s$ and $[\pm 45/0/90]$ for double sided repair. It is found that the SCF decreases with increasing patch thickness but shear stress in adhesive layer increases. However, a patch thickness of 1.3 mm could be chosen for repair which leads to a lower SCF and an intermediate shear stress level. It is also observed that with increase in adhesive thickness, the adhesive shear stress decreases but SCF increases and therefore a value of 0.15 mm for adhesive thickness can be used for the repair based on intermediate SCF and shear stress level. Further, as the patch diameter increases, the SCF and shear stress reduces. However, after 40 mm patch diameter there is not much reduction in shear stress at patch overlap edge. Therefore, a patch diameter of 40 mm is chosen to reduce both SCF and shear stress in the adhesive layer towards an integral repair system.

The results presented in this chapter shows that the technique of 3D−DIC is more suitable, accurate and promising for experimental study in composite patch repair domain. It reveals the critical

locations prone to damage and also useful for successfully monitoring the damage development in composite panels. However, the strength and failure mechanism prediction in composite structures by experiment is more involved, expensive and time consuming, hence finite element based PDM is gaining more importance and wider acceptance in recent years for this purpose. The next chapter deals with the development of PDM for predicting the strength and damage mechanism in open cutout and repaired panels. Same pure UD and quasi−isotropic panel configurations are again considered for progressive damage modeling, and the results predicted from PFA are compared with the experimental one.

Chapter 4

Progressive Failure Analysis of Open Cutout and Repaired CFRP Panel using Finite Element Method

4.1 Introduction

The damage evolution in composite structure is a complex phenomenon, comprising of several interacting failure modes like matrix cracking, fiber breakage, debonding and delamination. Damage initiation, its propagation and ultimate strength prediction of composite structure are of paramount importance for developing reliable and a safer design for utilizing them as primary load bearing one. Progressive failure analysis facilitates the simulation of degrading structural response and helps in developing the damage tolerant design, which is of primary concern in the aerospace industry.

Most of the work is on progressive damage modeling of an open cutout composite panel [38–41, 86–88, 90–92]. Couple of work exist on PFA of repaired composite panel [76, 93] and they are limited to double sided patch repair configuration. No work has been reported yet on PFA of single sided externally bonded patch repaired composite panel which is of practical importance, because both sides of the damaged panels are always not available to perform a double sided repair such as fuselage or wing of an aircraft.

In this chapter, a 3D finite element based progressive damage model (PDM) is developed for predicting the failure and post failure behaviour of open cutout and repaired panel. Both single and double sided repair configurations are considered. Same pure UD $[0°]_4$ and quasi−isotropic $[\pm 45/0/90]_s$ CFRP panels studied earlier are considered here for PFA. Stress based 3D−Hashin's failure criterion is employed for predicting the damage mechanism. Maximum shear stress and strain criterions are considered to account for patch debonding. Material property degradation method is implemented for damage modeling to account for the effect of damage on load bearing strength of the panels. Failure initiation load, ultimate strength and failure mechanisms are analyzed through the developed PDM. Load displacement behavior as well as path of damage progression predicted

by PDM simulation is compared with the experimental observation from DIC.

Furthermore, the characteristic distance is obtained from finite element analysis for various repair configurations based on maximum shear strain in adhesive layer.

4.1.1 Specimen configurations and experimental results

The specimen configurations for progressive failure analysis are same as that of experimental study which is discussed in chapter−3. However, for a quick overview the specimen configurations are given in Table 4.1 and the corresponding experimental results are briefly summarized in following sub−sections.

Table 4.1: Configurations selected for experiment and progressive failure analysis.

Label	Panel stacking sequence	Patch stacking sequence	Adhesive thickness (mm)
Pure UD laminate	$[0°]_4$	$[0°]_3$	0.185
Quasi−isotropic laminate	$[\pm 45/0/90]_s$	$[\pm 45]_s$	0.15

4.1.2 Summary of experimental results: pure UD panel $[0°]_4$

Experimental results obtained from quasi−static tensile test of open cutout, single and double sided repaired model using DIC technique are presented in this section. The strain field obtained from DIC shows us the critical location (prone to damage) and further helps us in predicting the damage initiation load since asymmetry in strain pattern shows up with the damage initiation.

The process of damage development in case of pure UD panel observed from experiment is elaborately discussed in chapter 3. However, a brief outcomes of the previous experimental results are presented in this section. Figures 4.1 (a)−(c) shows the whole field strain maps over the surface of an open cutout, single and double sided patch repaired panel. In case of open cutout panel, it is found that the highly localized strained zone (ε_{xx}) is present around the transverse edge of the hole as shown in Fig. 4.1 (a), and damage initiates from this location due to matrix cracking. With further increase in load, it is also found that the damage accumulates around the hole and then propagates with longitudinal splitting of fibers from both side of hole edge along loading direction (x−axis) towards the tabbed end. This kind of splitting is very much akin to pure UD cutout panel [163].

In case of single and double sided repaired panel as shown in Fig. 4.1 (b) and 4.1 (c)), it is found that a highly localized strained zone develops around the longitudinal overlap edge of the patch and it leads to debonding of patch starting from this location with increased loading. When the patch is partially debonded from the panel, longitudinal splitting in 0° fiber direction is prominently observed with an increasing load similar to that of open cutout panel. The final failure mechanism in the repaired panel has taken place with a complete debonding of the patch coupled with fiber splitting in the panel. It is also found that the adhesive layer remain intact with the patch.

4.1.3 Summary of experimental results: quasi−isotropic panel $[\pm 45/0/90]_s$

Figures 4.2 (a)−(c) shows the whole field surface strain maps of ε_{xx} of an open cutout, single and double sided patch repaired panel obtained from DIC. In case of open cutout panel as shown in Fig. 4.2 (a), it can be observed that a highly localized strained zone (ε_{xx}) is present around the

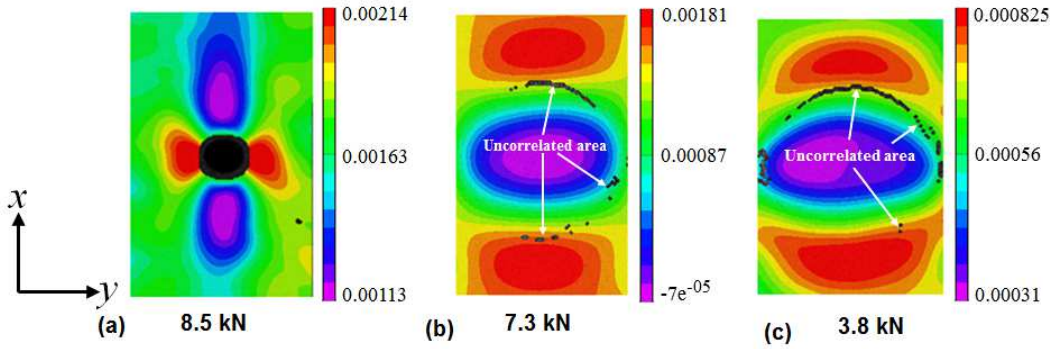

Figure 4.1: Whole field strain (ε_{xx}) distribution observed experimentally using DIC for $[0°]_4$ panel (a) open cutout panel (b) single sided repaired panel (c) double sided repiared panel

transverse edge of the hole zone and it is found to be parallel to +45° ply. The damage initiates from transverse edge of the hole. It is observed from the experiments that the final failure of the panel takes place with fiber breakages in ±45° and 0° plies along them across the panel width. In case of single sided repaired panel as shown in Fig. 4.2 (b), it can be observed that a highly strained zone (ε_{xx}) is present at both upper and lower edge of the patch along the loading direction. In case of double sided repaired panel as shown in Fig. 4.2 (c), it is found that a highly strained zone is present at both upper and lower edge of the patch along the loading direction as well as at the patch center. The final failure of the singe and double double sided repaired panel has taken place with complete debonding of the patch followed by the panel failure similar to the one observed in open cutout panel. Therefore it is evident form the experimental study that the damage zone in all three cases is confined around the net section across the width of the panel nearer to the hole. In the next sub−section failure mechanism predicted by PDM is discussed.

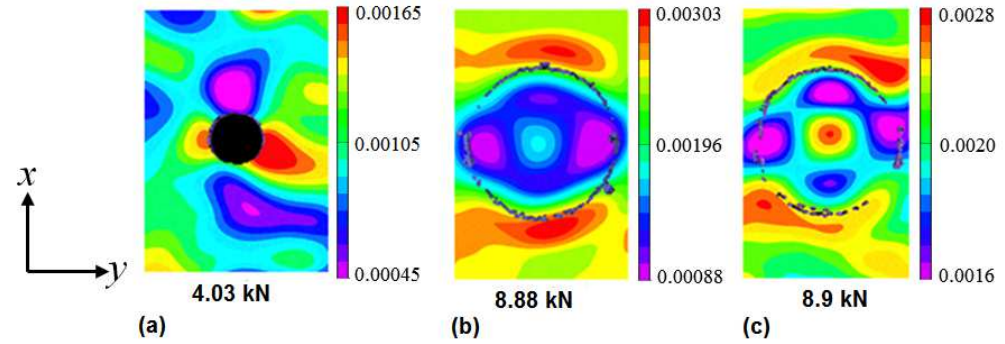

Figure 4.2: Whole field strain (ε_{xx}) distribution observed experimentally using DIC for $[\pm 45/0/90]_s$ panel (a) open cutout panel (b) single sided repaired panel (b) double sided repaired panel

4.2 Progressive damage modeling (PDM)

The developed progressive damage model mainly comprises of three steps: stress analysis, damage prediction and damage modeling. Theses three steps are discussed elaborately in chapter−1. The implementation of PDM algorithm is discussed in subsequent sub−sections.

4.2.1 Stress analysis

Initially, finite element model of an open cutout and repaired panels are developed. The FE model is then analyzed under given loading and boundary conditions to obtain the elemental stresses in principal material directions of the laminate. In this work, 3D modeling and analysis of an open cutout and repaired panel is carried out using ANSYS−13 software. The panel, patch and adhesive are modeled with 20−noded solid−186 element as per the dimensions given in Fig. 3.1. The mesh pattern around the hole and overlap edge is kept very fine as per the recommendation given in Ref. [166] in order to capture high stress gradient. A detailed study on mesh design in finite element analysis of composite laminates can be found in Ref. [167]. A mesh convergence study has been performed in the present work to arrive at the number of elements surrounding the hole and it is found to be 96. Firstly, a structured mesh is generated around the circular hole and it has a total of 73728 elements (96 circumferential; 96 radial; 8 elements along the thickness). Away from the hole, coarser mesh is adopted in order to reduce the total degree of freedom (dof). Each layer in patch and panel is assigned one element in thickness direction. The layer angles are defined by assigning appropriate element coordinate system. MPC algorithm is used to ensure perfect bonding between patch/adhesive and adhesive/panel interfaces. The degree of freedom along $x-$direction of all the nodes in the top face of the panel is coupled together and displacement in $x-$direction (u) is applied at the master node which is located at the center of that face. The dof associated with nodes present in bottom face are arrested in all three directions. The zoomed view of the finite element model of an open cutout and repaired panel is shown in Fig. 4.3.

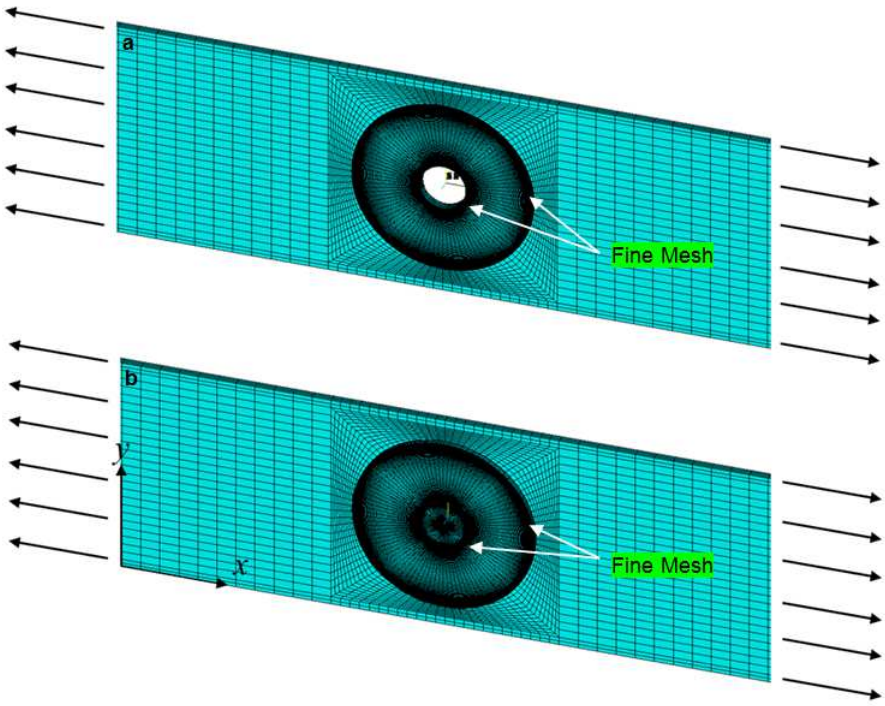

Figure 4.3: Finite element model (a) open cutout panel (b) repaired panel

4.2.2 Damage prediction: failure criterions for panel, patch and adhesive

In second step, the obtained elemental stress values from FE analysis along with material strength parameters (obtained from experiments) are substituted into a set of failure criterions to predict the failure of element and it's respective failure mode.

Failure criterion for panel and patch

Here, stress based 3D Hashin's failure criterions are used for predicting the damage in panel and patch. It is most widely accepted failure theory for predicting the damage in composite structures. Hashin's failure criteria is an interactive failure theory as more than one stress components are considered to evaluate the different failure modes. It offers the advantage of predicting the each failure mode separately. Four different failure modes are considered in this study and they are matrix tensile failure, matrix compression failure, fiber tensile failure and fiber compression failure. Here, compressive mode is considered to account for the compressive stress that develops locally near the hole along vertical diameter [168]. Hashin's failure criterion for the considered failure modes are taken from the Ref. [36] and they are given below.

1. Fiber failure under tensile load

$$\sigma_{xx} \geq 0 \tag{4.1}$$

$$\left(\frac{\sigma_{xx}}{X_T}\right)^2 + \frac{\sigma_{xy}^2 + \sigma_{xz}^2}{S_{xy}^2} = \begin{cases} \geq 1 & failure \\ < 1 & nofailure \end{cases} \tag{4.2}$$

2. Fiber failure under compressive load

$$\sigma_{xx} < 0 \tag{4.3}$$

$$\left(\frac{\sigma_{xx}}{X_C}\right)^2 = \begin{cases} \geq 1 & failure \\ < 1 & nofailure \end{cases} \tag{4.4}$$

3. Matrix failure under tensile load

$$\sigma_{yy} + \sigma_{zz} > 0 \tag{4.5}$$

$$\left(\frac{\sigma_{yy} + \sigma_{zz}}{Y_T}\right)^2 + \frac{\sigma_{yz}^2 - \sigma_{yy}\sigma_{zz}}{S_{xz}^2} + \frac{\sigma_{xy}^2 + \sigma_{xz}^2}{S_{xy}^2} = \begin{cases} \geq 1 & failure \\ < 1 & nofailure \end{cases} \tag{4.6}$$

4. Matrix failure under compressive load

$$\sigma_{yy} + \sigma_{zz} < 0 \tag{4.7}$$

$$\left[\left(\frac{Y_C}{2S_{yz}}\right)^2 - 1\right]\left(\frac{\sigma_{yy} + \sigma_{zz}}{Y_C}\right) + \frac{(\sigma_{yy} + \sigma_{zz})^2}{4S_{yz}^2} + \frac{\sigma_{yz}^2 - \sigma_{yy}\sigma_{zz}}{S_{yz}^2} + \frac{\sigma_{xy}^2 + \sigma_{xz}^2}{S_{xy}^2} = \begin{cases} \geq 1 & failure \\ < 1 & nofailure \end{cases} \tag{4.8}$$

where (σ_{ij}) $(i,j$ = x,y,z) denote the stress components. The parameters X_T, Y_T, Z_T denotes the allowable tensile strength along the respective material directions whereas X_C, Y_C, Z_C denotes the allowable compressive strength. The parameters S_{xy}, S_{xz} and S_{yz} denote allowable shear strength

Failure criterion for adhesive

In the repaired laminate, patch debonding plays an important and critical failure mode. The presence of debonding reduces the effective patch area and hence reduces the load transfer between patch and panel which in turn affects the load bearing capacity of repaired laminate. It is the weakest link in the repaired panel system. The patch debonding is mainly influenced by the presence of high shear stress/strain in the adhesive layer [20, 74]. The maximum shear stress and strain criterion is used for predicting the failure of adhesive layer at an elemental level as explained in Ref. [76]. As per the maximum shear stress criteria the adhesive elements are treated as failed when the following condition is satisfied:

$$\left(\frac{\sigma_1 - \sigma_3}{2}\right) \geq \tau_s \tag{4.9}$$

where σ_1 and σ_3 are the maximum and minimum principal stresses in the adhesive layer and τ_s is shear strength of the adhesive.

4.2.3 Damage modeling

In third step, once the damage is detected by a failure theory, a damage modeling technique is then incorporated to take into account the effect of damage on load bearing capacity of the laminate and further post−damage analysis is performed. The degradation is achieved by one of the most popular and widely used material property degradation method which assumes that the damaged element can be replaced by an equivalent element with degraded material properties. Once the failure is identified in any element, the material properties of the failed elements either that of the composite or adhesive are degraded to 5% of their original value according to the degradation rule given in Table 4.2 which is adopted from Ref. [169].

Table 4.2: Material property degradation rules (fiber orientation is along $x-$direction): $(\times)$ property to be degraded, $(-)$ unaffected property.

Failure Mode	E_{xx}	E_{yy}	E_{zz}	G_{xy}	G_{yz}	G_{xz}	ν_{xy}	ν_{yz}	ν_{xz}
Tensile matrix mode	−	×	×	−	×	−	−	×	−
Tensile fiber mode	×	−	−	×	−	×	×	−	×
Compressive matrix mode	−	×	×	−	×	−	−	×	−
Compressive fiber mode	×	−	−	×	×	×	×	−	×
More than one failure mode	×	×	×	×	×	×	×	×	×

For matrix failure in tension as well as in compression, since matrix bears the load in y and z directions, Young's modulus values E_{yy}, E_{zz} together with G_{yz} and ν_{yz} are degraded. This mode of failure affects only matrix directional properties (properties along transverse directions), therefore other material properties are unaffected.

For fiber failure in tension, since fibers are oriented in$x$ direction, Young's modulus value E_{xx} is degraded together with G_{xy}, G_{xz}, ν_{xy} and ν_{xz}. For fiber failure in compression, E_{xx}, G_{xy}, G_{yz}, G_{xz}, ν_{xy} and ν_{xz} are degraded. When more than one mode of failure is detected in an element, all the material properties are degraded so that the element cannot take load in any direction.

4.2.4 Implementation of PDM

The proposed progressive damage model is implemented through ANSYS parametric macro−routine as depicted by a flowchart shown in Fig. 4.4.

Initially, a 3D FE model is developed and analysis is performed by assigning appropriate material properties set to their initial values, boundary conditions, initial displacement value of 0.05 mm and subsequent increment. The elemental stresses together with material strength values are substituted into failure criterion corresponding to patch, panel and adhesive to identify the damage at elemental level. If no damage is detected, the applied displacement is incremented by a pre−defined value of 0.05 mm and process is repeated. If the damage is identified in any element, the material properties of the failed element are degraded according to the degradation rule and analysis is again repeated at the same load. This is because the analysis with degraded elemental properties re−distributes the stresses and may cause the failure of more elements at the same load level. The program checks for the complete failure of the laminate at every increment and the corresponding load and displacement values are noted. If the final failure is reached, the program stops, if not the program continues till complete failure has occurred.

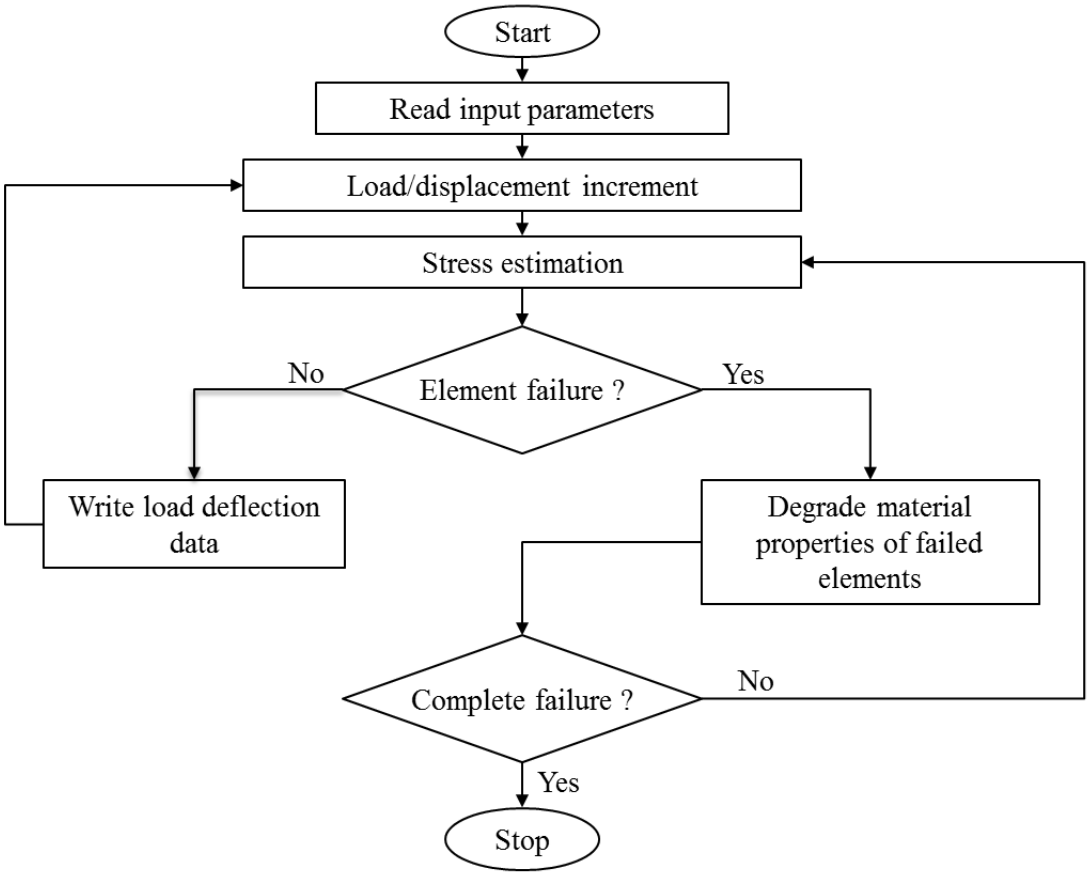

Figure 4.4: Flowchart depicting PDM algorithm

4.3 Progressive failure analysis results: pure UD panel $[0°]_4$

4.3.1 Validation of PDM algorithm

To validate the developed finite element based PDM, the stress−strain curve predicted by PDM simulation for an open cutout panel (pure UD) is compared against the stress−strain curve obtained from DIC experiment for the same configuration. Figure 4.5 (a) & (b) represents the linear region of stress−strain curve predicted by PDM and DIC respectively, and the comparison between them is shown in Fig. 4.6. The stress−strain curve is reported for a point taken away from the hole zone such as to avoid the influence of hole on stress/strain field. One can clearly observe that the slope of stress−strain curve obtained from both PDM and DIC is in close agreement. The value of Young's modulus in the longitudinal direction (E_{xx}) predicted by PDM is 81.9 GPa and the one obtained from DIC measurement is 80.8 GPa. The error associated with E_{xx} prediction from PDM is 1.3%, thereby confirming the accuracy of the implemented PDM algorithm.

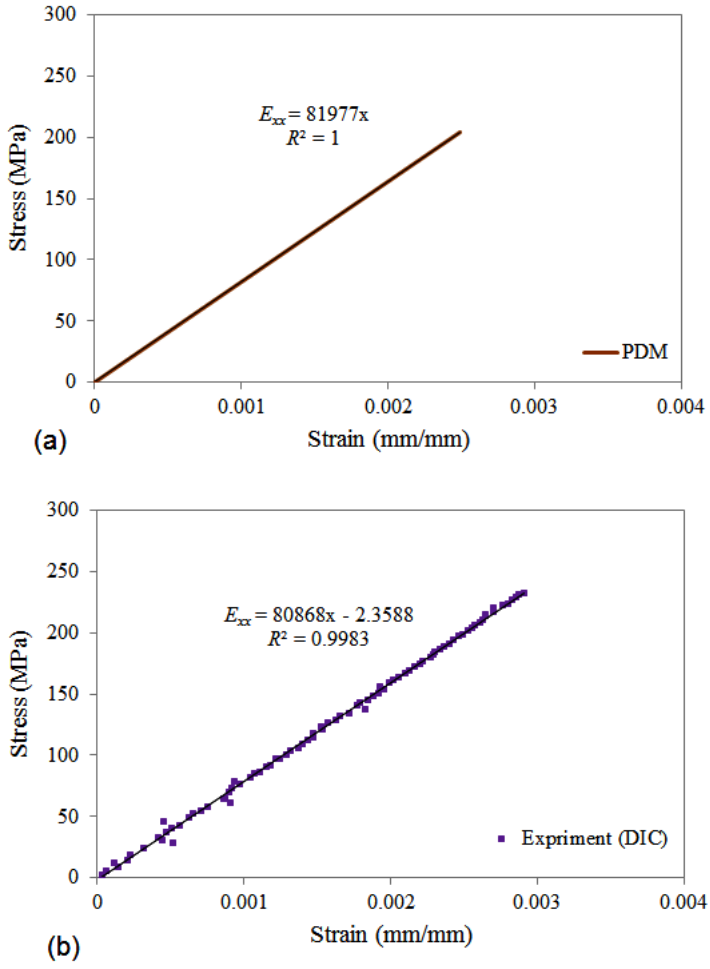

Figure 4.5: Stress−strain curve for open cutout panel (pure UD) (a) predicted by PDM (b) obtained from experiment

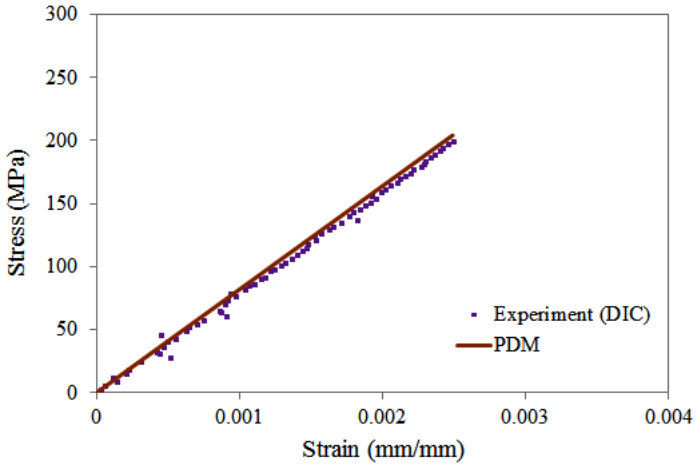

Figure 4.6: Stress strain curve for open cutout panel (pure UD): PDM vs. Experiment

4.3.2 Panel with open cutout

Figures 4.7−4.9 shows the progress of damage with increasing load in an open cutout panel predicted by PDM. It is found that the damage initiates from transverse edge of the hole in the form of tensile matrix cracking at a load of 6.58 kN, as shown in Fig. 4.7.

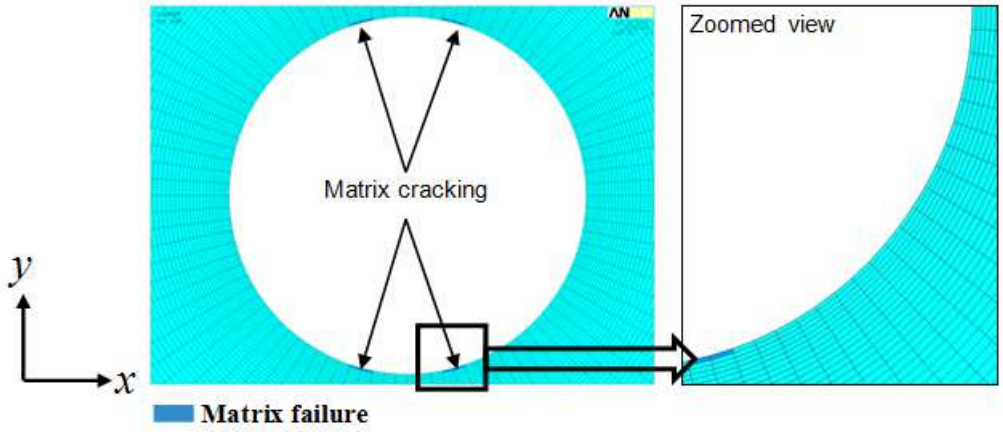

Figure 4.7: Damage initiation site near transverse edge of hole in an open cutout panel $[0°]_4$ at a load of 6.58 kN

With further increase in load, more matrix cracking develops and accumulates around the hole followed by local fiber tensile failure at 18.05 kN, as in Fig. 4.8 (a). At higher loads, the damage propagates with longitudinal splitting of 0° fibers from both side of hole edge along the loading direction ($x-$axis) towards the tab end which is shown in Fig. 4.8 (b).

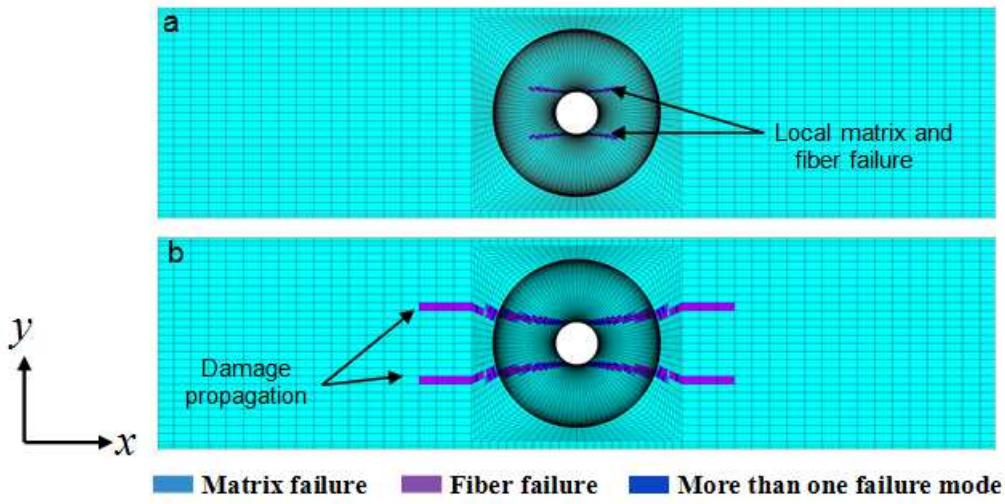

Figure 4.8: Damage progression in an open cutout panel $[0°]_4$ (a) 18.05 kN (b) 25.94 kN

The final failure predicted by PDM is compared with experimental results in Fig. 4.9. One can observe from theses plots that the location of damage initiation and propagation in an open cutout panel predicted by PDM is consistent with the experimental observations which is elaborately discussed in chapter 3.

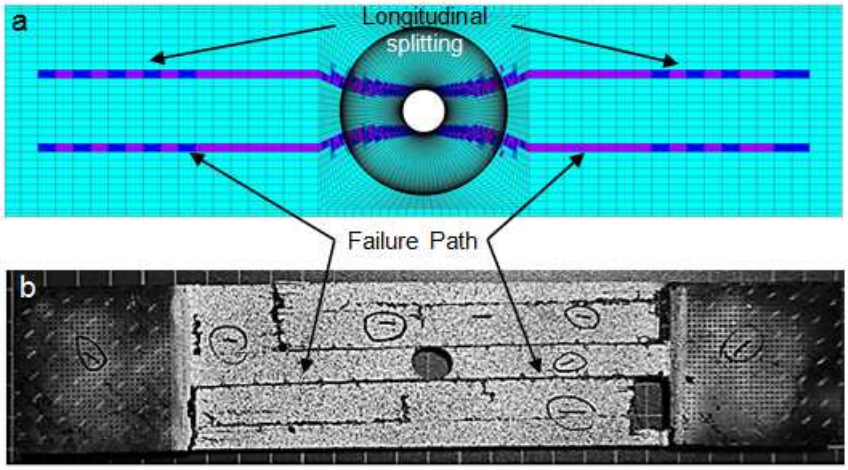

Figure 4.9: Damage mechanism in an open cutout panel $[0°]_4$ (a) predicted by PDM (b) experimentally observed

4.3.3 Single sided repaired panel

Figures 4.10−4.12 shows the evolution of damage in single sided repaired panel predicted by PDM. It is found from Fig. 4.10 that the damage initiated with matrix cracking around transverse edge of the hole at a load of 8.68 kN, as observed in case of open cutout panel. However, no damage is observed in patch and adhesive layer at this load.

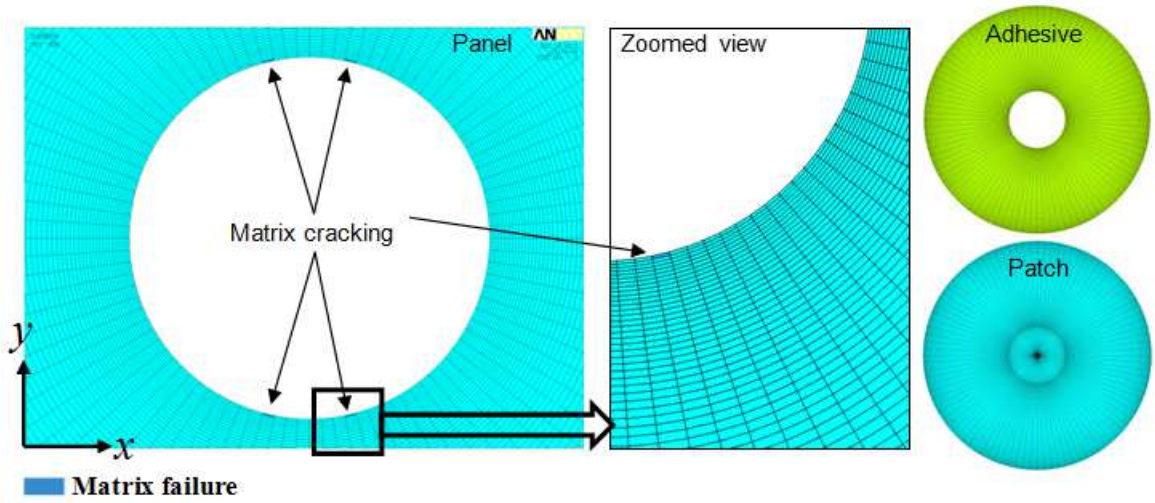

Figure 4.10: Damage initiation site near transverse edge of hole in single sided repaired panel $[0°]_4$ at a load of 8.68 kN

The damage prorogation shown in Fig. 4.11 reveals that, as the load increase, the damage in panel keeps accumulating around the hole edge with extensive matrix cracking followed by localized fiber tensile failure. The damage initiation in adhesive layer is observed near the hole edge due to high stress concentration which is shown in Fig. 4.11 (b). The failure of elements in adhesive layer is due to excessive shear stress leading to partial debonding of patch. This localized debonding of patch from the panel reduces effective area for the load transfer through it. It can be observe from Fig. 4.11 (e) that the damage propagation in adhesive layer intensifies with increasing load and the it grows towards the patch edge followed by partial patch debonding initiating at longitudinal patch overlap edge. With further increasing load, the damage in adhesive layer propagates towards the transverse edge of the patch. However, one can notice from Fig. 4.11 (d) & (g) that the damage in panel propagates with longitudinal splitting of 0° fibers along the loading direction ($x-$axis) from both side of the hole edge. The failure in patch as shown in Fig. 4.11 (f) & (i) reveals only localized matrix cracking.

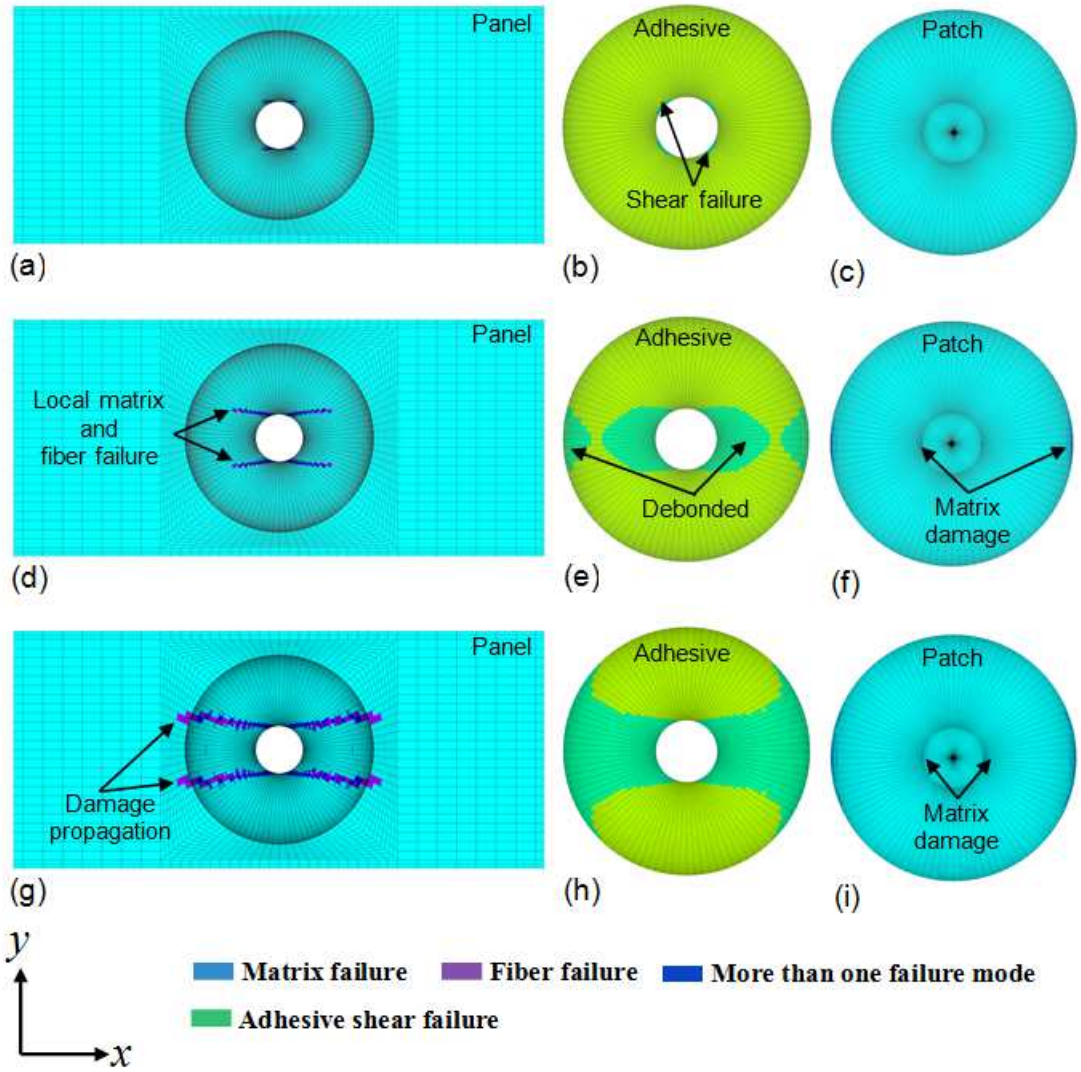

Figure 4.11: Damage progression in single sided repaired panel $[0°]_4$ (a−c) 15.88 kN (d−f) 24.19 kN (g−i) 27.18 kN

The final failure of single sided patch repaired panel predicted by PDM and its comparison with experimental result are shown in Fig. 4.12. It is found that as the load reaches to its ultimate value, the shear failure in adhesive layer is complete, leading to full debonding of patch from the panel, and they are shown in Fig. 4.12 (b) & (c) respectively. Only matrix cracking is observed in few elements of debonded patch. The final failure of the panel happens with complete debonding of the patch followed by extensive 0° fiber splitting in the panel, as shown in Fig. 4.12 (a). On comparison, it is found that the damage propagation predicted by PDM is in good agreement with the experimental observation.

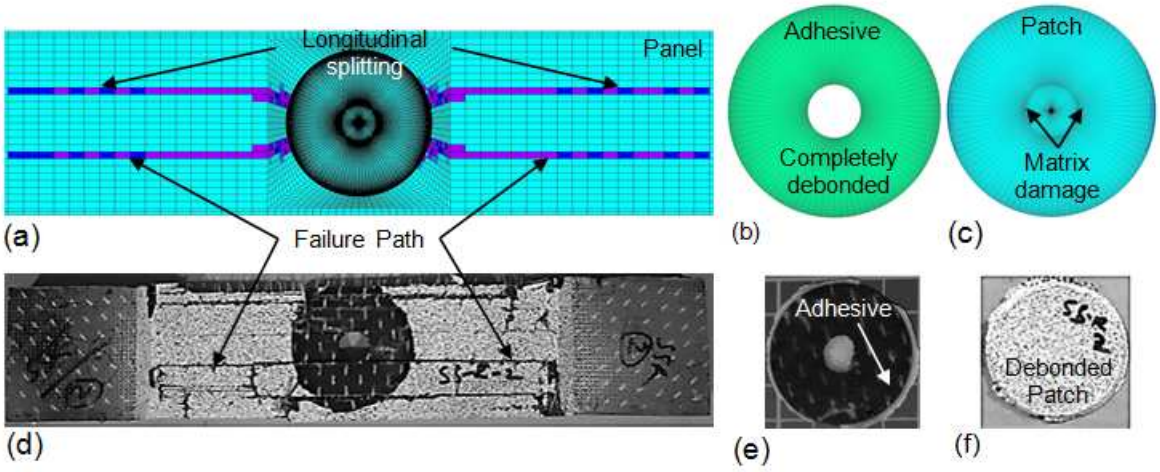

Figure 4.12: Damage mechanism in single sided repaired panel $[0°]_4$ (a−c) damage predicted by PDM (d−f) experimentally observed

4.3.4 Double sided repaired panel

Figures 4.13−4.15 shows the evolution of damage in double sided repaired panel predicted by PDM. In case of double sided repair, damage initiation is observed in panel at a load of 13.72 kN. Tensile matrix cracking is identified as first failure mode initiating at longitudinal overlap edge of the patch due to high stress concentration. The damage initiation location and mode is shown in Fig. 4.13.

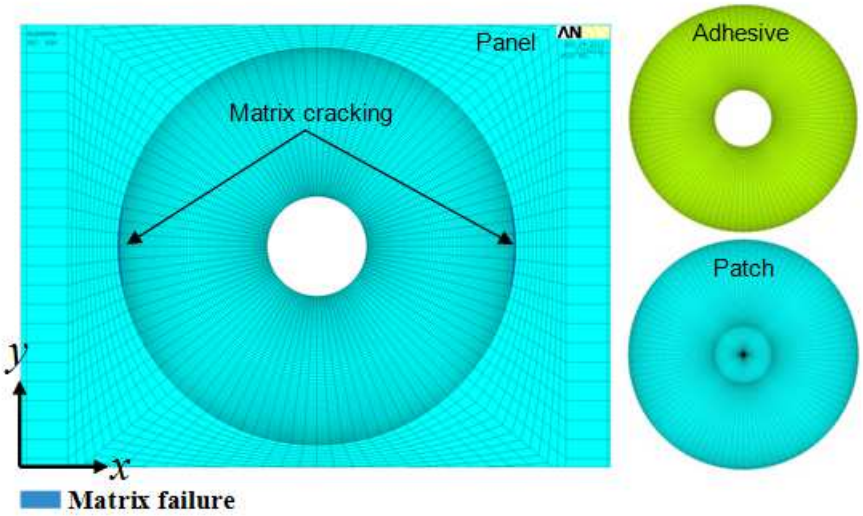

Figure 4.13: Damage initiation site near overlap edge of the patch in double sided repaired panel $[0°]_4$ at a load of 16.77 kN

The damage propagation in panel and patch debnoding due to shear failure in adhesive layer is shown Fig. 4.14. With increasing load, extensive matrix cracking in panel is observed near to patch overlap edge which can be seen from Fig. 4.14 (a).

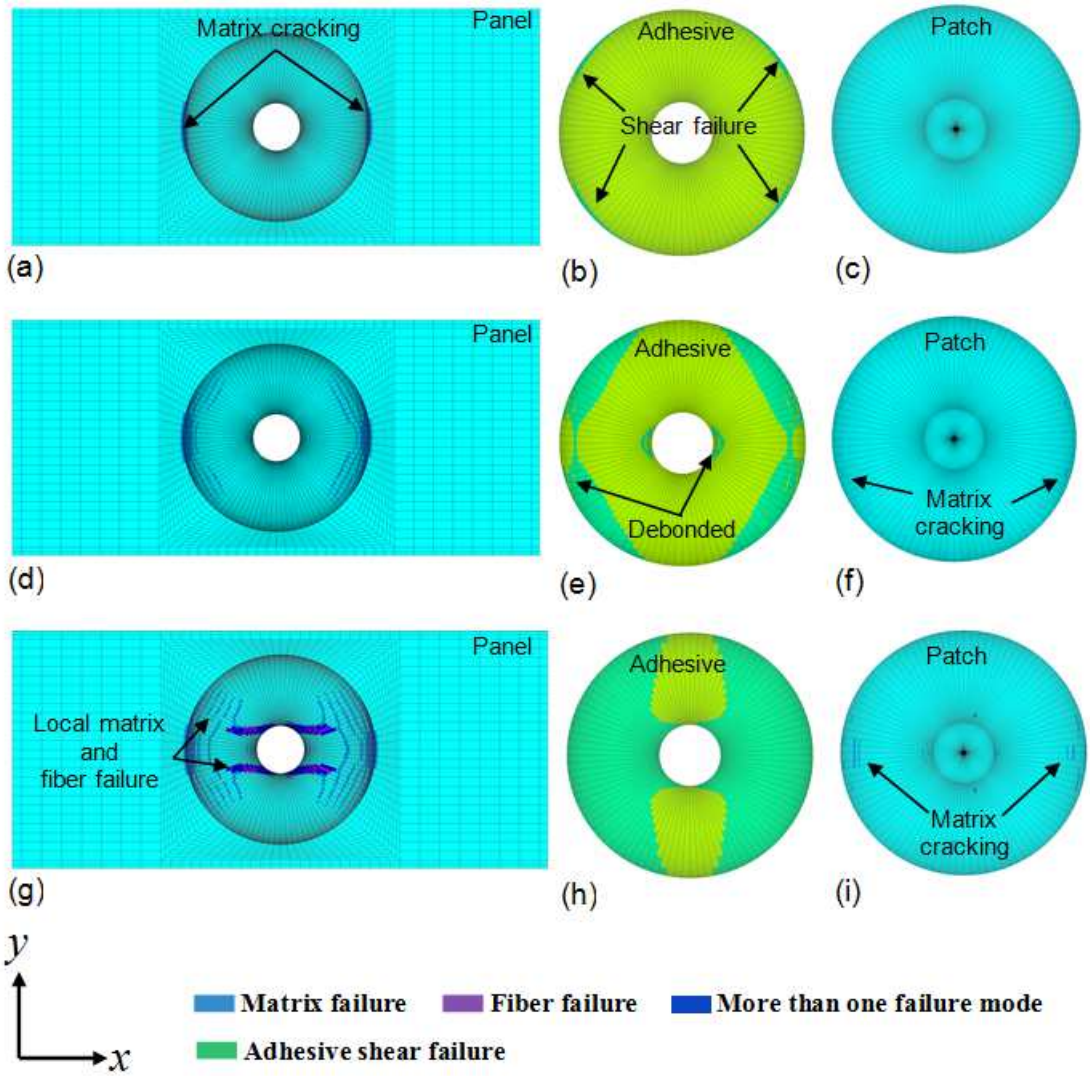

Figure 4.14: Damage mechanism in double sided repaired panel $[0°]_4$ (a−c) 21.34 kN (d−f) 25.13 kN (g−i) 28.83 kN

The shear failure in adhesive layer is found to occur at a load of 19.23 kN at four different high stress concentration locations along the patch overlap edge, as shown in Fig. 4.14 (b). The location of patch debonding initiation predicted by PDM is found to be similar to the results presented in Ref. [76].

At higher load, damage in panel is also found initiating from hole edge in the form of matrix cracking followed by local fiber tensile failure. Also, the patch debonding at higher load shifts towards the hole edge, as in Fig. 4.14 (e). Matrix cracking in few patch elements can be seen from Fig. 4.14 (f). Once the patch is partially debonded, longitudinal splitting of 0° fibers parallel to the loading direction ($x-$axis) is observed in the panel and it is shown in Fig. 4.14 (g). The shear failure in adhesive layer starts growing from hole edge to transverse edge of the patch.

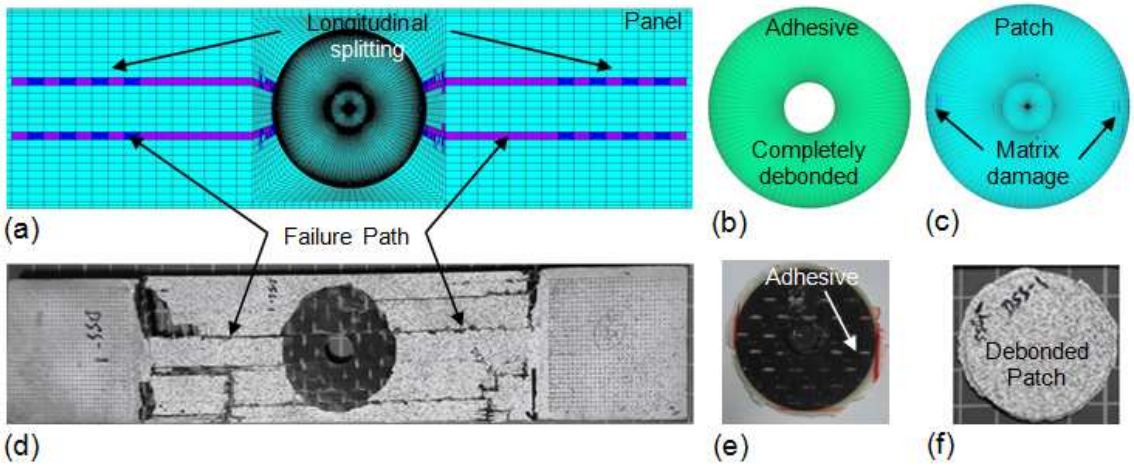

Figure 4.15: Damage mechanism in double sided repaired panel $[0°]_4$ (a−c) damage predicted by PDM (d−f) experimentally observed

As load keeps increasing, the patches fully debond from the panel due to complete shear failure in adhesive layer and final failure of the panel takes place which can be seen in Fig. 4.15 (a) & (b). The final failure of panel also involves extensive 0° fiber splitting. Matrix damage is faintly observed in the debonded patches and it is depicted in Fig. 4.15 (c). The damage propagation path predicted by PDM is found to be in good coherence with the experimental observations which is shown in Fig. 4.15 (d−f) , thereby once again confirming the accuracy of implemented PDM.

4.3.5 Load−displacement behaviour and strength of open cutout and repaired panel: PDM vs. Experiment

The load−displacement behaviour predicted by PDM for the case of open cutout and repaired panels are compared with one obtained from DIC and they are shown in Fig. 4.16. Table 4.3 presents a comparison between PDM simulation (maximum shear stress based) and experimental results in terms of maximum load and displacement value obtained for different cases. The ultimate strength predicted by simulation for all the three specimens are in agreement with the experimental data whereas the displacement is under−predicted by simulation. This can be attributed to the fact that the FE models are inherently stiff as compared to actual fabricated specimen. However, the choice and implementation of composite failure theory is very critical in the accuracy of PDM prediction. Besides this, there are approximations involved in the material property degradation rules as well as degradation factors. The above mentioned factors could be the reason for deviation between PDM and DIC results [170]. It is also found that the tensile strength of double sided repaired panel is more than the single sided repaired one.

4.3.6 Strength of repaired panel: Shear stress vs. Shear strain

Further, maximum shear strain criterion is considered to account for patch debonding due to shear failure of elements in adhesive layer. From PDM simulation, it is found that the damage initiation and its progression in the adhesive layer predicted by maximum shear strain criterion for all the cases are quite similar to the one obtained based on maximum shear stress criteria . The debonding

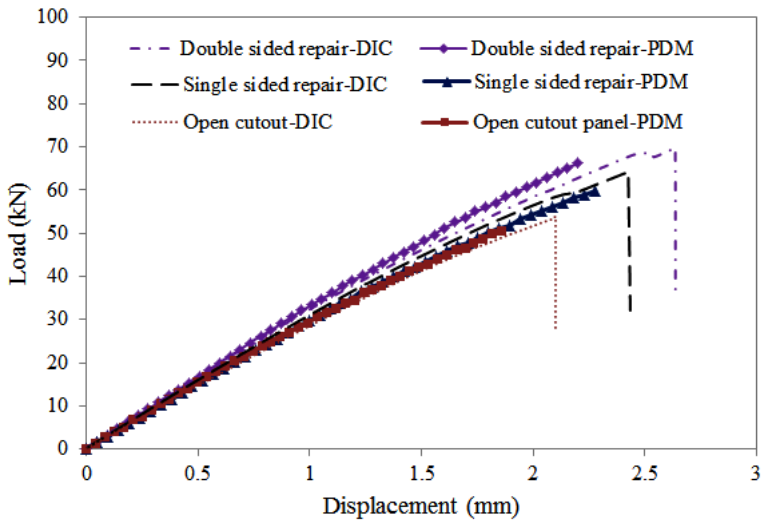

Figure 4.16: Load−displacement curve for open cutout and repaired panels: PDM vs. Experiment

Table 4.3: Maximum strength and displacement for $[0°]_4$ panel.

Specimen	Max. strength (MPa)		Max. displacement (mm)	
	Experiment	PDM	Experiment	PDM
Open cutout	594.11	561.45	2.18	1.90
Single sided repair	704.55	679.52	2.43	2.25
Double sided repair	755.88	741.27	2.50	2.20

load, maximum strength and maximum displacement for repaired configuration obtained from the two criterions are given in Table 4.4.

Table 4.4: Debonding load, maximum strength and maximum displacement predicted by two different failure criteria used for adhesive layer.

Parameter	UD−panel			
	Single sided		Double sided	
	Stress based	Strain based	Stress based	Strain based
Debonding Load (kN)	12.85	17.23	19.23	23.52
Max. Strength (MPa)	679.52	654.67	741.27	748.56
Max. Displacement (mm)	2.25	1.95	2.20	2.10

It can be observed from Table 4.4 that the debonding load in both single and double sided repair predicted by maximum strain failure criteria is significantly higher than the one predicted by maximum stress criteria. The tensile strength predicted by maximum strain failure criteria is lower in case of single sided repair and it is higher in case of double sided repair as compared to the values predicted by maximum stress criteria.

4.4 Progressive failure analysis results: quasi−isotropic panel $[\pm 45/0/90]_s$

4.4.1 Panel with open cutout

Figures 4.17−4.19 presents the development of damage with increasing load in an open cutout quasi−isotropic panel.

The initiation of damage in an open cutout panel is shown in Fig. 4.17. Tensile matrix cracking is identified as initial damage mode and it is firstly observed in 90° ply.

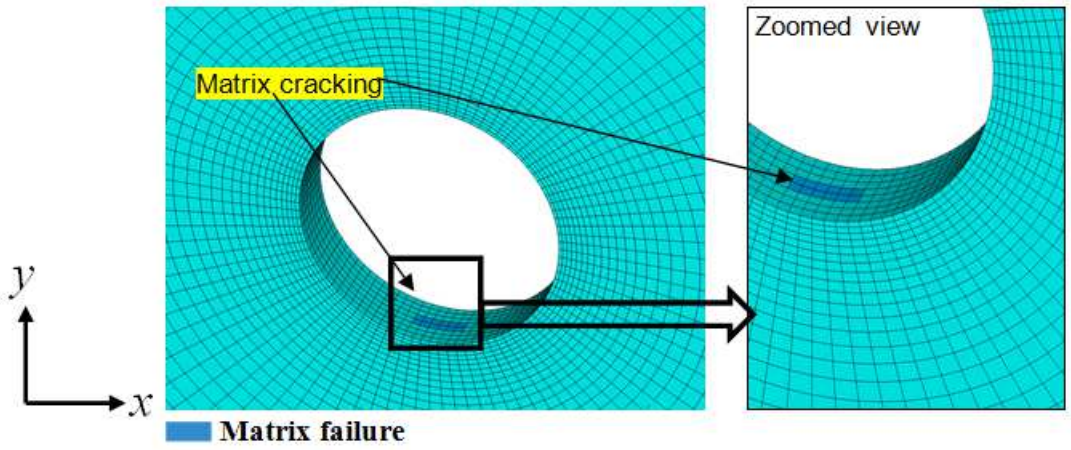

Figure 4.17: Damage initiation site in the 90° layer near transverse edge of hole in an open cutout quasi−isotropic panel $[\pm 45/0/90]_s$ at a load of 2.94 kN

Figures 4.18 shows the layer wise damage progress in an open cutout panel. It is found that the damage emanates from transverse edge of the hole due to high stress concentration in all the plies. One can observe that from ply−wise damage that, as the load increases, the matrix cracks in 90° ply starts growing rapidly in transverse direction across the width of the panel . However, the matrix crack propagates gradually along the fiber direction in 45° plies. Fewer matrix cracks followed by localized fiber tensile failure along with longitudinal split of very short length near the hole edge in 0° ply are observed. On further increase of load, extensive matrix cracking occurs in the plies and then fiber failure starts propagating in +45°, −45° and 0° plies across width of the panel.

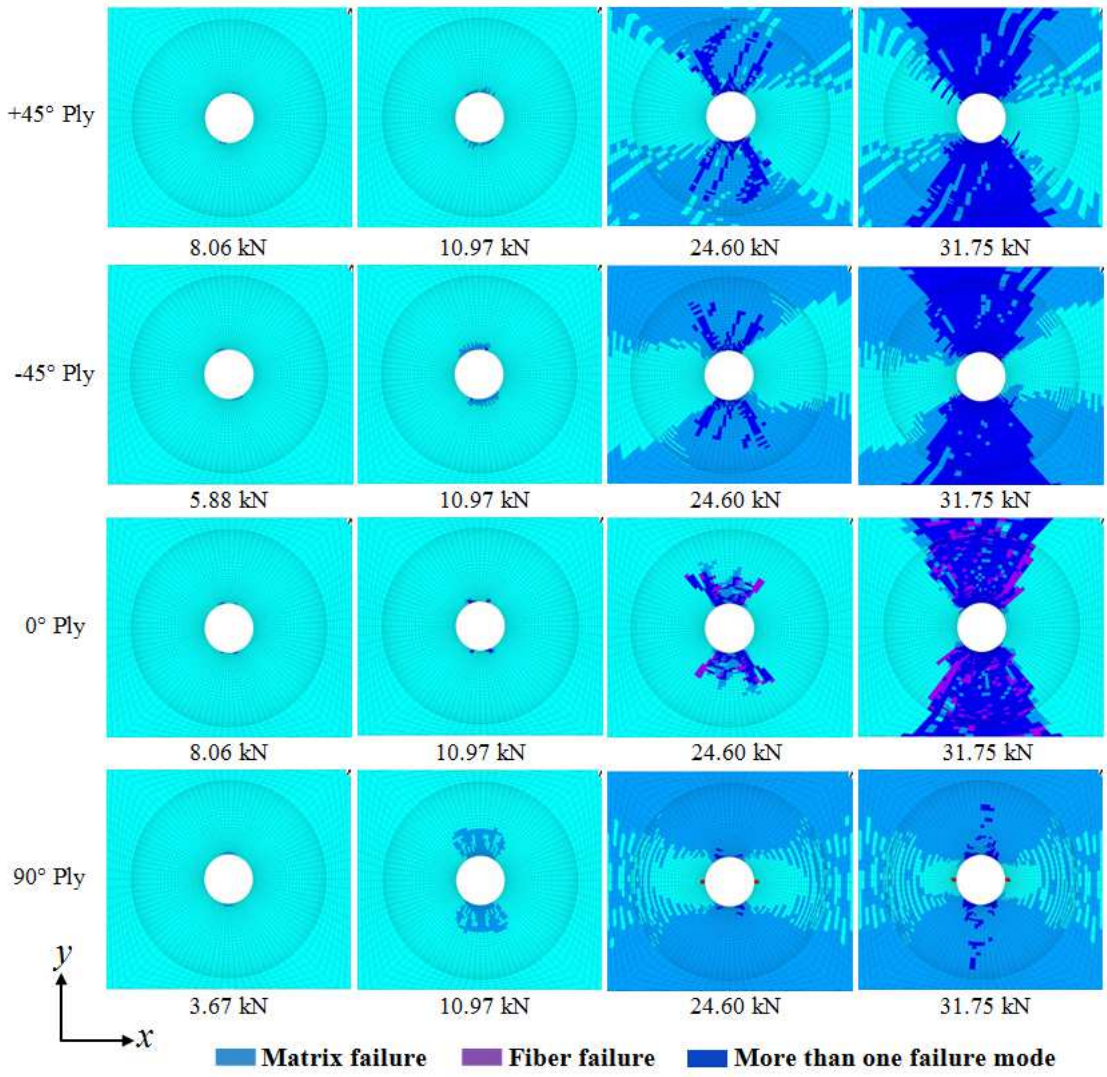

Figure 4.18: Ply wise damage progression in an open cutout quasi−isotropic panel $[\pm 45/0/90]_s$

The final failure in panel predicted by PDM and its comparison with experimental result is shown in Fig. 4.19. It is found that the final failure in panel takes place shortly after total fiber failure in 45° and 0° plies across the panel width. The final damage zone in an open cutout panel predicted by PDM is found to be consistent with the experimental observations as shown in the Fig. 4.19 .

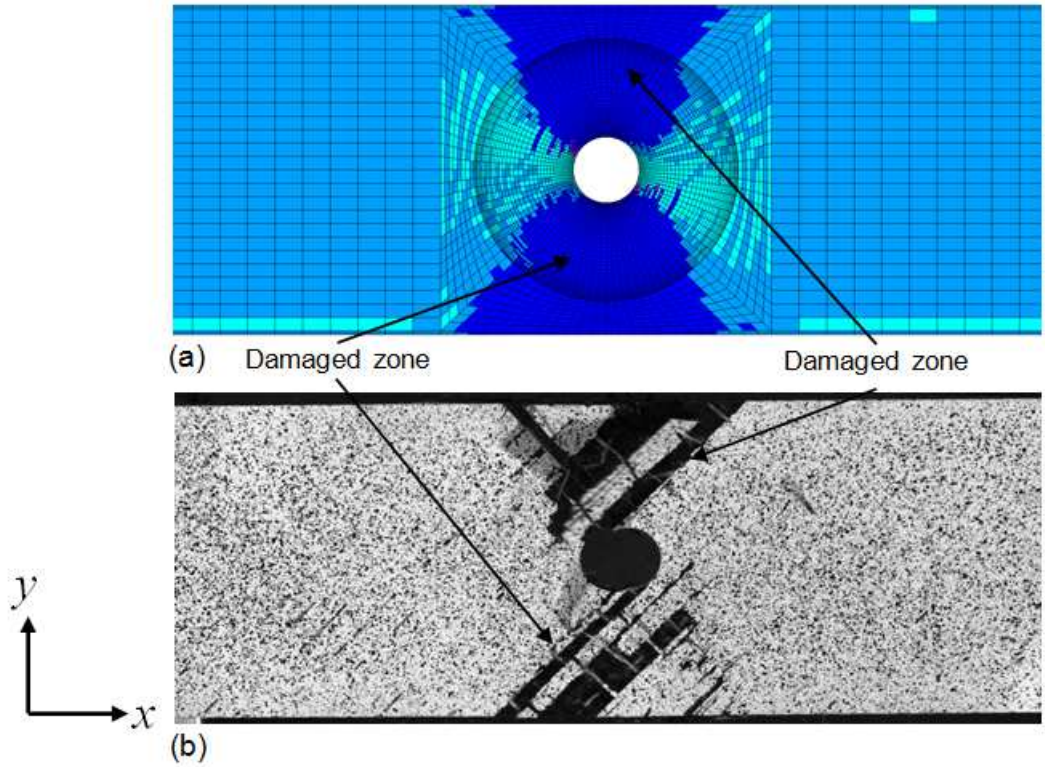

Figure 4.19: Damage mechanism in open cutout quasi−isotropic panel $[\pm 45/0/90]_s$ (a) predicted by PDM (b) experimentally observed

4.4.2 Single sided repaired panel

Figures 4.20−4.21 shows the damage mechanism in single sided repaired panel predicted by PDM. The initiation and propagation of damage in adhesive and patch as well as in surface ply (+45°) of the panel are shown here. Matrix cracking is the damage initiation mode and it is first observed in 90° layer around the hole boundary at a load of 3.05 kN, similar to the one as observed in case of open cutout panel. As the load increases, localized matrix cracking do occur at high stress concentration locations near the patch overlap edge, as in Fig. 4.20 (a). Further, the damage propagation involves matrix cracking and fiber failure in +45° ply along the fiber direction. Initially, partial patch debonding is observed due to shear failure in the adhesive layer near the hole edge, which can be seen in Fig. 4.20 (b). Adhesive failure is then seen near the patch overlap edge with increasing load. However, no failure in patch elements is observed.

The final failure of the panel as shown in the Fig 4.21, takes place soon after complete debonding of the patch. At this juncture, extensive matrix cracking and fiber failure are observed in 45° and 0° plies across the panel width. Also, fewer matrix cracking and localized fiber failures are observed in middle of the patch as shown in Fig. 4.21 (c). Once again the damage zone predicted by PDM is found to be in good coherence with the experimental observations as shown in Fig. 4.21 (d)−(f).

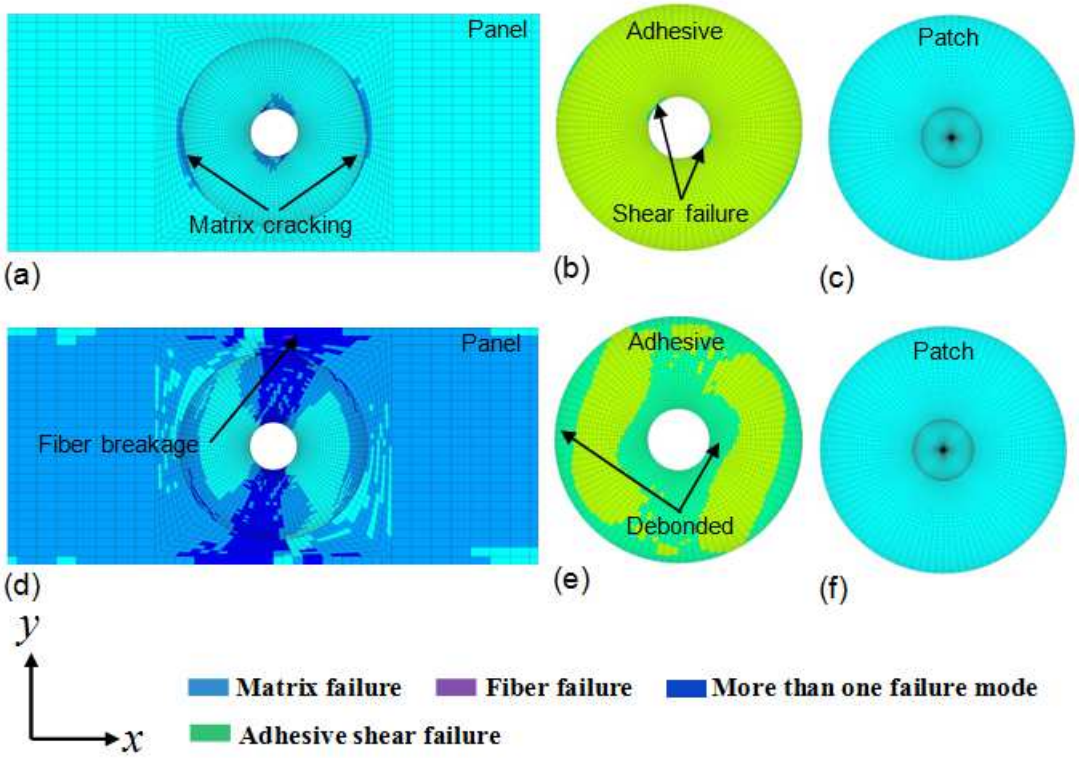

Figure 4.20: Damage progression in single sided repaired quasi−isotropic panel $[\pm 45/0/90]_s$ (a−c) 20.53 kN (d−f) 26.03 kN

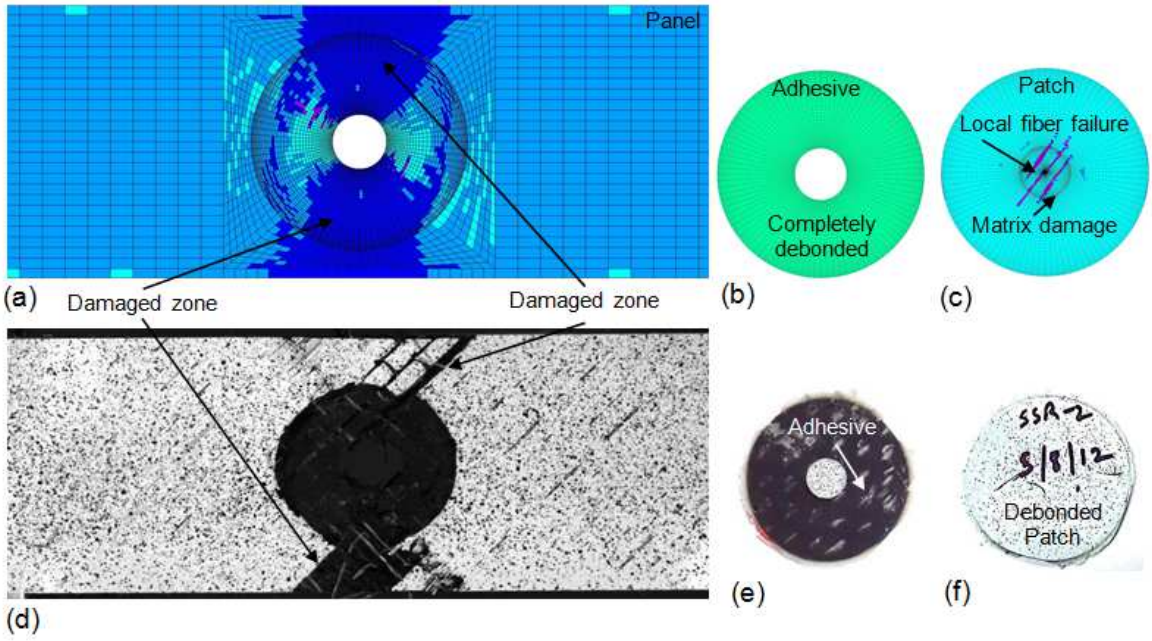

Figure 4.21: Damage mechanism in single sided repaired quasi−isotropic panel $[\pm 45/0/90]_s$ (a−c) damage predicted by PDM (d−f) experimentally observed

4.4.3 Double sided repaired panel

Figures 4.22−4.23 shows the evolution of damage in double sided repaired panel predicted by PDM. In case of double sided repair, the failure initiates with matrix cracking around the hole edge followed by local fiber tensile failure and localized matrix cracking near patch overlap edge with increasing loads. The failure initiation in adhesive layer leading to patch debonding is first observed near the patch overlap edge as shown in Fig. 4.22 (b) and later around the hole periphery at a higher loads. With further increase in load, the damage propagates in panel with extensive matrix cracking across the panel width and fiber failure starts propagating in +45° ply, as shown in Fig. 4.22 (d).

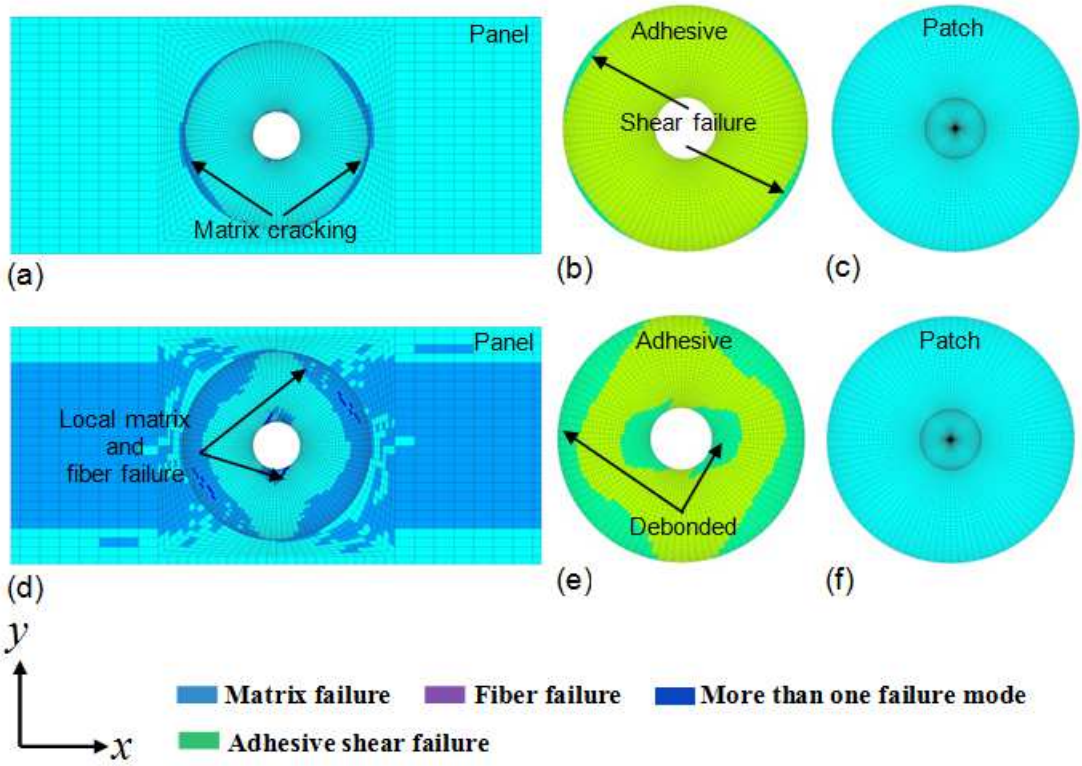

Figure 4.22: Damage mechanism in double sided repaired quasi−isotropic panel $[\pm 45/0/90]_s$ (a−c) 21.99 kN (d−f) 28.71 kN

The final failure of the panel takes place after complete debonding of the patch which can be observed from Fig. 4.23 (a)−(b). No damage is observed in debonded patch. Similar observations are made from the experiment and final failure zone predicted by PDM is found similar to that of experimental behaviour as shown in Fig. 4.23 (d)−(f).

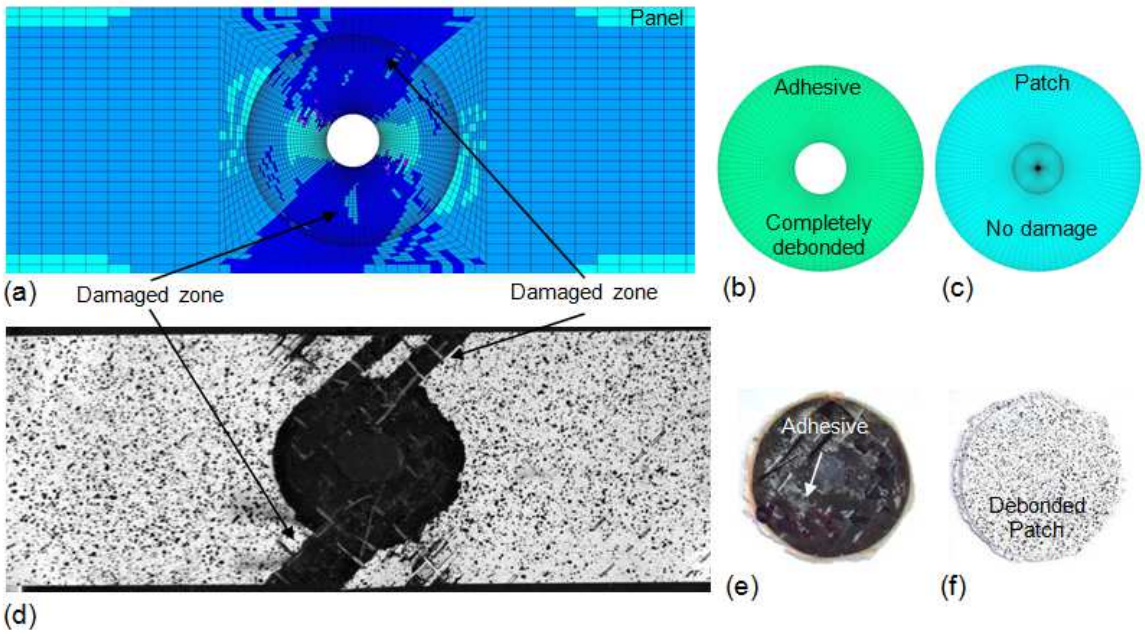

Figure 4.23: Damage mechanism in double sided repaired quasi−isotropic panel $[\pm 45/0/90]_s$ (a−c) damage predicted by PDM (d−f) experimentally observed

4.4.4 Strength of open cutout and repaired panel: PDM vs. Experiment

The ultimate strength and maximum displacement value predicted by PDM for all the three quasi−isotropic panels are shown in Table 4.5. Here the experimental values are compared with the PDM prediction and they are in good agreement. However, the displacement is under−predicted by simulation as explained earlier. Also one can note from the table that the double sided repair specimen has got higher strength because of more reinforcement as well as in−plane behaviour compared to single sided repair. However, in most of the practical application single sided repair is only possible due to no access to other side.

Table 4.5: Maximum strength and displacement for $[\pm 45/0/90]_s$ panel.

Specimen	Max. strength (MPa)		Max. displacement (mm)	
	Experiment	PDM	Experiment	PDM
Open cutout	271.41	265.41	1.90	1.65
Single sided repair	295.83	277.53	2.38	2.00
Double sided repair	351.91	343.89	2.97	2.25

4.5 Mechanics of failure in single and double sided repaired panel

The PDM study reveals that, in repaired panel subjected to tensile load, there are four different critical zones from which damage typically initiates due to high stress concentration. The identified damage prone locations are depicted in Fig. 4.24. To understand the mechanics of single and double sided repaired panel, a comparative plot of longitudinal stress (σ_{xx}) variation at net−section of the panel (pure UD) at a load of 8.5 kN is shown in Fig. 4.25. This figure clearly indicates a drastic reduction of σ_{xx} in case of double sided patch and also the variation is symmetric through the thickness of the panel. In case of single sided patch, σ_{xx} is more at unpatched surface and even it exceeds σ_{xx} value of unrepaired panel. This is because, in single sided bonded repair panel, there is a slight shift in the panel neutral axis and this shift will induce bending stresses in addition to in−plane tensile loading. Therefore stress through the thickness of the panel is linearly increasing in case of single side repaired model whereas it remains constant in case of both unrepaired and double side repaired model. The investigation of failure process of repaired panel also shows a different debonding mechanism in single and double sided repaired panel. In case of single sided repaired panel, the debonding of the patch initiates from zone C at the hole edge whereas it initiates from zone D at the overlap region in case of double sided repaired panel. The debonding mechanism in double sided repair is consistent with the behaviour discussed in literature [76]. However, the reason for a different debonding behavior in single sided repaired panel is attributed to the presence of additional bending phenomena.

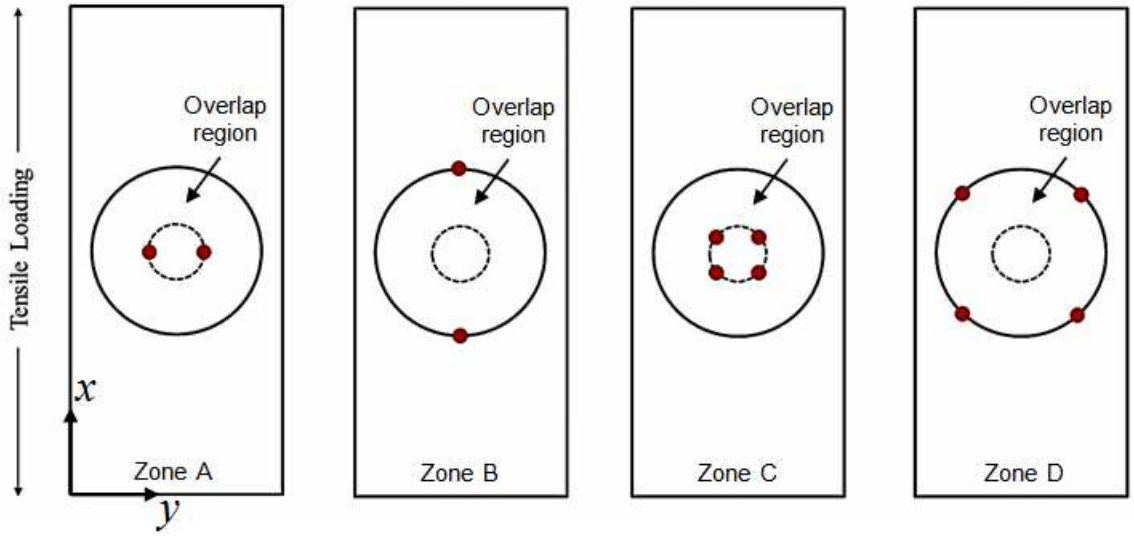

Figure 4.24: Damage prone locations in repaired panel

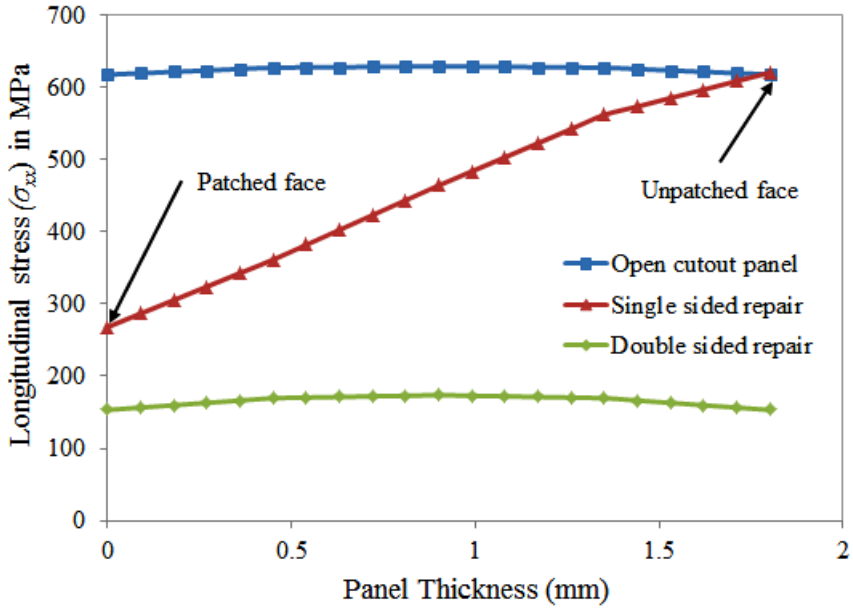

Figure 4.25: Comparison of longitudinal stress through the thickness of an open cutout, single and double sided repaired panel $[0°]_4$ obtained from FEA

4.6 Characteristic distance

The concept of characteristic distance based on a point stress/strain criterion or on an average stress/strain criterion has been used by several researchers [171–173] to predict the joint strength especially in adhesively bonded lap joint configuration because of the existence of singularity effect at the ends of overlap length or at re−entrant corners of joints. The procedure for evaluating the characteristic distance is well documented in the Ref. [171–173]. As per the point stress/strain criteria, the characteristic distance is defined as the distance between the singular point and the point at which the value of stress/strain is equal to failure stress/strain value of the material at experimental failure load [173]. The same approach is used here to evaluate the characteristics distance and assumed that the failure in the joints occurs when maximum shear strain in adhesive layer reaches to failure shear strain value at a distance from the singularity point. The characteristic distance for single and double sided repaired UD panel obtained from finite element analysis at experimental failure load is 0.52 mm and 0.91 mm respectively. For single and double sided repaired quasi−isotropic panel the characteristic distance is 0.11 mm and 0.32 mm respectively.

4.7 Closure

A finite element based 3−D progressive damage model is developed for predicting the failure and post failure behaviour of open cutout and repaired panel under in−plane tensile load. Pure UD $[0°]_4$ and quasi−isotropic $[\pm 45/0/90]_s$ panel of both single and double sided repair configuration are considered in this chapter.

In case of pure UD panel, damage always emanates with matrix cracking around the transverse edge of the hole which is identified as a damage prone location from DIC measurement due to high stress concentration. The damage initiation location is similar for both open cutout and single sided repaired panel. However, in case of double sided repaired panel the damage initiates in the form of matrix cracking at the patch overlap edge due to high stress concentration. The damage propagation in case of pure UD panels always occur perpendicular to the hole edge with extensive longitudinal splitting in 0° fibers running from both side of hole edge towards the tab end parallel to the loading direction which is very much consistent with the experiment. Also, it is found that the debonding load for both single and double sided repair configuration predicted by maximum strain based failure criteria is significantly higher than the one predicted by maximum stress criteria. However, the tensile strength predicted by maximum strain failure criteria is lower in case of single sided repair and it is higher in case of double sided repair as compared to the values predicted by maximum stress criteria.

In case of quasi−isotropic panels, the damage initiates in the form of transverse matrix cracking from the hole edge as expected from DIC measurement and it is first observed in 90° ply for all the cases. Also the fiber failure is firstly observed in 0° ply at the hole edge. The damage in case of quasi−isotropic panel consists of extensive matrix cracking and fiber failures running along it in 45° and 0° plies across the width of the panel. In case of repaired panel, the final failure of both pure UD and quasi−isotropic panel takes place soon after the complete debonding of the patch due to high shear stress in the adhesive layer, as observed in experimental study. However, the mechanism of patch debonding in single and double sided repair for both pure UD and quasi−isotropic panels are found to be different. In case of single sided repaired panel, patch debonding initiates from the transverse edge of the hole whereas it initiates at patch overlap edge in double sided repaired panel.

The load−displacement behaviour predicted by PDM for both pure UD and quasi−isotropic panel configurations are compared with the experimental data from DIC and they are found to be in good agreement. The tensile strength predicted by PDM in case of pure UD open cutout, single and double sided repair configuration presents an error of 5%, 4.5% and 3.3% respectively, in comparison to the experimental results. In case of quasi−isotropic panel, the error in tensile strength of open cutout, single and double sided repair configuration predicted by PDM is 4%, 5.1% and 1.5% respectively, in comparison to the experimental results. between PDM prediction and experimental results. The ultimate strength, damage initiation and its progression as well as damage zone predicted by PDM are found to be consistent with the experimental observations thereby confirming the accuracy of the developed PDM in−conjunction with finite element method.

Till now the behaviour of repaired panel of two different configurations has been studied extensively. However, to improve the performance of bonded repair of composite structures, it is essential to understand the behaviour of thin adhesive layer which plays a critical role in load transfer between the patch and panel. With this in view, the behaviour of thin adhesive layer is analyzed using global−cum−local DIC measurement and the results are presented in the next chapter.

Chapter 5

Strain Measurement in Adhesive Layer and Critical Shear Transfer Length Determination using DIC and FEA

5.1 Introduction

The adhesive layer plays a critical role in transferring the loads between patch and panel in repaired structure and it constitute the weakest link and acts as a common source of failure. An extensive amount of analytical, numerical and experimental research has been carried out to understand the behavior of adhesively bonded joints. A comprehensive review of analytical investigations that has been made on adhesively bonded joints pertaining to both single and double−lap configuration is presented by Banea and da Silva [174], and da Silva et al. [113]. A comparative study on different analytical models for adhesively bonded joints is also reported by da Silva et al. [175]. Most of the analytical models developed for adhesively bonded joints are two−dimensional by nature. These models present global response of the joint and can't account for change in geometry and complex mechanics as well as boundary condition being experienced at the joint. Also, they are formulated assuming linear elastic nature and therefore idealize the response of joint to avoid complexity. To overcome the limitations of analytical models, finite element analysis has been extensively used over the last two decades. A detailed review of several studies that has been carried out on finite element modeling of adhesively bonded joints is presented by da Silva et al. [114] and X He [176]. To validate the numerical prediction researchers have used several experimental techniques such as strain gauges [177–179], moiré interferometry [177, 180], photoelasticity [181] and digital image correlation (DIC) [182–192].

Most of the works exist on adhesive lap joint study between metal (like steel, aluminium) and composites. Adhesively bonded composite joints have also emerged as a potential means of repairing the damaged composite parts for attaining high structural efficiency and improved fatigue life. However, no significant whole field experimental work has been reported yet on analyzing the behaviour

of adhesive element in patch repaired composite panel. To improve the performance of bonded repair of composite structures, it is essential to understand the strength, stress/strain distribution and failure mechanism of adhesively bonded joints between composite adherends. Assessment of joint behaviour between composite adherend is very critical from design stand point.

In this chapter, the behaviour of adhesively layer in single and double sided patch repaired CFRP panels are investigated experimentally involving DIC. In first part of the experimental study, DIC technique is employed for material characterization of adhesive. In second part, critical strain zone in thin adhesively layer is detected using global−cum−local 2D−DIC measurement. Longitudinal, peel and shear strain distribution in the adhesive layer are also analyzed. Effective load/shear transfer length which is an essential parameter in patch design in repair domain is also predicted based on global strain analysis and further it is compared with the one predicted from FEA. Localized strain analysis using magnified optics is performed to get an insight into complex and localized strain field over the thin adhesive layer especially at critical zones leading to damage initiation. The critical failure mechanism is also investigated and correlated with the load−displacement behaviour. The influence of adhesive nature (ductile or brittle) on strain distribution in adhesive layer is also closely examined. Finally, the results obtained from FEA and DIC are compared with one another.

5.2 Determination of adhesive properties using 3D−DIC

5.2.1 Adhesive materials detail

In this study, two different types of adhesive materials namely Araldite AV138/HV998 and Araldite 2011 are used. Both are two−part epoxy based adhesive and they are manufactured by Huntsman [143]. Araldite AV138/HV998 adhesive is very brittle in nature whereas Araldite 2011 is an intermediate strength and high toughness adhesive.

5.2.2 Fabrication of adhesive specimens

Adhesive specimens are prepared as per ASTM D−638 standard [151]. The specimen dimensions are same as that of epoxy−matrix coupons as shown in Fig. 2.15. However, a different methodology is adopted to fabricate the adhesive specimens. The adhesive specimens are casted in split molds made of aluminium which is shown in Fig. 5.1. The aluminium mold is prepared with wire EDM (Electrical Discharge Machining) and then cleaned with acetone. The mold is placed on a flat Perspex sheet and a release agent (wax) is applied on interior surface of the mold to enable easy separation of cured adhesive. The resin (AV138) and hardener (HV998) is taken in the ratio of 10:4 by weight and mixed thoroughly. The resin−hardener mixture is poured into mold and then allowed for curing at room temperature. Araldite 2011 mixture supplied in tubes by manufacturers is poured into mold by using an applicator gun recommended by supplier (Huntsman), and it is also cured at room temperature. The cured adhesive samples are shown in Fig. 5.2 (a) & (b).

5.2.3 Experimental setup and test procedure

The details of experimental setup, test procedure are presented in chapter−2. The test for material characterization of adhesive is performed in displacement controlled mode and the test speed is fixed

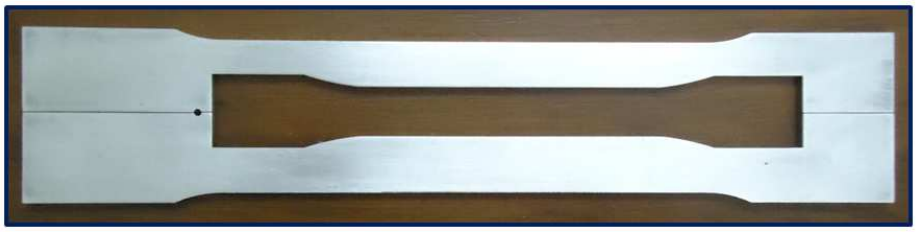

Figure 5.1: Split aluminium mold used for casting of adhesive specimens

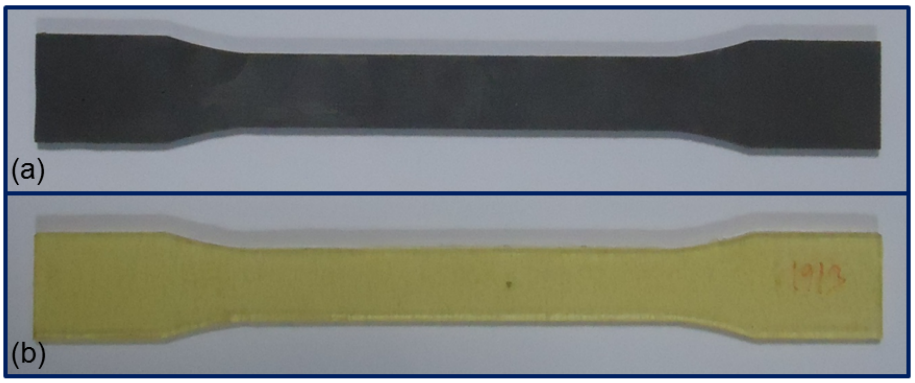

Figure 5.2: Adhesive specimen casting (a) Araldite AV138 / HV998 specimen (b) Araldite 2011 specimen

in accordance with ASTM standard [151]. Adhesive specimens are tested at a tensile loading rate of 3.75 mm/min and 15 images per second are grabbed using Vic−Snap software to obtain more data points for smooth experimental plot. The load and displacement data for each image being grabbed is recorded using a data acquisition system during each test. An axial extensometer of 20 mm gauge length is also attached to get a comparison between the properties obtained from DIC technique and extensometer.

5.2.4 Properties of adhesive material

The post−processing of grabbed images are performed in Vic−3D software. The area within the gauge length (20 mm) of extensometer is selected as region of interest (ROI) towards post−processing. The spatial resolution of ROI is 14.6 pixels/mm. A subset size of 29 x 29 pixels^2 is chosen along with a step size of 7 pixels for performing DIC calculations. The stress−strain curve for Araldite AV139/HV998 and Araldite 2011 obtained from DIC technique and extensometer is shown in Fig. 5.3 and Fig. 5.4 respectively. The Young's modulus (E) is estimated from initial slope of stress−strain curve and the Poisson's ratio (ν) is determined from the slope of lateral to linear strain plot obtained from DIC. It can be observed from the figure that the modulus value from DIC technique is closely matching with the extensometer data. The error between the DIC and extensometer value is 0.5% in case of Araldite AV138/HV998 adhesive and it is 1.9 % for Araldite 2011 adhesive. Estimated material properties of both the adhesives from the 3D DIC measurement are shown in Table 5.1.

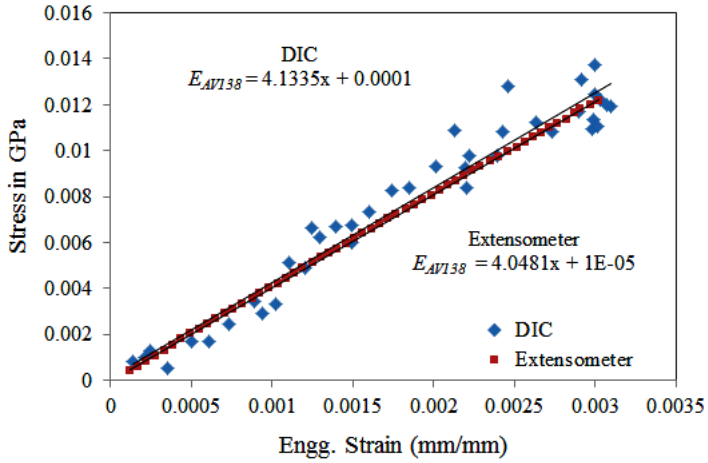

Figure 5.3: Comparative plot of stress−strain curve obtained from DIC and extensometer: Araldite AV138/HV998 adhesive

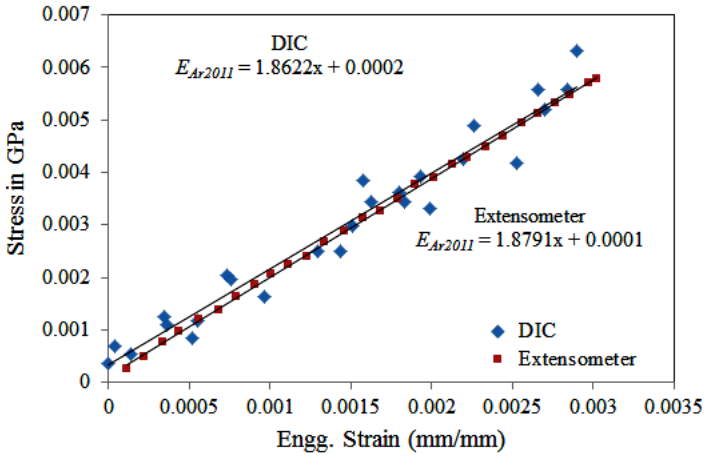

Figure 5.4: Comparative plot of stress−strain curve obtained from DIC and extensometer: Araldite 2011 adhesive

In case of Araldite 2011 adhesive, yield strength (σ_y) is obtained based on traditional 0.2% offset method $\sigma_{0.2}$ and it is found to be 24.35 MPa. The ultimate tensile strength (σ_{max}) and strain to failure for Araldite 2011 adhesive as deduced from stress−strain curve are 33.56 MPa and 8.83% respectively.

The carbon fiber mat used in this chapter is manufactured by Hindustan Technical Fabrics Ltd. India, having a weight of 230 gsm. The matrix is made from epoxy resin LY−556 mixed with hardener HY−951 supplied by Huntsman. The composite laminates are fabricated by hand layup technique as discussed in chapter−1. The in−plane material properties of CFRP composite laminate (230 gsm) as per ASTM standards and out of plane properties are determined by following the same procedure as discussed in chapter−2. The estimated CFRP properties are also summarized in Table 5.1.

Table 5.1: Material properties of adhesives and CFRP laminate (230 gsm) estimated using DIC technique.

Adhesive Properties		
	Araldite 2011	Araldite AV138/HV998
Young's modulus E (GPa)	1.86	4.13
Poisson's ratio (ν)	0.38	0.41
CFRP Composite Laminate		
Longitudinal modulus , E_{xx} (GPa)	84.16	
Transverse modulus, $E_{yy} = E_{zz}$ (GPa)	7.12	
Shear moduli, $G_{xy} = G_{xz}$(GPa)	3.30	
Shear modulus, G_{yz} (GPa)	2.47	
Poisson's ratio, $\nu_{xy} = \nu_{xz}$	0.31	
Poisson's ratio, ν_{yz}	0.43	

5.3 Specimen configurations and experimental methodology for adhesive strain measurement using DIC

5.3.1 Fabrication of patch repaired specimens

The typical model of the repaired panel is shown in Fig. 5.5. Both patch and panel are made of unidirectional carbon/epoxy composite laminate (carbon fiber mat is of 230 gsm) and are fabricated by the hand layup technique as explained in chapter−2. The length (L), width (W) and the thickness (t) of the panel are 250 mm, 50 mm and 1.6 mm respectively. The stacking sequence in the panel is $[0°]_4$ and fibers are oriented along the loading direction. A circular hole of 10 mm diameter (d) is drilled at the center of the panel using a diamond coated drill bit supplied by SECO−Jabro Tools. The hole is drilled to simulate the effect of damage removal as it happens in the case of low velocity impact damage. The panel with open hole is repaired with adhesively bonded rectangular patch having a stacking sequence of $[0°]_3$. Both single and double sided patch repair configurations are studied. The length (L_p), width (W_p) and thickness (t_p) of the patch are 60 mm, 50 mm and 1.2 mm respectively. Patch is bonded over the damaged area of panel using an adhesive of thickness t_a and then it is allowed to cure at room temperature. No filler material is used to fill the open hole in the panel before bonding the patches. Beveled aluminium tabs of dimension 50 mm x 50 mm x 2 mm are bonded at each end of the specimen for gripping purpose.

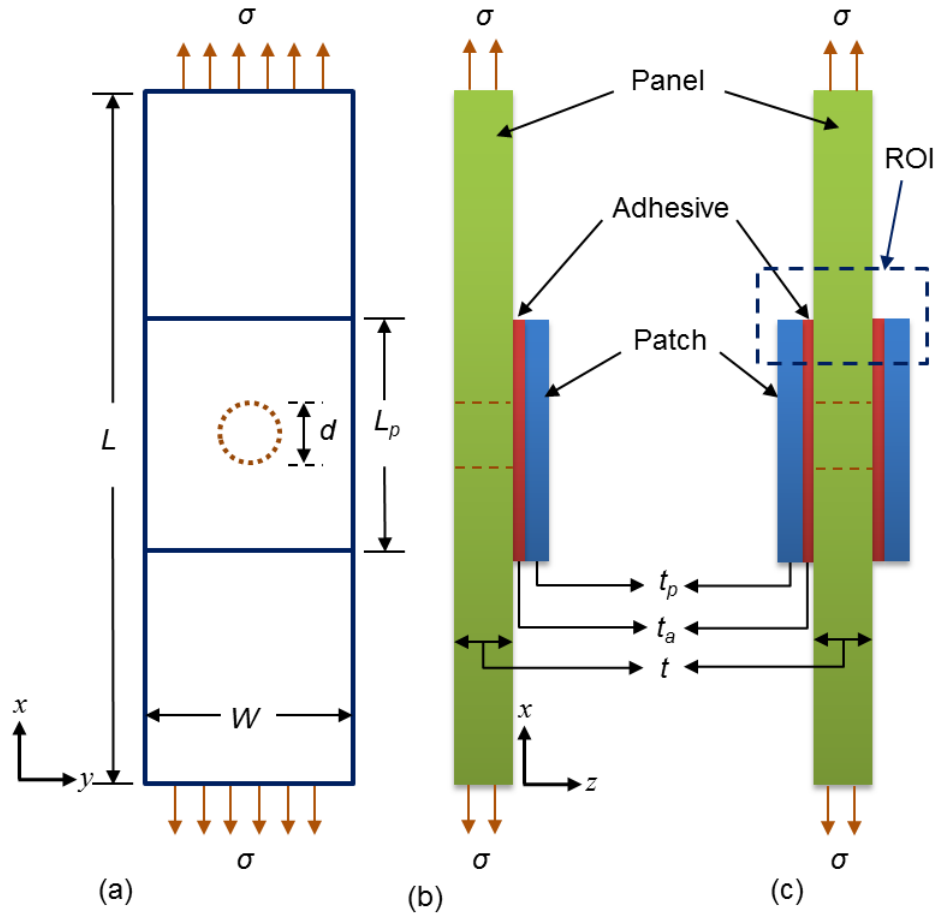

Figure 5.5: Specimen geometry of adhesively bonded patch repaired CFRP panel (a) front view (b) side view of single sided repair configuration (b) side view of double sided repair configuration

5.3.2 Adhesive thickness measurement

The adhesive thickness at interface between patch and panel is measured by an optical microscope (Olympus STM6) using an objective lens (Olympus MPLFLN 10x / 0.30) at a magnification of 10x. Figure 5.6 shows the image taken from optical microscope to evaluate the adhesive thickness in repaired panel. The measurement is taken at different locations and the average value is reported. The average adhesive thickness for a panel repaired with Araldite 2011 and Araldite AV138/HV998 adhesive are 0.21 mm and 0.2 mm respectively.

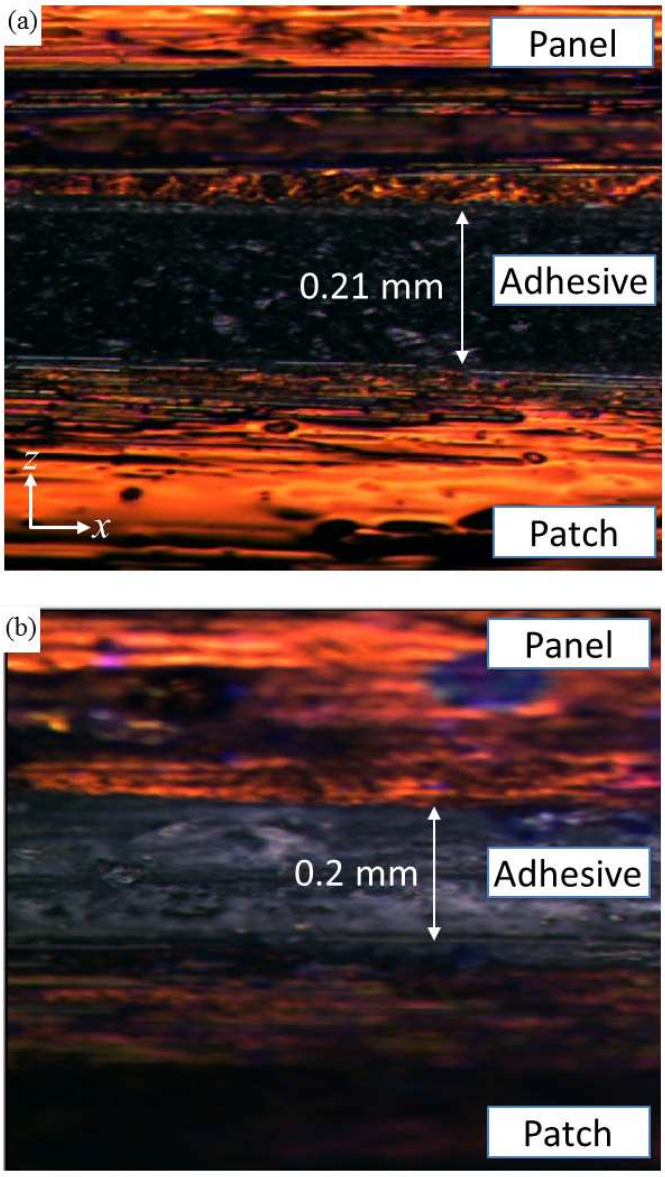

Figure 5.6: Adhesive thickness measured using optical microscope at a magnification of 10x (a) Araldite 2011 (b) Araldite AV138/HV998

5.3.3 Experimental setup and test procedure

To perform the DIC measurement, random speckle patterns are produced over the specimen surface using an acrylic paint of titanium white/carbon black color and the resulting average speckle diameter is found to be 38 μm. Two dimensional DIC setup is employed to capture the whole field strain developing in the adhesive layer between patch/panel interfaces. At first, whole field strain distribution is obtained along the entire length of adhesive layer such that the global behaviour of adhesive can be analyzed. For this purpose a TAMRON lens (Model: SP AF 180mm f/3.5 Di) mounted to the CCD camera is used. The camera is kept at distance of 0.65 m from the specimen surface so that entire adhesive layer could be captured during the test. Later, the localized behaviour of adhesive layer is investigated at critical areas such as patch overlap edge using magnified optics involving InfiniProbe TS−160 lens (from Infinity Photo−Optical Company) thereby by providing a magnification range of 0−16x. The working distance of camera from specimen surface is 64 mm as shown in Fig. 5.7. The specimen is fixed in hydraulic grips and camera is aligned perpendicular to ROI (region of interest). The ROI near the patch edge as shown in Fig. 5.5 (c) is zoomed in and tensile load is applied at a loading rate of 1 mm/min and 10 images per second are grabbed during the test.

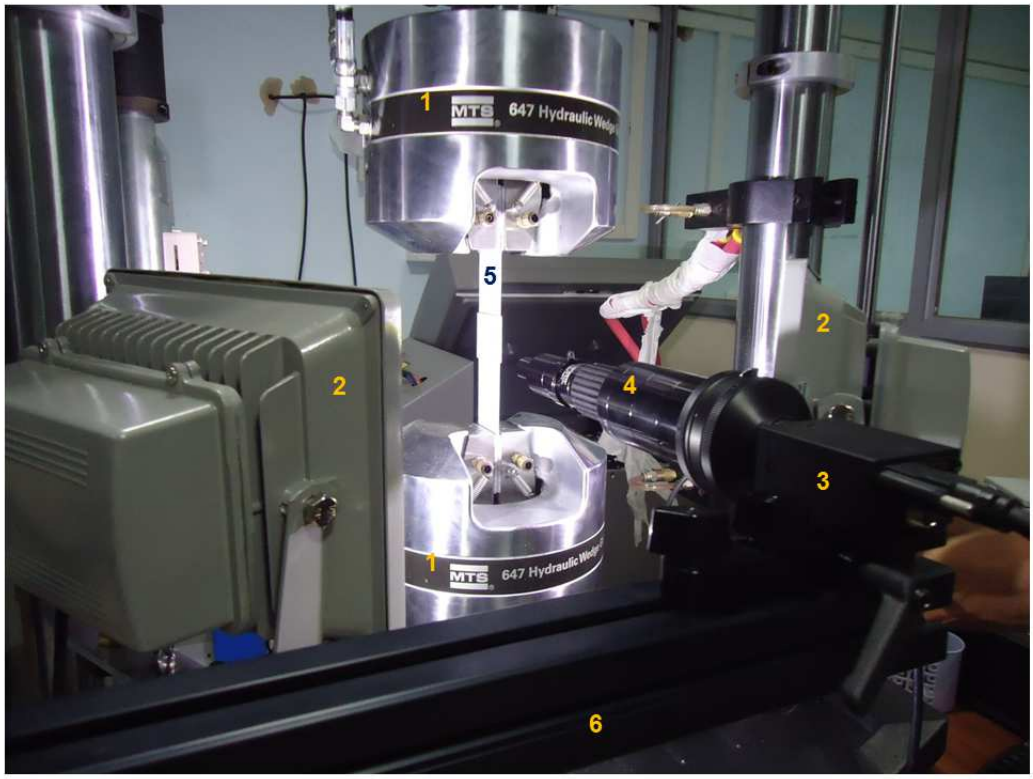

1. Hydraulic wedge grip 2. Light source 3. CCD camera 4. Probe lens 5. Specimen 6. Tripod

Figure 5.7: Experimental setup for localized adhesive strain measurement involving 2D DIC with tube lens

5.4 Global whole field strain analysis on Araldite 2011 adhesive layer: double sided patch repair configuration

In repaired panel the load is taken by the bonded patch through the adhesive layer over the damaged area. At first, the critical load transfer zone/ effective load transfer length is identified based on global response of adhesive layer by characterizing the strain field over the full length of adhesive layer between patch and panel. An area of 3.48 mm x 65 mm is chosen for correlation along with subset size of 21 x 21 pixels^2 and step size of 5 pixels. The spatial resolution is 26 pixels/mm.

5.4.1 Longitudinal strain (ε_{xx}) distribution

Figures 5.8 (a) and 5.9 (a) shows longitudinal strain (ε_{xx}) distribution in double sided patch repair configuration at 38.5 kN (intermediate load level) and 50.5 kN (load just before the patch debonding initiation) which corresponds to 54% and 70% of the ultimate load respectively. The longitudinal strain in panel is found maximum near the patch edge and it is highly concentrated around the root of adhesive joint. The variation of longitudinal strain in panel along line a−a at both the load level is shown in Fig. 5.10. The longitudinal strain value at 54% of failure load is 0.63% near the patch edge and it reduces rapidly as one moves away from patch edge towards the panel center (or cutout), reaching a value of 0.27% strain in center of the panel. This signifies that the panel is substantially loaded only over a small length near the root of adhesive joint whereas it is lightly loaded away from overlap edge (reduces almost 57%). The longitudinal strain distribution in panel at 70% of failure load also shows a similar variation except with higher magnitude, as shown in Fig. 5.9 (a). One can infer that the major portion of load is being transferred from panel to patch over a small zone which is termed as effective load transfer zone and the length of this zone is referred as effective load transfer length (L_e), which is shown in Fig. 5.8 (a). This is also known as essential overlap length in repair domain. It can be obtained from longitudinal strain variation along panel length extracted at a load just before the patch debonding initiation i.e, at 70 % of failure load which is shown in Fig. 5.10. A curve fit is obtained for extracted strain profile and the parameter L_e is deduced, which is approximately 17 mm i.e., about 28.3% of total the patch length.

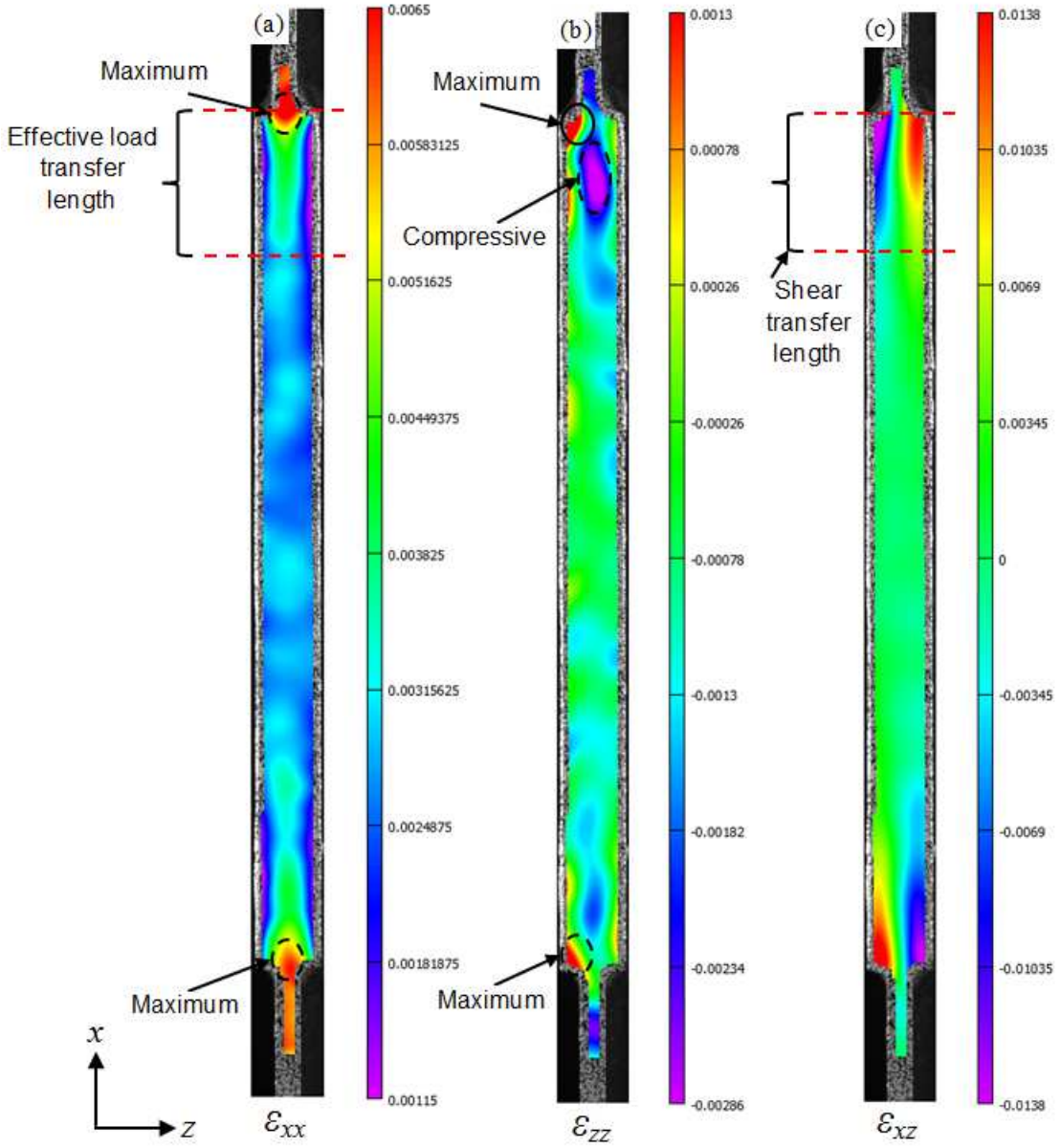

Figure 5.8: Strain distribution in panel, patch and adhesive layer in symmetrical patch repair configuration at 54% of failure load in case of Araldite 2011 (a) ε_{xx} (b) ε_{zz} (c) ε_{xz}

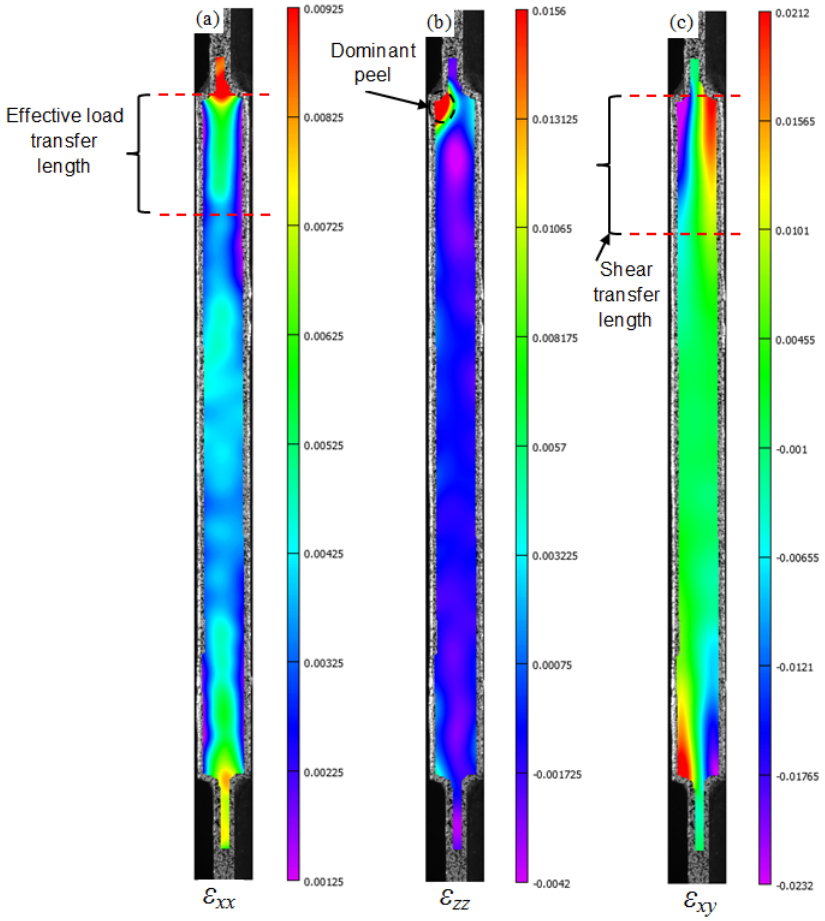

Figure 5.9: Strain distribution in panel, patch and adhesive layer in symmetrical patch repair configuration at 70% of failure load in case of Araldite 2011(a) ε_{xx} (b) ε_{zz} (c) ε_{xz}

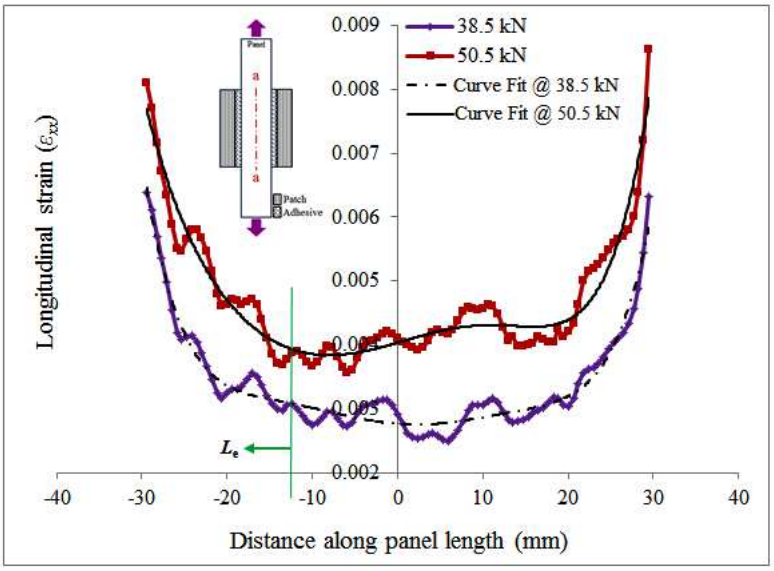

Figure 5.10: Longitudinal strain variation in CFRP panel under double sided patch at 54% and 70% of failure load (Araldite 2011)

5.4.2 Peel strain (ε_{zz}) distribution

Figures 5.8 (b) and 5.9 (b) shows peel strain (ε_{zz}) distribution at 38.5 kN and 50.5 kN of load level. At both the load levels the peel strain is found to be maximum at patch overlap edge confined to a narrow zone between panel/adhesive and adhesive/patch interfaces. On further observation one can find a region of dominant compressive strain just below the patch edge (black dotted loop). This behaviour seems obvious because the extreme patch overlap edge would peel away from the panel due to high peel strain inducing a compressive strain just below the high peel zone.

The variation of peel strain in left adhesive layer along bond length across line b−b at 54% and 70% of failure load is shown in Fig. 5.11. At both load level, the behaviour of peel strain variation is found similar except that the asymmetry is more pronounced at 70 % with larger strain on top end of left side adhesive layer. Asymmetry in peel strain distribution developed at higher load level which could be due to debond initiation since strain distribution is found to be symmetric at lower load level. It is found that the peel strain is distinctly high at the end of adhesive layer just near the root or patch overlap edge in comparison to remaining portion of adhesive layer where it is nearly of zero magnitude. However, one can notice that increased load (70% of failure load) has no significant influence on magnitude and variation of peel strain in entire adhesive layer (remains equivalent to zero) but the adhesive portion just at patch overlap edge or near joint corner shows a remarkable increase in peel strain magnitude (almost 12 times more than at 54% of failure load) similar to corner singularity behaviour.

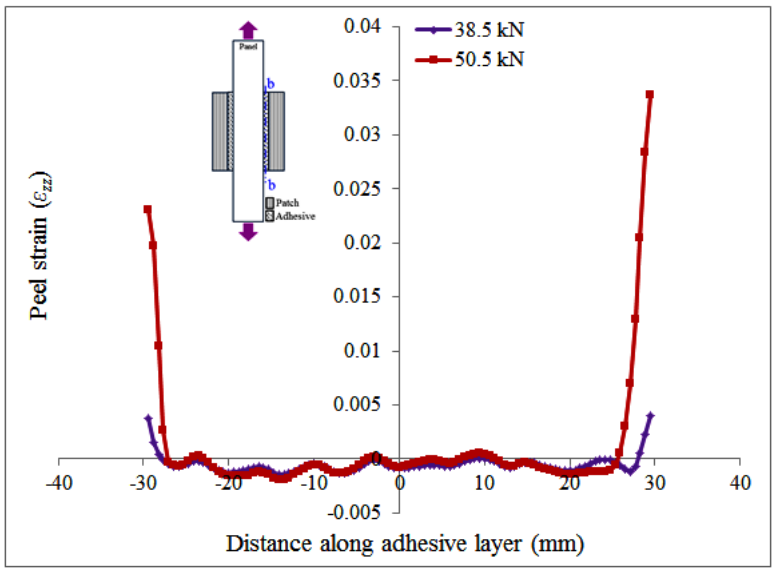

Figure 5.11: Peel strain variation in adhesive layer of double sided patch repaired panel at 54% and 70% of failure load (Araldite 2011)

One can infer from the above discussion that a very small length of adhesive layer near the patch overlap edge would drive the failure in adhesive joint once the peel strain at this location reaches its critical value. The high peel stresses could lead to early failure (interlaminar) in the composites due to its low transverse strength and thereby limiting the joint strength. The peel stresses in adhesive joints with composites can be reduced by some of the techniques proposed by da Silva et al. [193].

5.4.3 Shear strain (ε_{xz}) distribution

Figures 5.8 (c) and 5.9 (c) shows shear strain (ε_{xz}) distribution in double sided repair configuration at 38.5 kN and 50.5 kN load value. The distribution of shear strain at both the load level is found to be similar, with maximum magnitude near the patch overlap edge (2.4% strain) and it reduces progressively over the length of adhesive layer as one moves from that edge towards the panel center. Finally, it reaches to a very low magnitude (0.002% strain) at center of the adhesive layer. Such behaviour is also evident from the line plot of shear strain variation in adhesive layer along the bond length across line b−b, as shown in Fig. 5.12. Also, one can notice that at higher load (70% of failure load) the magnitude of shear strain gets amplified at the patch overlap edge. This observation reveals that the load is transferred from panel to patch through adhesive layer by shear mechanism and it happens over a small zone from the overlap edge. This zone is referred as shear transfer zone and the corresponding length is known as shear transfer length (L_s), as shown in Figs. 5.8 (c) and 5.9 (c). This parameter L_s is defined as the length over which the shear stress in adhesive layer decreases from its maximum value to nearly zero [194]. It can be determined from shear strain variation which is shown in Fig. 5.12 in a similar way as explained earlier and the value of L_s is found to be 18.26 mm (30.4% of total the patch length or 1.8 times the diameter of the cutout).

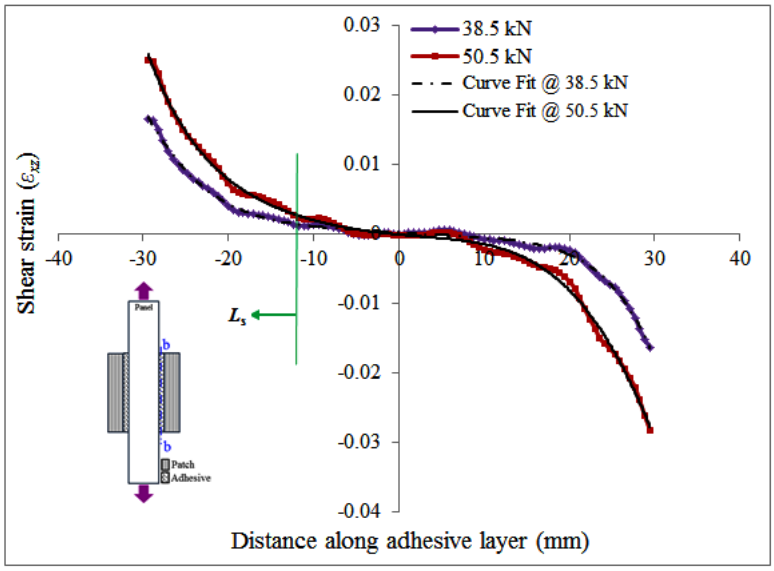

Figure 5.12: Shear strain variation in adhesive layer of double sided patch repaired panel at 54% and 70% of failure load (Araldite 2011)

5.4.4 Failure mechanism and load displacement behaviour

The crack initiation site and its progression in double sided patch repaired panel with increasing load is shown in Fig. 5.13. The damage development process is correlated with the load−displacement behaviour as shown in Fig. 5.14. The crack initiated at adhesive−panel interface in left side patch near the upper root of adhesive layer (dotted yellow line), as shown in Fig. 5.13 (b) and load at this juncture reaches until point b, which can be seen in Fig. 5.14. The crack initiation is consistent with anticipated behaviour because of predominant peel/shear strain concentration zone as explained earlier. The crack initiation is then followed by delamination in panel (solid yellow line) due to high peel strain. It is found that the delamination progressed to a very short length as depicted in Fig. 5.13 (c) till load point c and then the crack suddenly propagated along the panel−adhesive interface on both sides, which is clearly visible from Fig. 5.13 (d) and the load drops to point d, as shown in Fig. 5.14. The panel further takes up the load upto point e and it continues until point f after which leading to catastrophic panel failure. The excessive delamination mechanism observed from Fig. 5.13 (f) depicts the low through thickness strength of composite panel.

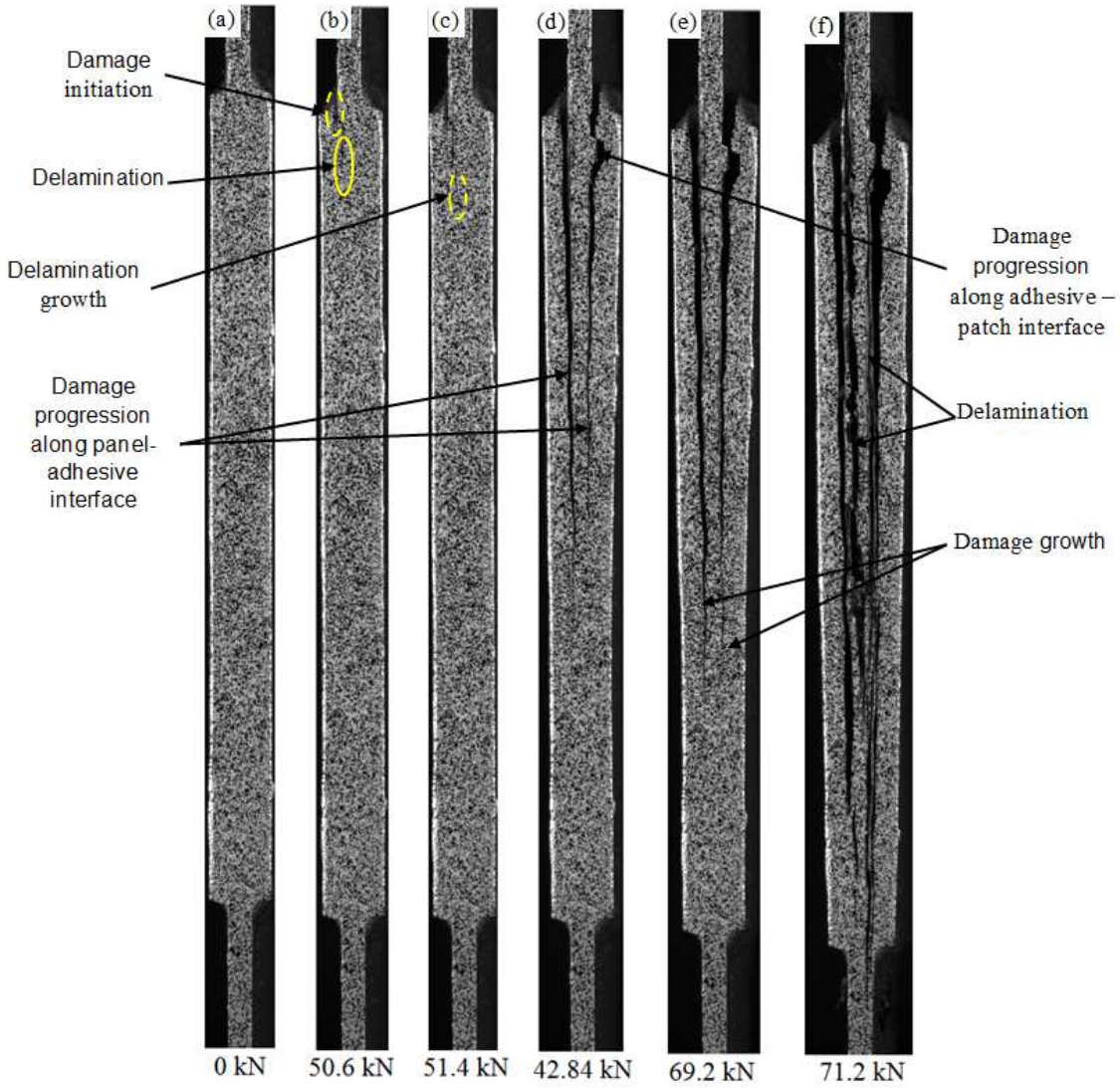

Figure 5.13: Damage progression with increasing load in double sided patch repaired panel repaired with Araldite 2011 adhesive

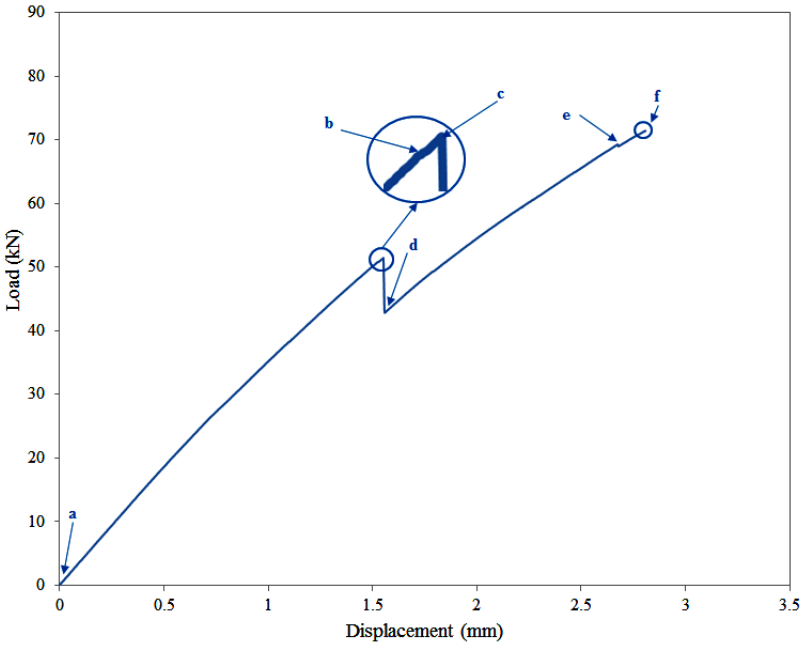

Figure 5.14: Load−displacement curve for DSPR panel

The result presented above shows global behavior of adhesive joint in repaired panel. It provides an estimate of effective load/shear transfer length or minimum overlap length an important parameter essentially useful in the design of patch in repair domain. It is identified that only a small region at patch overlap edge near the root or corner of adhesive joints experienced a very high peel and shear strain and the damage is found to initiate from those region. The global behaviour presents a qualitative representation of damage initiation site. DIC could not capture the exact localized phenomena at the root of adhesive joint responsible for damage initiation due to lower spatial resolution. Also it does not provide an insight into complex mechanism happening there. To achieve higher magnification probe lens is used which provides images with higher spatial resolution at the expense of reducing the region of interest under investigation.

5.5 Localized whole field strain analysis in Araldite 2011 adhesive layer: double sided patch repair configuration

5.5.1 Straight edge patch

The longitudinal (ε_{xx}), peel (ε_{zz}) and shear strain (ε_{xz}) distribution in adhesive layer of double sided patch repaired panel at a load of 13.35 kN is shown in Fig. 5.15. The ROI for correlation corresponds to a zone of 4.14 mm x 4.36 mm respectively. The spatial resolution is 417.8 pixel/mm. A subset size of 71 x 71 pixels^2 with a step size of 7 pixels is chosen for correlation. It is found that the magnified optics facilitates correlation at extreme edge of the patch near the root of adhesive joint which would help in investigating the localized behaviour in critical zone responsible for failure.

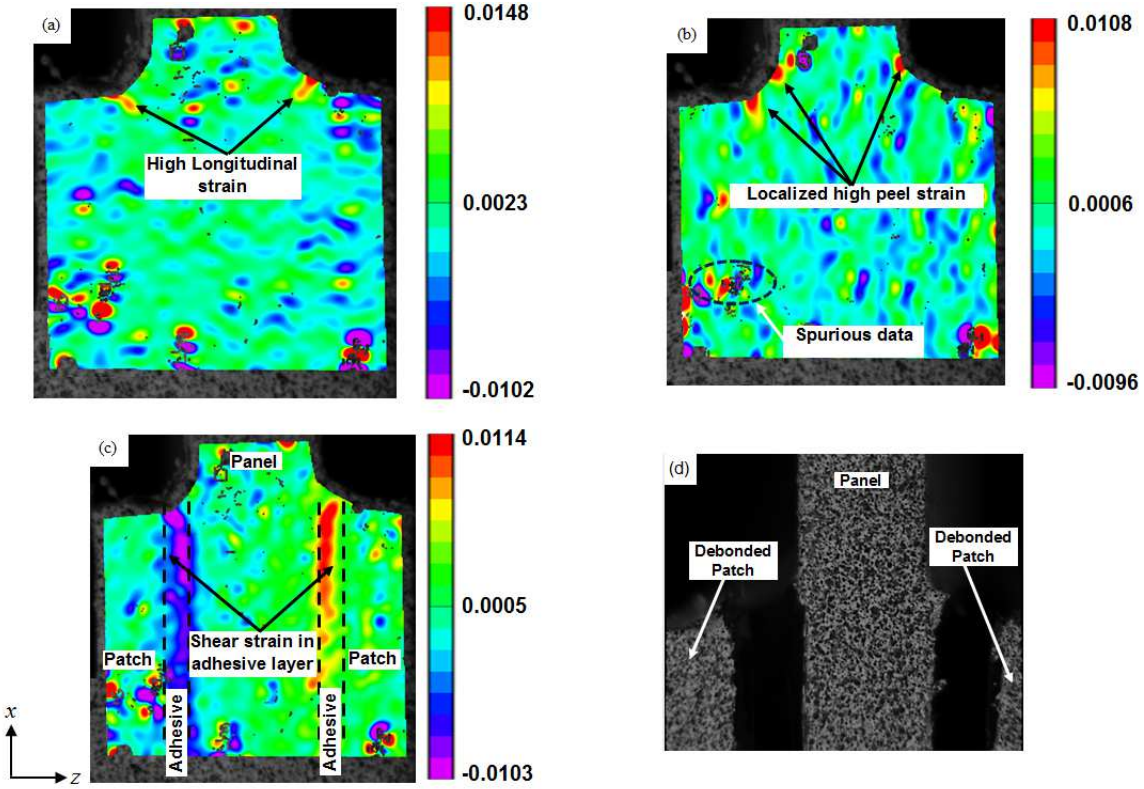

Figure 5.15: Localized whole field strain distribution in double sided patch repaired panel at a tensile load of 13.51 kN (Araldite 2011) (a) ε_{xx} (b) ε_{zz} (c) ε_{xz} (d) failure mechanism

It is found that the longitudinal strain is highly concentrated at the entrance of adhesive joint corner (instead of entire panel width as observed in global behaviour) on both the sides. Further investigation reveals that the panel is heavily loaded showing regions of high strain compared to the patch thereby ensuring the load transfer from panel to patches due to the presence of discontinuity. Localized high peel strain is observed just at entering root of panel/adhesive and adhesive/patch interface at lower load (band exist at higher load) near the overlap edge of the patch which depicts a differential straining effect in patch−panel−adhesive. The damage would initiate from these locations leading to patch debonding. However, band of peel strain observed at lower as well as

higher load in global response. It can also be observed from the figures that the maximum shear strain concentration also occurs nearer to patch overlap edge at patch/adhesive and adhesive/panel interface in the adhesive layer. The steep shear strain band as shown in Fig. 5.15 (c) represents that the load transfer is happening between the patch and panel across the adhesive layer. It can also be observed from the figure that the shear strain contour plot in both the adhesive layer (both left and right side of the panel) are smooth and similar, but they are in reverse nature due to coordinate axis system.

The closer view of final failure mechanism in the repaired panel is shown in Fig. 5.15 (d). On close observation, one can found that the damage initiated at the patch/adhesive interface near the patch overlap edge from peak strain zone as expected and then swiftly propagated towards the adhesive/panel interface followed by the progressive patch debonding over the interface area.

Figure 5.16 shows a comparison between localized peel and shear strain variation along the thickness of adhesive layer nearer to the patch overlap edge. The line considered for the plot is also depicted in the figure. One can observe that the magnitude of shear strain in adhesive layer is more as compared to the peel strain.

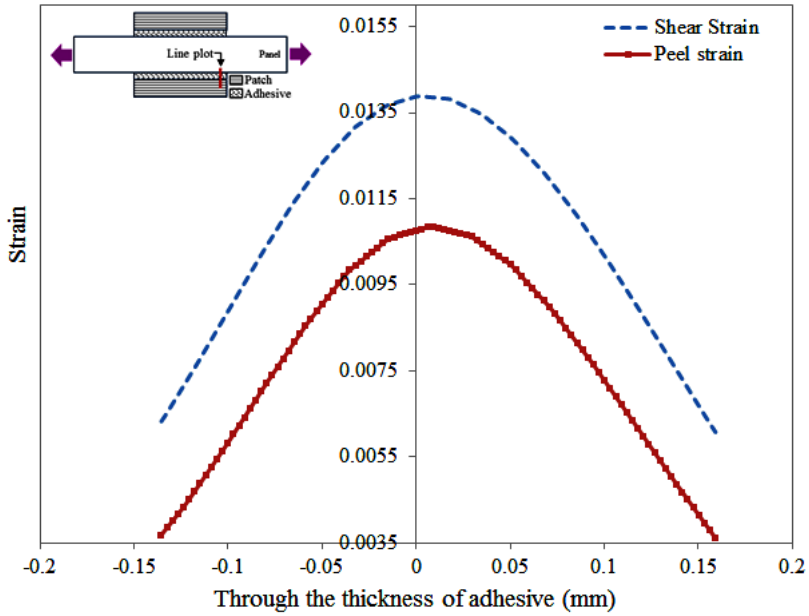

Figure 5.16: Comparison between localized peel and shear strain variation along adhesive thickness at 13.51 kN (Araldite 2011)

The variation of peel strain (ε_{zz}) at mid−thickness of adhesive layer along the bondline (joint length) is shown in Fig. 5.17. From the plot, one could see that the high peel strain exist near the patch overlap edge and reduces along the bondline. Similar observation is also made in Ref. [186]. The damage is found to be initiated at the patch/adhesive interface in the form of patch debonding near the patch overlap edge as expected. The damage then swiftly propagated towards the adhesive/panel interface followed by the progressive patch debonding over the interface area.

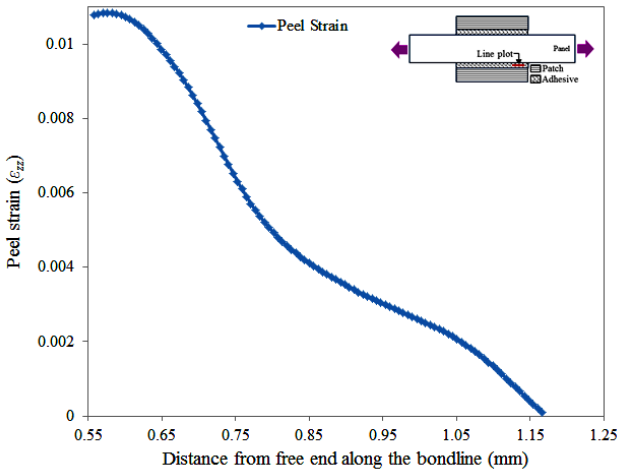

Figure 5.17: Localized peel strain variation along bondline in adhesive layer at 13.51 kN (Araldite 2011)

5.5.2 Tapered edge patch

The influence of patch edge tapering on strain level is investigated for the case of panel repaired with double sided patch using Araldite 2011 system. The details of the patch edge tapering is shown in the Fig. 5.18. The line diagram presenting the geometry of taper made on the joint at the patch edge is shown in Fig. 5.18 (a) whereas the angle achieved on the real joint at the patch edge (zoomed up view) is depicted in Fig 5.18 (b) for more clarity (only one side patch is shown here). To achieve this angle, the fabricated patch is first machined to obtain the right angle edges. The taper angle $\text{ø} = 30°$ is carefully marked at the patch edge and then manual polishing is done using fine grit emery paper P600 to achieve the specified angle at the patch edges.

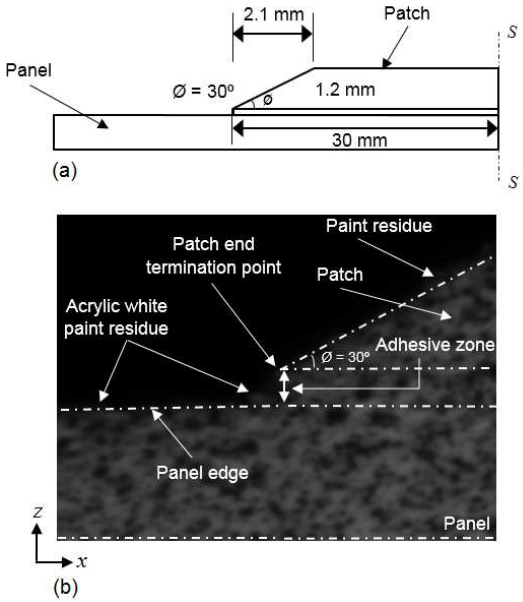

Figure 5.18: Patch edge tapering details (a) line diagram (b) angle depicted on actual joint

The area under investigation is then applied with white acrylic paint followed by black dots to generate random speckle pattern. On close observation, white paint residue could be seen near the patch/panel edge as well as near the step of the joint which are left un−cleaned because its cleaning may hamper the speckle pattern. The presence of paint residue at edges does not affect the DIC measurement.

Figure 5.19 shows the peel and shear strain distribution in the adhesive layer for a panel repaired with tapered patches. It is found that the high strain concentration exist in the adhesive layer near the patch overlap edge at patch/adhesive and also adhesive/panel interface quite similar to the observation made in case of panel repaired with straight edge patch. Fig. 5.20 shows a comparative plot of shear strain (ε_{xz}) in the adhesive layer (Araldite 2011) for the panel repaired with double sided straight edge and tapered edge patch at a tensile load of 13.5 kN. On comparison of Fig. 5.15 & 5.19 as well as from Fig. 5.20 it is evident that the edge tapering in the patch reduces the peak strain in the adhesive layer as compared to the panel repaired with straight edge patch.

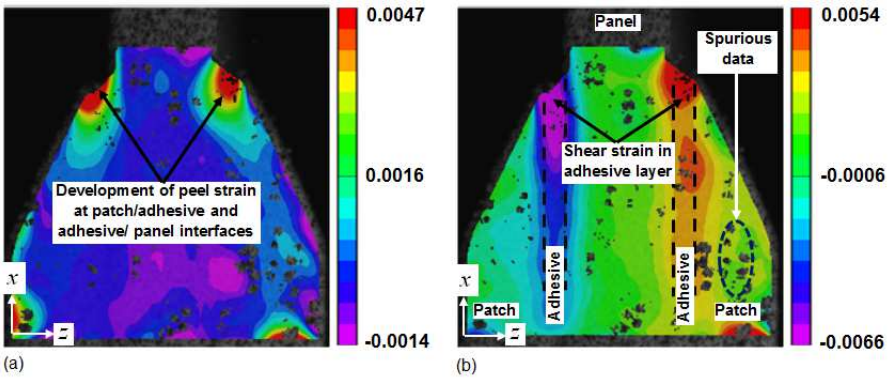

Figure 5.19: Whole field strain distribution in the adhesive layer for a panel repaired with tapered patches at a tensile load of 13.5 kN (Araldite 2011) (a) peel strain − ε_{zz} (b) shear strain− ε_{xz}

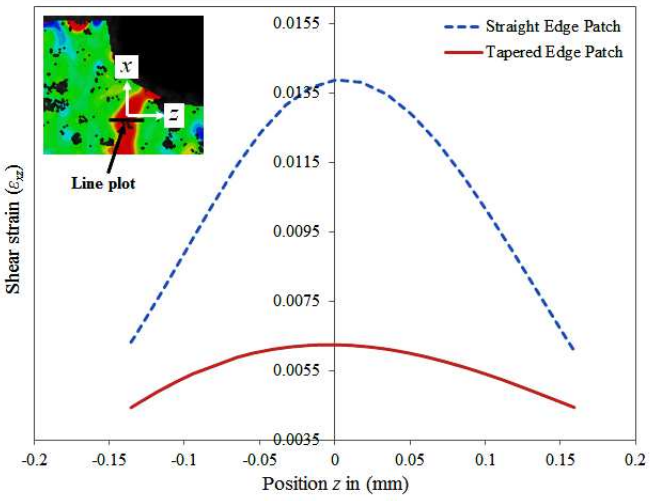

Figure 5.20: Comparative plot of shear strain (ε_{xz}) for the panel repaired with straight edge and tapered edge double sided patch using Araldite 2011 adhesive

5.6 Localized behaviour of strain distribution in Araldite AV138/HV998 adhesive layer: double sided patch repair configuration

An experimental study is also carried out to investigate the behavior of strain distribution in panel repaired with highly brittle Araldite AV138/HV998 adhesive system. The longitudinal, peel and shear strain distribution are found similar to that of Araldite 2011 system. However, the shear strain distribution in AV138/HV998 adhesive layer is found to be more localized and scattered rather than steep continuous band as observed in Araldite 2011 layer, as shown in Fig. 5.21. Here also, the failure initiated at patch/adhesive interface and then propagated along the adhesive/panel interface leading to final failure.

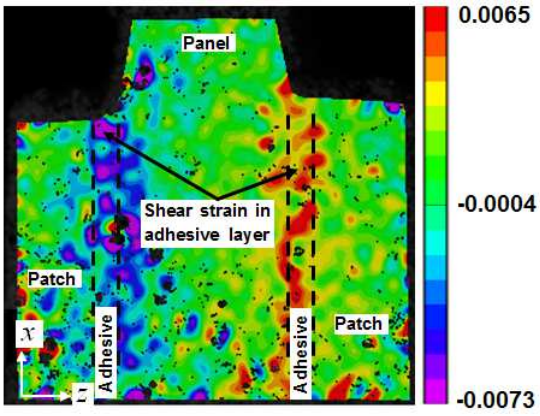

Figure 5.21: Localized whole field shear strain distribution in double sided patch repaired panel at 13.51 kN (Araldite AV138/HV998)

A comparative plot between Araldite 2011 and AV138/HV998 adhesive system in terms of shear strain variation over adhesive layer thickness is shown in Fig. 5.22. One can observe that shear strain variation in both adhesive layers is similar except that the brittle grade adhesive shows a scattered nature. The magnitude of shear strain is more in Araldite 2011 adhesive layer as compared to that of the AV138/HV998 system. This is due to the fact that the Araldite 2011 is ductile in nature and offers more elongation and hence more strain and steep continuous band as compared to brittle grade Araldite AV138/HV998 system. The damage in repaired panel bonded with Araldite AV138/HV998 system also initiated near the patch/adhesive interface and then propagated along the interface leading to patch debonding along interface.

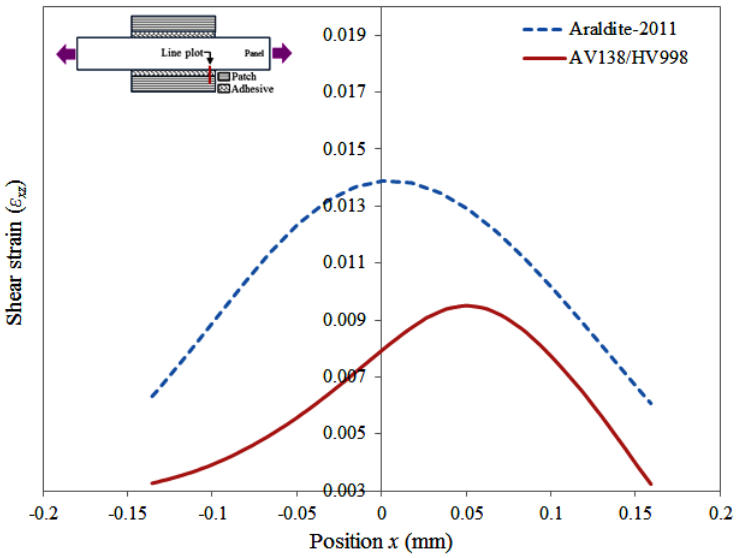

Figure 5.22: Comparative plot of shear strain (ε_{xz}) in adhesive layer for the panel repaired with Araldite 2011 and AV138/HV998 adhesive systems

5.7 Global whole field strain analysis on Araldite 2011 adhesive layer: single sided patch repair configuration

In this section, global whole field displacement and strain analysis along the length of adhesive layer is studied thoroughly. A subset size of 21 x 21 pixels^{2}along with step size of 5 pixels is chosen for correlation. The spatial resolution is 26 pixels /mm. .

5.7.1 In−plane displacement contours

The longitudinal (u, along loading) and transverse (w, perpendicular to loading) displacement field obtained from DIC at a load of 38.5 kN is shown in Fig. 5.23. It is evident from u and w displacement data that the displacement field is quite smooth, uniformly distributed about the panel center. However, on a closer look, one can observe that the width and angle of some of the fringes above the panel center is different than the one below it. Therefore, the fringes are relatively symmetrical about the mid span point of the overlap or panel center. The reason to this discrepancy could be attributed to the development of internal damage such as matrix cracking. One can also notice from w−displacement field which is shown in Fig. 5.23 (b) that the w−contour bands are diagonal and their angle varies along the panel length from beginning of the adhesive joint at patch overlap edge till the cutout zone. This observation implies that a differential deformation mechanism is happening in repaired configuration. The large angles at and near the patch overlap edge infer that a large amount of load is being transferred from panel to patch around this zone through the adhesive layer by shear deformation mechanism. The band almost becomes horizontal showing near zero angles just around the cutout zone which indicates that this zone has no significant influence on load transfer. The present finding is consistent with the results reported in Ref. [195] which were presented for double strap joint using moiré technique. The results in this section are especially presented in

pseudo random contours to facilitate a qualitative comparison with results reported using moiré technique [195]. On qualitative comparison between the two results it is found that the diagonal bands in the present single sided patch repaired panel case has got more angles in comparison with double strap joint. This finding seems obvious since there is a slight shift in neutral axis of single sided repair configuration and the load acts through an eccentricity which causes bending effect in addition to applied in−plane tensile load.

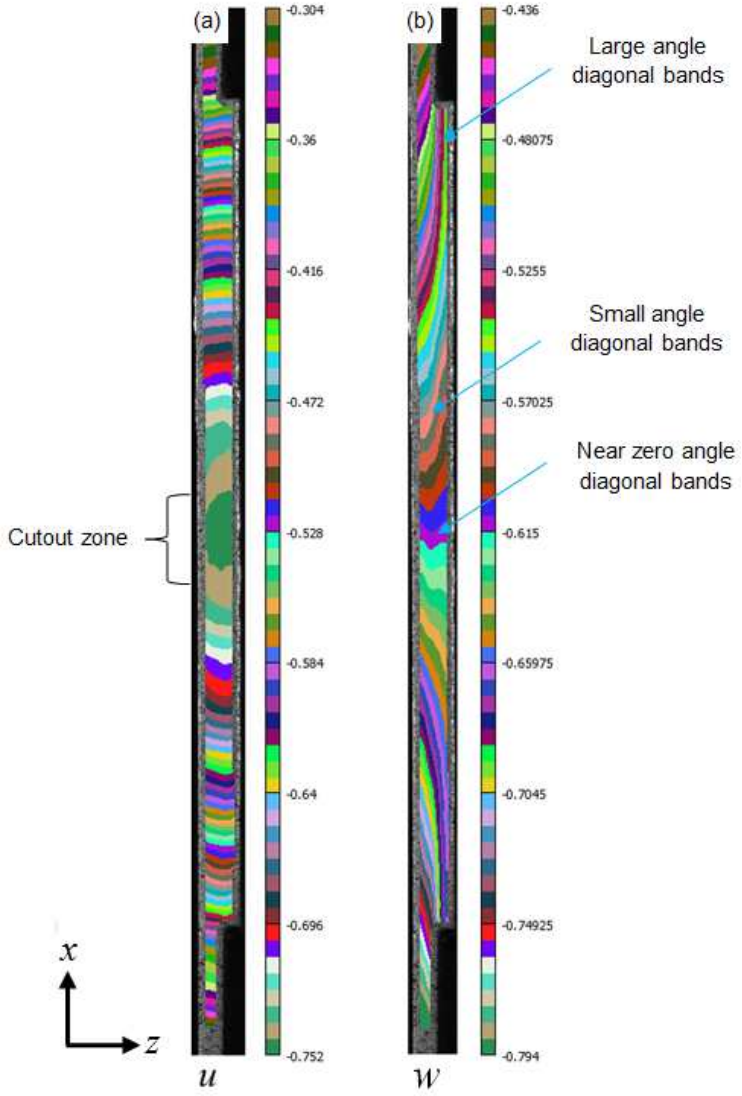

Figure 5.23: Displacement (mm) contours in single sided patch repaired panel (Araldite 2011) at 38.5 kN (a) longitudinal displacement, u (b) transverse displacement, w

To better understand the phenomenon of bending in single sided patch repair configuration, the transverse displacement (w) of a point P located in center of the panel is traced with increasing load using DIC and it is shown in Fig. 5.24. It is found that the transverse displacement of considered point varies linearly up to a certain load which signifies the influence of bending phenomena in single sided patch repaired panel configuration. The variation remains constant with further increase in load once the neutral axis coincided with the loading axis. The bending phenomenon in single sided patch repaired panel configuration is well explained in Ref. [194].

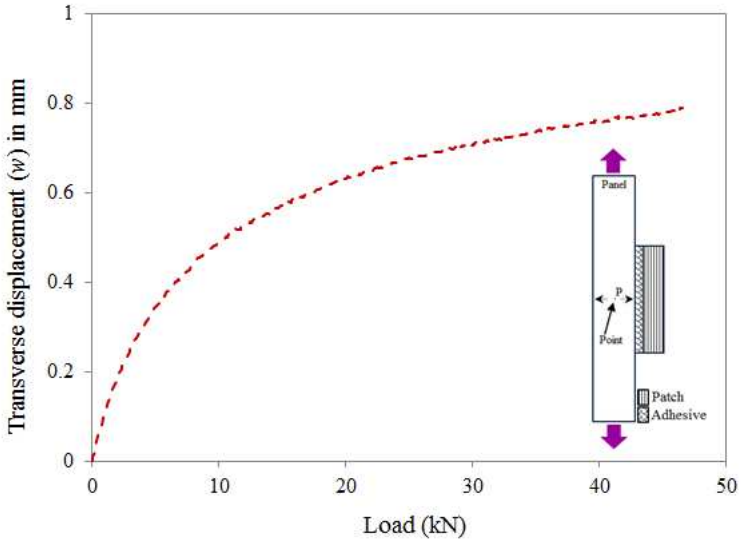

Figure 5.24: Variation of transverse displacement (mm) of point P in center of single sided patch repaired panel with increasing load using DIC

5.7.2 Longitudinal strain (ε_{xx}) distribution

Figure 5.25 (a) shows whole field longitudinal strain (ε_{xx}) distribution in single sided patch repaired panel at a load of 38.5 kN. The longitudinal strain in panel is found maximum near the patch overlap edge and it is highly concentrated at the corner of adhesive joint as observed in case of double sided patch repair configuration. The variation of longitudinal strain in panel along line a−a at 38.5 kN and 46.8 kN which corresponds to 56% and 68% of ultimate load respectively are shown in Fig. 5.26. The magnitude of ε_{xx} near the root is 0.0068 and it reduces to 0.004368 at center of the panel. The reduction in ε_{xx} magnitude is only 35% as one moves from the root or adhesive corner to the panel nearer to cutout. The variation of longitudinal strain here is similar to the one as observed in double sided repair configuration. However, the magnitude of longitudinal strain near the root as well as over the entire length of the panel between upper and lower patch edge is considerably higher than double sided repaired one. In single side repair the longitudinal strain is 9.23% higher than the double sided one. This could be due to the presence of bending phenomena in single sided repair configuration as discussed in earlier section. At 68% of ultimate load the variation of ε_{xx} shows a similar variation with strain magnitude shifted to a higher level. The sudden peak in strain magnitude just near the root signifies that major portion of applied load is transferred from panel to patch within this zone just near the patch overlap edge.

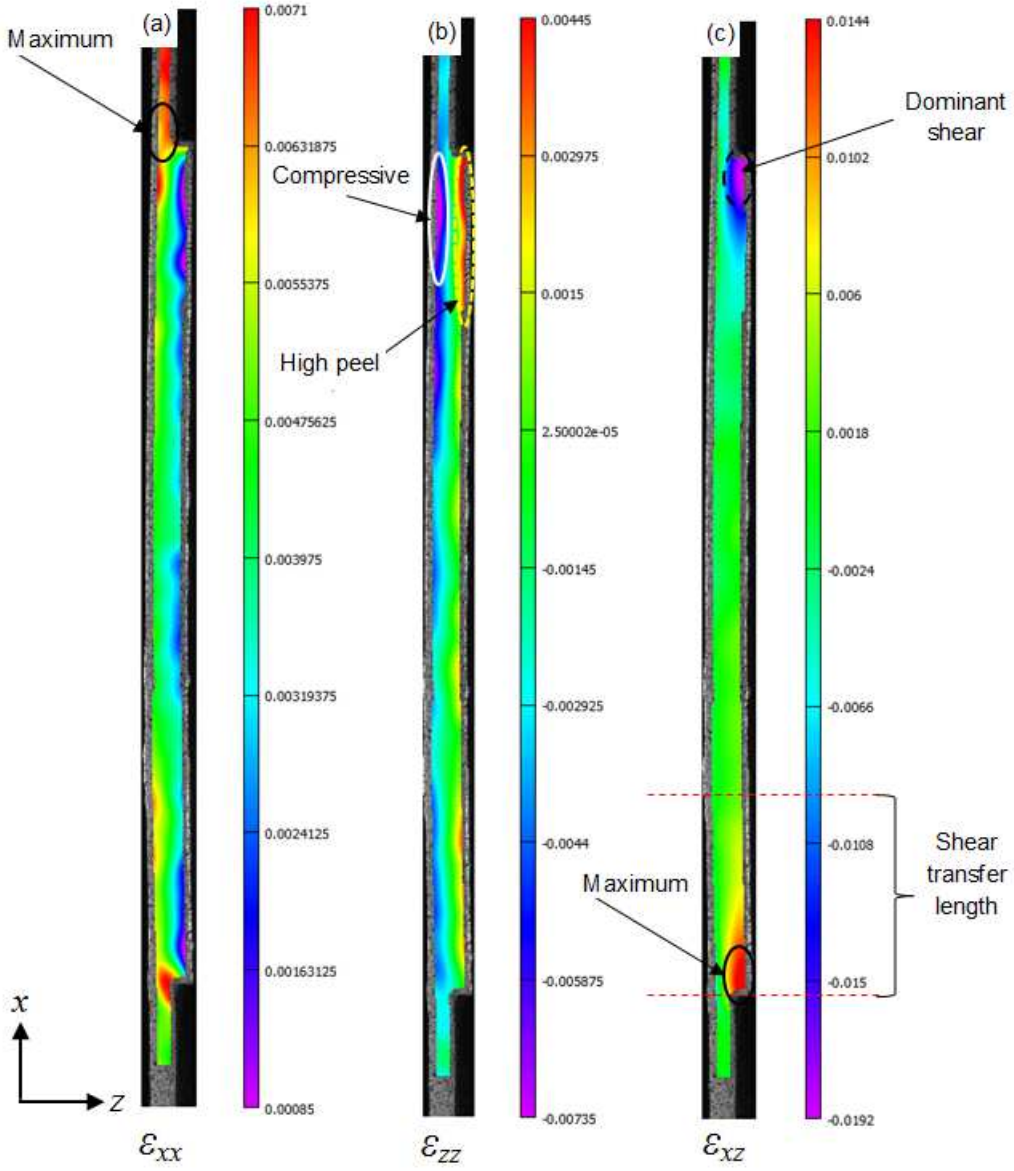

Figure 5.25: Strain distribution in panel, patch and adhesive layer in unsymmetrical patch repair configuration at 56% of failure load in case of Araldite 2011(a) ε_{xx} (b) ε_{zz} (c) ε_{xz}

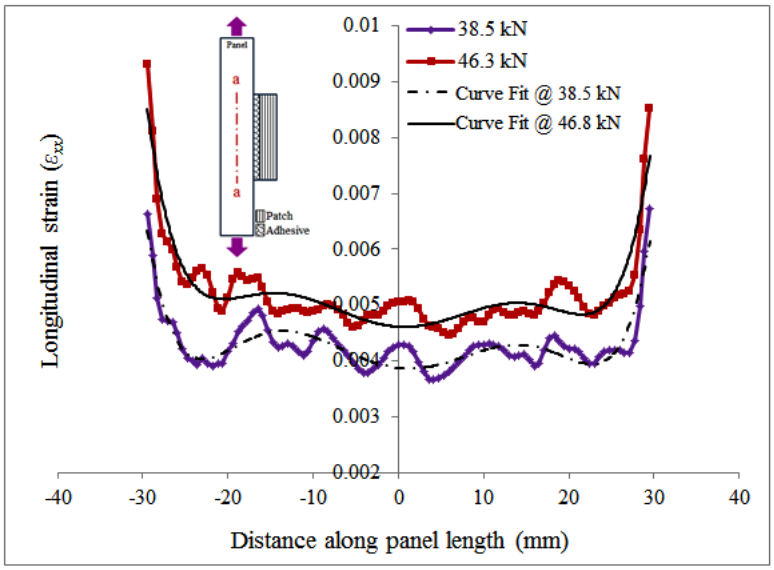

Figure 5.26: Longitudinal strain variation in CFRP panel under single sided patch at 56% and 68% of failure load (Araldite 2011)

5.7.3 Peel (ε_{zz}) and shear strain (ε_{xz}) distribution

The peel and shear strain distribution in single sided patch repaired panel at 38.5 kN are shown in Fig. 5.25 (b) and (c) respectively. The peel is found maximum over a length near the adhesive/patch interface at upper end of adhesive layer. Asymmetry in peel strain distribution is seen at this load with larger strain on upper side of adhesive layer as compared to the lower one, as shown in Fig. 5.25 (b). However, it is found that the peel strain distribution is symmetric at lower load level. A zone of compressive strain could be identified in panel over certain length (white line) opposite to higher peel zone and just below the patch overlap edge. This is due the development of high peel strain causing the patch to be peel away from panel inducing a compressive strain in panel. The shear strain is also found maximum at the patch overlap edge, as in shown in Fig. 5.25 (c). Shear strain also shows asymmetric behaviour with maximum magnitude being at the same location (dotted black circle) as high peel strain zone (upper end of adhesive layer). The asymmetry in strain field indemnifies the damage initiation. On comparison, it is found that the peel and shear strain distribution in adhesive layer of single sided repair is also presents similar behaviour as observed for the case of double sided repair configuration with amplified magnitude. In single sided repair, peel and shear strain is 238.46% and 39.46% more than double sided repair configuration, respectively. The variation of shear strain in adhesive layer along a line b-b at a load level of 38.5 kN and 46.8 kN is shown in Fig. 5.27. The shear strain variation at both the load levels shows a similar trend. On comparison of shear strain at two load levels one can find that the shear strain remains low over a certain length in center of the panel and then depicts a difference in shear strain magnitude over a zone till the patch overlap edge, as observed in double sided repair.

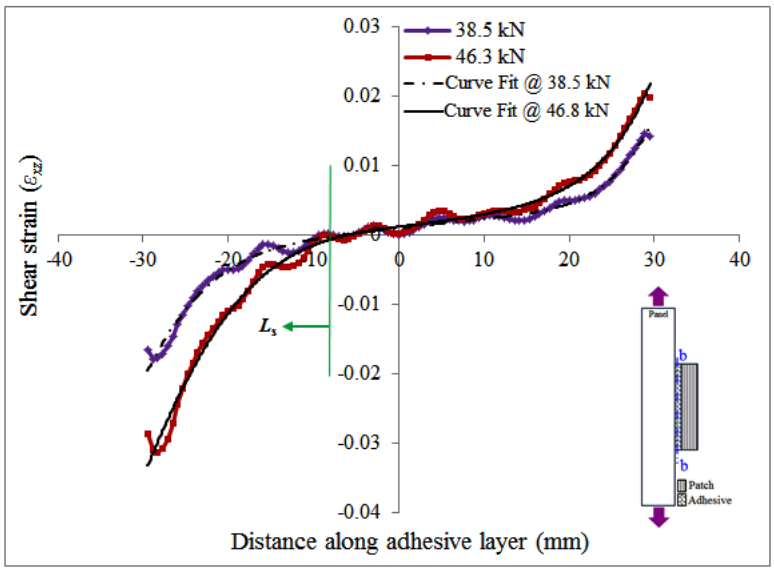

Figure 5.27: Shear strain variation in adhesive layer of single sided patch repaired panel at 56% and 68% of failure load (Araldite 2011)

The shear transfer length L_s in single sided repair can be also be obtained from shear strain variation in adhesive layer along bond length extracted at a load just before the patch debonding initiation i.e, at 68% of failure load which is shown in Fig. 5.27. A curve fit is obtained for strain profile and parameter L_s is deduced. It is found that the critical value of L_s is approximately 19.3 mm i.e., about 32% of total the patch length or 1.9 times the diameter of the cutout.

5.7.4 Failure mechanism and load displacement behaviour

Figure 5.28 shows the damage progression in single sided patch repaired panel which is further correlated with its load−displacement behaviour as shown in Fig. 5.29. As the load reaches to point b as in Fig. 5.29 , the damage initiates at upper end corner of patch/adhesive interface (see Fig. 5.28 (c)) where the high peel/shear strain concentration is observed and it suddenly propagated to 80 % of adhesive layer with mixed mechanism of adhesive and cohesive failure reflecting the reduction in load at point c. Delamination initiation could also be seen at higher load (point d) from Fig. 5.28 (d), signifying the low inter−lamina strength due to high through thickness/peel strain. The growth of delamination which is shown in Fig. 5.28 (e) causes reduction in load to point e and as the load reaches to point f extensive delamination and debonding is observed leading to final failure of panel in a catastrophic manner.

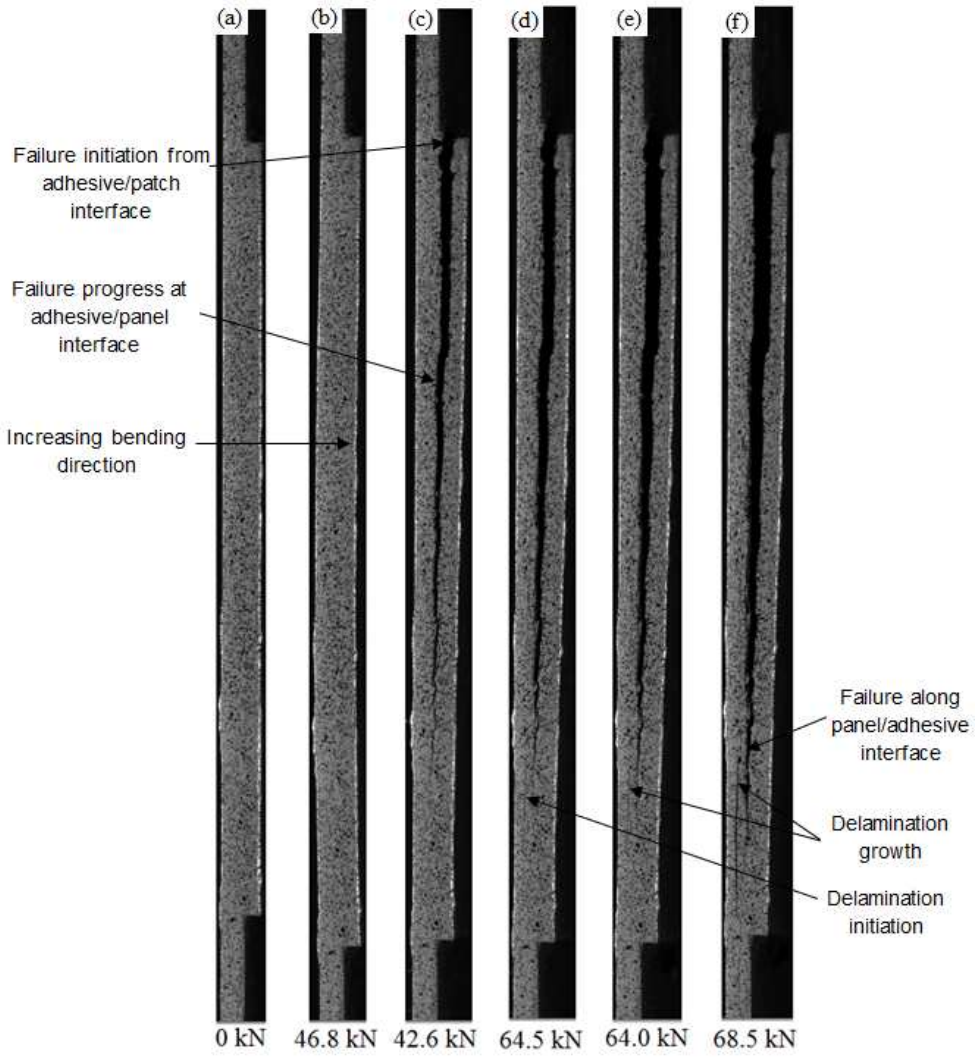

Figure 5.28: Damage progression with increasing load in panel repaired with Araldite 2011 adhesive

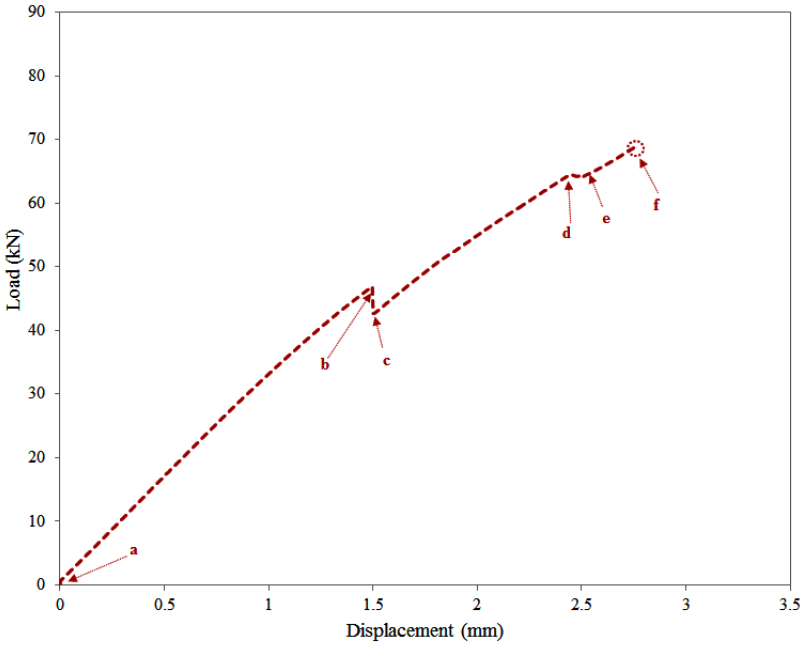

Figure 5.29: Load displacement curve for single sided patch repaired panel

5.8 Localized whole field strain analysis in Araldite 2011 adhesive layer: single sided patch repair configuration

In this section localized strain analysis in adhesive layer of a panel repaired with single sided straight and tapered edge patch is discussed.

5.8.1 Straight edge patch

The longitudinal (ε_{xx}), peel (ε_{zz}) and shear strain (ε_{xz}) distribution in adhesive layer of single sided patch repaired panel at a load of 23.9 kN is shown in Fig.5.30. The ROI for correlation corresponds to a zone of 2.42 mm x 3.18 mm respectively. The spatial resolution is 591 pixel/mm. A subset size of 71 x 71 pixels^2 with a step size of 7 pixels is chosen for correlation. It can be observed from the figures that the magnified optics facilitates the correlation at extreme edge of the patch near the root/corner of adhesive joint which were not possible in global behavior of adhesive joint due to lower spatial resolution as discussed earlier. Higher spatial resolution would help us in investigating localized behaviour in critical zones responsible for failure.

It is found that the longitudinal strain is highly concentrated at the entrance of adhesive joint corner at panel/adhesive interface. Also, localized high peel strain is observed just at entering root of panel/adhesive interface. High peel strain concentration would lead to damage initiation from this location leading to patch debonding. Further investigation shows that the maximum shear strain concentration also occurs nearer to overlap edge of the patch at panel/adhesive interface in adhesive layer. The steep band of shear strain (red zone) as shown in Fig. 5.30 (c) represents that the load transfer happening between the patch and panel across the adhesive layer.

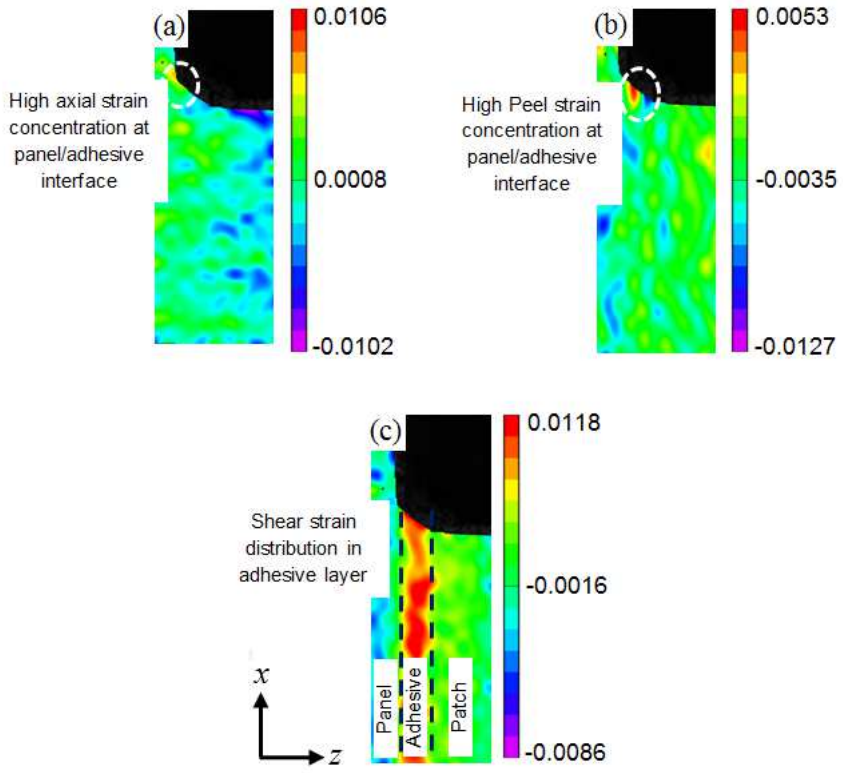

Figure 5.30: Localized whole field strain distribution in adhesive layer for a panel repaired with single sided straight edge patch at a tensile load of 23.9 kN (Araldite 2011) (a) ε_{xx} (b) ε_{zz} (c) ε_{xz}

However global strain analysis could not reveal such strain localization occurrences. Global strain analysis shows longitudinal strain to be maximum across panel width near patch overlap edge rather than localized at panel/adhesive interface. Also, the zone of maximum peel and shear strain observed in global analysis is overlapping at adhesive and patch which is not obvious. However, local strain analysis reveals peel strain to be concentrated at panel adhesive interface and steep band of shear strain an adhesive layer as discussed earlier.

Figure 5.31 shows damage monitoring in adhesive layer based on peel strain distribution with increasing load. The peel strain is found maximum (white line) at panel/adhesive interface, as shown in Fig. 5.31 (b). With increasing load the maximum peel strain shifted to the adhesive/patch interface and along the bondline (black line, which can be seen from Fig. 5.31 (c). The zone of maximum peel strain then advances along the bondline at patch/adhesive interface as depicted in Fig. 5.31 (d) with further increase in load. On close observation one can find that a zone of compressive strain is also present adjacent to the maximum peel strain zone (red line) and it gets intensified similar to the peel strain with increasing load. The damage initiation from Fig. 5.31 (e) could be seen in the form of discontinuity in correlation in adhesive layer once the peel strain reaches to critical value. It can also be noticed that the damage propagates at the adhesive/patch interface along maximum peel strain path. These observations could only be possible due to localized strain analysis rather than global strain analysis.

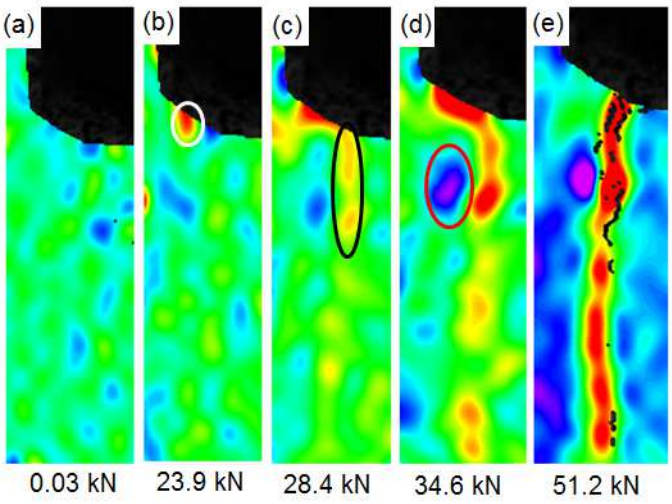

Figure 5.31: Damage monitoring in adhesive layer of single sided repair with increasing load based on peel strain – ε_{zz}

5.8.2 Tapered edge patch

The influence of patch edge tapering on strain level in adhesive layer using DIC is investigated here. The tapering of patch edge is done in similar way as explained for double sided repair case. The ROI for correlation corresponds to a zone of 2.29 mm x 3.68 mm respectively. The spatial resolution is 511 pixel /mm. A subset size of 71 x 71 pixels^2 with a step size of 7 pixels is chosen for correlation. The longitudinal (ε_{xx}), peel (ε_{zz}) and shear strain (ε_{xz}) distribution at a load of 23.9 kN is shown in Fig. 5.32. It is found that the strains are highly concentrated near the entrance of adhesive joint at panel/adhesive interface and there is no significant influence of patch edge tapering on longitudinal and shears strain level in the adhesive layer as compared to the peel strain.

The variation of longitudinal, peel and shear strain in adhesive layer along the bond length close to patch overlap edge at a load of 23.9 kN are shown in Fig. 5.33. The line considered for the plot is shown there. It is found that the strain decreases with increasing bond length away from patch overlap edge and also the shear strain is more dominant in adhesive layer followed by longitudinal and then peel strain in single sided patch repaired panel configuration. This is also true for the panel repaired with straight edge patch, as shown in Fig. 5.30.

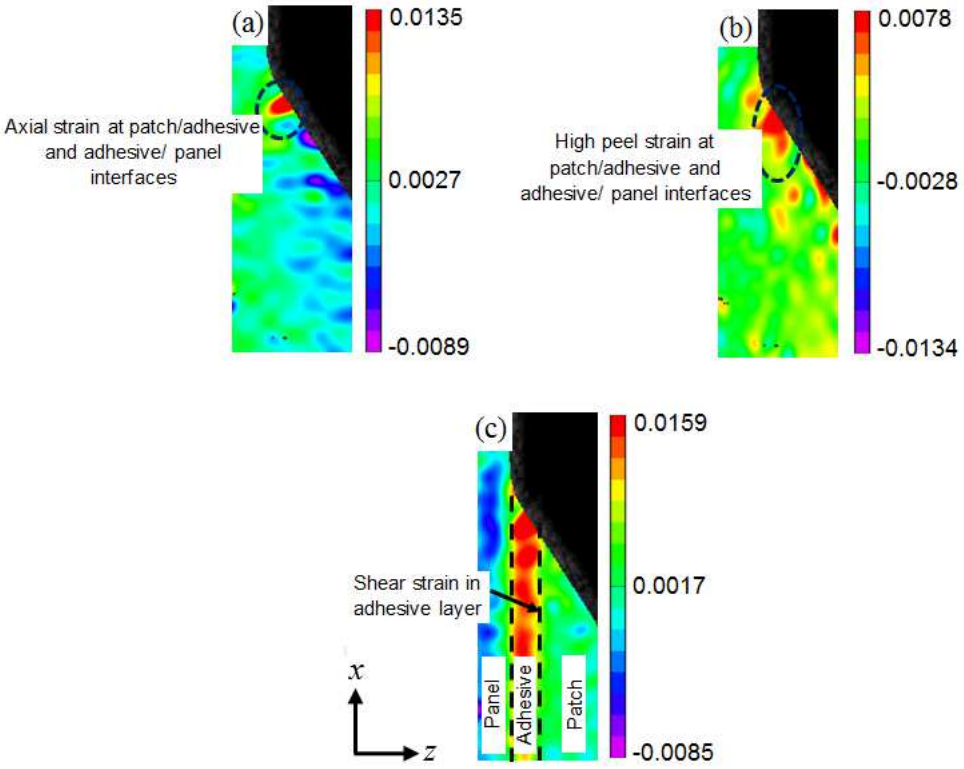

Figure 5.32: Localized whole field strain distribution in adhesive layer for a panel repaired with single sided tapered edge patch at a tensile load of 23.9 kN (Araldite 2011) (a) ε_{xx} (b) ε_{zz} (c) ε_{xz}

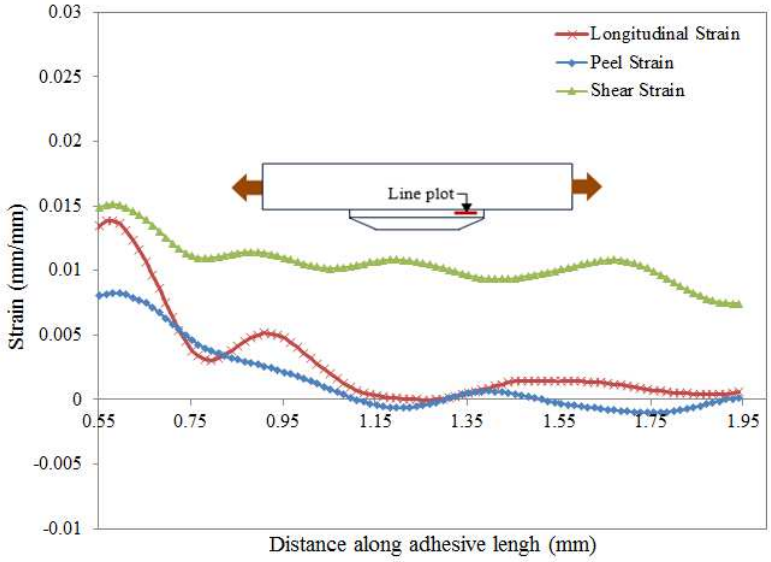

Figure 5.33: Comparative plot of strain variation in adhesive layer for the panel repaired with tapered edge patch obtained from DIC at a tensile load of 23.9 kN (Araldite 2011)

Figure 5.34 shows a comparative plot between panel repaired with straight and tapered edge patch in terms of peel strain variation in the adhesive layer considered near the patch overlap edge. The variation of peel strain in adhesive layer between the two cases is found similar except that the magnitude of peel strain shifted up when the panel is repaired with tapered edge patch. The magnitude of longitudinal, peel and shear strain is increased from 0.0106, 0.0053 and 0.0118 to 0.0135, 0.0078 and 0.0159 respectively for the case of panel repaired with tapered edge patch. Similar observation has been found in Ref. [185] which was reported for a steel panel bonded with CFRP composite laminate on both side. One can conclude that any tapering ratio may not be effective in reducing the strain level in adhesive layer of single sided repair and a thorough investigation in terms of tapering parameter needs to be done for further reduction.

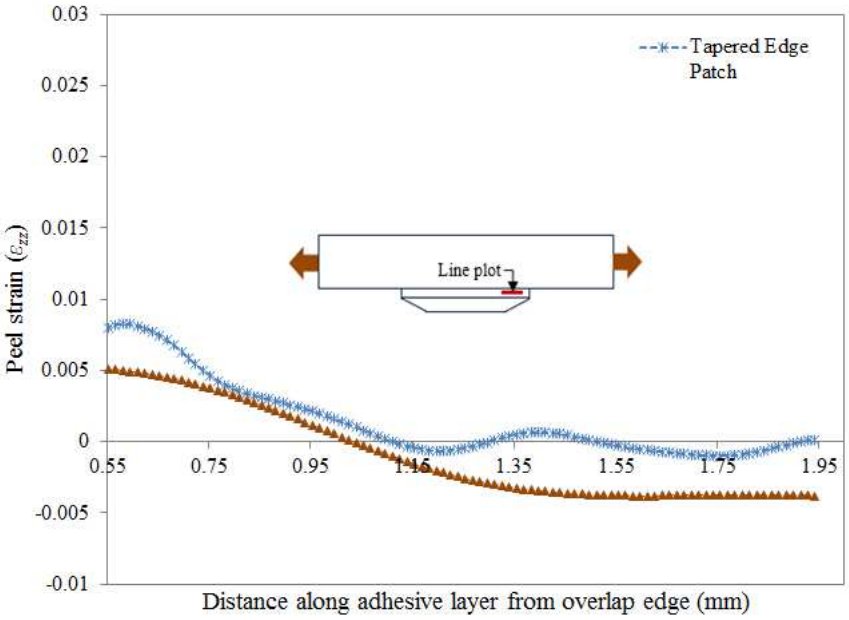

Figure 5.34: Comparative plot of peel strain variation in adhesive layer between panels repaired with straight and tapered edge patch obtained from DIC at a tensile load of 23.9 kN (Araldite 2011)

5.9 Finite element modeling and analysis: double sided patch repair configuration

A linear 3−D FEA of repaired panel is carried out using ANSYS−13 software. The FE model is built with 20−noded solid 186 brick element. The geometry and dimensions of panel and patch are kept same as that of experimental model. The mesh pattern around the hole and patch edge is kept very fine to capture the high stress gradient around it. Around the circular hole there are 15360 elements (96 circumferential; 40 radial; 4 thickness). The meshing surrounding the hole is chosen based on mesh convergence study. Every layer is meshed with one element in thickness direction for both patch and panel. In thickness direction, the panel is meshed with four elements, adhesive with ten elements and patch with three elements. Firstly, a parametric study is carried out to study the effect of number of elements in adhesive layer along thickness direction and also along its length near the patch overlap edge on peel and shear strain. It is found that the number of elements through the thickness of adhesive has negligible influence on peel and shear strain whereas the refinement of elements in adhesive along its length near the patch edge has significant influence on peel and shear strain showing a corner singularity behaviour. Therefore, the meshing in adhesive near the patch edge is chosen based on recommendation made in Ref. [114, 196] and similar meshing pattern is adopted for both patch and panel. The patch is bonded on to the panel over the hole region using adhesive layer. MPC algorithm is employed for ensuring a perfect bonding between patch/panel and panel/adhesive interface. The elastic modulus and Poisson's ratio of adhesive used in this analysis are obtained experimentally and they are in Table 5.1. Fibers in the panel and patch are aligned parallel to the loading direction. The panel is fixed at bottom face and an in−plane tensile load of 13.5 kN is applied at the top face along x−direction so as to simulate the experimental boundary conditions. The results obtained from FEA are compared with the experimental data for the same load. The zoomed view of finite element model of the repaired panel is shown in the Fig. 5.35.

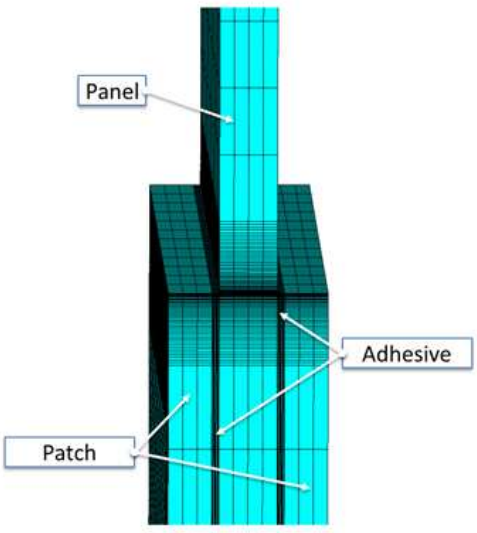

Figure 5.35: Finite element model of DSPR panel (zoomed up view)

Figure 5.36 shows the strain distribution in the adhesive layer (Araldite 2011) obtained from

FEA at a load of 13.5 kN. The FEA results are presented with adjusted scale to match against DIC scale. It can be observed from the figure that a high peel and shear strain concentration exist near the patch overlap edge at patch/adhesive interface. The strain field obtained from FEA is found to be consistent with the DIC technique as discussed earlier.

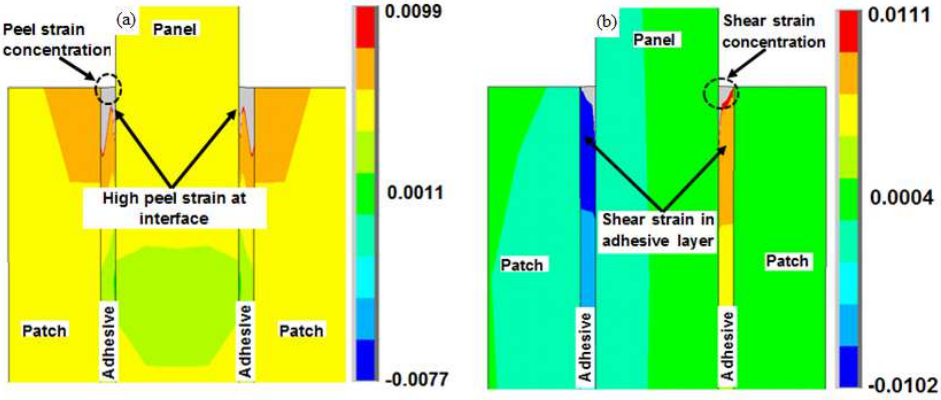

Figure 5.36: Whole field strain distribution in adhesive layer from FEA at a tensile load of 13.5 kN (a) peel strain – ε_{zz} (b) shear strain – ε_{xz} (Araldite 2011)

A comparative plot between DIC and FEA result in terms of shear strain variation along the thickness of repaired configuration across line c−c at a load of 13.5 kN is shown in Fig. 5.37. It can be observed from FEA plot that the shear strain varies linearly along panel thickness, decreases at entrance of panel−adhesive interface due to differential straining effect, increases along the adhesive layer showing peaks at center of adhesive and then decreases along the patch thickness. DIC plot despite local fluctuation in data reflects a similar variation as that of FEA and therefore a good correlation exist between the DIC and FEA result.

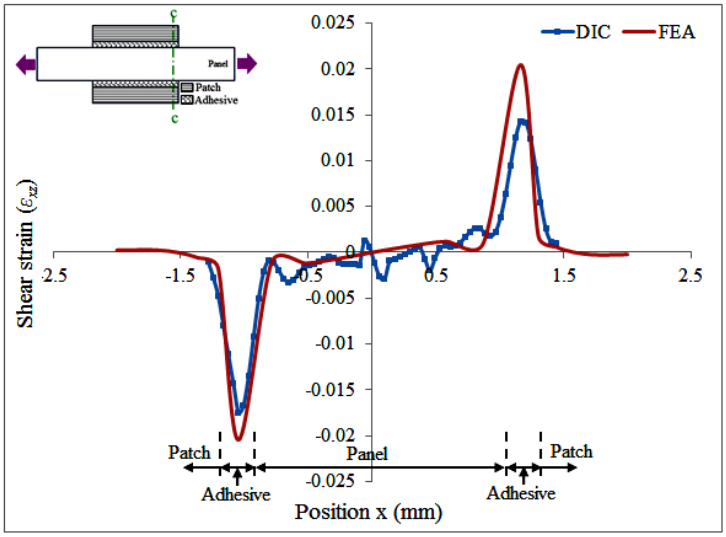

Figure 5.37: Shear strain variation in double sided repair panel at 13.51 kN (Araldite 2011): DIC vs. FEA

Figure 5.38 shows the comparative plot of shear strain variation in adhesive layer (Araldite 2011) between DIC and FEA along the joint length (bondline). The line considered for the comparative plot is also shown in the figure. It can be observed that the shear strain is maximum near the adhesive end and it reduces as one moves away from the adhesive end along the bondline or joint length. Similar observation has been made in Ref. [184]. Besides small difference in magnitude, ε_{xz} variation from both DIC and FEA has a similar trend and relatively shows a good agreement.

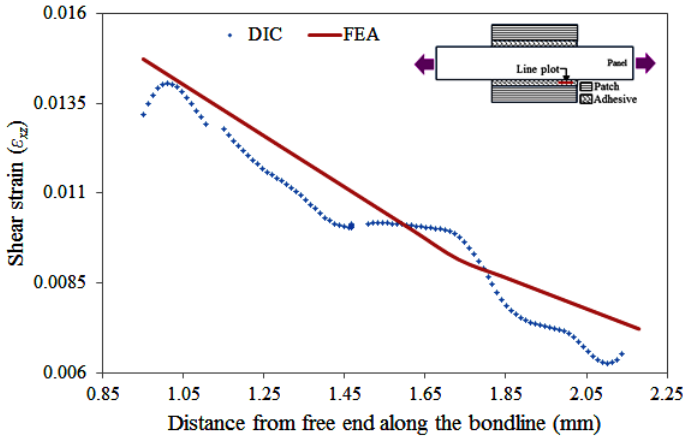

Figure 5.38: Shear strain distribution along adhesive length at 13.51 kN (Araldite 2011): DIC vs. FEA

5.9.1 Shear transfer length (L_s) from FEA

In this sub−section a procedure is presented to predict the shear transfer length from FEA and it also compared with the experimental results discussed earlier. To estimate the shear transfer length finite element analysis is carried out at patch debonding load (in this case 70 % of ultimate load) to obtain the shear strain distribution in adhesive layer. The shear strain distribution in adhesive layer at this load (50.5 kN) is shown in Fig. 5.39 and it is further compared with the one obtained from DIC. Shear transfer length is a length over which the shear strain in adhesive layer reduces from its maximum value to nearly zero as defined earlier. The value of this length is found to be 18.97 mm from FEA which is close to the one estimated from DIC. Also, one can see a close agreement between the DIC and FEA results beside the difference in magnitude at extreme patch edge. This is due to the fact the correlation could not be achieve from DIC just at the edge, which can be seen from Fig. 5.8 or 5.9.

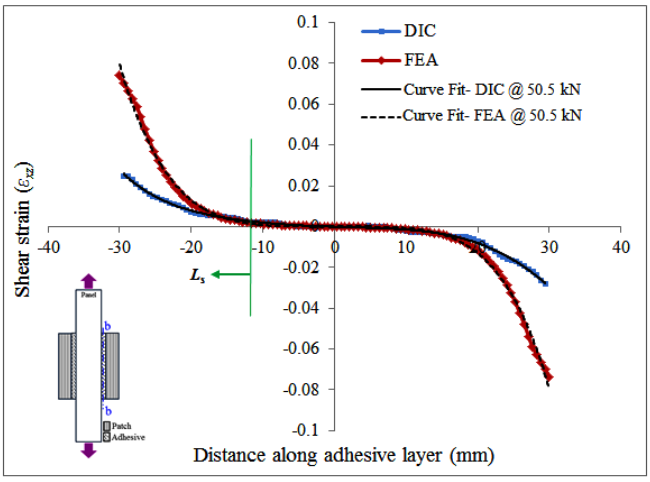

Figure 5.39: Shear transfer length from shear strain distribution along adhesive length at 50.5 kN (Araldite 2011): DIC vs. FEA

5.10 Finite element modeling and analysis: single sided patch repair configuration

The meshing pattern in single sided patch repair is similar to the double sided one as disused in earlier section. Figure 5.40 shows the strain distribution in the adhesive layer obtained from FEA at a load of 23.9 kN for panel repair with single sided tapered edge patch. The FEA results are presented with adjusted scale to match against DIC scale. It can be observed from the figure that a high peel and shear strain concentration exist close to the patch overlap edge at panel/adhesive interface, which is similar to the experimental results as shown in Fig. 5.32. Also a zone of compressive strain could be identified in Fig. 5.40 (a) just below the patch overlap edge due to high peel strain as observed from DIC measurement. The strain distribution obtained from FEA is found to be consistent with experimental observation as presented earlier.

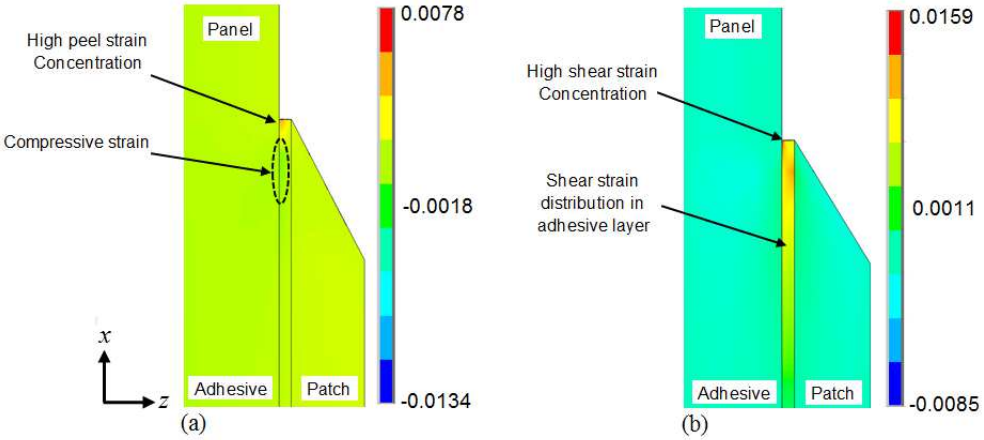

Figure 5.40: Strain distribution in Araldite 2011 adhesive layer at a tensile load of 23.9 kN obtained from FEA (a) peel strain – ε_{zz} (b) shear strain – ε_{xz}

5.10.1 Shear transfer length (L_s) from FEA

In single sided repair configuration also, shear transfer length is predicted from FEA and it is further compared with the experimental one. To estimate the shear transfer length from FEA, similar procedure is adopted as discussed in case of double sided one. The shear strain distribution in adhesive layer of panel repaired with straight edge patch at debonding initiation load (46.8 kN) is shown in Fig. 5.41, which is further compared with the one obtained from DIC. The value of shear transfer length is found to be 20.2 mm from FEA which is slightly higher than the one estimated from DIC. This deviation could be because of difference in exact location of line plot extracted from FEA and DIC especially due to unavoidable bending in single sided repair configuration. However, one can see a close agreement between the DIC and FEA results beside the difference in magnitude at extreme patch edge.

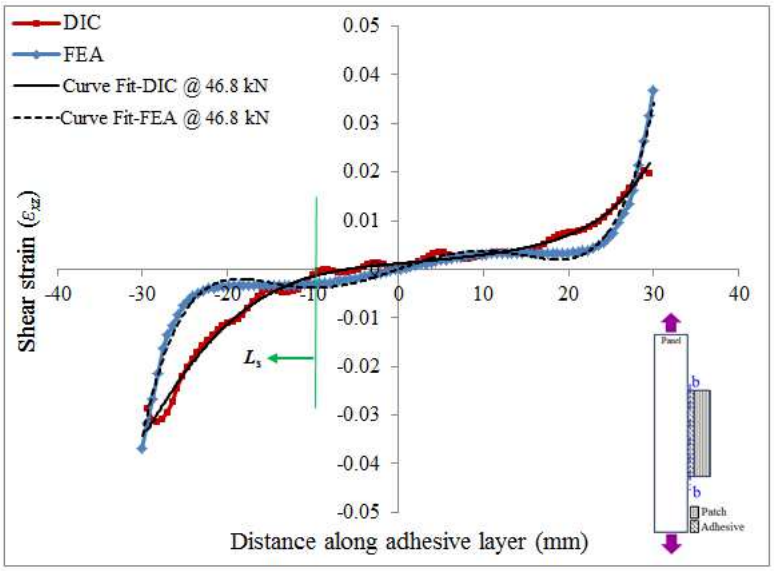

Figure 5.41: Shear strain variation in the adhesive layer of a panel repaired with single sided straight edge patch at 46.8 kN (Araldite 2011): DIC vs. FEA

5.11 Closure

In this chapter, an experimental study involving DIC technique is presented to characterize the strain field in thin adhesively layer in case of single and double sided patch repaired CFRP panel under tensile load. Global−cum−local strain field analysis of adhesive layer in the repaired configuration is carried out to fully understand its behaviour. The longitudinal, peel and shear strains in single and double sided repair are found to be maximum near the corner or root of adhesive joint at the patch overlap edge. Based on global strain analysis it is found that only a small zone near the patch edge facilitates the load transfer from panel to patch through the adhesive layer by shear deformation mechanism. The effective shear transfer length for single and double sided repair configuration is found to be 38.5% and 28.3% of total the patch length respectively. Conventional DIC along with magnified optics is found to be capable of exactly capturing the localized complex strain field at the patch overlap edge. The global and local strain analysis are complementary to each other and helps in understanding the complex strain field that develops the thin adhesive layer.

In case of single sided repair, it is found that the presence of bending load in addition to in−plane tensile load amplifies the strain levels, particularly a remarkable increase in peel strain is observed as compared to double sided repair configuration for a given load. Also, the shear strain in adhesive layer is found to be significantly higher compared to peel strain in case of single sided repair. The failure in both single and double sided repair initiates from high peel/shear strain concentration zone in the form of patch debonding. The failure propagates with mixed mechanism of adhesive and cohesive failure followed by delamination. The final failure in both the cases takes place with patch debonding along with extensive delamination in panel.

It is also found that the single sided panel repaired with tapered edge patch shows higher strains in the adhesive layer near the patch overlap edge in comparison to the one repaired with straight edge patch. However, similar patch edge tapering in case of double sided repair reduces the strain level at the patch overlap edge in comparison to straight edge patch. The influence of adhesive nature on strain distribution in the adhesive layer for double sided repaired panel reveals that the ductile adhesive leads to higher shear strain as compared to the brittle one. Finally, a finite element based study is carried out to get the whole field strain distribution in the adhesive layer and its predictions are compared with the DIC results and they appear to be in good coherence.

The present study in this chapter reveals that the DIC technique along with magnified optics is suitable and accurate for analyzing local cum global strain field over the thin adhesive layer.

In the previous chapters, the behaviour of repaired panels have been investigated to improve the performance of repaired panels. However, the performance of repaired panel also rely on different parameters involved in repair domain such as patch shape, patch thickness, patch overlap length, patch stacking sequence, adhesive thickness, etc. In chapter−3, the influence of patch stacking sequence, patch thickness, patch overlap length and adhesive thickness have been analyzed through FEA based parametric study. In the next chapter the influence of different patch shapes on repair efficiency is presented using FEA for the case of both pure UD and quasi−isotopic configurations. A multi−objective genetic algorithm in conjunction with FEA is then implemented to arrive at optimized dimension of the best patch shape and adhesive thickness for higher repair efficiency. Experimental results obtained based on optimized patch dimension and adhesive thickness are also presented.

Chapter 6

Optimization of Repair Parameters using GA and FEA

6.1 Introduction

The performance of repaired composite panel depends on several patch and adhesive parameters. The influence of repair parameters such as patch thickness, patch overlap length, patch stacking sequence, adhesive thickness, adhesive strength etc., on repair efficiency have been investigated through finite element based parametric study by several researchers [20, 76–78, 82, 84], however none of them have studied in detail the the influence of patch shape on the repair performance. Till date, parametric study exist on understanding the influence of various parameters individually on repair efficiency. However, it is difficult to arrive at the optimum value of different repair parameters independently through a parametric study.

In this chapter, at first, a linear 3D finite element analysis is performed to study the the influence of patch shape on repair efficiency followed by other parameters. The study is conducted for both pure UD and quasi−isotropic panels of different stacking sequence. Different patch shapes like circle, rectangle, square, ellipse, oval and octagon are considered. The CFRP panels are repaired by double sided pure UD patches adhesively bonded over the damaged area. Stress concentration factor is estimated before and after the repair to quantify the repair efficiency [74, 84]. The SCF reduction is deduced for different patch shapes maintaining a constant patch volume. Since peel stress at the patch edge plays an important role in the bonded patch repair performance therefore it is also considered as part of this study. Failure analysis of open cutout and repaired panel for certain best performing patch shapes in case of pure UD panel based on 3D−Hashin's failure criterion [36] is also presented to investigate the influence of patch shape on failure initiation strength apart from SCF and peel stress. Finally, a genetic algorithm based optimization approach in−conjunction with FEA is implemented for the dimensional optimization of identified best patch shape as well as adhesive layer thickness for obtaining higher repair performance. Tsai−Wu failure index and adhesive shear failure index are considered as objective functions for multi−objective optimization using GA. Experimental study is then carried out with the obtained optimum patch dimensions and adhesive thickness, and the whole field strain analysis using DIC as well as the percentage restoration in ultimate strength of repaired panels are discussed.

6.2 Specimen geometry and material properties

The typical model for the damaged specimen is shown in Fig. 6.1. The panel is made of UD Carbon/Epoxy composite laminate having eight layers. The length (L), width (W) and the thickness (t) of the panel are 250 mm, 50 mm and 1.6 mm respectively. The panel has got a circular hole of 10 mm diameter (d) so as to simulate the effect of damage removal. This type of removal happens in the case of low velocity impact damage. The panel is repaired with patch symmetrically bonded to each side of the specimen over the damage area. A circular patch of diameter D is also shown in the figure. The patch material is similar to that of parent laminate with a stacking sequence of $[0°]_4$ and its thickness (t_p) is 0.8 mm. The patch is bonded to the panel using highly brittle adhesive material (Araldite AV138/HV998 from Huntsman). The thickness of adhesive (t_a) is taken as 0.1 mm. The panel is subjected to an in−plane tensile load of 10 kN ($\sigma = 125MPa$) along $x-$direction. The dimensions of the panel and the material properties are taken from Ref. [82], the adhesive properties are taken from Ref. [197]. In case of pure UD panel the configuration is $[0°]_8$ and for quasi−isotropic panels the configurations are $[0/\pm 45/90]_s$, $[0/90/\pm 45]_s$, $[\pm 45/0/90]_s$ and $[90/0/\pm 45]_s$.

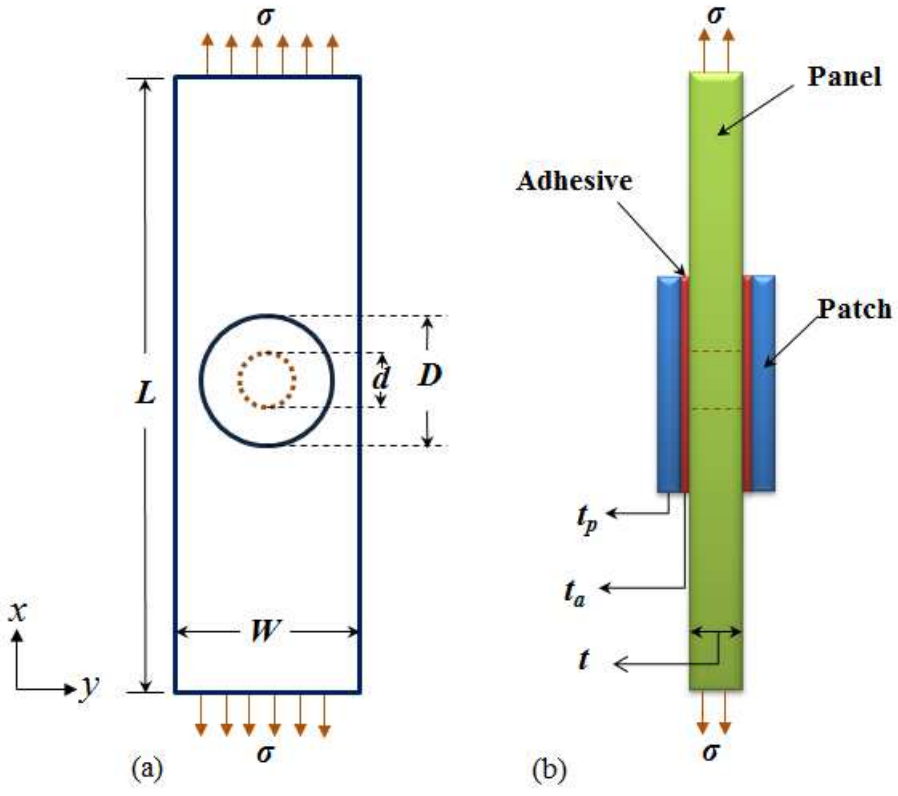

Figure 6.1: Specimen geometry of double sided repaired panel (a) front view (b) side view

6.3 Finite element modeling

6.3.1 Modeling of the damaged panel

FEA is the most effective tool for computing SCF in open cutout and repaired composite panels. In this work 3D modeling and analysis of open cutout and repaired panel is carried out using ANSYS−13 software. The mesh pattern around the hole and patch edge is kept very fine in order to capture the high stress concentration. A mesh convergence study has already been performed by the authors to arrive at the number of elements surrounding the hole and it is found to be 96. The mesh around the circular hole has a total of 4068 elements (96 circumferential; 6 radial; 8 elements along the thickness). The panel, patch and adhesive are modeled with 20−noded solid elements as per the dimensions shown in Fig. 6.1. In thickness direction, the panel is meshed with eight elements, adhesive with two elements and patch with four elements. Each layer in patch and panel is assigned one element in thickness direction. Mesh morphology surrounding the hole in the panel would vary with respect to the chosen patch shape. A tensile load of 10 kN is being applied as a pressure load of 125 MPa on the top surface of the panel. The bottom face is arrested in $x-$direction and the mid plane nodes of the panel are constrained in $z-$direction.

6.3.2 Modeling of the patch and repaired panel

In this work the composite panel is repaired with adhesively bonded composite patches. The model has a total of 15360 elements (96 circumferential; 40 radial with a spacing ratio of 0.2; 4 elements along the thickness). The layer angles are defined by assigning appropriate element coordinate system [198]. Since effective patch shape is to be investigated which can greatly reduce the SCF, shapes such as square, rectangle, circle, ellipse, octagon and oval are modeled keeping area of all the patches to be same. In this work four different areas are considered and they are 600,750, 900 and 1000 (in mm^2). The thickness of patch is kept constant (0.8 mm) and hence the volume. The patches are centered with respect to the panel and bonded over the cutout using adhesive. The thickness of the adhesive is taken as 0.1 mm. The mesh pattern in adhesive layer is generated similar to that of patch and it is bonded to the patch/panel using multi point constraint algorithm. A layer configuration of 0° is chosen for the patch so that the fiber is kept parallel to the loading direction ($x-$axis) for maximizing the load carrying capacity. The geometry of different patch configurations is shown in Fig. 6.2. The finite element model of the symmetrically repaired panel having different patch shapes is shown in Fig. 6.3.

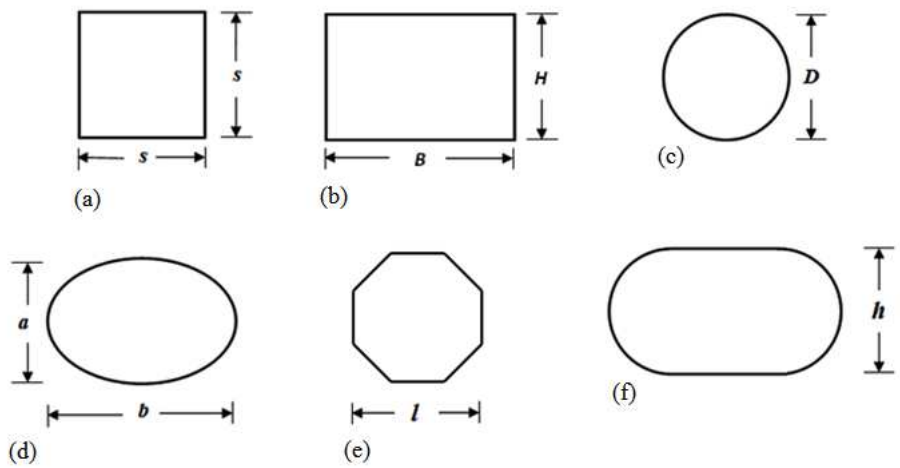

Figure 6.2: Geometry of different patch shapes (a) square (b) rectangle (c) circular (d) elliptical (e) octagonal (f) oval

6.3.3 Square patch

The geometry of square patch is shown in Fig. 6.2 (a) and the respective finite element model is shown in Fig. 6.3 (a). The side length are 24.5, 27.38, 30 and 31.62 (in mm) corresponding to the areas 600, 750, 900 and 1000 (in mm^2) respectively.

6.3.4 Rectangular patch

The FE model of rectangular patch is shown in see Fig. 6.3 (b). Two possible cases are considered here, one is keeping a constant width (B) with varying patch height (H) and the second one is keeping a constant height with varying patch width. In first case, for a width of 23 mm four different patch heights 26, 32.6, 39.13 and 43.47 (in mm) are considered. In the next case for a constant height of 23 mm with four different patch widths 26, 32.6, 39.13 and 43.47 (in mm) are chosen. For both the cases the corresponding areas are 600, 750, 900 and 1000 (in mm^2).

6.3.5 Circular patch

The finite element model of circular patch is shown in Fig. 6.3 (c). Circular patch of four different radii 13.82, 15.45, 16.92 and 17.84 (in mm) corresponding to the areas 600, 750, 900 and 1000 (in mm^2) are considered.

6.3.6 Elliptical patch

Elliptical patch as shown in Fig. 6.3 (d) is created by scaling the circular patch area appropriately in horizontal and vertical direction. Two different cases of the elliptical patch are considered: one in which major axis of ellipse is kept parallel to the loading direction ($x-$axis) called longitudinal ellipse and the second is transverse ellipse in which major axis is perpendicular to the loading direction. In this work the minor axis of the ellipse is taken as 27 mm whereas the values of major axis length are 28.28, 35.35, 42.42 and 47.13 (in mm) respectively. The corresponding areas are 600, 750, 900 and 1000 (in mm^2).

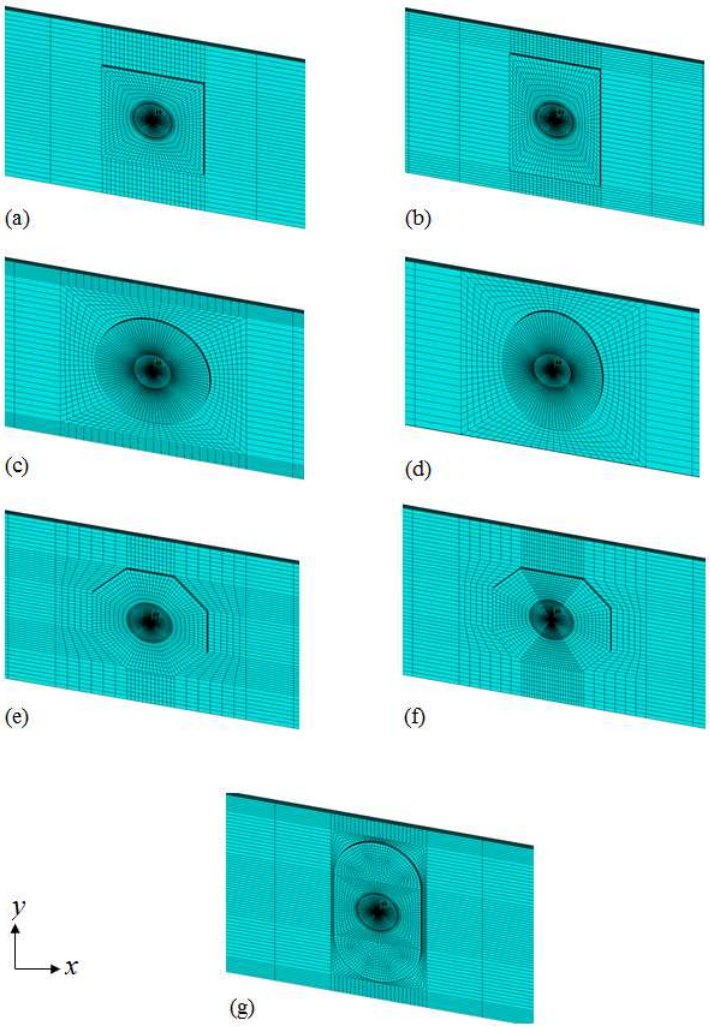

Figure 6.3: Finite element model of double sided patch repaired panel with different patch shapes (a) square (b) rectangle (c) circular (d) elliptical (e) octagonal (f) extended octagon (g) oval

6.3.7 Octagonal patch

Here two different geometry of octagonal shape are considered: regular octagonal as shown in Fig. 6.3 (e) and extended octagon as shown in Fig. 6.3 (f)). In case of regular octagonal patch two different cases are possible: one in which regular octagon is resting on its vertex and in second case octagon is resting on its edge or side of the octagon is parallel to loading direction ($x-$axis). Regular octagon is generated from the square area. The octagonal patch is studied for four different side length (l) 26.91, 30.08, 32.96 and 34.73 (in mm) which corresponds to the area 600, 750, 900 and 1000 (in mm^2). Extended octagon is created by extending two parallel sides and the corners are chamfered at 45° such that the area of extended and regular octagon is kept same. The extended octagonal patch is also studied for four different side length (l) 27.32, 31.49, 35.44 and 37.96 (in mm).

6.3.8 Oval patch

The geometry and finite element model of oval patch is shown in Fig. 6.2 (f) and Fig. 6.3 (g) respectively. It is generated by appending the rectangular one with semi−circle on both sides of it. The height (h) of rectangle is kept same as that of circle diameter. Two different cases of oval patch are considered: one in which the dimension h is parallel to loading axis (longitudinal oval patch) and the other in which dimension h is perpendicular to loading axis (transverse oval patch). Four different values of h are considered; 19.54, 21.85, 23.93 and 25.23 (in mm) correspond to the areas 600, 750, 900 and 1000 (in mm^2).

6.4 Comparison of analytical and FEA results for an open cutout panel

Firstly for the open cutout panel, a comparison between the theoretical value and the stress estimated from the finite element model is being made. The theoretical stress is calculated according to Lekhnitskii's equation given in Ref. [199]. As per Lekhnitskii's derivation, the longitudinal stress σ_{xx} at any point on $y-$axis along the net−section of open cutout panel can be approximated by,

$$\sigma_{xx}(0,y) = \frac{\sigma_0}{2}\left[2 + \left(\frac{r}{y}\right)^2 + 3\left(\frac{r}{y}\right)^4 - (1+n-3)\left\{5\left(\frac{r}{y}\right)^6 - 7\left(\frac{r}{y}\right)^8\right\}\right] \quad ;(y > r) \tag{6.1}$$

where n is obtained by,

$$n = \sqrt{2\left(\frac{E_{11}}{E_{22}} - 2\nu_{12}\right) + \frac{E_{11}}{G_{12}}} \tag{6.2}$$

where σ_{xx} is longitudinal stress in loading direction, σ_0 is the applied stress, r is the radius of hole and y is the position along net−section of open cutout panel.

The comparative plot of σ_{xx} variation along the net−section of open cutout panel between analytical and finite element result is shown in Fig. 6.4. It can be observed from figure that normal stress is maximum at hole edge and it reduces as one moves away from the hole towards panel edge. It is also evident from the figure that the longitudinal stress variation from both analytical and FE model has a similar trend and relatively shows a good agreement thereby confirming the adequacy of the mesh in FE model of the panel.

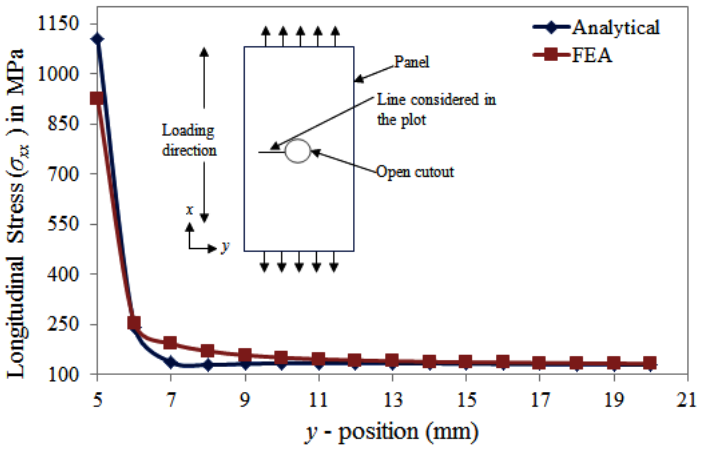

Figure 6.4: Longitudinal stress variation along the net−section in case of open cutout panel: analytical vs. FEA

6.5 Efficiency of adhesively bonded patch repair

In an externally bonded patch repaired composite panel, the longitudinal stress is the most predominant component which causes the failure and affects the load carrying capacity [74, 75]. Longitudinal stress is maximum at two locations: transverse extremities of hole and longitudinal extremities of patch overlap edge (on skin) known to be damage prone locations as discussed earlier. So, the repair efficiency in case of externally bonded composite structure is mainly analyzed by comparing the longitudinal stress before and after the repair and is generally represented in normalized form i.e., SCF [74, 84]. The adhesive/adherend interface is another critical location where the damage may initiate. The inter−laminar shear and peel stress are the main stress component to initiate failure at that interface [74, 75]. The moderate peel and shear stress concentrations at the overlap edge, arising from the differential straining effects on the structure and patches hampers high efficiency of externally bonded patch repairs [78]. The high shear and peel stress in the adhesive layer at the patch edges causes them to be partially or completely detach from the panel thereby limiting the repair efficiency [76]. Hence, the shear and peel stress concentration in the repaired configuration are always considered for repair performance assessment.

To understand the mechanics of double sided patch repair and evaluate their repair efficiency, open cutout panel bonded with circular patch is firstly considered. The efficiency of adhesively bonded repair is analyzed in terms of SCF reduction after the repair. The SCF is evaluated using Eq. 6.3 and it is given as the ratio of maximum stress in longitudinal direction to the remote stress.

$$SCF = \frac{(\sigma_0)_{max}}{\sigma_0} \tag{6.3}$$

The panel is repaired with a circular patch of area 1000 mm^2 having a stacking sequence of $[0°]_4$. Figure 6.5 shows the variation of longitudinal stress in an open cutout and repaired panel along the net−section. The maximum stress in an open cutout and repaired panel are 923.55 MPa and 229.43 MPa respectively. The SCF is reduced from 7.38 before repair to 1.83 after the repair, resulting in a reduction of 75% in the SCF. This is due to the fact that the load is transferred through the

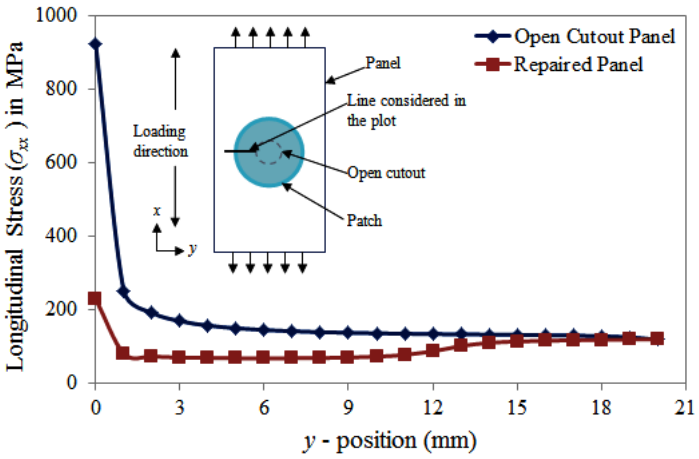

Figure 6.5: Comparative plot of longitudinal stress variation between open cutout and repaired panel along the net−section

patch over the damaged area and hence a reduction in SCF is observed after the repair. The SCF reduction is analyzed for various patch shapes to investigate their influence on repair performance and they are discussed in following section.

6.6 Influence of patch shapes on repair efficiency: pure UD panel

6.6.1 Square patch

Figure 6.6 shows the variation of SCF with respect to the size of square patch. From the figure it can be observed that the SCF reduction is directly proportional to the patch size, as the patch size increases the SCF decreases. This is due to the fact that the increase in patch size increases the overlapping area which leads to more load transfer through the patch and hence more reduction in SCF is observed. Thus patch with maximum allowable area is preferred in the case of square shape.

6.6.2 Rectangular patch

Figure 6.7 shows the variation of SCF with respect to the size of rectangular patch. It can be observed from figure that for fixed height case with increasing width the SCF reduces initially and then raises after patch width of 33 mm. For the other case the SCF decreases with patch height. However, the performance of rectangular patch with larger width is better as compared to the one with larger height. This is because one with larger width provides more reinforcement along the loading direction and hence more directional stiffness as compared to the other one. Hence, rectangular patch with larger width ($B > H$) is preferred.

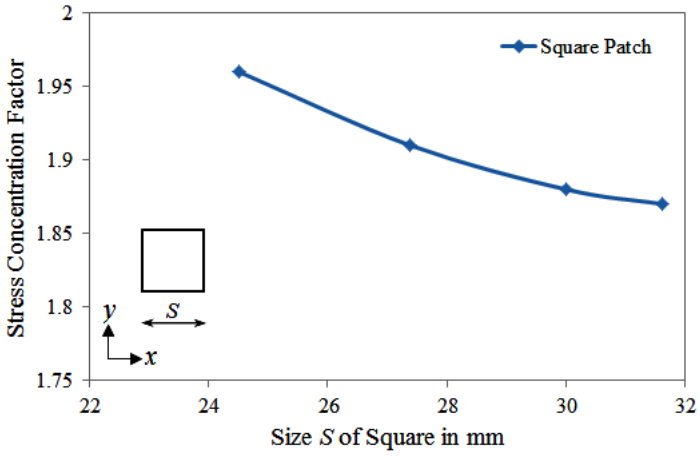

Figure 6.6: Variation of SCF with the side length S of square patch

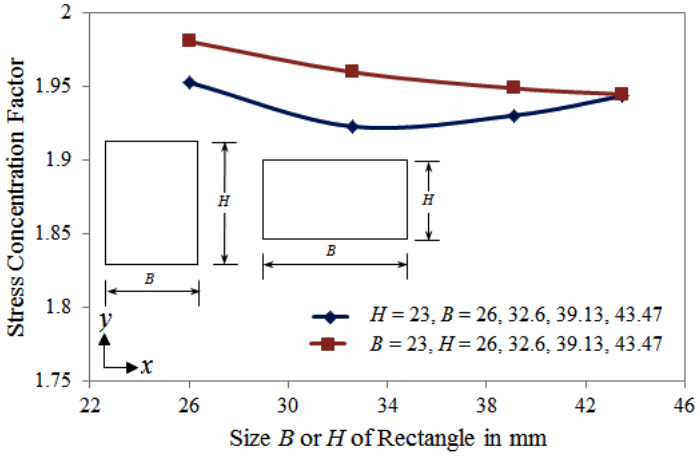

Figure 6.7: Variation of SCF with rectangular patch size B or H

6.6.3 Circular patch

Figure 6.8 shows the variation of SCF with respect to the diameter of circular patch. It is evident from the figure that as diameter of the patch increases, overlapping area increases and hence SCF decreases and it shows a similar behaviour to that of square patch model.

6.6.4 Elliptical patch

Figure 6.9 shows the variation of SCF with respect to the major axis of elliptical patch. It can be observed from figure that the SCF reduction in case of transverse elliptical patch is more as compared to the longitudinal one. This is because the transverse elliptical patch provides more overlapping area across the highly stress region of the panel and hence more load transfer happens through the patch in this region leading to SCF reduction. The behaviour of longitudinal ellipse is very similar to that of rectangular patch with fixed height.

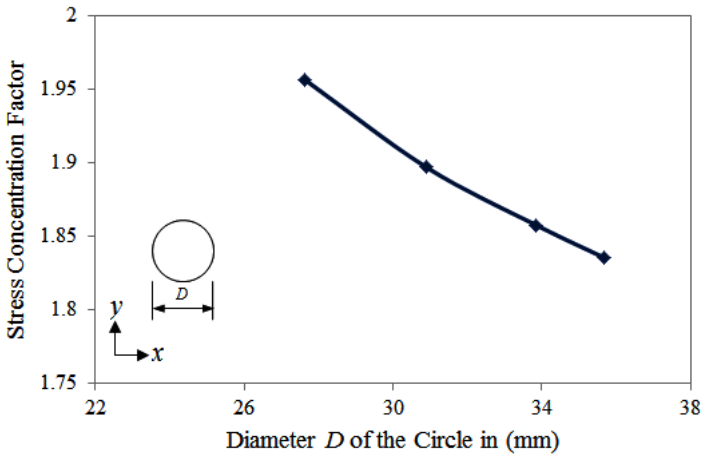

Figure 6.8: Variation of SCF with the diameter D of circular patch

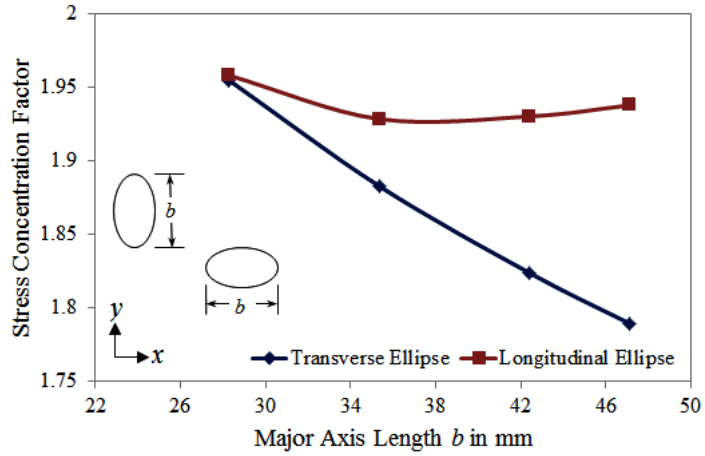

Figure 6.9: Variation of SCF with major axis b for elliptical patch

6.6.5 Octagonal patch

Figure 6.10 shows the variation of SCF with respect to the size of octagonal patch. It can be observed from figure that the SCF reduction is proportional to the size of octagonal patch. It is because as patch size increases the overlapping or load transfer area increases over the damaged area thereby decreasing SCF similar to that of circular patch model. However, the edge based octagonal patch (side parallel to loading axis) performs better than the vertex based octagonal patch. Further it is evident from Fig. 6.11 that the SCF reduction in case of extended octagonal patch is same as that of the edge based octagonal patch. Hence, both extended as well as edge based octagonal patch shape is preferred.

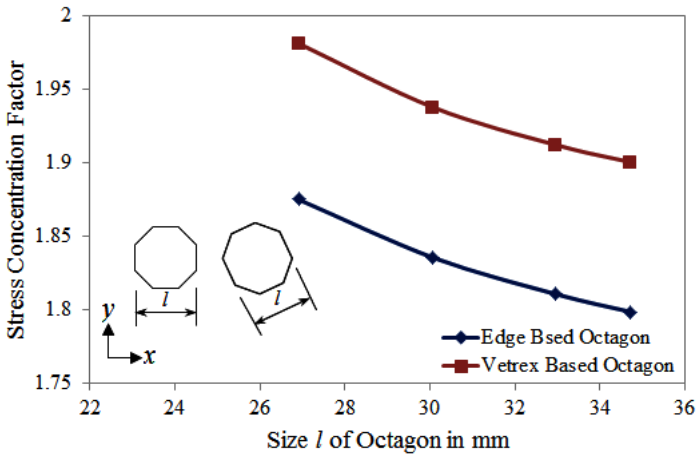

Figure 6.10: Variation of SCF with the distance l for regular octagonal patches

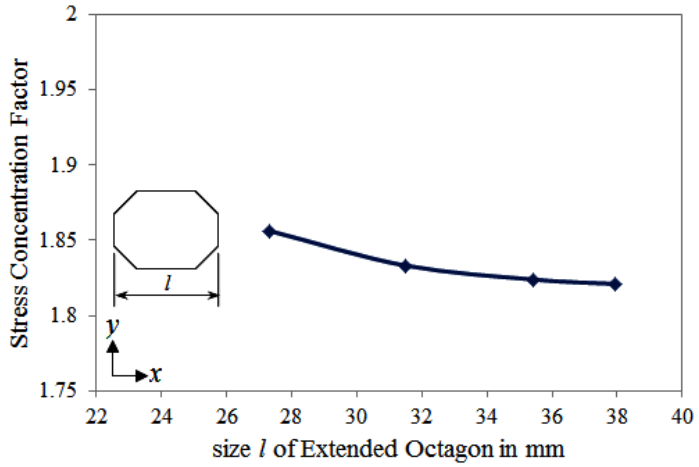

Figure 6.11: Variation of SCF with the distance l for extended octagonal patch

6.6.6 Oval patch

Figure 6.12 shows the variation of SCF with respect to the dimension h of oval patch. It is observed from the figure that the behaviour of longitudinal oval patch is similar to that of rectangular patch with fixed height. However, the behaviour of transverse oval patch is similar to that of rectangular patch with fixed width. It is also observed from figure that the performance of longitudinal oval patch is better than the transverse one for the smaller dimension of the patch. As the dimension of patch increases more than 23 mm reduction in SCF is observed in case of transverse oval patch in contrast to the longitudinal one. Hence, the transverse oval patch is preferred.

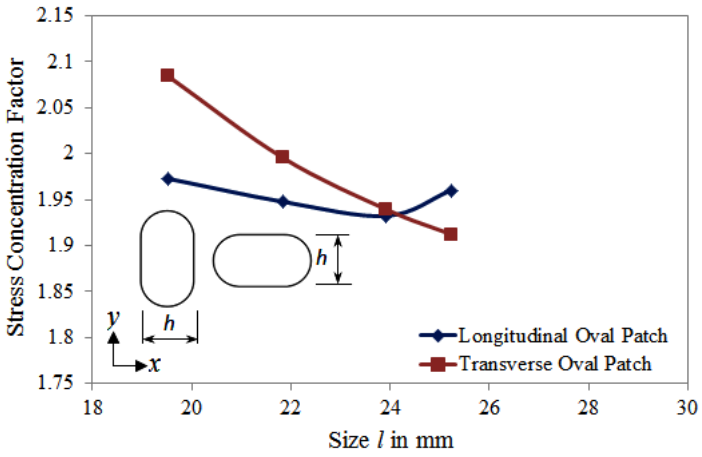

Figure 6.12: Variation of SCF with the dimension h for oval patch

6.7 Comparative study of different patch shapes: pure UD panel

The influence of various possibilities of a given patch shape on SCF reduction is studied in the previous sub−sections. Only certain patch shapes are chosen based on their performance. A comparative study is done in this section among those chosen patch shapes to identify the best performing shape. Four different patch areas are considered: 600, 750, 900 and 1000 (in mm^2). The thickness of patch is kept constant and hence the volume. In previous section it is shown that the rectangular patch with greater width performs better than the one with greater height. Hence, the rectangular patch with greater width is considered here for comparison. The performance of transverse elliptical patch, edge based octagonal patch and transverse oval patch is found to be better than their counter parts because of higher directional stiffness and hence they are considered here. Also square, circular and extended octagonal patch shape is further included for an overall comparison. Further, the peel stress (σ_{zz}) and failure strength is also included in this section for performance comparison of various patch shape. The study is done for the patch area of 1000 mm^2.

6.7.1 Based on SCF

Figure 6.13 shows the variation of SCF with respect to area for all the patch shape mentioned in above section. It can be observed from figure that the SCF reduction is greater for larger patch area and vice−versa for all the shapes except the rectangular patch with fixed height i.e, the SCF is decreasing with increasing patch area because load transfer by patch increases with patch area. It is evident from the figure that the extended octagonal patch is more efficient in terms of SCF reduction as it provides more directional stiffness compared to other patch shapes. It is closely followed by the edge based octagonal patch. The performance of transverse elliptical patch is same as that of extended octagonal patch for largest patch area. However, it can be observed from the figure that the SCF reduction is more prominent with increasing patch area in case of extended octagonal patch as compared to other shapes. Now, one needs to look at the peel stress and failure strength values for final recommendation and it is presented in next sub−sections.

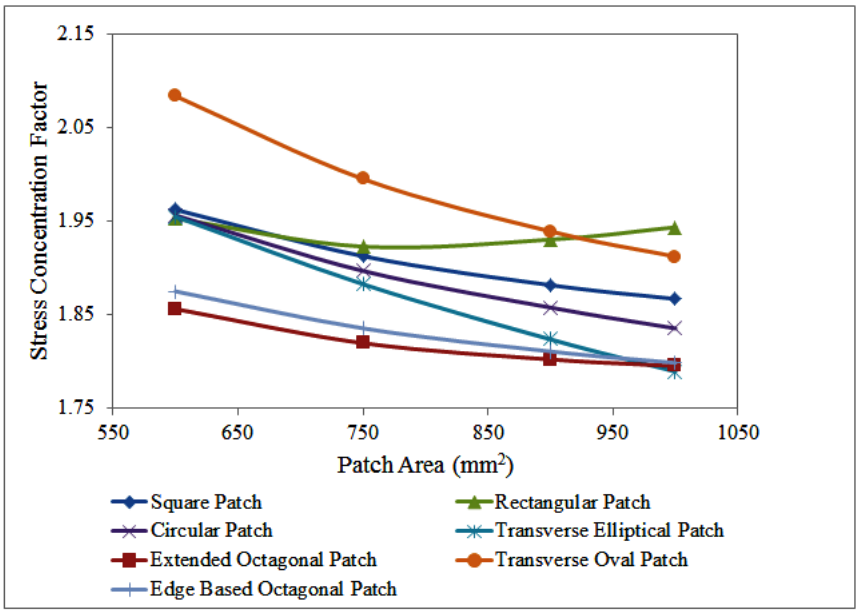

Figure 6.13: Comparative plot showing SCF variation with respect to patch area for different patch shapes

6.7.2 Based on peel stress

The variation of peel stress in adhesive layer with respect to different patch configurations is shown in Fig. 6.14. High peel stress develops due to the differential straining effects between panel and patch. Obviously they are related to patch stiffness and therefore one gets different peel stress values for different patch shapes. It is found that in case of transverse elliptical, circle, extended octagonal and edge based octagonal patch the maximum peel stress develops at longitudinal extremities of the patch overlap edge and for square and rectangular shape it is developed at longitudinal extremities of the hole edge at adhesive/adherend interface. The observed maximum peel stress locations are consistent with the observation made in Ref. [20]. It can be observed from the figure that the transverse elliptical patch appears to be the under performing one in terms of peel stress. The edge based octagonal patch performs better as compared to all other patch shapes in terms of lower peel stress. However, the peel stress developed in case of extended octagonal patch is found to be comparable to the edge based octagonal patch. Since extended octagonal patch shows slightly more SCF reduction as compared to the edge based octagonal patch therefore it is recommended for the repair of UD laminate with [0°] layup.

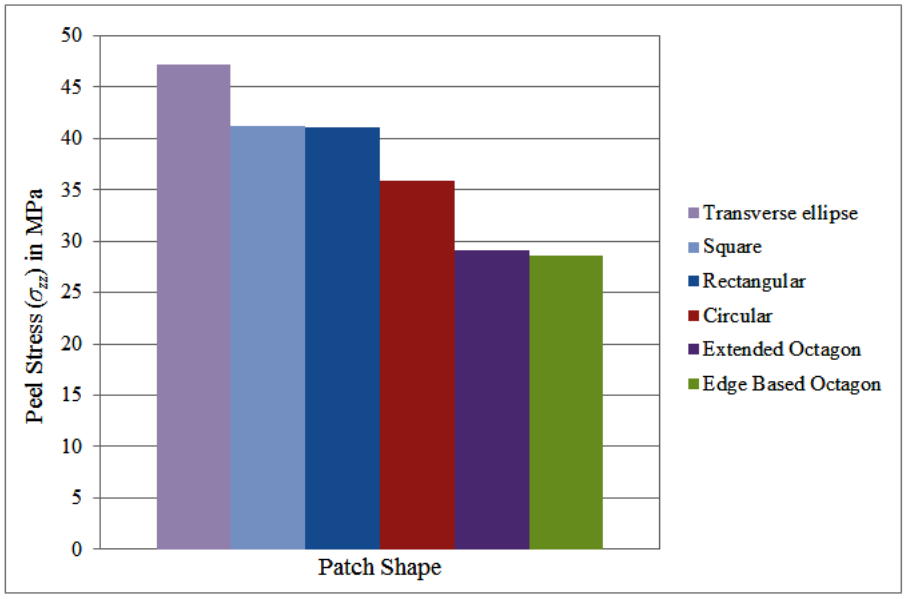

Figure 6.14: Comparative plot of peel stress for different patch shapes

6.7.3 Based on strength predicted using failure criterions

In this sub−section, the failure analysis of unrepaired and repaired panel is carried out to investigate the influence of various patch shape on failure initiation strength apart from SCF and peel stress. A stressed based 3D−Hashin's failure criterion [36] is used to predict the damage in repaired panel because it is an interactive failure theory and predicts each failure mode separately. Four different failure modes are considered in this study and they are matrix failure in tension and compression, fiber failure in tension and compression. The maximum shear stress criterion is used for predicting the failure of adhesive layer to monitor the patch debonding [76]. The failure criterions for composite laminate are taken from Ref. [36] and for adhesive it is taken from. [76]. From the analysis, it is found that the damage in open cutout panel initiates with matrix cracking around the hole. However, damage in repaired panel initiates with patch debonding at the overlap edge followed by localized matrix cracking. The results presented here are very much consistent with those in Refs. [74, 76, 142]. The debonding load and strength at failure initiation for various patch shapes are presented in Table 6.1. It can be found that the extended octagon patch has got the maximum values. Hence, extended octagonal patch shape is preferred for the repair of pure UD panel. This study further reinforces the selection of extended octagonal patch shape apart from SCF and peel stress reduction criterion thereby strengthening the basis for selection of patch shape.

Table 6.1: Influence of patch shape on patch debonding load and failure initiation strength (pure UD panel)

Patch Shape	Patch Debonding Load (kN)	Failure Initiation Strength (MPa)
Notched panel	-	118.07
Square	18.68	348.21
Rectangular ($B > H$)	17.86	340.45
Circular	19.43	374.05
Transverse ellipse	16.88	329.21
Edge based octagon	22.04	383.01
Extended octagon	22.09	389.42
Transverse oval	18.23	344.78

6.8 Influence of patch shapes on repair efficiency: quasi−isotropic panels

In this section influence of patch shape on damaged quasi−isotropic laminate is analyzed. In the present work four different stacking sequences for the panel are considered: $[0/\pm 45/90]_s$, $[0/90/\pm 45]_s$, $[\pm 45/0/90]_s$ and $[90/0/\pm 45]_s$. All are balanced laminates. The panel is repaired with different patch shapes having an identical area of 1000 mm^2. The stacking sequence of the patch is $[0^\circ]_4$.

6.8.1 Based on SCF and peel stress

The influence of patch shapes on SCF and peel stress for different quasi−isotropic laminates is presented in Table 6.2 and 6.3 respectively. In case of $[0/\pm 45/90]_s$ and $[0/90/\pm 45]_s$ configuration, from Table 6.2 it is clear that the transverse elliptical, square and rectangular shape are more efficient in terms of SCF reduction as compared to other ones, because they provide more directional stiffness along the loading direction as well as more reinforcement and greater overlap bonding over the high stressed zone. A comparative study is done among these three patch shapes based on peel stress for identifying the efficient one having lowest peel stress. From Table 6.3, it is found that the rectangular patch ($B > H$) or fixed height shows a lowest peel stress value because it has got largest overlap length followed by square, rectangular ($H > B$) and transverse elliptical shapes respectively. Hence, the transverse elliptical patch appears to be under−performing in terms of peel stress. Thus, on overall comparison the rectangular patch with greater width is preferred over the other shapes for the repair of laminate with a stacking sequence of $[0/\pm 45/90]_s$ and $[0/90/\pm 45]_s$. In case of $[\pm 45/0/90]_s$ and $[90/0/\pm 45]_s$ laminate, the transverse oval patch configuration is more efficient in terms of SCF reduction as compared to other patch shapes. The performance of longitudinal and transverse elliptical patch is the same and also closer to the transverse oval patch. However, transverse oval patch is having lower peel stress. Hence, the transverse oval patch is preferred for the repair of panel with a stacking sequence of $[\pm 45/0/90]_s$ and $[90/0/\pm 45]_s$.

Table 6.2: Influence of patch shape on SCF for different quasi−isotropic panels

	Panel Stacking Sequence			
Patch Shape	$[0/\pm 45/90]_s$	$[0/90/\pm 45]_s$	$[\pm 45/0/90]_s$	$[90/0/\pm 45]_s$
Square	3.70	3.76	2.57	2.55
Rectangular ($B > H$)	3.72	3.77	2.59	2.57
Rectangular ($H > B$)	3.71	3.76	3.71	2.64
Circular	4.04	4.07	2.55	2.53
Transverse ellipse	3.70	3.74	2.35	2.34
Longitudinal ellipse	4.84	4.86	2.35	2.34
Edge based octagon	4.11	4.12	2.64	2.62
Vertex based octagon	4.67	4.68	2.57	2.55
Extended octagon	4.27	4.28	2.64	2.62
Longitudinal oval	4.63	4.65	2.61	2.59
Transverse oval	3.97	3.99	2.33	2.32

Table 6.3: Influence of patch shape on peel stress (σ_{zz}) in MPa for different quasi−isotropic panels.

	Panel Stacking Sequence			
Patch Shape	$[0/\pm 45/90]_s$	$[0/90/\pm 45]_s$	$[\pm 45/0/90]_s$	$[90/0/\pm 45]_s$
Square	63.33	63.67	-	-
Rectangular ($B > H$)	54.93	55.09	-	-
Rectangular ($H > B$)	70.83	71.28	-	-
Transverse ellipse	85.72	85.92	80.31	77.75
Longitudinal ellipse	-	-	66.42	65.51
Transverse oval	-	-	55.83	54.62

6.9 Parametric optimization using genetic algorithm approach

In composite structures domain, researchers [94, 96, 97, 110, 200] have first employed GA approach for optimization of stacking sequence. In the present work, genetic algorithm available in MATLAB global optimization toolbox is used to obtain the optimal value of various parameters involved in composite repair so that maximum repair efficiency can be obtained. Genetic algorithm is an efficient global search optimization method which operates on a population of potential solutions applying the principle of survival of the fittest to produce successively better approximations to a solution [46]. GA utilizes three basic operators namely selection, crossover, and mutation. These three operators are repeated continuously until the optimal solution is obtained. Mostly numerical technique such as FEA is preferred for generating the initial population for GA based optimization. The optimization problem can be stated as:

$$Minimize \quad f(x) \tag{6.4}$$

$$subjected\ to \quad x_i^L \leq x_i \leq x_i^U \quad , i = 1, 2, 3, ..., n \tag{6.5}$$

where $f(x)$ is the objective function, x_1, x_2, x_3,.....x_i are the design variables and x_i^L and x_i^U are the lower and upper bound on the design variables.

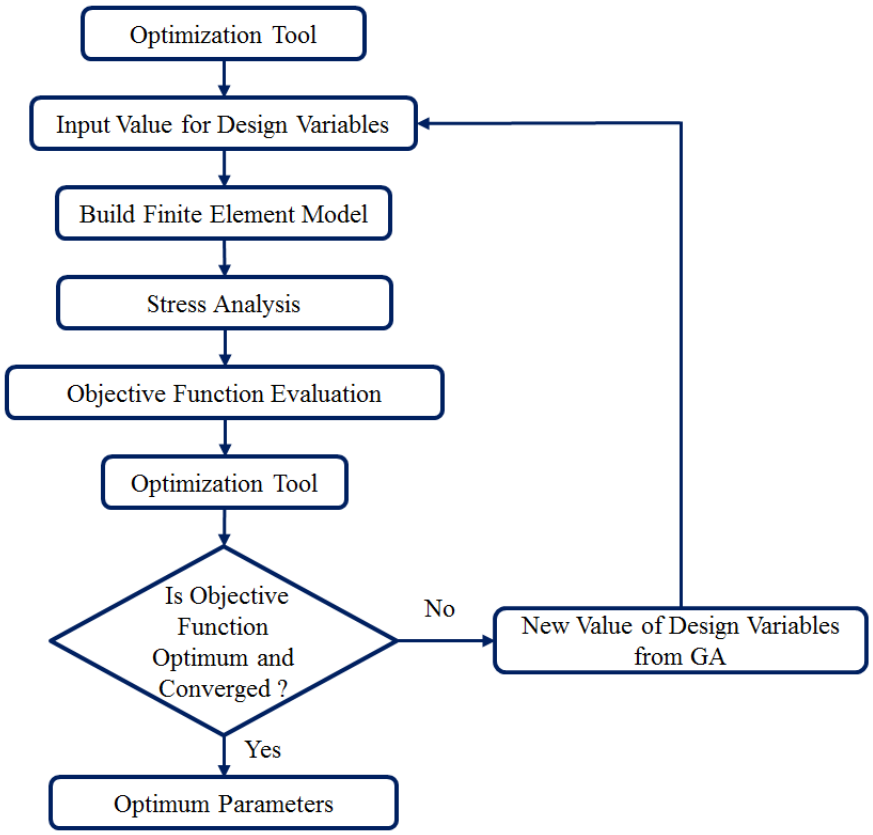

Figure 6.15: Optimization flowchart depicting the methodology implemented

To obtain maximum repair efficiency, SCF should be minimized which is considered as an objective function here. The adhesive and patch parameters are the design variables. The optimization scheme implemented in the present study is represented by a flowchart as given in Fig. 6.15. The sizing optimization is performed by developing an interface between optimization tool in MATLAB and FEA software ANSYS. The optimization process starts with assigning of initial value of the parameters. These parameters are read in APDL (ANSYS Parametric Design Language) and stress analysis is performed to evaluate SCF. The SCF value is read into optimization algorithm and then solution optimality and convergence criteria are checked. If the solution is optimal and convergence criteria are met the program exit out of the loop and the design variables and convergence history are plotted. If not, the search for optimum parameter continues till it is obtained.

6.9.1 Optimization of repair parameters: pure UD panel

The influence of patch shapes on repair efficiency of pure UD laminate is studied in the previous sub−section 6.6. It is found that extended octagonal patch performs better in case of repair of UD laminate with $[0°]$ layup. Having arrived at the shape, one needs to obtain the optimum dimension for a given shape so that maximum reduction in SCF can be achieved. In this section GA in−conjunction with FEA is used for arriving at the optimum dimension of the patch applied to repair of UD laminate of $[0°]_8$ configuration. The recommended patch shape for $[0°]_8$ panel is extended octagonal shape and it is assigned $[0°]_4$ configuration. The area of patch (Ap), patch thickness (tp), chamfer length

(lp) and adhesive thickness (ta) are the considered different design variables. The lower and upper bound of design variables and the GA parameters used in optimization algorithm are summarized in Table 6.4. The lower and upper bound on design variables is governed by the panel geometry. The bounds for patch area and chamfered length depend on the hole diameter and panel width. The patch thickness bounds are chosen based on panel thickness and fiber layer thickness. Also good adhesive bond strength can be produced with smaller adhesive layer thickness. In genetic algorithm, tournament selection method is used for randomization as it chooses random set of individuals and picks out the best among them. It is more effective in terms of solution optimality and convergence time. The heuristic crossover is used as genetic operator. Adaptive feasible function is used as mutation operator.

Table 6.4: Parameters used in optimization scheme: pure UD repaired panel.

GA−parameters		
Population size	20	
Elite size	2	
Crossover fraction	0.8	
Selection scheme	Tournament	
Crossover scheme	Heuristic	
Mutation scheme	Adaptive feasible	
Design Parameters	Lower bound	Upper bound
Patch area (Ap) in mm^2	600	2200
Patch thickness (tp) in mm	0.2	1.6
Chamfer length (lp) in mm	4	20
Adhesive thickness (ta) in mm	0.05	0.25

The convergence is assumed to be reached when average change in fitness value is less than the function tolerance (1e^{-}6). The convergence history of fitness value (objective function) with number of generation is shown in Fig. 6.16. It is found that the convergence is achieved after fifty one generations. However, the optimum solution is achieved at twenty ninth generation giving magnitude of maximum longitudinal stress as 188.5 MPa. The SCF for panel with optimized patch dimension and adhesive thickness is found to be 1.508 as compared to 7.38 when unrepaired. For same optimum patch configuration and adhesive thickness the peel stress is 21 MPa. The optimized dimensions are given in Table 6.5 and optimal patch geometry is shown in Fig. 6.17. Using the same procedure given in optimum patch size and adhesive thickness can be obtained for quasi−isotropic panels too.

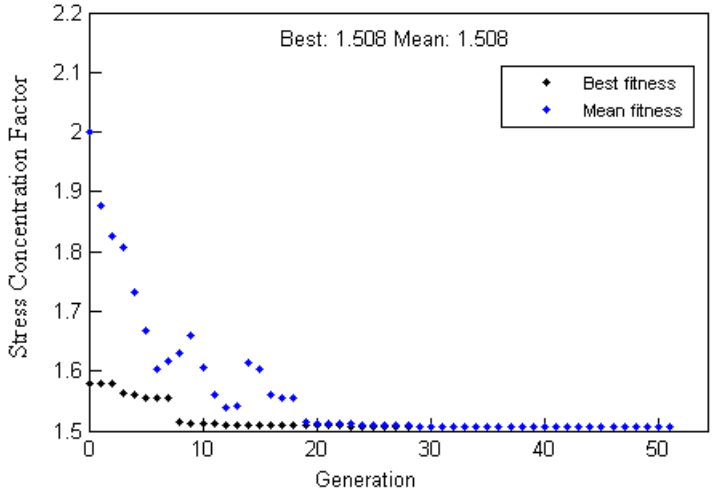

Figure 6.16: Convergence plot for GA algorithm

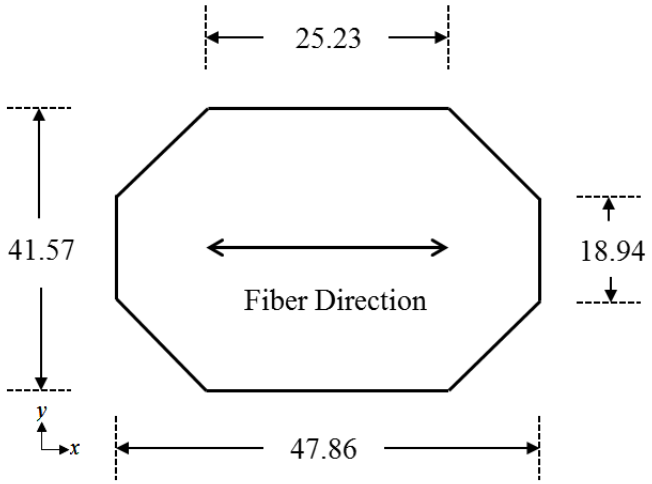

Figure 6.17: Optimized patch geometry for extended octagonal patch shape (in mm)

Table 6.5: Optimized repair parameters.

Design Parameters	Optimum value
Patch area (Ap)	1733.651 (mm^2)
Patch thickness (tp)	0.995 (mm)
Chamfer length (lp)	15.997 (mm)
Adhesive thickness (ta)	0.126 (mm)

6.10 Optimization of repair parameters using multi−objective genetic algorithm with Tsia−Wu and maximum shear stress failure criteria

In single objective optimization as discussed in section 6.9, the solution is only a single point but in multi−objective optimization, the solution is family of points known as Pareto−optimal set. In case of a single objective optimization, the comparison is trivial since a vector solution X is better than Y if the corresponding objective function (fitness) value $f(X)$ is greater than $f(Y)$. If there are N objective functions, two solutions X and Y must be related in terms of dominance of one solution over the other with respect to all N objectives. As a result of the multi−objective search process, convergence is achieved on a Pareto−optimal region of non−dominated solutions which can be subjectively managed by the decider to identify the preferred solution [201]. The application of GA and other rank−based algorithms to multi−objective optimization is of great attention in mechanics area.

In bonded composite patch repair application, multi−objective optimization is essential because the strength of repaired panel is influenced by the stress level in patch and panel as well as shear/peel stress level in the adhesive layer. Therefore, multi−objective optimization in conjunction with FEA is further carried out in this section to obtain the optimized patch dimensions and adhesive thickness for attaining higher strength. Since, the design of most of the structural elements are essentially based on the ultimate values of stresses/strains, the failure criterion is usually considered as a benchmark for determining their strength. Therefore, a failure criteria is integrated with the developed optimization scheme and multi−objective optimization study in case of repaired panel is performed. Tsai−Wu failure criteria is implemented for identifying the failure in CFRP patch and panel whereas maximum shear stress criteria is considered for shear failure of adhesive layer leading to patch debonding.

6.10.1 Multi−objective optimization problem statement

The statement of the present optimization problem is to maximize the strength of repaired panel by obtaining the optimized value of patch dimensions and adhesive thickness. Since, in adhesively bonded patch repaired panel, the patch helps in redistribution of the load over the damaged area by transferring a portion of the load to the panel through the adhesive layer. Therefore, two objectives are considered in the developed multi−optimization scheme. The first objective is to reduce the stress level in CFRP panel and patch based on Tsai−Wu failure index (FI_{TW}) and the second objective is to reduce the shear stress level in the adhesive layer based on adhesive shear failure index (FI_{τ}). The strength of the repaired panel is reflected by the value of these failure indices (FI_{TW} and FI_{τ}), i.e, the lower the failure indices are, the stronger the repaired panel is for a given load scenario. Hence, the failure indices FI_{TW} and FI_{τ} are the two objective functions. Patch dimensions and adhesive thickness are the design variables whose optimized value has to be obtained corresponding to the minimum value of failure indices FI_{TW} and FI_{τ} such that the strength of repaired panel as a whole can be maximized.

This multi−objective optimization problem can formally be stated as:

$$Minimize \quad f_i(x) \quad , i = 1, 2 \tag{6.6}$$

$$subjected\ to \quad x_j^L \leq x_j \leq x_j^U \quad , j = 1, 2, 3, ..., n \tag{6.7}$$

where $f_1(x) = FI_{TW}$, $f_2(x) = FI_\tau$ are the objective functions, x_1, x_2, x_3,.....x_j are the design variables corresponding to patch dimensions and adhesive thickness, x_j^L and x_j^U are the lower and upper bound of the design variables.

Tsai−Wu (TW) failure criteria

The first objective function, Tsai−Wu failure index FI_{TW} can be written as [202–204]:

$$FI_{TW} = F_{ij}\, \sigma_i\, \sigma_j + F_i\, \sigma_i \leq 1 \quad ;\ i, j = 1, 2, ..., 6 \tag{6.8}$$

where σ_i is the stress components, and F_i, F_{ij} are the experimentally determined material strength parameters. The CFRP patch and panel elements are treated as failed when FI_{TW} reaches or exceeds unit.

The Tsai−Wu criterion given by Equation(6.8) is the simplest of the tensor polynomials. It is most commonly used model taking account of failure mode interaction. Because of its general nature, this theory contains almost all other polynomial theories as special cases. For orthotropic material under plane stress assumptions, the Equation(6.8) reduces to:

$$FI_{TW} = F_{11}\, \sigma_1^2 + F_{22}\, \sigma_2^2 + 2\, F_{12}\, \sigma_1\, \sigma_2 + F_{66}\, \tau_{12}^2 + F_1\, \sigma_1 + F_2\, \sigma_2 \leq 1 \tag{6.9}$$

Here the strength coefficients $F_{11}, F_{22}, F_{66}, F_1$, and F_2 can be estimated from X_T, X_C, Y_T, and Y_C obtained experimentally. However, F_{12}, which reflects the effect of the interaction between the two normal stresses, is difficult to obtain experimentally. Hence, for TW failure criterion F_{12} is chosen as:

$$F_{12} = -\frac{1}{\sqrt{X_T X_C Y_T Y_C}} \tag{6.10}$$

The other strength coefficients can be evaluated as:

$$F_1 = \frac{1}{X_T} - \frac{1}{X_C} \tag{6.11}$$

$$F_{11} = \frac{1}{X_T X_C} \tag{6.12}$$

$$F_2 = \frac{1}{Y_T} - \frac{1}{Y_C} \tag{6.13}$$

$$F_{22} = \frac{1}{Y_T Y_C} \tag{6.14}$$

$$F_{66} = \frac{1}{S_{12}^2} \tag{6.15}$$

Maximum shear stress failure criteria

The second objective function, adhesive shear failure index (FI_τ) can be written as [76]:

$$FI_\tau = \left(\frac{\sigma_1 - \sigma_3}{2}\right) \leq \tau_s \tag{6.16}$$

where σ_1 and σ_3 are the maximum and minimum principal stresses in the adhesive layer and τ_s is shear strength of the adhesive. The adhesive elements are treated as failed when FI_τ reaches or exceeds unity.

The failure indices FI_{TW} and FI_τ are determined from the FE solution of the repaired panel. The value of failure indices are read into the optimization algorithm and over successive iterations the optimized value of patch dimensions and adhesive thickness are obtained that corresponds to the minimum value of failure indices which provides higher repair strength.

6.10.2 Optimized repair parameters: pure UD $[0°]_4$ and quasi−isotropic repaired panel $[\pm 45/0/90]_s$

Both pure UD $[0°]_4$ and quasi−isotropic $[\pm 45/0/90]_s$ panel configurations are considered for optimization study using multi−objective genetic algorithm in−conjunction with FEA together with Tsia−Wu and maximum shear stress failure criteria. The corresponding panels are repaired with identified best patch shape as recommended in section 6.7 and 6.8 respectively, and the optimization is carried out for double sided patch repair configuration. Extended octagonal patch shape of configuration $[0°]$ is considered for the repair of pure UD panel whereas oval patch shape of configuration $[\pm 45]s$ is for quasi−isotropic case. The panels and patches are made of same carbon/epoxy composite laminate as discussed in chapter 2 & 3. The FE model of the repaired panel is developed using the same approach as described in section 6.3. The material properties and strength parameters used in the optimization study is taken from chapter 2 and they are give in Table 2.9. The patches are bonded with Araldite 2011 adhesive whose properties are determined from DIC as discussed in chapter 5 and they are given in Table 5.1.

The optimization scheme implemented here is similar to the one described in section 6.9 and it is represented by a flowchart as depicted in Fig. 6.15. To begin the optimization process, initial value of design variables are specified. Theses design variables are read into ANSYS input file and the stress analysis is performed to obtain the value of failure indices FI_{TW} and FI_τ. The failure indices value is read into optimization algorithm and it is then checked for solution optimality and convergence criteria. If the solution optimality and convergence are achieved, the program terminates with optimal design variables. If not, the search continues till the optimal design variables are arrived.

Optimization results: pure UD $[0°]_4$ double sided repaired panel

The multi−objective GA solver in MATLAB is used to solve multi−objective optimization problem. The lower and upper bound of design variables and the GA parameters used in optimization algorithm are kept same as summarized in Table 6.4. The population size is specified as 50 and tolerance limit for convergence is set to 1e^{-}3. The optimal solution is arrived from the Pareto front as shown in Fig. 6.18. Pareto plot shows the trade−off between two objective functions FI_{TW} and FI_{τ} value. It is also defined as the set of non−inferior solutions. A non−inferior solution is the one in which an improvement in one objective requires a degradation of another. For example, in Fig. 6.18, A and B are clearly non−inferior solution points because an improvement in one objective leads to degradation in the other objective, i.e. at point A, FI_{τ} value is higher whereas at point B, FI_{TW} is higher. Therefore, selection of non−inferior solution point would be at point C leading to lower FI_{TW} and FI_{τ}.

The optimal solution obtained at point C results in minimum FI_{TW} value of 0.24 and FI_{τ} value of 0.091. The value of FI_{τ} shown in the pareto plot is represented in its normalized form and the applied stress is used for normalization. The value of FI_{τ} at point C is 14.4 in MPa. The corresponding optimized patch dimensions and adhesive thickness are given in Table 6.18. The optimal patch dimensions are: patch thickness $tp = 0.7\,t$, patch width $tw = 0.73\ t$, patch overlap length (longitudinal) $lpo = 4.38\,r$ (r is radius of open cutout), total patch length $lp = 1.46\,tw$. The optimized adhesive thickness is $ta = 0.2\,tp$.

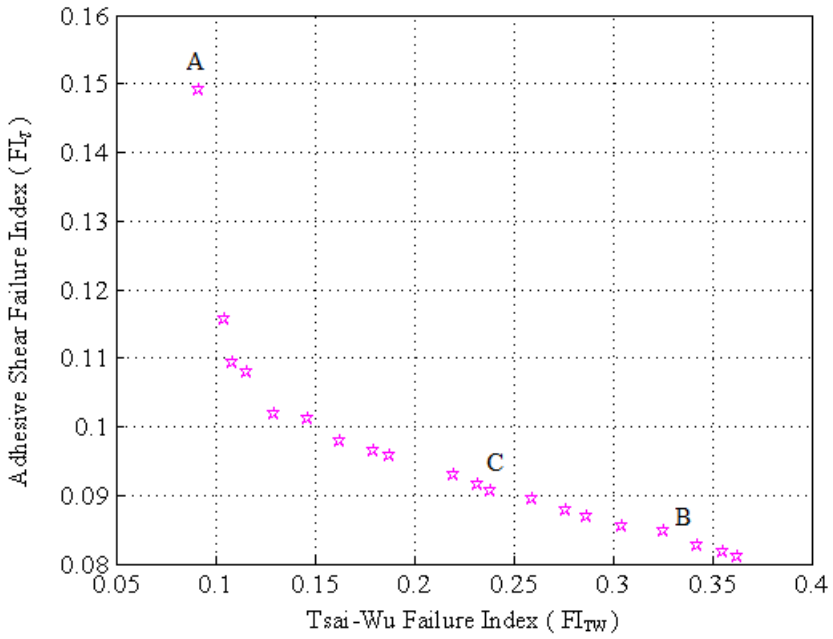

Figure 6.18: Pareto front obtained from multi−objective optimization study: pure UD double sided repaired panel

Table 6.6: Optimized repair parameters: pure UD $[0°]_4$ panel.

Design Parameters	Optimum value
Patch area (Ap)	1828.78 (mm^2)
Patch thickness (tp)	0.99 (mm)
Chamfer length (P)	12.21 (mm)
Adhesive thickness (ta)	0.2 (mm)

Optimization results: quasi−isotropic $[\pm 45/0/90]_s$ double sided repaired panel

The optimization study is also performed for quasi−isotropic panel by keeping the same GA parameters as used in pure UD case. The lower and upper bound of design variables used here are given in Table 6.7 and they governed by the panel geometry. The pareto plot obtained from the optimization study is shown in Fig. 6.19. The predicted optimized patch dimensions and adhesive thickness for the repair of quasi−isotopic panel corresponding to optimal point C are given in Table 6.8.

The optimal patch dimensions are: patch thickness $tp = 0.67\,t$, patch width $tw = 0.8\ t$, patch overlap length (longitudinal) $lpo = 1.25\,r$ (r is radius of open cutout), total patch length (longitudinal) $lp = 0.56\,tw$. The optimized adhesive thickness is $ta = 0.11\,tp$.

Table 6.7: Lower and upper bound of design variables: quasi−isotropic repaired panel.

Design Parameters	Lower bound	Upper bound
Patch area (Ap) in mm^2	400	1200
Patch thickness (tp) in mm	0.4	2.4
Adhesive thickness (ta) in mm	0.05	0.3

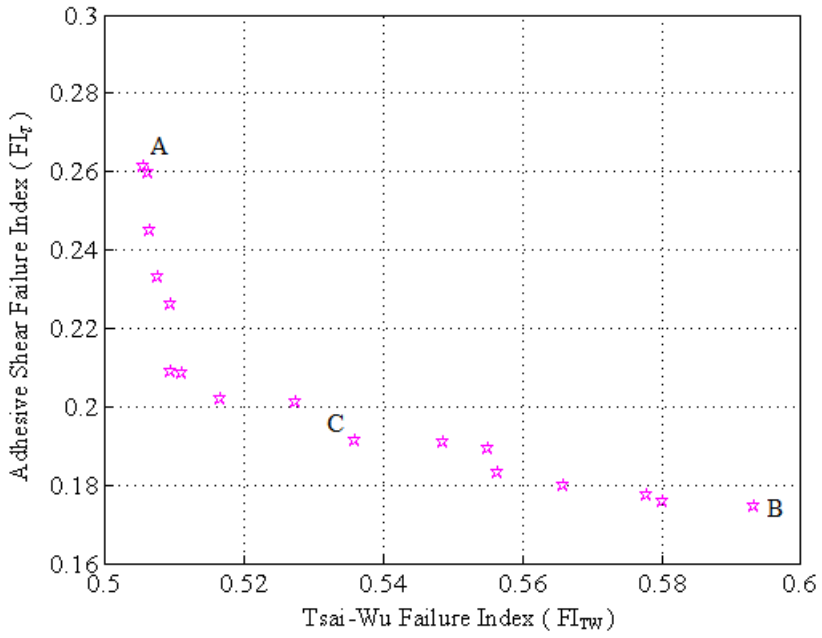

Figure 6.19: Pareto front obtained from multi−objective optimization study: quasi−isotropic double sided repaired panel

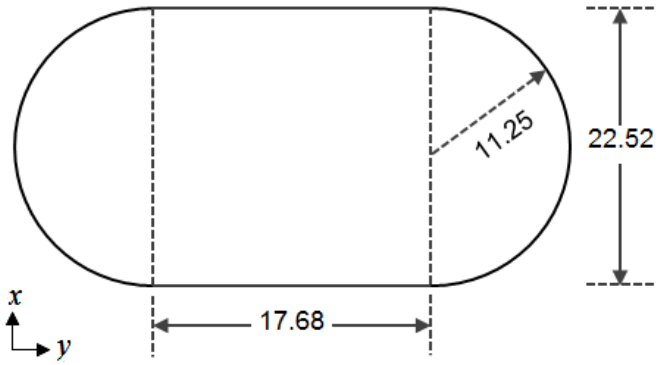

Figure 6.20: Optimized patch geometry for oval patch shape (in mm)

Table 6.8: Optimized repair parameters: quasi−isotropic panel.

Design Parameters	Optimum value
Patch area (Ap)	796.56 (mm^2)
Patch thickness (tp)	1.88 (mm)
Adhesive thickness (ta)	0.19 (mm)

6.10.3 Experimental study with optimized patch dimensions and adhesive thickness

The specimens are fabricated with the aforementioned optimum patch dimensions, and whole field strain analysis is carried out using DIC for the case of both pure UD and quasi−isotropic double sided patch repaired panel. The same patch dimensions are used for the single−sided repair configuration for a comparative study. Two types of specimens are prepared in both the cases: one without filling the open cutout in the panel, and the other in which the open cutout in the panel is filled with Araldite 2011 adhesive which acts as a filler material. The specimen fabrication process, experimental setup and the test procedure is same as discussed in chapter 3. The obtained experimental result are presented in the following sub−sections.

6.10.4 Whole field strain analysis: pure UD configuration

The images acquired by the camera system are post−processed using the available Correlated Solutions Vic−3D software to obtain the whole strain distribution over the patch and panel surface. The ROI chosen for correlation is 47.5 mm × 94.5 mm which corresponds to 585 × 1170 pixels^2. The spatial resolution is 12.3 pixels/mm. A subset size of 29 ×29 pixels^2 is selected along with a step size of 7 pixel for DIC calculation.

Figures 6.21 (a)−(b) shows the whole field strain maps over the surface of single and double sided patch repaired panel at a load of 7.5 kN. The open cutout in both the the panel is filled with the adhesive material. The uncorrelated area is observed around the patch edge due to shading or sudden step.

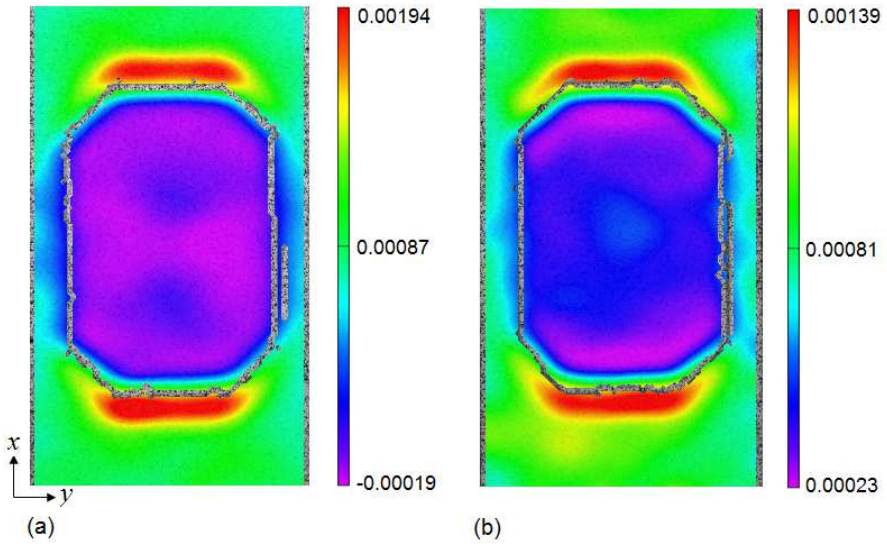

Figure 6.21: Whole field strain longitudinal strain (ε_{xx}) distribution observed experimentally using DIC for $[0°]_4$ panel repaired with optimized extended octagonal patch at a load of 7.5 kN (a) single sided repair (b) double sided repair

In case of both single and double sided repaired panel, the maximum value of ε_{xx} is observed at upper and lower edge of the patch along the $x-$direction (loading direction). This is because one cannot measure the strain at the hole in repaired configuration and therefore overlap edge bears the maximum strain due to high stress concentration, leading to to debonding of patch starting from this location with increased loading. The value of ε_{xx} is found to be minimum at the patch center in single sided repair whereas in double sided repair it is minimum at the zone between patch overlap edge and patch center. The failure initiates with partial patch debonding at overlap edge and the damage development is found to be similar to the one as discussed in chapter-3.

6.10.5 Whole field strain analysis: quasi$-$isotropic panel configuration

The ROI chosen for correlation is 47.6 mm $\times$ 70.5 mm which corresponds to 585 $\times$ 875 pixels^2. The spatial resolution is 12.3 pixels/mm. A subset size of 29 $\times$29 pixels^2 along with a step size of 7 pixel is selected for DIC calculations.

Figures 6.22 (a)$-$(b) shows the whole field surface strain map of ε_{xx} in single and double sided patch repaired panel obtained from DIC. Here also the filler material is used in open cutout in the panel. In case of both single and double sided repaired panel, it can be observed that a highly strained zone (ε_{xx}) is present at both upper and lower edge of the patch along the loading direction. The highly strained zone at patch overlap edge is due to high peel/shear stress aiding in patch debonding from the panel. It is found that the damage initiates from the hole edge and the final failure of the panel takes place with complete debonding of patch from parent panel followed by fiber breakages in $\pm45°$ and $0°$ plies along them across the panel width. No damage is observed in the debonded patch and the damage zone in all cases is confined around the net$-$section across the width of the panel nearer to the hole.

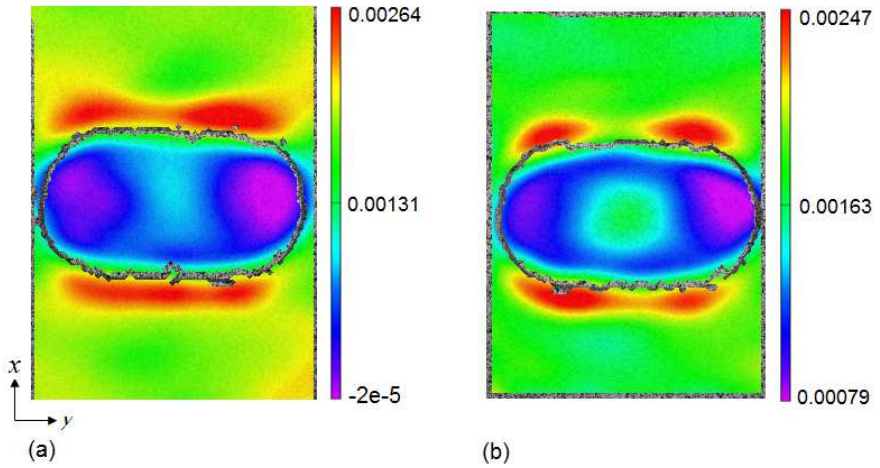

Figure 6.22: Whole field strain (ε_{xx}) distribution observed experimentally using DIC for $[\pm 45/0/90]_s$ panel repaired with oval patch at a load of 8.8 kN(a) single sided repair (b) double sided repair

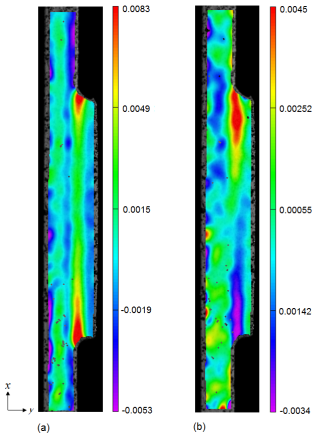

Figure 6.23: Shear strain variation in adhesive layer of single sided patch repaired panel at load of 18.08 kN(Araldite 2011)(a) Peel strain (ε_{xx}) strain (b) Shear strain (ε_{xz})

Further, the strain measurement in adhesive layer of quasi−isotropic panel repaired with oval patch is carried out using 2D−DIC. Global strain analysis in adhesive layer is performed by using the same procedure as discussed in chapter 5. The peel and shear strain distribution in single and double quasi−isotropic panel repaired with optimized oval patch is shown in Fig. 6.23 and Fig. 6.24 respectively. The peel and shear strain distribution present a similar nature as discussed in chapter−5. From the strain maps of both single and double sided repair, it can be observed that the peel strain is maximum at the patch overlap edge near the corner of the adhesive joint. This high stress concentration near the patch overlap edge leads to patch debonding as the load increases. Also, it is evident from both the cases that the maximum shear strain is located at the patch overlap edge between the adhesive−patch interface. This shear strain concentration is due to abrupt change in geometry at the patch end. In both the cases, it is found that the damage initiates from the adhesive−panel interface due to adhesive layer failure, as expected because of high stress concentration zone as predicted by DIC.

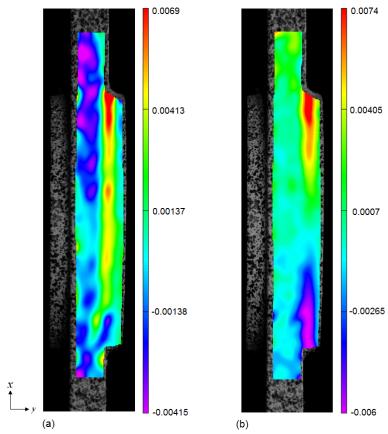

Figure 6.24: Shear strain variation in adhesive layer of double sided patch repaired panel at load of 18.01 kN(Araldite 2011)(a) Peel strain (ε_{xx}) strain (b) Shear strain (ε_{xz})

6.10.6 Strength of panels repaired with optimized patch geometry: pure UD and quasi−isotropic panel configuration

The average load carrying capacity of pure UD and quasi−isotropic panels repaired with corresponding optimized patch geometry and adhesive thickness are given in Table 6.9. The ultimate load taken by the panels repaired after filling the open cutout in the panel are also reported in the table.

In case of pure UD panel, it is found that the single sided repair configuration with filler material in open cutout in the panel carries 0.65 kN more load as compared to the one without filler material, showing an improvement of 0.9 % in ultimate load value. The double sided patch repaired panel with filler material carries 1.24 kN more load than its counterpart. Therefore, one can conclude that the effect of filler material on ultimate load value in double sided repaired panel is more as compared to the single sided one. Also, the double sided repair configuration carries more load than single sided repair. Further, the ultimate value of the load taken by the pure UD panel repaired with circular patch as discussed in chapter 3 is compared with the one repaired with optimized extended octagonal patch here. It is found that the panel repaired with optimized extended octagonal patch (with filler material in open cutout in the panel) have got 8.3 kN and 9.76 kN more load in case of single and double side repair respectively, as compared to the one repaired with circular patch shape. Therefore, on overall comparison in case of pure UD panel, it can be conclude based on the obtained results that, with optimized patch geometry and adhesive thickness, one can achieve 88.5% of virgin panel strength in case of single sided repair and 97.5% in case of double sided repair.

In case of quasi−isotropic panel, it is found that the single and double sided repair configuration with filler material has got 1.13 kN and 2.06 kN more load respectively as compared to the one without filler material. Also, the double sided repair is more effective than single sided repair. Further, on comparison, it is found that the panel repaired with optimized oval patch (with filler material in open cutout in the panel) have got 7.19 kN and 8.03 kN more load in case of single and double side repair respectively as compared to the one repaired with circular patch shape (as discussed in chapter 3). Therefore, on overall comparison it can be conclude based on the obtained results that, with optimized patch geometry and adhesive thickness in case of quasi−isotropic case, one can achieve 81.3% of virgin strength in case of single sided repair and 95.73% of virgin strength

in case of double sided repair.

Table 6.9: Ultimate Load of the panels repaired with optimized patch dimensions and adhesive thickness: pure UD and quasi−isotropic configuration.

Load (kN)				
Panel Configuration	Single Sided		Double Sided	
	without filler	with filler	without filler	with filler
Pure UD	70.45	71.10	76.12	78.36
Quasi−isotropic	41.53	42.66	48.17	50.23

Table 6.10: Percentage restoration in ultimate strength of the panels repaired with optimized patch dimensions and adhesive thickness (with respect to virgin panel strength): pure UD and quasi−isotropic configuration.

Restoration (%)				
Panel Configuration	Single Sided		Double Sided	
	without filler	with filler	without filler	with filler
Pure UD	87.6	88.5	94.7	97.5
Quasi−isotropic	79.1	81.3	91.8	95.7

6.11 Closure

A finite element based study is presented in this chapter to understand the influence of patch shape on repair performance. Both pure UD and quasi−isotropic double sided panel configurations are studied. Reduction in SCF and peel stress level are considered for evaluating repair efficiency. Failure initiation strength in case of pure UD panel is then predicted from 3D Hashin's failure criterion for arriving at best patch shape. It is found that there is a drastic reduction in SCF irrespective of patch shape in repaired panels as compared to the open cutout panel. It is also observed that the reduction in SCF increases with increasing patch area because of increased load transfer done by the patch. It is found that the extended octagonal patch performs better in case of repair of pure UD panel. The study on quasi−isotropic panels reveals that the patch shape are sensitive to the panel stacking sequence in repair performance and therefore one needs to appropriately choose the patch shape depending on panel stacking sequence. In case of panels with stacking sequence of $[0/\pm 45/90]_s$ and $[0/90/\pm 45]_s$ rectangular patch with greater width ($B > H$) has performed better. On the other hand transverse oval patch has performed better for the panels with stacking sequence of $[\pm 45/0/90]_s$ and $[90/0/\pm 45]_s$.

Finally, a GA based approach in−conjunction with FEA is used for arriving at the optimum dimension of best patch shape and adhesive thickness applied repair of pure UD $[0°]_4$ and quasi−isotropic panel with stacking sequence $[\pm 45/0/90]_s$. Multi−objective optimization is performed based on Tsai−Wu failure index and adhesive shear failure index and optimal patch dimensions and adhesive thickness are obtained for the case of double sided patch repair. Same patch dimensions and adhesive thickness are retained for single sided repair. From the experiment it is found in case of pure UD configuration that, the panel repaired with optimized extended octagonal patch have got 8.3 kN and 9.76 kN more load in case of single and double side repair respectively, as compared to the one repaired with circular patch shape. With optimized patch and adhesive thickness in pure UD case, the ultimate tensile strength of damaged panel is restored to 88.5% and 97.5% of virgin panel strength in case of single and double sided repair respectively. In case of quasi−isotropic panel, it is found that the panel repaired with optimized oval patch have got 7.19 kN and 8.03 kN more load in case of single and double side repair respectively as compared to the one repaired with circular patch shape. With optimized patch and adhesive thickness in quasi−isotropic case, the ultimate tensile strength of damaged panel is restored to 81.3% and 95.73%of virgin panel strength in case of single and double sided repair respectively.

Chapter 7

Conclusions and Recommendations for Future Work

7.1 Conclusions

Most of the research in composite patch repair application has been focused mainly on restoring the integrity of cracked aluminium panels since the aircrafts were mainly made of aluminium. Presently, aircraft structural components are mostly made of composites, which are more prone to damage due to low velocity impacts during its service life. Since more and more composites are now being used in today's applications, more repair of composite structures have to be administered in the near future. Therefore, it is essential to understand the behaviour of patch repaired composite panels including its damage mechanism to ensure the higher efficiency of repair resulting in increased integrity of damaged structure closer to the original one.

The present research work focused on understanding the tensile behaviour of open hole Carbon fiber reinforced polymer repaired with the adhesively bonded patch. Both pure unidirectional and quasi−isotropic panels are considered in this study. The DIC technique is first explored for suitable and accurate determination of CFRP laminate properties utilizing whole field strain data and the obtained results are compared with analytical one. The sensitivity of DIC parameters on material properties and complex strain field such as in the case of open cutout composite panel have been investigated for instilling confidence in DIC's utility. Full field strain variation over the surface of the panel as well as the patch is analyzed using 3D DIC technique. Damage initiation and its propagation in open cutout and repaired panel is successfully monitored using DIC. A 3D finite element based PDM is developed for strength and the failure mechanism prediction. The predictions of developed PDM are found to be in good coherence with the experimental observation. Adhesive layer behaviour is also successfully analyzed based on global−cum−local strain field analysis in repaired configuration using DIC. Effective load transfer/shear transfer length is introduced based on the strain profile obtained from global strain analysis and it is compared with the FEA prediction. Further, a linear 3D finite element analysis is performed to identify the best patch shape. Finally, a genetic algorithm based approach in−conjunction with FEA is implemented for the dimensional optimization of identified best patch shape as well as adhesive layer thickness for obtaining higher repair efficiency. Experimental study is then carried out with the obtained optimum patch dimen-

sions and adhesive thickness, and the whole field strain analysis using DIC as well as as well as the percentage restoration in ultimate strength of repaired panels are discussed.

The chapterwise summary of contributions made in this thesis is presented in subsequent paragraphs.

In chapter−2, a detailed methodology is presented for evaluating all the elastic constants as per ASTM standard towards characterizing CFRP laminate using DIC technique. Table 2.9 summarizes the CFRP properties obtained from DIC. The obtained DIC results are compared with the one obtained from extensometer and micro−mechanics based analytical models namely *rule of mixture* and *Halpin− Tsai model*. It is found that the value of longitudinal modulus obtained from DIC measurement and extensometer is in close agreement with an error of 0.8%. The error between DIC measurement and theoretically estimated value for the case of longitudinal modulus and in−plane Poisson's ratio is found to be 1.3% and 2.9% respectively, thereby confirming the accuracy of DIC technique. Further, an elaborate study is also carried out to investigate the influence of DIC parameters such as speckle size, subset size, step size and region of interest on material properties of matrix and composite laminate. It is found that the speckles with relatively small and closely spaced (denser) pattern provides improved displacement resolution and helps in capturing minute strain gradient. The subset size has shown to have more influence on material properties as compared to step size. Optimum value of subset size and step size predicted for characterization of both matrix and composite material are found to be consistent with each other. The lower and upper bound for subset size is found to be 21 × 21 and 41 × 41 pixels^2 whereas for step size it is of 6 and 9 pixels respectively. The aspect ratio of predicted optimum ROI is found to be 1.23 which is very much close to the aspect ratio of camera resolution 1.2 being used here. Therefore, it is suggested that the aspect ratio of ROI chosen for correlation should be the same as that of camera's aspect ratio for better correlation. Furthermore, an open cutout CFRP panel is also studied to demonstrate the influence of DIC parameters on complex strain field. It is observed that the strain field surrounding the hole is more sensitive to step size rather than subset size. Lower step size results in highly pixilated strain field, showing sensitivity of local strain at the expense of computational time along with random scattered noisy pattern whereas higher step size mitigates the noisy pattern at the expense of losing the detail present in the actual data. Based on comparison between DIC and FEA results, it is found that a step size of 5 or 7 pixels can be chosen as it provides a close match with FEA result pertaining to the trend and magnitude. The subset size variation mainly presents a smoothing effect, eliminating noise from the strain field while maintaining the details in the data and their natural trend. The subset size variation has shown negligible influence on magnitude of strains. However, increase in subset size significantly reduces the strain value at hole edge due to discontinuity in correlation.

In chapter−3, results from both experiment and numerical study are presented to analyze the performance of externally bonded patch repair on pure UD $[0°]_4$ and quasi−isotropic $[\pm 45/0/90]_s$ CFRP panels under tensile loading. The strain field obtained from DIC shows up the critical locations (prone to damage) and further helps us in predicting the damage initiation since asymmetry in strain pattern appears with damage initiation. It is found that the highly localized strains always develop around the transverse edge of the hole as well as at patch overlap edge in both pure UD and quasi−isotropic panels. The damage in the panels always initiates with matrix cracking around the hole. The damage propagation in pure UD case is always perpendicular to the hole

edge with extensive fiber splitting along the loading direction. In case of quasi−isotropic panel, damage propagates with extensive matrix cracking in all the plies and fiber failures running along the fiber direction in 45° and 0° plies across the panel width. The final failure of repaired panels in both pure UD and quasi−isotropic cases happens with complete debonding of the patch. In case of pure UD configuration, single sided repair restores 76% of undamaged or virgin panel strength whereas double sided repair restores 85% of virgin panel strength. For the case of quasi−isotropic panels, single and double sided repair restores 71% and 82% of virgin panel strength respectively. Therefore, double sided patch configuration is recommended for repair application. Finally, full field strain variations obtained from FEA are compared with the experiment results in both the cases and they are found to be in good coherence. Further,a finite element based study is carried out to understand the mechanics of composite patch repair on damaged CFRP panel of configuration $[\pm 45/0/90]_s$. It is found that the SCF decreases with increasing patch thickness but shear stress in adhesive layer increases. It is also observed that with increase in adhesive thickness, the adhesive shear stress decreases but SCF increases. Further, as the patch diameter increases, the SCF and shear stress reduces. Based on SCF and shear stress level, a patch thickness of 1.3 mm, adhesive thickness of 0.15 mm and a patch diameter of 40 mm is chosen towards an integral repair system.

In chapter−4, a finite element based 3D progressive damage model is developed for predicting the failure and post failure behaviour of open cutout and repaired panel under in−plane tensile load and the results are compared with the experimental results presented in chapter 3. Stress based 3D−Hashin's failure criterion is employed for predicting the damage mechanism. Maximum shear stress and strain criterions are considered to account for patch debonding. Material property degradation method is implemented for damage modeling to account for the effect of damage on load bearing strength of the panels. From PDM it is found that, in case of pure UD panel, damage always emanates with matrix cracking around the transverse edge of the hole which is identified as a damage prone location from DIC measurement due to high stress concentration. The damage initiation location is similar for both open cutout and single sided repaired panel. However, in case of double sided repaired panel the damage initiates in the form of matrix cracking at the patch overlap edge due to high stress concentration. The damage propagation in case of pure UD panels always occur perpendicular to the hole edge with extensive longitudinal splitting as observed in experimental results. It is also found that, the tensile strength predicted by maximum strain failure criteria used for adhesive is lower in case of single sided repair and it is higher in case of double sided repair as compared to the values predicted by maximum stress criteria. In case of quasi−isotropic panels, the damage initiates is also in the form of transverse matrix cracking from the hole edge as expected from DIC measurement and it is first observed in 90° ply for all the cases. The damage in case of quasi−isotropic panel consists of extensive matrix cracking and fiber failures running along it in 45° and 0° plies across the width of the panel. In case of repaired panel, the final failure of both pure UD and quasi−isotropic panel takes place soon after the complete debonding of the patch due to high shear stress in the adhesive layer, as observed in experimental study. The tensile strength predicted by PDM in case of pure UD open cutout, single and double sided repair configuration presents a variation of 5%, 4.5% and 3.3% respectively, in comparison to the experimental results whereas in case of quasi−isotropic panel, the variation in tensile strength of open cutout, single and double sided repair configuration predicted by PDM is 4%, 5.1% and 1.5% respectively.

In chapter−5, an experimental study involving DIC technique is presented to characterize the strain field in adhesively layer in case of single and double sided patch repaired CFRP panel under tensile load. The longitudinal, peel and shear strains in single and double sided repair are found to be maximum near the corner or root of adhesive joint at the patch overlap edge. The effective shear transfer length for single and double sided repair configuration is found to be 32% and 30.4% of total the patch length respectively. Conventional DIC along with magnified optics is found to be capable of exactly capturing the localized complex strain field at the patch overlap edge. The global and local strain analysis are complementary to each other and helps in understanding the complex strain field that develops in the adhesive layer. In case of single sided repair, it is found that the presence of bending load in addition to in−plane tensile load amplifies the strain levels, particularly a remarkable increase in peel strain is observed as compared to double sided repair configuration for a given load. Also, the shear strain in adhesive layer is found to be significantly higher compared to peel strain in case of single sided repair. It is also found that the single sided panel repaired with tapered edge patch shows higher strains in the adhesive layer near the patch overlap edge in comparison to the one repaired with straight edge patch. However, similar patch edge tapering in case of double sided repair reduces the strain level. The influence of adhesive nature on strain distribution in the adhesive layer for double sided repaired panel reveals that the ductile adhesive leads to higher shear strain as compared to the brittle one. Finally, a finite element based study is carried out to get the whole field strain distribution in the adhesive layer and its prediction is compared with the DIC results and they appear to be in good coherence.

In chapter−6, a linear 3D finite element analysis is performed to study the the influence of patch shape on repair efficiency in case of double sided patch repair configuration. It is found that there is a drastic reduction in SCF irrespective of patch shape in repaired panels as compared to the open cutout panel. It is found that the extended octagonal patch performs better in case of repair of pure UD panel. The study on quasi−isotropic panels reveals that the patch shape are sensitive to the panel stacking sequence in repair performance and therefore one needs to appropriately choose the patch shape depending on panel stacking sequence. In case of panels with stacking sequence of $[0/\pm 45/90]_s$ and $[0/90/\pm 45]_s$ rectangular patch with greater width ($B > H$) has performed better. On the other hand transverse oval patch has performed better for the panels with stacking sequence of $[\pm 45/0/90]_s$ and $[90/0/\pm 45]_s$. Finally, a GA based approach in−conjunction with FEA is used for arriving at the optimum dimension of best patch shape and adhesive thickness applied repair of pure UD $[0^\circ]_4$ and quasi−isotropic panel with stacking sequence $[\pm 45/0/90]_s$. Multi−objective optimization is performed based on Tsai−Wu failure index and adhesive shear failure index and optimal patch dimensions and adhesive thickness are obtained for the case of double sided patch repair. Same patch dimensions and adhesive thickness are retained for single sided repair. From the experiment it is found in case of pure UD configuration that, the panel repaired with optimized extended octagonal patch have got 8.3 kN and 9.76 kN more load in case of single and double side repair respectively, as compared to the one repaired with circular patch shape. With optimized patch and adhesive thickness in pure UD case, the ultimate tensile strength of damaged panel is restored to 88.5% and 97.5% of virgin panel strength in case of single and double sided repair respectively. In case of quasi−isotropic panel, it is found that the panel repaired with optimized oval patch have got 7.19 kN and 8.03 kN more load in case of single and double side repair respectively as compared to the one repaired with circular patch shape. With optimized patch and adhesive thickness in

quasi−isotropic case, the ultimate tensile strength of damaged panel is restored to 81.3 % and 95.73 %of virgin panel strength in case of single and double sided repair respectively.

7.1.1 Concluding Remarks

- The DIC technique is found to be a most suitable and accurate method for composite characterization utilizing whole field strain data and also helps in damage monitoring based on the surface strain anomalies.
- It is found that the damage in open cutout and repaired panel for all the cases always initiates with matrix cracking followed by damage propagation along the fiber direction. The final failure of repaired panel happens with complete debonding of the patch and single sided repair is found to be less efficient than the double sided repair in-terms of ultimate tensile strength.
- The progressive failure analysis reveals that the debonding behaviour in single sided repair is distinct than the double sided repair. The predictions of the developed PDM are found to be consistent with the experimental observation.
- Global cum local strain analysis is recommended to fully understand the behaviour of thin adhesive layer, playing a crucial role in load transfer between patch and panel. It is proposed that the patch overlap length should be in the range of 1.5−2 times the diameter of the cutout.
- Extended octagonal patch shape is recommended for the repair of pure UD panel whereas rectangular and oval patch shapes are recommended for the repair of quasi−isotropic panels.
- With optimized patch dimension and adhesive thickness it is possible to restore the repaired panel strength of about 95%−97.5% of virgin panel strength.

7.2 Recommendations for future work

The properties of CFRP laminates presented in chapter−2 are evaluated based on full field strain data obtained from DIC measurements. At least five number of tests are required to perform for determining all the in−plane elastic constants and strength parameters as per ASTM standard. To reduce the number of tests involved, the heterogeneous strain field offered by composite materials can be exploited for direct characterization of such materials. Therefore, the experimental characterization of CFRP laminate by employing the technique of virtual field method (VFM) could be the next attempt to get the maximum number of parameters from fewer tests.

The results presented in chapter−2 and −3 show that the prominent strain component i.e., longitudinal strain obtained from DIC is more closer to the FEA result as compared to transverse strain. The significant loss in displacement/strain data near the hole due to edge un−correlation could be one of the reasons for deviation between FEA and DIC measurement. Therefore, it is suggested to develop an improved strain estimation algorithm that could carry out the hole edge (boundary) correlation for accurate displacement and strain measurement. Also, there is a considerable deviation between the shear strain obtained from DIC and FEA results. The current DIC algorithm is finding it difficult to capture precisely the high strain gradients and highly non−linear shear strain data, and therefore some improvement in the present DIC algorithm could be done in that direction as one of the future work.

Linear elastic behaviour of adhesively bonded patch repair is investigated based on finite element analysis. Both CFRP panel and adhesive are considered as linear elastic material. The present work can be extended to study the non−linear response of adhesively layer by including it's behaviour as material non−linearity to precisely deduce the strain field. Also the viscoelastic nature of the CFRP laminate could be modeled for precisely capturing it's behaviour .

Hashin's failure criterions is considered in this work for predicting the damage in CFRP laminate. The present study can be extended to compare the predictive capability of different interactive and non−interactive failure theories towards bonded patch repair application. Their prediction could be compared with the experimental results for their accuracy.

The integrity of the repaired structure essentially relies on the workmanship. Therefore, appropriate NDT method such as Infrared Thermography can be explored to detect and ensure the proper bonding at the interface between patch and panel. The failure mechanism in open cutout and repaired panel can also be studied using NDT methods and the results can be compared with progressive damage results presented in this thesis.

In addition, the fractographic analysis of the tested specimen is recommended to investigate the fractured surface morphology which will further provide the information on void content, ply integrity, heterogeneity of fiber distribution, adhesive behviour, that would further help us to understand the damage mechanism in open cutout and repaired panels.

Tensile behaviour of adhesively bonded patch repair is being studied thoroughly as part of the current work. However, in practical applications the loading in the structures is generally complex and one may encounter different kinds of loading case or a combination of them. Therefore, to better understand the behaviour of the repaired composite panel under different loading conditions, the study of behaviour of repaired panel under compressive load could be the next logical attempt. Compressive behaviour is more interesting to be studied because it involves delamination and micro−buckling of fibers which is not primary concern in tensile loading case. Furthermore, the

behaviour of repaired panel under combined load could also be studied.

The response of the composite structure under fatigue loading is of great importance for aircraft structural applications. Therefore, the current work could be extended for the study of repaired CFRP laminate under fatigue load towards understanding the damage initiation, progression and failure mechanism, which would be the basis for the structural reliability assessment.

References

[1] https://images.google.com/; http://thedesigninspiration.com/articles/lamborghini-sesto-elemento-with-carbon-fiber-structure/; http://www.ruwings.ru/photo/var/albums/Boeing-787-Dreamliner/6.jpg?m=1350846786 .

[2] http://scienceinnews.blogspot.in/2012/09/carbonfibreanewerainaircraftdesign.html .

[3] A. J. Fawcett and G. D. Oakes. Boeing composite airframe damage tolerance and service experience. In Proceedings of the FAA workshop for composite damage tolerance and maintenance. National Institute for Aviation Research, Chicago, IL., 2006 .

[4] http://www.tech.plym.ac.uk/sme/mats324 .

[5] J. M. Berthelot and J. M. Cole. Mechanical Behaviour of Composite Materials and Structures. Mechanical Engineering Series. Springer, 1999.

[6] M. C. LafarieFrenot, C. HnaffGardin, and D. Gamby. Matrix cracking induced by cyclic ply stresses in composite laminates. *Composites Science and Technology* 61, (2001) 2327–2336.

[7] http://www.google.co.in/imgres/beoing787dreamlinerfire .

[8] http://www.dsto.defence.gov.au/research/5598/; http://www.compositesworld.com/articles/insitucompositerepairbuildsonbasics .

[9] R. Talreja and C. V. Singh. Damage and Failure of Composite Materials. Ist edition. Cambridge University Press, 2012.

[10] MILHDBK173F. Composite Materials Handbook. Department of Defense USA, 2002.

[11] S. R. Reid and G. Zhou. Impact behaviour of fibrereinforced composite materials and structures. Woodhead Publishing Limited, Abington Hall, Abington, Cambridge CB1 6AH, England, 2000.

[12] F. L. Matthews, G. A. O. Davies, D. Hitchings, and C. Soutis. Finite element modelling of composite materials and structures. Woodhead Publishing Ltd and CRC Press LLC, Abington Hall, Abington. Cambridge CB1 6AH, England, 2003.

[13] B. Harris. Engineering Composite Material. The Institute of Materials, London, 1999.

[14] M. R. Bhutt. Non destructive evaluation of defects and damage in composite materials and structures. *Journal of the Indian Institute of Science* 93, (2013) 751–765.

[15] W. J. Staszewski, C. Boller, and T. G. R. Health Monitoring of Aerospace Structures: Smart Sensor Technologies and Signal Processing. John Wiley & Sons, Ltd., 2004.

[16] Y. BarCohen. Emerging NDE Technologies and Challenges at the Beginning of the 3rd Millennium Part I. *Materials Evaluation* 58, (2000) 17–30.

[17] Y. BarCohen. Emerging NDE Technologies and Challenges at the Beginning of the 3rd Millennium Part II. *Materials Evaluation* 58, (2000) 141–150.

[18] A. Baker, L. R. F. Rose, and R. Jones. Advances in the Bonded Composite Repair of Metallic Aircraft Structure. Elsevier Science Ltd, Australia, 2002.

[19] A. Baker and P. R. Jones. Bonded Repair of Aircraft Structures. Springer, 1998.

[20] C. Soutis and F. Hu. Design and performance of bonded patch repairs of composite structures. *Proceedings of the Institution of Mechanical Engineers, Part G: J of Aerospace Engg* 21, (1997) 263–271.

[21] Q. Wang and N. Wu. A review on structural enhancement and repair using piezoelectric materials and shape memory alloys. *Smart Materials and Structures* 21.

[22] Q. Wang, S. T. Quek, and K. M. Liew. On the repair of a cracked beam with a piezoelectric patch. *Smart Materials and Structures* 11, (2002) 404–410.

[23] I. M. Daniel. Failure of composite materials. *Strain* 43, (2007) 4–12.

[24] U. Icardi, S. Locatto, and A. Longo. Assessment of recent theories for predicting failure of composite laminates. *Transactions of the ASME* 60, (2007) 76–86.

[25] M. J. Hinton, A. S. Kaddour, and P. D. Soden. Failure criteria in fibre reinforced polymer composites. Elsevier, Amsterdam, Netherlands, 2004.

[26] M. J. Hinton, A. S. Kaddour, and P. D. Soden. A comparison of the predictive capabilities of current failure theories for composite laminates, judged against experimental evidence. *Composites Science and Technology* 62, (2002) 1725–1797.

[27] M. N. Nahas. Survey of failure and postfailure theories of laminated fiberreinforced composites. *Composites Technology & Research* 8, (1986) 138–153.

[28] A. C. Orifici, I. Herzberg, and R. S. Thomson. Review of methodologies for momposite material modeling incorporating failure. *Composite Structures* 86, (2008) 194–210.

[29] C. F. Jenkins. Report On Materials Of Construction Used In Aircraft And Aircraft Engines. Technical Report, Great Britain Aeronautical Research Committee 1920.

[30] M. E. Waddoups. Advanced Composite Material Mechanics For Design And Stress Analysis. Technical Report, General Dynamics, Fort Worth Division Report FZM4763, Fort Worth, TX. 1967.

[31] S. W. Tsai and E. M. Wu. A general theory of strength for anisotropic materials. *Composite Materials* 5, (1971) 58–80.

[32] V. D. Azzi and S. W. Tsai. Anisotropic strength of composites. *Experimental Mechanics* September, (1965) 283–288.

[33] O. Hoffman. The brittle strength of orthotropic materials. *Composite Materials* 1, (1967) 200–206.

[34] C. C. Chamis. Failure criteria for filamentary composites. *Composite Materials:Testing and Design, STP 460, ASTM, Philadelphia* 336–351.

[35] Z. Hashin and A. Rotem. A fatigue failure criterion for fiber reinforced materials. *Journal of Composite Materials* 7, (1973) 44–64.

[36] Z. Hashin. Failure criteria for unidirectional fibre composites. *ASME Journal of Applied Mechanics* 47, (1980) 329–334.

[37] A. Puck and H. Schrmann. Failure analysis of FRP laminates by means of physically based phenomenological models. *Composite Science and Technology* 62, (2002) 1633–1662.

[38] F. K. Chang and K. Y. Chang. A progressive damage model for laminated composites containing stress concentrations. *Journal of Composite Materials* 21, (1987) 834–855.

[39] F. K. Chang, L. B. Lessard, and J. M. Tang. Compression response of laminated composites containing an open hole laminates. In SAMPE Quarterly, volume 4. 1988 46–51.

[40] F. K. Chang and L. B. Lessard. Damage tolerance of laminated composites containing an open hole and subjected to compressive loadings: Part I-Analysis. *Composite Materials* 25, (1991) 2–43.

[41] L. B. Lessard and F. K. Chang. Damage tolerance of laminated composites containing an open hole and subjected to compressive loadings: part IIexperiment. *Composite Materials* 25, (1991) 44–64.

[42] P. Pal and C. Ray. Progressive failure analysis of laminated composite plates by finite element method. *Journal of Reinforced Plastics and Composites* 21, (2002) 1505–1513.

[43] R. Kathiravan and R. Ganguli. Strength design of composite beams using gradient and particle swarm optimization. *Composite Structures* 81, (2007) 471–479.

[44] P. K. Gudla and R. Ganguli. An automated hybrid geneticconjugate gradient algorithm for multimodal optimization problems. *Applied Mathematics and Computation* 167, (2005) 1457–1474.

[45] J. H. Holland. Adaptation in Natural and Artificial Systems. University of Michigan Press, Ann Arbor, 1975.

[46] D. E. Goldberg. Genetic Algorithms in Search, Optimization, and Machine Learning. AddisonWesley Publishing, Lancaster, 1989.

[47] R. H. Lopez, M. A. Luersen, and E. S. Cursi. Optimization of laminated composites considering different failure criteria. *Composites: Part B* 40, (2009) 731–740.

[48] B. Pan, K. Qian, H. Xie, and A. Asundi. Two-dimensional Digital Image Correlation for In-plane Displacement and Strain Measurement: A Review. *Measurement Science and Technology* 20.

[49] W. H. Peters and W. F. Ranson. Digital imaging techniques in experimental stress analysis. *Optical Engineering* 21, (1982) 427–431.

[50] W. H. Peters, W. F. Ranson, M. A. Sutton, T. C. Chu, and J. Anderson. Application of digital correlation methods to rigid body mechanics. *Optical Engineering* 22, (1983) 738–742.

[51] M. A. Sutton, W. J. Wolters, W. H. Peters, W. F. Ranson, and S. R. McNeil. Determination of displacements using an improved digital image correlation method. *Image Vision Computing* 1, (1983) 133–139.

[52] T. C. Chu, W. F. Ranson, and M. A. Sutton. Applications of digitalimage correlation techniques to experimental mechanics. *Experimental Mechanics* 25, (1985) 232–244.

[53] M. A. Sutton, C. Mingqi, W. Peters, Y. Chao, and S. R. McNeill. Application of an optimized digital correlation method to planar deformation analysis. *Image Vision Computing* 4, (1986) 143–150.

[54] M. A. Sutton, S. R. McNeil, J. Jang, and M. Babai. Effects of subpixel image restoration on digital correlation error estimates. *Optical Engineering* 27, (1988) 870–877.

[55] H. A. Bruck, S. R. McNeil, M. A. Sutton, and W. H. Peters. Digital image correlation using Newton Raphson method of partial differential correction. *Experimental Mechanics* 29, (1989) 261–267.

[56] M. A. Sutton, J. L. Turner, H. A. Bruck, and T. A. Chae. Fullfield representation of discretely sampled surface deformation for displacement and strain analysis. *Experimental Mechanics* 31, (1991) 168–177.

[57] M. A. Sutton, S. R. McNeil, J. D. Helm, and Y. J. Chao. Advances in twodimensional and threedimensional computer vision. *Photomechanics:Topics in Applied Physics* 77, (2000) 323–372.

[58] H. W. Schreier, R. J. Braasch, and M. A. Sutton. Systematic errors in digital image correlation caused by intensity interpolation. *Optical Engineering* 39, (2000) 2915–2921.

[59] M. A. Sutton, S. R. McNeill, J. Helm, and Y. Chao. Photomechanics, Topics in Applied Physics, volume 77, chapter Advances in twodimensional and threedimensional computer vision, 323372. Springer, 2000.

[60] M. A. Sutton, J. J. Orteu, and H. W. Schreier. Image Correlation for Shape and Deformation Measurements, Basic Concepts, Theory and Applications. Springer, 2009.

[61] A. Giachetti. Matching techniques to compute image motion. *Image Vision Computing* 18, (2000) 247–260.

[62] W. Tong, H. Tao, N. Zhang, and J. L. G. Hector. Timeresolved strain mapping measurements of individual PortevinLe–Chatelier deformation bands. *Scripta Materialia* 53, (2005) 87–92.

[63] B. Pan, H. Xie, Z. Guo, and T. Hua. Full-field strain measurement using a two-dimensional Savitzky-Golay digital differentiator in digital image correlation. *Optical Engineering* 46.

[64] B. Pan. Reliability-guided digital image correlation for image deformation measurement. *Appl. Opt.* 48, (2009) 1535–1542.

[65] L. B. Meng, G. C. Jin, and X. F. Yao. Application of iteration and finite element smoothing technique for displacement and strain measurement of digital speckle correlation. *Optics and Lasers in Engineering* 45, (2007) 57–63.

[66] C. C. Wang, J. Deng, G. A. Ateshian, and C. T. Hung. An automated approach for direct measurement of twodimensional strain distributions within articular cartilage under unconfined compression. *Biomechanical Engineering* 124, (2002) 557–567.

[67] G. F. Xiang, Q. C. Zhang, H. W. Liu, X. P. Wu, and X. Y. Ju. Timeresolved deformation measurements of the Portevin–Le Chatelier bands. *Scripta Materialia* 56, (2007) 721–724.

[68] B. Pan, A. Asundi, H. Xie, and J. Gao. Digital image correlation using iterative least squares and pointwise least squares for displacement field and strain field measurements. *Optics and Lasers in Engineering* 47, (2009) 865–874.

[69] M. A. Sutton, J. H. Yan, V. Tiwari, H. W. Schreier, and J. J. Orteu. The effect of outof-plane motion on 2D and 3D digital image correlation measurements. *Optics and Lasers in Engineering* 46, (2008) 746–757.

[70] D. Garcia and J. J. Orteu. Accurate calibration of a stereovision sensor: comparison of different approaches. In 5th Workshop on Vision Modeling. 2000 .

[71] J. J. Orteu. 3D computer vision in experimental mechanics. *Optics and Lasers in Engineering* 47, (2009) 282–291.

[72] R. I. Hartley and P. Sturm. Triangulation. *Computer Vision and Image Understanding* 68, (1997) 146–157.

[73] L. Toubal, M. Karama, and B. Lorrain. Stress concentration in a circular hole in composite plate. *Composite Structures* 68, (2005) 31–36.

[74] C. Soutis, D. M. Duan, and P. Goutas. Compressive behaviour of CFRP laminates repaired with adhesively bonded external patches. *Compos Structure* 45, (1999) 289–301.

[75] F. Z. Hu and C. Soutis. Strength prediction of patchrepaired CFRP laminates loaded in compression. *Composite Science and Technology* 60, (2000) 110–314.

[76] X. Liu and G. Wang. Progressive failure analysis of bonded composite repairs. *Composite Structures* 81, (2007) 331–340.

[77] X. J. Gong, P. Cheng, J. Rousseau, and S. Aivazzadeh. Effect of local stresses on static strength and fatigue life of patched composite panels. In 16th International Conference on Composite Materials (ICCM16). Kyoto, Japan, 2007 .

[78] R. D. S. G. Campilho, M. F. S. F. deMoura, D. A. Ramantani, J. J. L. Morais, and J. J. M. S. Domingues. Tensile behaviour of threedimensional carbonepoxy adhesively bonded single and doublestrap repairs. *Adhesion & Adhesives* 29, (2009) 678–686.

[79] R. D. S. G. Campilho, M. F. S. F. deMoura, D. A. Ramantani, J. J. L. Morais, and J. J. M. S. Domingues. Buckling strength of adhesivelybonded single and doublestrap repairs on carbonepoxy structures. *Composites Science and Technology* 70, (2010) 371–379.

[80] P. Cheng, X. J. Gong, and S. Aivazzadeh. Optimisation of patched repair for CFRP laminates. In Proceedings of 17th International Conference on Composite Materials. Edinburgh, UK., 2009 .

[81] P. Cheng, X. J. Gong, and S. Aivazzadeh. Design and optimization of composite laminates repaired by bonding external patches. In Proceedings of 18th International Conference on Composite Materials. Jeju, Korea, 2011 .

[82] P. Cheng, X. J. Gon, D. Hearn, and S. Aivazzadeh. Tensile behaviour of patchrepaired CFRP laminates. *Composite Structures* 93, (2011) 582–589.

[83] H. Park and C. Kong. A study on low velocity impact damage evaluation and repair technique of small aircraft composite structure. *Composites: Part A* 42, (2011) 1179–1188.

[84] C. H. Shiuh and M. Chao. Adhesively bonded patch repair of composite laminates. *Adhesion Science and Technology* 25, (2011) 2569–2585.

[85] S. E. Yamada and C. T. Sun. Analysis of laminate strength and its distribution. *Composite Materials* 12, (1978) 275–284.

[86] S. C. Tan. A progressive failure model for composite laminates containing openings. *Composite Materials* 25, (1991) 556–577.

[87] F. Yang and C. L. Chow. Progressive damage of unidirectional graphite/epoxy composites containing a circular hole. *Journal of Composite Materials* 32, (1998) 504–525.

[88] S. R. Hallett and M. R. Wisnom. Experimental investigation of progressive damage and the effect of layup in notched tensile tests. *Journal of Composite Materials* 40, (2006) 119–141.

[89] I. Lapczyk and J. A. Hurtado. Progressive damage modeling in fiber reinfrced materials. *Composites: Part A* 38, (2007) 2333–2341.

[90] R. M. OHiggins, M. A. McCarthy, and C. T. McCarthy. Comparison of openhole tension characteristics of high strength glass and carbon fibrereinforced composite materials. *Composites Science and Technology* 68, (2008) 2770–2778.

[91] T. E. Tay, G. Liu, V. B. C. Tan, X. S. Sun, and D. C. Pham. Progressive failure analysis of composites. *Journal of Composite Materials* 42, (2008) 1921–1966.

[92] B. M. Zhang and L. Zhao. Progressive damage and failure modeling in fiberreinforced laminated composites containing a hole. *International Journal of Damage Mechanics* 21, (2011) 893–911.

[93] T. E. Tay, M. Ridha, G. Liu, and V. B. C. Tan. Progressive failure of notched and repaired composite. In Proceedings of 17th International Conference on Composite Materials (ICCM17). Edinburgh, UK, 2009 .

[94] K. J. Callahan and G. E. Weeks. Optimum design of composite laminates using genetic algorithms. *Composites Engineering* 2, (1992) 149–160.

[95] S. Nagendra and R. H. Z. G. Z. Stacking sequence optimization of simply supported laminates with stability and strain constraints. *AIAA J* 30, (1992) 2132–2137.

[96] L. R. Riche and R. T. Haftka. Optimization of laminate stacking sequence for buckling load maximization by genetic algorithm. *AIAA Journal* 31, (1993) 951–956.

[97] N. R. Ball, P. M. Sargent, and D. O. Ige. Genetic algorithm representations for laminate layups. *Artificial Intelligence in Engineering* 8, (1993) 99–108.

[98] J. H. Park, J. H. Hwang, C. S. Lee, and W. Hwang. Stacking sequence design of composite laminates for maximum strength using genetic algorithms. *Composite Structures* 52, (2001) 217–231.

[99] L. R. Riche and J. Gaudin. Design of dimensionally stable composites by evolutionary optimization. *Composite Structure* 41, (1998) 97–111.

[100] E. Potgeiter and N. Stander. The genetic algorithm applied to stiffness maximization of laminated plates: review and comparison. *Struct Optim* 15, (1998) 221–229.

[101] K. Sivakumar, N. G. R. Iyengar, and K. Deb. Optimum design of laminated composite plates with cutouts using a genetic algorithm. *Composite Structures* 42, (1998) 265–279.

[102] S. Nagendra, D. Jestin, Z. Gurdal, R. T. Haftka, and L. T. Watson. Improved genetic algorithm for the design of stiffened composite panels. *Composite Structures* 58, (1996) 543–555.

[103] E. Madenci, V. Kradinov, and D. R. Ambur. Application of genetic algorithm for optimum design of bolted composite lap joints. *Composite Structures* 77, (2007) 148–159.

[104] P. M. Pawar and R. Ganguli. Modelling progressive damage accumulation in thin walled composite beams for rotor blade applications. *Composites Science and Technology* 66, (2006) 2237–2249.

[105] Q. S. Ramon, R. Pedro, and P. J. Davim. Multiobjective optimization of cutting parameters for drilling laminate composite materials by using genetic algorithms. *Composite Science and Technology* 66, (2006) 3083–3088.

[106] C. Swann and A. Chattopadhyay. Optimization of piezoelectric sensor location for delamination detection in composite laminates. *Eng Optim* 38, (2006) 511–528.

[107] J. L. Pelletier and S. S. Vel. Multiobjective optimization of fiber reinforced composite laminates for strength, stiffness and minimal mass. *Composite Structures* 84, (2006) 2065–2080.

[108] F. S. Almeida and A. M. Awruch. Design optimization of composite laminated structures using genetic algorithms and finite element analysis. *Composite Structures* 88, (2009) 443–454.

[109] M. Walker and R. E. Smith. A technique for the multiobjective optimization of laminated composite structures using genetic algorithms and finite element. *Composite Structures* 62, (2003) 123–128.

[110] J. D. Mathias, X. Balandraud, and M. Grediac. Applying a genetic algorithm to the optimization of composite patches. *Computers and Structures* 84, (2006) 823–834.

[111] R. Brighenti. Patch repair design optimization for fracture and fatigue improvements of cracked plates. *Solids and Structures* 44, (2007) 1115–1131.

[112] D. A. Sutter. Threedimensional Analysis Of A Composite Repair And The Effect of Overply Shape Variation On Structural Efficiency. Technical Report, Department of the Air Force, Air Force Institute of Technology, USA 2007.

[113] L. F. M. da Silva, P. J. C. D. Neves, R. D. Adams, and J. K. Spelt. Analytical models of adhesively bonded joints Part I: Literature survey. *International Journal of Adhesion & Adhesives* 29, (2009) 319–330.

[114] L. F. M. da Silva and R. D. S. G. Campilho. Advances in numerical modeling of adhesive joints. Springer, Berlin:Heidelberg, 2012.

[115] D. F. Adams, L. A. Carlsson, and R. B. Pipes. Experimental Characterization of Advanced Composite Materials. 3rd edition. CRC Press LLC, 2003.

[116] P. Hung and S. A. Voloshin. Inplane strain measurement by digital image correlation. *Brazilian Society of Mechanical Sciences and Engineering* 25, (2003) 215–221.

[117] G. Cloud. Optical Methods of Engineering Analysis. Cambridge University Press, 1998.

[118] K. P. Rastogi. Photomechanics; Topics in Applied Physics. Springer, 2000.

[119] Y. Surrel. Fullfield optical methods for mechanical engineering: essential concepts to find one's way. In International Conference on Composites Testing and Model Identification. Bristol, U.K., 2004 .

[120] M. Grediac. The use of fullfield measurement methods in composite material characterization: interest and limitations. *Composites Part A* 35, (2004) 751–761.

[121] L. Robert, F. Nazaret, T. Cutard, and J. J. Orteu. Use of 3D digital image correlation to characterize the mechanical behavior of a fiber reinforced refractory castable. *Experimental Mechanics* 47, (2007) 761–773.

[122] M. J. Vassoler and A. E. Fancelloa. Error analysis of the digital image correlation method. *Mecanica Computacional* 29, (2010) 6149–6161.

[123] Y. Wang, P. Lava, S. Coppieters, S. M. De, P. V. Houtt, and D. D. Investigation of the uncertainty of DIC under heterogeneous strain states with numerical tests. *Journal of Strain* 48, (2012) 453–462.

[124] B. Pan, H. Xie, Z. Wang, K. Qian, and Z. Wang. Study on subset size selection in digital image correlation for speckle patterns. *Optics Express* 16, (2008) 7037–7048.

[125] H. W. Schreier and M. A. Sutton. Systematic errors in digital image correlation due to undermatched subset shape functions. *Experimental Mechanics* 42, (2002) 303–310.

[126] B. Pan, M. H. Xie, Q. B. Xu, and L. F. Dai. Performance of subpixel registration algorithms in digital image correlation. *Measurement Science and Technology* 17, (2006) 1615–1621.

[127] Y. Z. Wang, Q. H. Li, W. J. Tong, and T. J. Ruan. Statistical analysis of the effect of intensity pattern noise on the displacement measurement precision of digital image correlation using selfcorrelated images. *Experimental Mechanics* 47, (2007) 701–707.

[128] F. Y. Sun and J. H. Pang. Study of optimal subset size in digital image correlation of speckle pattern images. *Optics and Lasers in Engineering* 45, (2007) 967–974.

[129] J. G. Um and H. J. Kim. Experimental error assessment for image correlation analysis on a paper tensile specimen. *Journal of Industrial and Engineering Chemistry* 13, (2007) 214–218.

[130] M. Bornert, F. Bremand, P. Doumalin, J. C. Dupre, M. Fazzini, M. Grediac, F. Hild, S. Mistou, J. Molimard, J. J. Orteu, L. Robert, Y. Surrel, P. Vacher, and B. Wattrisse. Assessment of digital image correlation measurement errors: methodology and results. *Experimental Mechanics* 49, (2009) 353–370.

[131] D. I. Baere, V. W. Paepegem, N. Lammens, P. Lava, D. Debruyne, C. Cofaru, W. Philips, and J. Degrieck. Experimentally induced errors in digital image correlation measurement of small strains with large gradients. In 5th International Conference on Emerging Technologies in NonDestructive Testing (ETNDT5). Ioannina, Greece, 2011 .

[132] P. Lava, S. Cooreman, S. Coppieters, and D. Debruyne. Sources of systematic errors in the determination of heterogeneous strain fields obtained via DIC. In Application of Imaging Techniques to Mechanics of Materials and Structures; Conference Proceedings of the Society for Experimental Mechanics Series, volume 4. 2013. 271–281.

[133] Lopez, A. R, W. F. E. l. Chiti, M. L, J. H. Dagher, D. L. Thompson, and E. P. Hess. Composite material testing using a 3D digital image correlation. In COMPOSITES 2004 Convention and Trade ShowAmerican Composites Manufactures Association. Tampa, Florida USA, 2004 .

[134] P. Melrose, A. R. Lopez, and L. Muszynski. Elastic properties of sandwich composite panels using 3D digital image correlation with the hydromat test system. In SEM X International Congress & Exposition on Experimental & Applied Mechanics. Costa Mesa, California USA, 2004 .

[135] W. F. E. l. Chiti, A. R. Lopez, J. H. Dagher, D. L. Thompson, M. L, and E. P. Hess. Experimental approach for characterizing VARTM composites using a 3D digital image correlation system. In SEM Annual Conference & Exposition on Experimental and Applied Mechanics. Portland, Oregon, 2005 .

[136] K. Berube and A. R. Lopez. Fullfield strain measurements for determining mechanical properties of marine composite laminates. In SEM XI International Congress & Exposition on Experimental & Applied Mechanics. Orlando, Florida, USA, 2008 .

[137] P. Feraboli, E. Peitso, and T. Cleveland. Modulus measurement for prepregbased discontinuous carbon fiber/epoxy systems. *Composite Materials* 43, (2009) 1947–1965.

[138] A. Makeev, Y. He, B. Shonkwiler, E. Lee, H. Schreier, and Y. Nikishkov. A method for measurement of threedimensional constitutive properties for composite materials. In 18th International Conference on Composite Materials (ICCM18). South Korea, 2011 .

[139] L. Qin, Z. Zhang, X. Li, X. Yang, Z. Feng, Y. Wang, H. Miao, L. He, and X. Gong. Fullfield analysis of shear test on 3D orthogonal woven C/C composites. *Composites: Part A* 43, (2012) 310–316.

[140] F. Laurina, J. S. Charriera, D. Levequea, J. F. Mairea, A. Mavela, and P. Nuneza. Determination of the properties of composite materials thanks to digital image correlation measurements. *Procedia IUTAM* 4, (2012) 106–115.

[141] M. A. Caminero, S. Pavlopoulou, P. M. Lopez, B. G. Nicolaisson, C. Pinna, and C. Soutis. Analysis of adhesively bonded repairs in composites: Damage detection and prognosis. *Composite Structures* 95, (2013) 500–517.

[142] M. A. Caminero, P. M. Lopez, C. Pinna, and C. Soutis. Damage monitoring and analysis of composite laminates with an open hole and adhesively bonded repairs using digital image correlation. *Composites Part B: Engineering* 53, (2013) 76–91.

[143] http://www.huntsman.com/ .

[144] Vic Snap/Vic 2D/Vic3D software. Correlated solutions Inc, 2010, http://www.correlatedsolutions.com/ .

[145] Standard Test Method for Tensile Properties of Polymer Matrix Composite Materials. D3039/D3039M08. 2008.

[146] Standard test method for compressive properties of unidirectional or crossply fiberresin composites. ASTM D341087. 1987.

[147] Standard Test Method for InPlane Shear Response of Polymer Matrix Composite Materials by Tensile Test of a +45 Laminate. D3518/D3518M94. 2007.

[148] P. Mallick. Fiber Reinforced Composites: Materials, Manufacturing, and Design. 3rd edition. Taylor & Francis Group, LLC, New York, 2007.

[149] R. M. Christensen. The numbers of elastic properties and failure parameters for fiber composites. *Journal of Engineering Materials and Technology* 120, (1998) 110–113.

[150] Standard Test Methods for Constituent Content of Composite Materials. D317199. 2000.

[151] Standard Test Method for Tensile Properties of Plastics. D63810 2010.

[152] M. R. Jones. Mechanics of Composite Materials. 2nd edition. CRC Press LLC, 1998.

[153] K. A. Kaw. Mechanics of Composite Materials. 2nd edition. CRC Press LLC, 2006.

[154] R. Cintron and V. Saouma. Strain Measurements With The Digital Image Correlation System Vic2D. Technical Report, Center for Fast Hybrid Testing, University of Colorado 2008.

[155] ANSYS Inc. Release 13.0. ANSYS APDL Users Guide, Canonsburg, November 2010. .

[156] T. V. R. S. Umamaheswar and S. Ripudaman. Modeling of a patch repair to a thin cracked sheet. *Engg Fract Mech* 62, (1999) 267–289.

[157] O. A. Chukwujekwu, S. Navdeep, U. E. Enemouh, and S. V. Rao. Design, analysis and performance of adhesively bonded composite patch repair of cracked aluminium aircraft panels. *Composite Structures* 71, (2005) 258–270.

[158] M. L. Pastor, X. Balandraud, M. Grediac, and J. L. Robert. On the fatigue response of aluminium specimens reinforced with carbon epoxy patches. *Composite Structures* 83, (2008) 237–246.

[159] H. H. Toudeshky, B. Mohammadi, and H. R. Daghyani. Mixed mode fracture analysis of aluminium repaired panels using composite patches. *Comp Sci Technology* 66, (2006) 188–198.

[160] H. H. Toudeshky, B. Mohammadi, and S. Bakhshandeh. Mixedmode fatigue crack growth of thin aluminium panels with singleside repair using experimental and numerical methods. *Fatigue Frac Engg Mat Struct* 30, (2007) 629–639.

[161] C. H. Duong. A Unified approach to geometrically nonlinear analysis of tapered bonded joints and doublers. *International J Solids and Structures* 43, (2005) 3498–3526.

[162] L. F. M. da Silva, E. Ramos, M. V. Figueiredo, and T. R. Strohaecker. Influence of the adhesive, the adherend and the overlap on the single lap shear strength. *Journal of Adhesion and Interface* 7, (2006) 1–9.

[163] P. B. Philip, S. Arunkumar, and B. C. Prasad. Comparison of damage path predictions for composite laminates by explicit and standard finite element analysis tools. In Proceedings of the AIAA/ASME/ASCE/AHS/ASC 47th Structures, Structural Dynamics & Materials Conference: AIAA. 2006 .

[164] Araldite2011, Structural Adhesive, Technical Data Sheet, Huntsman, 2009 .

[165] V. R. S. Turaga, Umamaheswar, and S. Ripudaman. Modelling of a patch repair to a thin cracked sheet. *Engineering Fracture Mechanics* 62, (1999) 267–289.

[166] W. R. Broughton, L. E. Crocker, and J. M. Urquhart. Strength Of Adhesive Joints: A Parametric Study. Technical Report, National Physical Laboratory: Materials centre, UK 2001.

[167] T. E. Tay, F. Shen, K. H. Lee, A. Scaglione, and S. M. Di. Mesh design in finite element analysis of postbuckled delamination in composite laminates. *Composite Structures* 47, (1999) 603–611.

[168] S. Shimizu. Tension buckling of plate having a hole. *ThinWalled Structures* 45, (2007) 827–833.

[169] C. T. McCarthy, M. A. McCarthy, and V. P. Lawlor. Progressive damage analysis of multibolt composite joints with variable bolt–hole clearances. *Composites: Part B* 36, (2005) 290–305.

[170] C. M. Sanchez and M. J. Greene. Evaluation Of Progressive Failure Analysis And Modeling Of Impact Damage In Composite Pressure Vessels, A Report. Technical Report, NASA USRP 2011.

[171] M. Lee, C. H. Wang, and E. Yeo. Effects of adherend thickness and taper on adhesive bond strength measured by portable pulloff tests. *International Journal of Adhesion and Adhesives* 44, (2013) 259–268.

[172] X. Zhao. Stress and failure analysis of adhesively bonded lap joints. Ph.D. thesis, Department of Mechanical Engineering, University of Bristol, UK 1991.

[173] P. K. Sahoo, B. Dattaguru, C. M. Manjunatha, and C. R. L. Murthy. Advances in Modeling and Design of Adhesively Bonded Systems, chapter Strength Prediction Methods for Adhesively Bonded Lap Joints between Composite–Composite/Metal Adherends. Scrivener Publishing LLC, 2013.

[174] M. D. Banea and L. F. M. da Silva. Adhesively bonded joints in composite materials: An overview. *Proceedings of the Institution of Mechanical Engineers, Part L: Journal of Materials Design and Applications* 223, (2009) 1–18.

[175] L. F. M. da Silva, P. J. C. D. Neves, R. D. Adams, A. Wang, and J. K. Spelt. Analytical models of adhesively bonded joints Part II: Comparative study. *International Journal of Adhesion & Adhesives* 29, (2009) 331–341.

[176] X. He. A review of finite element analysis of adhesively bonded joints. *International Journal of Adhesion & Adhesives* 31, (2011) 248–264.

[177] M. Y. Tsai and J. Morton. An experimental investigation of nonlinear deformations in single lap joints. *Mechanics of Materials* 20, (1995) 183–194.

[178] V. Shenoy, I. A. Ashcroft, G. W. Critchlow, A. D. Crocombe, and M. M. A. Wahab. An investigation into the crack initiation and propagation behaviour of bonded singlelap joints using backface strain. *International Journal of Adhesion & Adhesives* 29, (2009) 361–371.

[179] A. Derewonko, J. Godzimirski, K. Kosiuczenko, T. Niezgoda, and A. Kiczko. Strength assessment of adhesivebonded joints. *Computational Materials Science* 43, (2008) 57–64.

[180] A. Asundi. Deformation in adhesive joints using moir interferometry. *International Journal of Adhesion and Adhesives* 7, (1987) 39–42.

[181] J. A. Schroeder. Photoelastic stress analysis of bonded lap shear joints having thermoplastic adherends. *The Journal of Adhesion* 32.

[182] K. W. Colavito, M. Das, D. Hahs, J. Gorman, E. Madenci, and S. Smeltzer. Digital image correlation technique to extract adhesive strains in lap joints. In 49th AIAA/ASME/ASCE/AHS/ASC Structures, Structural Dynamics, and Materials Conference. 2008 .

[183] K. W. Colavito, J. Gorman, E. Madenci, and S. Smeltzer. Refinements in digital image correlation technique to extract adhesive strains in lap joints. In 50th AIAA/ASME/ASCE/AHS/ASC Structures, Structural Dynamics, and Materials Conference. 2009 .

[184] M. P. Moutrille, K. Derrien, D. Baptiste, X. Balandraud, and M. Grediac. Throughthickness strain field measurement in a composite/aluminium adhesive joint. *Composites: Part A* 40, (2009) 985–996.

[185] Z. Y. Wang, L. Wang, W. Guo, H. Deng, J. W. Tong, and F. Aymerich. An investigation on strain/stress distribution around the overlap end of laminated composite single lap joints. *Composite Structure* 89, (2009) 589–595.

[186] R. Haghani, M. AlEmrani, and R. Kliger. Effects of geometrical modifications on behaviour of adhesive joints used to bond CFRP laminates to steel members – experimental investigation. In Nordic Steel Construction Conference (NSCC). Malmo, Sweden, 2009 .

[187] B. Q. Guo, H. Xie, J. G. Zhu, and H. X. Wang. Study on the mechanical behavior of adhesive interface by digital image correlation. *Science China: Physics, Mechanics & Astronomy* 54, (2011) 574–580.

[188] P. D. Ruiz, F. Jumbo, J. M. Huntley, I. A. Ashcroft, and G. M. Swallowe. Experimental and numerical investigation of strain distributions within the adhesive layer in bonded joints. *Journal of Strain* 47, (2011) 88–104.

[189] A. J. Comer, K. B. Katnam, W. F. Stanley, and T. M. Young. Characterising the behaviour of composite single lap bonded joints using digital image correlation. *International Journal of Adhesion & Adhesives* 40, (2013) 215–223.

[190] K. B. Katnam, J. X. Dhote, and T. M. Young. Experimental analysis of the bondline stress concentrations to characterize the influence of adhesive ductility on the composite single lap joint strength. *The Journal of Adhesion* 89, (2013) 486–506.

[191] G. Crammond, B. S. W, and J. M. Dulieu-Barton. Through thickness load transfer in adhesively bonded composite joints. In Proceedings of the Society for Experimental Mechanics Series. 2013 111–114.

[192] R. L. V. Kumar, M. R. Bhat, and C. R. L. Murthy. Experimental analysis of composite single-lap joints using digital image correlation and comparison with theoretical models. *Journal of Reinforced Plastics and Composites* 32, (2013) 1858–1876.

[193] L. F. M. da Silva and R. D. Adams. Techniques to reduce peel stresses in adhesive joints with composites. *Int J Adhes Adhes* 27, (2007) 227–235.

[194] C. N. Duong and C. H. Wang. Composite Repair: Theory and Design. Elsevier Publications, Great Britain, 2007.

[195] M. Y. Tsai and J. Morton. An investigation into the stresses in doublelap adhesive joints with laminated composite adherends. *Solids and Structures* 47, (2010) 3317–3325.

[196] S. Kumar and M. K. L. Advances in Modeling and Design of Adhesively Bonded Systems. WileyScrivener, 2013.

[197] L. F. M. da Silva and J. C. Q. L. Maria. Joint strength optimization by the mixedadhesive technique. *Adhesion and Adhesives* 29, (2009) 509–514.

[198] E. J. Barbero. Finite Element Analysis of Composite Materials. Boca Raton: CRC Press, Taylor and Francis group, 2008.

[199] G. Lekhnitskiis, W. S. Tsai, and T. Cheron. Anisotropic plates. Gordon and Breach Science Publishers, New York, 1968.

[200] K. Sivakumar, N. G. R. Iyengar, and K. Debb. Optimization of composite laminates with cutouts using genetic algorithm, variable metric and complex search methods. *Engineering Project Organization Journal* 32, (2000) 635–657.

[201] Matlab2010a. MATLAB R2010a. Natick, USA: Math Works Inc., 2000.

[202] U. Topal and . Uzman. Strength optimization of laminated composite plates. *Journal of Composite Materials* 42, (2008) 1731–1746.

[203] R. Satheesh, G. N. Naik, and R. Ganguli. Conservative design optimization of laminated composite structures using genetic algorithms and multiple failure criteria. *Journal of Composite Materials* 44, (2010) 369–387.

[204] G. N. Naik, S. Gyan, R. Satheesh, and R. Ganguli. Minimum weight design of fibre reinforced laminated composite structures with maximum stress and Tsai–Wu failure criteria. *Journal of Reinforced Plastics and Composites* 30, (2010) 179–192.

List of Publications (Based on Thesis)

International Journal Publications

1. Kashfuddoja M and Ramji M. Whole−Field Strain Analysis And Damage Assessment Of Adhesively Bonded Patch Repair Of CFRP Laminates Using 3D−DIC And FEA. Composite Part B: Engineering. 53, 46−61, 2013.

2. Kashfuddoja M and Ramji M. Design Of Optimum Patch Shape And Size For Bonded Repair On Damaged Carbon Fibre Reinforced Polymer Panels. Materials and Design. 54, 174−183, 2014.

3. Kashfuddoja M and Ramji M. An Experimental And Numerical Investigation Of Progressive Damage Analysis In Bonded Patch Repaired CFRP Laminates. Journal of Composite Materials. 2013. DOI: 10.1177/0021998314521058.

4. Kashfuddoja M, Prasath RGR and Ramji M. Study on Experimental Characterization of Carbon Fibre Reinforced Polymer Panel using Digital Image Correlation: A Sensitivity Analysis. Optics and Lasers in Engineering. 62, 17−30, 2014.

5. Kashfuddoja M and Ramji M.Critical Analysis of Adhesive Layer Behaviour in Patch Repaired CFRP Panel Involving Digital Image Correlation. Journal of Composite Materials. 2014. DOI: 10.1177/0021998314541312.

6. Kashfuddoja M and Ramji M.Assessment of Local Strain Field in Adhesive Layer of an Unsymmetrically Repaired CFRP Panel Using Digital Image Correlation. International Journal of Adhesion and Adhesives, (Recommended publication with revision). 2014.

7. Kashfuddoja M and Ramji M. Multi−objective optimization of Adhesively Bonded Patch Repaired CFRP laminate using Failure Criteria : Experimental Validation. Journal of Reinforced Plastics and Composites, (To be communicated). 2014.

International Conference Publications

1. Kashfuddoja M and Ramji M. Experimental Investigation Of Repaired CFRP Laminates Using 3D−DIC. 11th Asian Conference on Experimental Mechanics, 2nd International Symposium on Experimental Mechanics, 2012 SEM Fall Conference, 2nd International Symposium on Experimental Mechanics (11th ACEM, 7th ISEM), November 9−11, Taipei, Taiwan, 2012.

2. Kashfuddoja M and Ramji M. Parametric Study On Patch Repaired CFRP Laminates Using FEA. Indo−Danish International Conference on Wind Energy: Materials, Engineering and Policies (WEMEP−2012), November 22−23, 2012, Hyderabad.

3. Kashfuddoja M and Ramji M. 3−D Progressive Failure Analysis Of Bonded Patch Repaired CFRP Laminates Under Tensile Load. Third Asian Conference on Mechanics of Functional Materials and Structures (ACMFMS)−2012, December 5−8, 2012, IIT Delhi.

4. Kashfuddoja M and Ramji M. Influence Of Patch Shape On Performance Evaluation Of Bonded Repaired CFRP Laminates. International Congress on Computational Mechanics and Simulation (ICCMS)−2012, December 10−12, 2012, IIT Hyderabad.

5. Kashfuddoja M and Ramji M. Adhesive Strain Measurement In Patch Repaired CFRP Laminate Using 2D DIC. The 19th International Conference On Composite Materials (ICCM−19), July 28−August 2. 2013, Montreal, Canada.

6. Kashfuddoja M and Ramji M. Optimization of Parameters Involved in Repair of CFRP Panel using Multi−objective Genetic Algorithm and Failure Criteria. 9th International Symposium on Advanced Science and Technology in Experimental Mechanics (9th ISEM), November 1−6. 2014, New Delhi, India.